Quantum Monte Carlo Simulation of Electron-Phonon Models and Computational Studies of Quantum Spin Systems

By

Owen Bradley

DISSERTATION

Submitted in partial satisfaction of the requirements for the degree of

DOCTOR OF PHILOSOPHY

in

PHYSICS

in the

OFFICE OF GRADUATE STUDIES

of the

UNIVERSITY OF CALIFORNIA

DAVIS

Approved:

Richard T. Scalettar, Chair

Rajiv R. P. Singh

Bruno Nachtergaele

Committee in Charge

2023

Contents

List of Figures

Abstract

We explore the emergence of a variety of quantum phases of matter by performing computational studies of several model Hamiltonians. We begin by introducing the Holstein Hamiltonian which describes the electron-phonon interaction on a lattice, and present Determinant Quantum Monte Carlo (DQMC) simulations which reveal the subtle interplay between superconductivity and charge density wave order, focusing on the doped square lattice. We perform a finite-size scaling analysis of pair susceptibility data to accurately determine critical transition temperatures in this model. A recently developed Hybrid Monte Carlo (HMC) algorithm is used to explore charge ordering on the kagome lattice, where we discover a long-ranged charge ordered phase. We then discuss integer-spin Kitaev honeycomb models, and present numerical studies of their thermodynamic behavior. We illustrate the sensitivity of the quantum spin liquid phase to single-ion anisotropy, and discuss the rich variety of thermodynamic behavior in these models. The disordered Ising antiferromagnet on the triangular lattice is also analyzed using transfer matrix calculations and classical Monte Carlo techniques. Our focus here is on the robustness of residual entropy plateaus to disorder and other perturbations, and discuss the relevance of these results to experimental systems. Finally, we present a study of the triangular lattice Hubbard model in a magnetic field, focusing on large U/t at temperatures beyond the exchange parameter $J = 4t^2/U$. Motivated by recent experiments on triangular lattice compound LCSO, we compare our numerical results for magnetization and entropy to experimental data.

Acknowledgments

Throughout my PhD there have been many people supporting and encouraging me along the way. I have been fortunate enough to have both Richard Scalettar and Rajiv Singh as co-advisors since my first year, and would like to extend my sincere gratitude to both. Their passion for physics and deep intuition for the subject has left a great impression on me, and they have always been available to discuss research and provide insightful guidance at any time. My time in graduate school has been a highly enjoyable journey thanks to their patience and the supportive environment they created. I have also greatly benefited from their support in attending conferences and summer schools throughout my PhD, which introduced me to the broader condensed matter community.

I would also like to thank a number of collaborators I have worked with during my PhD, who provided their expertise for several projects in this thesis, with whom I have benefited from many helpful discussions. These include George Batrouni, Kipton Barros, Steve Johnston, Ehsan Khatami, Jaan Oitmaa, Cole Miles, and Diptiman Sen. I would also like to extend my thanks towards office mates and fellow group members, past and current, including Ben Cohen-Stead, Yuxi Zhang, Chunhan Feng, Bo Xiao, Wei-Ting Chiu, Yutan Zhang, Eduardo Padilla, and Michael Flynn. Together they created a wonderful environment for discussing science and helped me immensely in various ways during my research projects.

I am also very grateful to have entered graduate school alongside friends who have supported me and made my experience much more enjoyable, including Matt Bellardini, Mac Robertson, Rahim Ullah, Victoria Norman, Andrew Ballin, Patty Bolan, Adam Kunesh, Sean Colin-Ellerin, and many more. My time in Davis has been such a fun experience thanks to their friendship and moral support.

Finally, I would like to thank my parents for their unwavering support during my time in graduate school. They have always been a source of encouragement during my PhD, and have continuously supported my academic pursuits and my decision to attend graduate school abroad. Without their support none of my accomplishments to date would have been possible.

CHAPTER 1

Introduction

1.1. The Many-Body Problem in Condensed Matter Physics

One of the central themes of condensed matter physics over the past few decades has been the concept of *emergence*, i.e. the onset of new kinds of phenomena arising from the collective behavior of large numbers of particles. The emergence of exotic phases of matter, for example in systems exhibiting superconductivity, charge density wave order, or quantum spin liquid behavior, is a consequence of the interactions between large ensembles of correlated electrons or strongly interacting quantum spins. These phases could not be predicted in advance through an understanding of single-particle behavior alone, and defy any explanation through classical physics. In principle, one could determine the behavior of a large number of interacting particles by solving the many-body Schrödinger equation, which governs their time evolution. This pursuit to understand the properties of many-body systems, and their emergent phases, through a quantum mechanical description of their constituents is a central goal of condensed matter physics today.

However, directly solving the many-body Schrödinger equation becomes completely infeasible for systems of more than a few particles. Moreover, the amount of computational storage one would require grows exponentially with the number of particles. This is the essence of the 'many body problem', and over the past few decades has led to the development of a range of analytical and numerical techniques under the umbrella of quantum many-body physics. Rather than attempting to exactly solve the many-body Schrödinger equation, instead an effective Hamiltonian can be formulated which is simpler to understand and study. Such a model should describe the key interactions which govern the physics of the material under study, while neglecting the less important degrees of freedom. Although studies of these effective models on finite-size lattices are still limited by our computational resources, since they capture the essential

physics of the condensed matter system of interest, we can nevertheless understand its behavior in the thermodynamic limit.

For example, the *Holstein model* is a simplified description of the electron-phonon interaction, where phonons are modeled as dispersionless quantum harmonic oscillators on each site of a regular lattice, along with a fixed on-site electron-phonon coupling. Although its Hamiltonian is too simplified to exactly describe any real material, it exhibits several emergent phases at low temperature, and thus provides a framework to understand the interplay between competing states of matter. A second prominent example is the *Hubbard model*, which is the simplest description of the electron-electron interaction between itinerant electrons on a lattice. Not only do these models capture the essential physics of real systems, they are amenable to study using powerful computational techniques such as Quantum Monte Carlo (QMC) simulation, Exact Diagonalization (ED), and other numerical methods. We will now introduce these two model Hamiltonians in more detail.

1.2. Model Hamiltonians: the Holstein and Hubbard Models

In 1950, the discovery of the isotope effect, i.e. the dependence of the superconducting transition temperature in a material on the ionic mass ($T_c \sim M^{-1/2}$) was an early indication that interactions between electrons and the underlying lattice could be related to superconductivity [1]. Since then, the study of electron-phonon interactions as a mechanism for superconductivity has attracted a great deal of interest. One of the most prominent effective models for the electron-phonon interaction is the Holstein model. This model was introduced in 1959 by Theodore Holstein as a description of the motion of a single tightly-bound electron within a one-dimensional molecular crystal, where on each site there is a diatomic molecule with a single vibrational degree of freedom [2]. For a single electron, the Holstein model serves as a description of a 'polaron', i.e. an electron dressed by moving in a sea of phonons. However, the Hamiltonian can equally be used to describe two-dimensional lattices of ions (or layered systems), where each ion is treated as a quantum harmonic oscillator (QHO) which is independent of its neighbors, along with multiple itinerant electrons in the system.

The Hamiltonian can be expressed as the sum of three parts: an electron kinetic energy term $\hat{K}$, the kinetic and potential energies of each oscillator $\hat{U}$, and an electron-phonon interaction term $\hat{V}$. Using the formalism of second quantization, the complete expression for the Holstein Hamiltonian is given by

$$\hat{H} = \underbrace{-t \sum_{\langle \mathbf{i},\mathbf{j}\rangle,\sigma} \left(\hat{c}^{\dagger}_{\mathbf{i}\sigma} \hat{c}_{\mathbf{j}\sigma} + \hat{c}^{\dagger}_{\mathbf{j}\sigma} \hat{c}_{\mathbf{i}\sigma} \right) - \mu \sum_{\mathbf{i}\sigma} \hat{n}_{\mathbf{i}\sigma}}_{\equiv \hat{K}} + \underbrace{\frac{1}{2} \sum_{\mathbf{i}} \hat{P}^2_{\mathbf{i}} + \frac{\omega_0^2}{2} \sum_{\mathbf{i}} \hat{X}^2_{\mathbf{i}}}_{\equiv \hat{U}} + \underbrace{\lambda \sum_{\mathbf{i}\sigma} \hat{n}_{\mathbf{i}\sigma} \hat{X}_{\mathbf{i}}}_{\equiv \hat{V}} . \tag{1.1}$$

Here, $\hat{c}^{\dagger}_{\mathbf{i}\sigma}$ and $\hat{c}_{\mathbf{i}\sigma}$ are creation and annihilation operators for an electron of spin $\sigma = \{\uparrow, \downarrow\}$ situated at site $\mathbf{i}$ of a lattice. The notation $\langle \mathbf{i}, \mathbf{j} \rangle$ indicates that the sum in the first term is over all nearest-neighbor pairs of sites. The first term therefore represents itinerant electrons hopping between neighboring sites, where the parameter t is the nearest-neighbor hopping integral, which sets the energy scale. In the second term, μ is the chemical potential, which controls the overall filling (i.e. the total number of electrons) of the system. $\hat{n}_{\mathbf{i},\sigma} = \hat{c}^{\dagger}_{\mathbf{i},\sigma} \hat{c}_{\mathbf{i},\sigma}$ is the number operator, which gives the number of electrons occupying a site. Due to the Pauli exclusion principle, the possible occupation states for a single site are $|0\rangle$, $|\uparrow\rangle$, $|\downarrow\rangle$, and $|\uparrow\downarrow\rangle$ only. For convenience, this term is grouped with the hopping term to define $\hat{K}$ — the electron kinetic energy.

On each site of the lattice there is a local quantum harmonic oscillator with fixed frequency ω_0. That is, we consider there to be a dispersionless optical phonon mode associated with each lattice site, with $\hat{X}_{\mathbf{i}}$ and $\hat{P}_{\mathbf{i}}$ the corresponding displacement and momentum variables, with the phonon mass normalized to $M = 1$. The third and fourth terms in Eq. 1.1 are thus the phonon kinetic energy and potential energy, respectively, which we group together to define $\hat{U}$. Electrons are coupled to the local phonon modes through an on-site electron-phonon interaction $\hat{V}$, with a fixed coupling strength λ. This on-site term involves the coupling of the phonon displacement variable $\hat{X}_{\mathbf{i}}$ with the electron occupation $\hat{n}_{\mathbf{i},\sigma}$.

We can see that a number of simplifying assumptions have been made. First, only electron hopping between nearest-neighbor lattice sites is incorporated into the Hamiltonian, i.e. any next-nearest neighbor terms are treated as less essential. Secondly, although a completely dispersionless phonon mode may be inexact for many real materials, the fact that phonon frequencies are considered momentum-independent i.e. $\omega(\mathbf{q}) = \omega_0$ is a reasonable approximation

for describing optical phonon modes. Treating the electron-phonon coupling as a momentum-independent constant i.e. $\lambda(\mathbf{q}) = \lambda$ is another simplification. Even though in real materials the electron-phonon coupling can have a non-trivial dependence on momentum, this simplification makes numerical simulation of the model much more feasible, and yet the resulting Hamiltonian gives rise to the kinds of complex ordered phases observed in real systems, such as charge density wave order and superconductivity.

The form of the electron-phonon interaction $\hat{V}$ can be motivated by writing this term in momentum space, by introducing the Fourier transform of the electron creation and annihilation operators via:

$$\hat{c}_{\mathbf{j},\sigma} = \frac{1}{\sqrt{N}} \sum_{\mathbf{k}} \hat{c}_{\mathbf{k},\sigma} e^{i\mathbf{k}\cdot\mathbf{j}} \tag{1.2}$$

$$\hat{c}^{\dagger}_{\mathbf{j},\sigma} = \frac{1}{\sqrt{N}} \sum_{\mathbf{k}} \hat{c}^{\dagger}_{\mathbf{k},\sigma} e^{-i\mathbf{k}\cdot\mathbf{j}} \tag{1.3}$$

where N is the total number of lattice sites, and noting that the phonon displacement $\hat{X}_{\mathbf{j}}$ can be expressed in terms of phonon creation and annihilation operators $\hat{b}^{\dagger}_{\mathbf{j}}$ and $\hat{b}_{\mathbf{j}}$ as follows

$$\hat{X}_{\mathbf{j}} = \frac{1}{2\omega_0} \left(\hat{b}^{\dagger}_{\mathbf{j}} + \hat{b}_{\mathbf{j}} \right) \tag{1.4}$$

$$\hat{b}_{\mathbf{j}} = \frac{1}{\sqrt{N}} \sum_{\mathbf{q}} \hat{b}_{\mathbf{q}} e^{i\mathbf{q}\cdot\mathbf{j}} \tag{1.5}$$

$$\hat{b}^{\dagger}_{\mathbf{j}} = \frac{1}{\sqrt{N}} \sum_{\mathbf{q}} \hat{b}^{\dagger}_{\mathbf{q}} e^{-i\mathbf{q}\cdot\mathbf{j}} \tag{1.6}$$

where $\hat{b}^{\dagger}_{\mathbf{q}}$ and $\hat{b}_{\mathbf{q}}$ are their respective Fourier transforms. Substituting these relations into $\hat{V}$ yields the following expression for the electron-phonon interaction in momentum space

$$\hat{V} = \frac{\lambda}{2\omega_0} \frac{1}{\sqrt{N}} \sum_{\mathbf{q},\mathbf{k},\sigma} \left[\hat{b}^{\dagger}_{\mathbf{q}} \hat{c}^{\dagger}_{\mathbf{k}-\mathbf{q},\sigma} \hat{c}_{\mathbf{k},\sigma} + \hat{b}_{\mathbf{q}} \hat{c}^{\dagger}_{\mathbf{k}+\mathbf{q},\sigma} \hat{c}_{\mathbf{k},\sigma} \right]. \tag{1.7}$$

This has a natural interpretation in terms of the two basic processes one should account for when describing the electron-phonon interaction. The first term in square brackets represents emission of a phonon with momentum $\mathbf{q}$, with an electron changing momentum from $\mathbf{k} \to \mathbf{k} - \mathbf{q}$. The second term describes absorption of a phonon with momentum $\mathbf{q}$, with an electron changing momentum from $\mathbf{k} \to \mathbf{k} + \mathbf{q}$.

A key feature of the Holstein model is that the electron-phonon interaction leads to an effective electron-electron attraction, causing electrons to pair and potentially condense into an long-range ordered phase such as a charge density wave or superconducting state. This is most easily seen by examining the single-site limit ($t = 0$) of the Holstein model. Here the Hamiltonian simplifies to

$$\hat{H} = \frac{1}{2}\hat{P}^2 + \frac{\omega_0^2}{2}\hat{X}^2 - \mu(\hat{n}_\uparrow + \hat{n}_\downarrow) + \lambda\hat{X}(\hat{n}_\uparrow + \hat{n}_\downarrow), \tag{1.8}$$

where $\hat{n}_\uparrow$ and $\hat{n}_\downarrow$ are the occupation numbers for spin-up and spin-down electrons on a single site, which can take values of 0 or 1 only. Completing the square, we can write

$$\hat{H} = \frac{1}{2}\hat{P}^2 + \frac{\omega_0^2}{2}\left[\hat{X} + \frac{\lambda}{\omega_0^2}(\hat{n}_\uparrow + \hat{n}_\downarrow)\right]^2 - \frac{1}{2}\frac{\lambda^2}{\omega_0^2}(\hat{n}_\uparrow + \hat{n}_\downarrow)^2 - \mu(\hat{n}_\uparrow + \hat{n}_\downarrow), \tag{1.9}$$

where we find that the third (negative) term represents an effective electron-electron attraction $U_{\text{eff}} = -\frac{\lambda^2}{\omega_0^2}$.

For the single-site case, the potential energy has a double-well structure, with minima corresponding to overall occupations of $(\hat{n}_\uparrow + \hat{n}_\downarrow) = 0$ or $(\hat{n}_\uparrow + \hat{n}_\downarrow) = 2$, while a singly-occupied site is higher energy. The electron-phonon interaction can therefore give rise to pairing of electrons. For example, on a square lattice at half-filling (an average of one electron per site) a checkerboard pattern of alternating doubly-occupied and empty sites can form—a periodic modulation of charge known as a charge density wave (CDW). Away from half-filling, the tendency to pair can result in superconducting order. The Holstein Hamiltonian, despite its simplifications, thus represents a paradigmatic model of the electron-phonon interaction which can provide insight into the competition between CDW order and superconductivity in real materials. For example, the bismuthates $BaBiO_3$ exhibit CDW order at half-filling, but when doped with K or Pb, a superconducting transition occurs which is thought to be driven by strong electron-phonon coupling [3, 4].

One of the most widely studied models of strongly correlated electron systems is the Hubbard model, which incorporates an electron-electron interaction. It was introduced in 1963 by John Hubbard, originally to explain the properties of transition metal oxides such as FeO and NiO which are antiferromagnetic insulators [5]. However, it has also been applied to the study of high-T_c superconductors, in particular the cuprates which exhibit d-wave superconductivity. As in the

Holstein model, electrons are free to hop between neighboring sites of an underlying lattice, however the interaction term introduces an energy cost to doubly-occupied sites, reflecting on-site Coulomb repulsion. The Hubbard Hamiltonian is given by

$$\hat{H} = -t \sum_{\langle \mathbf{i},\mathbf{j} \rangle, \sigma} \left(\hat{c}^{\dagger}_{\mathbf{i},\sigma} \hat{c}_{\mathbf{j},\sigma} + \hat{c}^{\dagger}_{\mathbf{j},\sigma} \hat{c}_{\mathbf{i},\sigma} \right) - \mu \sum_{\mathbf{i}} \left(\hat{n}_{\mathbf{i},\uparrow} + \hat{n}_{\mathbf{i},\downarrow} \right) + U \sum_{\mathbf{i}} \hat{n}_{\mathbf{i},\uparrow} \hat{n}_{\mathbf{i},\downarrow}, \tag{1.10}$$

where $U > 0$ is the (repulsive) Hubbard interaction parameter. On bipartite lattices, fixing the chemical potential at $\mu = U/2$ ensures the system is at half-filling, i.e. $\langle \hat{n} \rangle = 1$. These are geometries which can be divided into two sublattices A and B, such that each A site is surrounded by B sites, and vice versa, as in the square or honeycomb lattices. It can be seen that doubly-occupied sites (for which $\hat{n}_{\mathbf{i},\uparrow} \hat{n}_{\mathbf{i},\downarrow} = 1$) increase the total energy by U. Hence the interaction term promotes the formation of local magnetic moments i.e. sites that are only singly-occupied. The Hubbard model at half-filling has antiferromagnetic order, and at large U exhibits Mott insulating behavior, where electrons will not hop to neighboring singly-occupied sites due to the large energy cost involved.

As an effective Hamiltonian, a number of simplifying assumptions are reflected in Eq. 1.10. The first is that hopping between next-nearest neighbor sites (i.e. sites belonging to the same sublattice on bipartite geometries) is not considered. The second simplification is that it considers a single orbital per site only, which can accommodate no more than a pair of spin-up and spin-down electrons (however, there are extensions of the model for multi-orbital systems). In the basic version of the Hubbard model, long range Coulomb interactions are also neglected, i.e. the interaction between electrons on neighboring lattice sites. Despite these simplifications, the Hubbard model has been extensively applied to describe the qualitative behavior of many strongly correlated electron systems, in particular materials exhibiting antiferromagnetic order, Mott insulating behavior, and d-wave superconductivity, and it remains one of the most widely studied models in condensed matter physics today [6, 7, 8, 9, 10, 11].

1.3. Models of Magnetism and Quantum Spin Liquids

Several chapters in this thesis are devoted to studying the thermodynamic behavior of both classical and quantum spin systems. For a variety of models, we will study quantities such as entropy and magnetization as a function of temperature or other parameters in the Hamiltonian,

such as magnetic field strength or single-ion anisotropy. Calculating these quantities can provide information about the onset of different phases, and thus act as signatures which can be used to construct a phase diagram for a model Hamiltonian, or be compared to experimental measurements of real materials. As an introduction to this work, we will present here the model Hamiltonians studied, which each describe interacting spins situated on each site of an underlying lattice: the Ising model, Heisenberg model, and Kitaev model.

The most basic model of magnetic behavior is the *Ising model*, which was originally proposed to describe ferromagnetic materials exhibiting a net magnetic moment even in the absence of an applied magnetic field. This is a classical spin model where at each site i of a lattice there is a spin which can only take one of two discrete values: $S_i = 1$ (spin-up) or $S_i = -1$ (spin-down), and spins interact with their nearest-neighbors only. The energy of a particular configuration of spins is given by

$$H = -J \sum_{\langle i,j \rangle} S_i S_j, \tag{1.11}$$

where the sum is over all nearest-neighbor pairs, and J is the coupling strength. $J > 0$ corresponds to a ferromagnetic interaction, where it is energetically favored for neighboring spins to align. $J < 0$ corresponds to an antiferromagnetic interaction where it is energetically favored for neighboring spins to be anti-parallel. The model on a square lattice is exactly solvable [12], and exhibits a phase transition to a long-range ordered ferromagnetic or antiferromagnetic state depending on the sign of J, as the temperature is lowered below $T_c = \frac{2}{\ln\left(1+\sqrt{2}\right)} J \approx 2.269J$.

For bipartite geometries like the square lattice Ising model, all bonds will be satisfied in the ground state (which has all spins parallel for $J > 0$ or anti-parallel $J < 0$). However, we can consider an antiferromagnetic Ising model on a triangular lattice, which is an illustrative example of geometric frustration. With spins situated at the vertices of a triangular plaquette, it is not possible to place each spin such that is anti-parallel to its neighbors. Therefore there will necessarily be bonds in the triangular lattice which are not satisfied, and thus no unique ground state configuration. Instead there is an exponentially large ground state degeneracy reflected in a non-zero residual entropy of the system even as the temperature $T \to 0$ [13, 14].

If the spins are treated quantum mechanically, we obtain the quantum *Heisenberg model* which describes the exchange interaction between neighboring spins. The Hamiltonian for the Heisenberg

model is given by

$$\hat{H} = \sum_{i,j} J_{ij} \hat{\mathbf{S}}_i \cdot \hat{\mathbf{S}}_j, \tag{1.12}$$

where $\hat{\mathbf{S}}_i$ is a spin operator for site i, with $\hat{\mathbf{S}}_i^2 = S(S+1)$ for the spin-S case. Components of spin satisfy the commutation relation $[\hat{S}_i^\alpha, \hat{S}_i^\beta] = i\epsilon_{\alpha,\beta,\gamma}\hat{S}_i^\gamma$. In the simplest case, the exchange parameter J_{ij} can be taken to be non-zero only if i and j are nearest-neighbors, and the same for all bonds i.e. $J_{ij} = J$. It should be noted that there is a mapping between the Hubbard model at large U (which promotes local magnetic moments) and the spin-1/2 antiferromagnetic Heisenberg model, with an effective exchange parameter $|J| = \frac{4t^2}{U}$.

On the triangular lattice, with nearest-neighbor interactions J_1 only, the ground state is an ordered 120° phase, with three-sublattice order [15] even for the extreme quantum case of spin$-1/2$. However, if a next-nearest neighbor interaction J_2 is included, a spin liquid phase can emerge depending on the ratio J_2/J_1. This is a phase lacking any magnetic ordering even down to zero temperature. For large J_2/J_1, an antiferromagnetic striped phase can occur on the triangular lattice, further illustrating the rich variety of behavior contained in this relatively simple Hamiltonian.

Quantum phases which lack any magnetic ordering at zero temperature have attracted a lot of attention in recent years, particularly since the introduction of the *Kitaev model*, which is an exactly solvable model exhibiting such behavior [16]. The spin-1/2 Kitaev model on the honeycomb lattice is a prototypical example of a quantum spin liquid. This is a state of quantum matter which has no magnetic ordering, and has a high degree of long-range entanglement, i.e. the ground state wavefunction cannot be perturbatively related to a product ground state. On the honeycomb lattice, one can identify three different bond directions which we label x, y, and z bonds. The Hamiltonian for the Kitaev honeycomb model is given by

$$\hat{H} = -K_x \sum_{\langle i,j \rangle} \hat{S}_i^x \hat{S}_j^x - K_y \sum_{(i,j)} \hat{S}_i^y \hat{S}_j^y - K_z \sum_{[i,j]} \hat{S}_i^z \hat{S}_j^z, \tag{1.13}$$

where $\langle i,j \rangle$ denotes all pairs of sites joined by an x-bond, (i,j) denotes all pairs of sites joined by a y-bond, and $[i,j]$ denotes all pairs of sites joined by a z-bond. In contrast to the Heisenberg

model, which has a $\hat{\mathbf{S}}_i \cdot \hat{\mathbf{S}}_j$ term along every link in the lattice, the Kitaev model incorporates bond-directional interactions. K_x, K_y, and K_z are coupling strengths along the three bond directions, which may differ, although a common simplification is to consider $K_x = K_y = K_z \equiv K$.

In the absence of a magnetic field the spin-1/2 case can be solved exactly, yielding a spectrum which depends on the relative magnitude of the Kitaev couplings. In the case $|K_x| = |K_y| = |K_z|$, or if there is only weak anisotropy between the three couplings, the energy spectrum is gapless, and the model has excitations in the form of itinerant Majorana fermions i.e. emergent quasiparticles which are their own antiparticle. However, if one of the couplings exceeds the sum of the other two, e.g. if $|K_z| > |K_x| + |K_y|$, a gapped phase emerges and these Majorana excitations are gapped out.

In recent years, a number of material candidates have been identified as having bond-directional Kitaev interactions, for example α-$RuCl_3$ and honeycomb iridates such as Na_2IrO_3 and Li_2IrO_3 [17]. These iridate systems consist of Ir^{4+} ions with an effective $S = 1/2$ moment due to strong spin-orbit coupling, each surrounded by edge-sharing octahedra of oxygen ions. However, recently Kitaev models with integer spins have been proposed to describe the behavior of several compounds, e.g. the honeycomb Ni oxides $A_3Ni_2XO_6$ (A = Na, Li) (X = Bi, Sb) for the spin-1 case [18]. It should be noted that these higher spin extensions of the Kitaev model are no longer exactly solvable, and the study of their properties using numerical methods is currently an active area of research.

1.4. Outline of Thesis

In the next chapter, an overview of several computational methods used in this thesis is presented. In each of the subsequent chapters, these tools are revisited and their application to a specific problem is discussed in more detail. Chapter 2 presents a broad summary of these techniques, which include Determinant Quantum Monte Carlo (DQMC), Hybrid Monte Carlo (HMC) methods and Exact Diagonalization (ED).

Each subsequent chapter of this thesis presents a separate project I have worked on during my PhD, adapted from a published work or preprint. Each is self-contained and includes an introductory section presenting additional background information specific to each project, in more detail than in this chapter. Although these studies relate to different models and types of phenomena, a common theme is the success of simple effective Hamiltonians in capturing the

physics of strongly correlated electron or quantum spin systems, and the power of modern computational techniques in discovering their properties.

Chapter 3 presents a DQMC study of the doped square lattice Holstein model. Early studies of this model hinted at a superconducting phase at low temperature when the system is doped away from half-filling, however computational limitations on both temperature and lattice size precluded definitive results. Our work analyzes much larger systems at significantly lower temperatures than in any previous QMC simulation of the model, and for the first time obtains precise estimates for the superconducting transition temperature in the two-dimensional Holstein model through a finite-size scaling procedure.

Chapter 4 presents a study of the kagome lattice Holstein model, using a recently developed HMC algorithm which allows for simulation of even larger systems, up to 775 sites in this work. This is the first numerical study of the Holstein model on this particular geometry, which has recently attracted significant attention due to the discovery of CDW order in a panoply of kagome metals. In our work we discover an emergent CDW phase in the kagome lattice Holstein model at a filling of $\langle n \rangle = 2/3$, with an ordering wavevector at the K-points of the Brillouin zone, and determine the CDW transition temperature.

Chapter 5 presents a numerical study of the spin-1 Kitaev honeycomb model with different kinds of single-ion anisotropy. Although the pure spin-1 Kitaev model is a quantum spin liquid, we find that this phase is rather easily destroyed in the presence of large enough single-ion anisotropy in the [111] direction, which is expected to occur in real materials. We find the quantum spin liquid phase is also immediately unstable in the presence of any [100] anisotropy. We map out the full phase diagram of this model, which shows that any [111] anisotropy must be small compared to the Kitaev couplings to realize a quantum spin liquid ground state in any real material.

In Chapter 6 we study a modified version of the Kitaev model for integer spins first introduced by Baskaran, Sen, and Shankar [19], which is built from commuting operators at each site of the honeycomb lattice and thus does not have intersite entanglement. Yet, the system remains highly degenerate and the model exhibits residual entropy as $T \to 0$. We discover a rich variety of thermodynamic behaviors in the model, and find striking differences between both ferromagnetic

and antiferromagnetic couplings, as well as the spin-1 and spin-2 cases. We discuss the relevance of these results to the standard spin-S Kitaev model.

In Chapter 7 we study the triangular-lattice Ising antiferromagnet (TIAF), an iconic model of frustrated magnetism exhibiting residual entropy. We study how plateaus in the entropy and magnetization are influenced by the presence of second-neighbor interactions and disorder in the exchange variables, and find that they are quite sensitive to these effects. We provide quantitative estimates for how large these perturbations can be before entropy and magnetization plateaus are destroyed, thereby explaining the challenge in observing them experimentally in TIAF systems such as $TmMgGaO_4$.

In Chapter 8 we study another model on the triangular lattice: the half-filled Hubbard model in a magnetic field. We investigate thermodynamic properties such as the entropy function $S(T, h)$ and magnetization $M(T, h)$, focusing on moderate to large U values (up to $U/t = 32$) at temperatures larger than the exchange parameter $J = \frac{4t^2}{U}$. We analyze in detail how the thermodynamic properties of a finite-U model deviate from the Heisenberg limit, and discuss the relevance of our results to a recent experimental study of the triangular lattice material $Lu_3Cu_2Sb_3O_{14}$ (LCSO).

Finally, Chapter 9 presents concluding remarks which summarize the results of these studies and highlights their interconnected nature.

1.5. List of Publications

Chapters 3–8 of this thesis contain material from the following publications or preprints:

1. **O. Bradley**, G. G. Batrouni, and R. T. Scalettar, *Superconductivity and charge density wave order in the two-dimensional Holstein model*, Phys. Rev. B **103**, 235104 (2021).

2. **O. Bradley**, B. Cohen-Stead, S. Johnston, K. Barros, and R. T. Scalettar, *Charge order in the kagome lattice Holstein model: A Hybrid Monte Carlo study*, npj Quantum Materials **8**, 21 (2023).

3. **O. Bradley** and R. R. P. Singh, *Instabilities of spin-1 Kitaev spin liquid phase in presence of single-ion anisotropies*, Phys. Rev. B. **105**, L060405 (2022).

4. **O. Bradley**, J. Oitmaa, D. Sen, and R. R. P. Singh, *Thermodynamic behavior of modified integer-spin Kitaev models on the honeycomb lattice*, Phys. Rev. E. **103**, 022109 (2021).

5. **O. Bradley**, C. Feng, R. T. Scalettar, and R. R. P. Singh, *Robustness of entropy plateaus: A case study of triangular Ising antiferromagnets*, Phys. Rev. B. **100**, 064414 (2019).

6. **O. Bradley**, Y. Zhang, J. Oitmaa, and R. R. P. Singh, *High-temperature magnetization and entropy of the triangular lattice Hubbard model in a Zeeman field*, arXiv 2303.03550 (2023).

Although not the main focus of this thesis, I have also co-authored the following publications during my PhD:

7. B. Cohen-Stead, **O. Bradley**, C. Miles, G. Batrouni, R. Scalettar, and K. Barros, *Fast and scalable quantum Monte Carlo simulations of electron-phonon models*, Phys. Rev. E **105**, 065302 (2022).

8. C. Miles, B. Cohen-Stead, **O. Bradley**, S. Johnston, R. Scalettar, and K. Barros, *Dynamical tuning of the chemical potential to achieve a target particle number in grand canonical Monte Carlo simulations*, Phys. Rev. E **105**, 045311 (2022).

CHAPTER 2

Overview of Numerical Methods

We will now present an overview of several numerical methods used in this thesis, including both classical and quantum Monte Carlo techniques, and exact diagonalization. In subsequent chapters, additional details regarding how these techniques are applied to a specific model Hamiltonian under study are contained in a separate methods section. This chapter provides the necessary background material to understand these methods and how they are implemented algorithmically.

2.1. Classical Monte Carlo

Monte Carlo methods are algorithms which involve repeated random sampling to perform numerical integration or sample probability distributions in an unbiased way. They are particularly useful when an analytical solution to a problem is not possible or is computationally infeasible. A basic example illustrates how the methods can be used to estimate π numerically. Consider generating N pairs of independent variables (x_i, y_i) which are both randomly drawn from uniform distributions over $[0, 1]$. We then count how many of these points lie within a quarter-circle with unit radius, i.e. satisfying $x_i^2 + y_i^2 \leq 1$. The fraction of points in this region provides an estimate for $\pi/4$, which by the law of large numbers, becomes more and more exact as $N \to \infty$, with the error in the estimate proportional to $1/\sqrt{N}$. A second example shows how the method can be used to evaluate a definite integral, say $\int_0^1 f(x)dx$. We can randomly generate N variables $x_1, x_2, \ldots x_N$ each drawn from a uniform distribution over $[0, 1]$. An approximation for the integral is then given by $\frac{1}{N}\sum_{i=1}^{N} f(x_i)$, which again becomes more exact as $N \to \infty$. However, we can also consider integrals of the form $\int_0^1 p(x)f(x)dx$, where $p(x)$ is some probability distribution function (in the context of statistical physics, this may be the Boltzmann distribution). Now, estimating this integral requires sampling x_i from the distribution $p(x)$, which may be difficult. In this case, a Markov Chain Monte Carlo (MCMC) method can be used to

generate representative samples, as we will discuss further below. First we will provide some background details on Markov chains.

Consider a one-dimensional random walk between integer values on the real number line, starting at $x = 0$ at time $t = 0$. This is a discrete-time process where at each timestep, the walker moves one step to the right (from x to $x + 1$) with probability p, or to the left (from x to $x - 1$) with probability $1 - p$. This is a simple example of a stochastic process where the probability P of observing a particular value of x at time t, i.e. $x(t)$, depends on $x(t-1)$ only and not on the position of the walker at previous times. This defines the Markov condition. More generally, if a sequence of configurations X of a system (i.e. $X(0)$, $X(1)$, $X(2)$, ..., $X(t)$) satisfies the condition

$$P\Big(X(t) = x(t)\Big|X(0) = x(0), X(1) = x(1), \ldots, X(t-1) = x(t-1)\Big) = P\Big(X(t) = x(t)\Big|X(t-1) = x(t-1)\Big) \tag{2.1}$$

then these configurations form a *Markov chain*.

We can define q_{nm} as the transition probability for the system to move to state n if it is currently in state m, and define $P_n(t)$ as the probability that the system is in state n at time t. By the Markov condition, we have that

$$P_n(t+1) = \sum_m q_{nm} P_m(t). \tag{2.2}$$

The transition probabilities q_{nm} form elements of a square transition matrix $\mathbf{Q}$. In matrix form, we can rewrite the above equation as $\mathbf{P}(t+1) = \mathbf{Q}\mathbf{P}(t)$. Here $\mathbf{P}(t)$ is a column vector where the elements are probabilities for the system to be in each individual state at time t. When the system is in any given state, the transition probabilities must be non-negative and sum to 1, i.e. we have that $q_{nm} \geq 0$, and $\sum_n q_{nm} = 1$ for all states m, that is the columns of $\mathbf{Q}$ sum to 1. These two properties mean that $\mathbf{Q}$ is a *stochastic matrix*. By the Perron-Frobenius theorem, it will have a unique 'stationary' eigenvector $\mathbf{v}$ with eigenvalue $\lambda = 1$, i.e. $\mathbf{v} = \mathbf{Q}\mathbf{v}$, with all other eigenvalues $|\lambda| < 1$ (provided the corresponding Markov process is ergodic, as described below). As a result, as $t \to \infty$, $\mathbf{P}(t)$ converges to $\mathbf{v}$, which we call the *stationary distribution* $\mathbf{P}^{\text{st}}$.

Now, for the MCMC method to converge to a target stationary distribution, the process must be ergodic. This means that any state must be reachable from any other state in a finite number of steps. A second condition is that the global balance equation is satisfied, which states that the total probability 'influx' to any state n must equal the total probability 'outflux' out of that state.

This follows directly from the property of the stationary distribution that $\mathbf{P}^{\text{st}} = \mathbf{Q}\mathbf{P}^{\text{st}}$. We can insert a factor of $\sum_m q_{mn} = 1$ on the left-hand side to obtain

$$\sum_m q_{mn} P_n^{\text{st}} = \sum_m q_{nm} P_m^{\text{st}} \quad \forall n, \tag{2.3}$$

which defines the global balance condition. The left side is the total probability flux out of state n, and the right side is the total probability flux into state n. It is clear that this will be satisfied if the probability influx and outflux between all possible pairs of states is balanced, although this is a stronger condition called *detailed balance*:

$$q_{mn} P_n^{\text{st}} = q_{nm} P_m^{\text{st}} \quad \forall n, m. \tag{2.4}$$

The methods we will be using (both classical and quantum Monte Carlo algorithms) satisfy the detailed balance condition (and are ergodic), therefore convergence to a desired stationary distribution will be ensured.

As a concrete example of how MCMC is applied to a classical model, we will consider the Ising model, i.e. a lattice of N spins each taking a value $S = \pm 1$. There are 2^N possible configurations of the system, which for large N becomes too large to enumerate. Instead we can use MCMC to generate representative samples with a probability given by the Boltzmann distribution, which gives the probability for the system to be in a particular configuration C with energy E_C:

$$P(C) = \frac{1}{Z} e^{-\beta E_C}, \tag{2.5}$$

where $\beta = 1/T$ is the inverse temperature, and $Z = \sum_C e^{-\beta E_C}$ is the partition function, which involves a sum over all possible configurations of the system and thus becomes infeasible to explicitly compute for large N. This also means it is not feasible to explicitly calculate the thermal average of some physical observable O (e.g. net magnetization), which is given by

$$\langle O \rangle = \frac{1}{Z} \sum_C O(C) e^{-\beta E_C}. \tag{2.6}$$

Instead, we can make measurements of O on each of our representative samples and calculate an average value, which should give a good approximation as the number of sampled configurations increases.

We can use the following definition for the transition probability to go from state m to state n:

$$q_{n \leftarrow m} = \min \left[1, \frac{P(n)}{P(m)} \right] = \min \left[1, e^{-\beta(E_n - E_m)} \right], \tag{2.7}$$

which can be shown to satisfy detailed balance. For the case of the Ising model, this means that given a current configuration m and a proposed configuration n, an update from m to n will be accepted if $E_n \leq E_m$. If $E_n \geq E_m$, the move is accepted with probability $e^{-\beta(E_n - E_m)}$. This is known as the Metropolis-Hastings algorithm. In a basic implementation, we can start with a randomized initial configuration of spins, and at each timestep propose a change to a new configuration by flipping the spin at a randomly chosen site.

Since the MCMC simulation described above should converge to the Boltzmann distribution after a sufficient time, we can obtain an estimate $\overline{O}$ for an observable quantity $O(C)$ by calculating

$$\overline{O} = \frac{1}{N_{\text{meas}}} \sum_{i=1}^{N_{\text{meas}}} O(C_i), \tag{2.8}$$

where N_{meas} is the number of measured configurations (a sufficient number of warm-up updates should be made before measurements are taken to ensure equilibrium has been reached). However, to obtain accurate error bars on our estimate $\overline{O}$ we must consider that successive configurations generated are clearly correlated. Thus if we make measurements too frequently, although our estimate $\overline{O}$ will still be correct, the error bar will be wrong. Therefore one should either only take measurements of configurations that are separated by a time exceeding the autocorrelation time, or use an appropriate binning procedure. In the latter case, one chooses a bin size m and averages the data over each of the $n_{\text{bin}} = N_{\text{meas}}/m$ bins, obtaining n_{bin} binned measurements. Then we can use the standard error of the mean (SEM) of these n_{bin} values as the error bar associated with a reported measurement.

2.2. Determinant Quantum Monte Carlo

To perform a Monte Carlo simulation of a quantum model such as the Holstein or Hubbard models, we need to use quantum Monte Carlo (QMC) methods. This similarly involves importance sampling of configurations, with updates accepted or rejected according to the Metropolis criterion. However, the initial set up is more involved and requires writing the partition function as a path integral, and introducing an 'imaginary time' axis which, as we will see, maps a quantum d-dimensional system to a classical system in $d+1$ dimensions. In this section, we will introduce the Determinant Quantum Monte Carlo (DQMC) algorithm [20] by examining how it can be applied to the Holstein model.

Recall that the Holstein model can be expressed as $\hat{H} = \hat{K} + \hat{U} + \hat{V}$, where $\hat{K}$ is the electron kinetic energy term, $\hat{U}$ contains the phonon energy terms, and $\hat{V} = \lambda \sum_{i\sigma} x_i \hat{c}^\dagger_{i\sigma} \hat{c}_{i\sigma}$ is the electron-phonon coupling term which is quadratic in fermionic operators. The initial step is to rewrite the partition function $Z = \mathrm{Tr}(e^{-\beta \hat{H}})$ by discretizing the inverse temperature, writing $\beta = \Delta\tau L$:

$$Z = \mathrm{Tr}\left[e^{-\Delta\tau\hat{H}} e^{-\Delta\tau\hat{H}} \dots e^{-\Delta\tau\hat{H}}\right] \tag{2.9}$$

$$= \mathrm{Tr}\left[e^{-\Delta\tau(\hat{K}+\hat{V}+\hat{U})} e^{-\Delta\tau(\hat{K}+\hat{V}+\hat{U})} \dots e^{-\Delta\tau(\hat{K}+\hat{V}+\hat{U})}\right] \tag{2.10}$$

$$\approx \mathrm{Tr}\left[\left(e^{-\Delta\tau\hat{K}} e^{-\Delta\tau\hat{V}} e^{-\Delta\tau\hat{U}}\right)\left(e^{-\Delta\tau\hat{K}} e^{-\Delta\tau\hat{V}} e^{-\Delta\tau\hat{U}}\right) \dots \left(e^{-\Delta\tau\hat{K}} e^{-\Delta\tau\hat{V}} e^{-\Delta\tau\hat{U}}\right)\right] \tag{2.11}$$

The last step uses the Suzuki-Trotter approximation, which states that for non-commuting operators ($[\hat{A}, \hat{B}] \neq 0$) we have that $e^{-\Delta\tau(\hat{A}+\hat{B})} = e^{-\Delta\tau\hat{A}} e^{-\Delta\tau\hat{B}} + O(\Delta\tau)^2$. If $\Delta\tau$ is kept small then the error (which scales as $(\Delta\tau)^2$) becomes negligible and we can perform the decomposition shown above. The trace is now over the product of L terms, which we can index by $\tau = 1, \dots, L$, where τ is known as the 'imaginary time'.

Let us now perform the trace over both the electron and phonon degrees of freedom:

$$Z = \mathop{\mathrm{Tr}}_{\{n_{i\sigma}\}} \mathop{\mathrm{Tr}}_{\{x_{i\tau}\}} \left[\left(e^{-\Delta\tau\hat{K}} e^{-\Delta\tau\hat{V}} e^{-\Delta\tau\hat{U}}\right)\left(e^{-\Delta\tau\hat{K}} e^{-\Delta\tau\hat{V}} e^{-\Delta\tau\hat{U}}\right) \dots \left(e^{-\Delta\tau\hat{K}} e^{-\Delta\tau\hat{V}} e^{-\Delta\tau\hat{U}}\right)\right], \tag{2.12}$$

where we note that the phonon field $\{x_{i\tau}\}$ has acquired an additional index: i denotes the spatial site, and τ denotes the 'time slice' along the imaginary time axis. To calculate this we can insert an identity operator for the phonon position at each imaginary time slice, where the state $|x_{i,\tau}\rangle$

represents the phonon field (i.e. the set of phonon displacements) at a particular imaginary time τ:

$$Z = \int_{-\infty}^{\infty} \prod_{i,\tau} dx_{i,\tau} \operatorname*{Tr}_{\{n_{i\sigma}\}} \Big[\langle x_{i,1}|e^{-\Delta\tau\hat{K}}e^{-\Delta\tau\hat{U}}e^{-\Delta\tau\hat{V}}|x_{i,2}\rangle\langle x_{i,2}|e^{-\Delta\tau\hat{K}}e^{-\Delta\tau\hat{U}}e^{-\Delta\tau\hat{V}}|x_{i,3}\rangle \dots \\ \dots \langle x_{i,L}|e^{-\Delta\tau\hat{K}}e^{-\Delta\tau\hat{U}}e^{-\Delta\tau\hat{V}}|x_{i,1}\rangle \Big]. \tag{2.13}$$

We want to eventually show that the partition function can be written in terms of the phonon variables $x_{i\tau}$ only. To do this, we let the $\hat{K}$ and $\hat{V}$ terms act on the states $\langle x_{i,\tau}|$ giving

$$Z = \int_{-\infty}^{\infty} \prod_{i,\tau} dx_{i,\tau} \langle x_{i,1}|e^{-\Delta\tau\hat{U}}|x_{i,2}\rangle\langle x_{i,2}|e^{-\Delta\tau\hat{U}}|x_{i,3}\rangle \dots \langle x_{i,L}|e^{-\Delta\tau\hat{U}}|x_{i,1}\rangle \\ \operatorname*{Tr}_{\{n_{i\sigma}\}} \left[e^{-\Delta\tau\hat{K}}e^{-\Delta\tau\hat{V}(x_{i,1})}e^{-\Delta\tau\hat{K}}e^{-\Delta\tau\hat{V}(x_{i,2})} \dots e^{-\Delta\tau\hat{K}}e^{-\Delta\tau\hat{V}(x_{i,L})} \right], \tag{2.14}$$

where we can now evaluate the resultant $\langle x_{i,\tau}|e^{-\Delta\tau\hat{U}}|x_{i,\tau+1}\rangle$ terms by again applying the Suzuki-Trotter approximation. This yields

$$\langle x_{i,\tau}|e^{-\Delta\tau\hat{U}}|x_{i,\tau}\rangle \approx \langle x_{i,\tau}|e^{-\Delta\tau\frac{1}{2}\omega_0^2\sum_i \hat{X}_i^2}\ e^{-\Delta\tau\frac{1}{2}\sum_i \hat{P}_i^2}|x_{i,\tau+1}\rangle \tag{2.15}$$

$$= e^{-\Delta\tau\frac{1}{2}\omega_0^2\sum_i x_{i,\tau}^2}\langle x_{i,\tau}|e^{-\Delta\tau\frac{1}{2}\sum_i \hat{P}_i^2}|x_{i,\tau+1}\rangle \tag{2.16}$$

$$= e^{-\Delta\tau\frac{1}{2}\omega_0^2\sum_i x_{i,\tau}^2}\int_{-\infty}^{\infty}\prod_i dp_i\langle x_{i,\tau}|e^{-\Delta\tau\frac{1}{2}\sum_i \hat{P}_i^2}|p_i\rangle\langle p_i|x_{i,\tau+1}\rangle \tag{2.17}$$

$$= e^{-\Delta\tau\frac{1}{2}\omega_0^2\sum_i x_{i,\tau}^2}\int_{-\infty}^{\infty}\prod_i dp_i\langle x_{i,\tau}|p_i\rangle e^{-\Delta\tau\frac{1}{2}\sum_i p_i^2}\langle p_i|x_{i,\tau+1}\rangle, \tag{2.18}$$

where again we have inserted an identity in terms on phonon momentum states. Noting that $\langle x|p\rangle = \frac{1}{\sqrt{2\pi}}e^{ipx}$, we can explicitly calculate this integral. We find that

$$\langle x_{i,\tau}|e^{-\Delta\tau\hat{U}}|x_{i,\tau+1}\rangle = \exp\left(-\Delta\tau\left[\frac{\omega_0}{2}\sum_i x_{i,\tau}^2 - \frac{1}{2}\sum_i\left(\frac{x_{i,\tau+1}-x_{i,\tau}}{\Delta\tau}\right)^2\right]\right) \equiv e^{-S_{\mathrm{B}}}, \tag{2.19}$$

where we can define the exponentiated term as the bosonic (phonon) action S_{B}.

The partition function can now be written as

$$Z = \int_{-\infty}^{\infty}\prod_{i,\tau} dx_{i,\tau}\, e^{-S_{\mathrm{B}}}\prod_{\sigma}\operatorname*{Tr}_{\{n_i\}}\left[e^{-\Delta\tau\hat{K}}e^{-\Delta\tau\hat{V}(x_{i,1})}e^{-\Delta\tau\hat{K}}e^{-\Delta\tau\hat{V}(x_{i,2})}\dots e^{-\Delta\tau\hat{K}}e^{-\Delta\tau\hat{V}(x_{i,L})}\right]. \tag{2.20}$$

Since $\hat{K}$ and $\hat{V}$ are quadratic in fermion creation and annihilation operators, they can be expressed as $\hat{K} = \underline{\hat{c}}^\dagger \bar{K} \underline{\hat{c}}$ and $\hat{V}(x_{i,\tau}) = \underline{\hat{c}}^\dagger \bar{V}(x_{i,\tau}) \underline{\hat{c}}$, where $[\underline{\hat{c}}^\dagger]^T = (\hat{c}_1^\dagger, \hat{c}_2^\dagger \dots \hat{c}_N^\dagger)$ is a row vector containing fermion creation operators for each site in the lattice. $\bar{K}$ and $\bar{V}$ are both $N \times N$ matrices, where N is the total number of spatial lattice sites. Now, since $\hat{K}$ and $\hat{V}$ are quadratic in fermion operators they obey the following identity:

$$\mathrm{Tr}\left[e^{-\Delta\tau\hat{K}} e^{-\Delta\tau\hat{V}(x_{i,1})} \dots e^{-\Delta\tau\hat{K}} e^{-\Delta\tau\hat{V}(x_{i,L})}\right] = \det\left[\mathbb{1} + e^{-\Delta\tau\bar{K}} e^{-\Delta\tau\bar{V}(x_{i,1})} \dots e^{-\Delta\tau\bar{K}} e^{-\Delta\tau\bar{V}(x_{i,L})}\right], \tag{2.21}$$

which has transformed our expression in terms of operators into a matrix expression interpretable by a computer. The matrix $\bar{K}$ is an $N \times N$ tight-binding hopping matrix (with the chemical potential term $-\mu$ included along its diagonal). For each imaginary time τ, $\bar{V}(x_{i,\tau})$ is an $N \times N$ matrix which is a function of the phonon displacements at every site at that time-slice, and has $\lambda x_{i,\tau}$ terms along its diagonal only, i.e. we have

$$\bar{K} = \begin{pmatrix} -\mu & -t & 0 & 0 & \cdots & -t \\ -t & -\mu & -t & 0 & \cdots & 0 \\ 0 & -t & -\mu & -t & \cdots & 0 \\ 0 & 0 & -t & -\mu & \cdots & 0 \\ \vdots & \vdots & \vdots & \vdots & \ddots & \vdots \\ -t & 0 & 0 & 0 & \cdots & -\mu \end{pmatrix} \qquad \bar{V}(x_{i,\tau}) = \begin{pmatrix} -\lambda x_{1,\tau} & 0 & 0 & \cdots & 0 \\ 0 & -\lambda x_{2,\tau} & 0 & \cdots & 0 \\ 0 & 0 & -\lambda x_{3,\tau} & \cdots & 0 \\ \vdots & \vdots & \vdots & \ddots & \vdots \\ 0 & 0 & 0 & \cdots & -\lambda x_{N,\tau} \end{pmatrix} \tag{2.22}$$

where we assume periodic boundary conditions (with the form of $\bar{K}$ here specific to $d = 1$). We can define

$$\bar{M} = \mathbb{1} + e^{-\Delta\tau\bar{K}} e^{-\Delta\tau\bar{V}(x_{i,1})} \dots e^{-\Delta\tau\bar{K}} e^{-\Delta\tau\bar{V}(x_{i,L})}, \tag{2.23}$$

which will be another $N \times N$ matrix. Since neither $\bar{K}$ or $\hat{V}$ depend on the fermion spin, $\bar{M}$ is identical for both spin species. Thus when we take the product over the two spin species in Eq. 2.20 we get the square of the determinant of $\bar{M}$. The partition function now becomes

$$Z = \int_{-\infty}^{\infty} \prod_{i,\tau} dx_{i,\tau} e^{-S_\mathrm{B}} \left[\det(\bar{M})\right]^2 \tag{2.24}$$

$$= \int_{-\infty}^{\infty} \prod_{i,\tau} dx_{i,\tau} W(\{x_{i\tau}\}) \tag{2.25}$$

where $W(\{x_{i\tau}\}) = e^{-S_{\mathrm{B}}} \left[\det\bigl(\bar{M}\bigr)\right]^2$ is a function of the phonon field only. We can now perform random sampling over the phonon field (using the Metropolis-Hastings algorithm), where $W(\{x_{i\tau}\})$ plays the role of a Monte Carlo weight for a given configuration. As in classical Monte Carlo simulations, we can calculate various physical quantities for each sampled configuration, with the resulting measurements becoming precise after a sufficient number of Monte Carlo steps.

Elements of the inverse of $\bar{M}$ give the fermionic Green's function, from which measurements of other physical quantities can be obtained. We have that

$$G_\sigma(i,j) = \langle \hat{c}_{i\sigma} \hat{c}^\dagger_{i\sigma} \rangle = \left[\bar{M}_\sigma\right]^{-1}_{ij}, \tag{2.26}$$

where we the keep the subscript σ here, since in general we can have $\bar{M}_\uparrow \neq \bar{M}_\downarrow$ e.g. as for the Hubbard Hamiltonian. The fact that $\bar{M}$ is symmetric with respect to spin in the Holstein model means that $\det\bigl(\bar{M}_\uparrow\bigr)\det\bigl(\bar{M}_\uparrow\bigr) = [\det\bigl(\bar{M}\bigr)]^2$ is always non-negative. If this were not the case, $W(\{x_{i\tau}\})$ can potentially become negative and thus can not be interpreted as a probabilistic weight, a limitation known as the sign problem [21].

A basic implementation of the DQMC algorithm for the Holstein model is given below. It should be noted there are many possible refinements to the algorithm which can improve computational efficiency and numerical stabilization which we will not present here [22, 23, 24].

(1) Initialize the phonon field $\{x_{i,\tau}\}$

(2) Evaluate $\det\bigl(\bar{M}\bigr) = \det\Bigl[\mathbb{1} + e^{-\Delta\tau \bar{K}} e^{-\Delta\tau \bar{V}(x_{i,1})} \ldots e^{-\Delta\tau \bar{K}} e^{-\Delta\tau \bar{V}(x_{i,L})}\Bigr]$

(3) Sweep through the spacetime lattice $\{x_{i,\tau}\}$ i.e. NL sites, and suggest a move to the phonon displacement: $x_{i,\tau} \to x_{i,\tau} + \Delta x_{i,\tau}$

(4) Calculate the new matrix $\bar{M}'$ and $\det\bigl(\bar{M}'\bigr)$ for this proposed configuration

(5) Calculate the probability $P = \min\left(1, e^{-\Delta S} \frac{\det \bar{M}'}{\det \bar{M}}\right)$, where ΔS is the change in phonon action

(6) Generate a random number r with $0 < r < 1$ and accept the move if $r < P$, otherwise reject the proposed move

(7) Once all NL sites have been updated, make measurements of the fermionic Green's function and other physical quantities (only after thermalization i.e. once a sufficient number of warm-up sweeps N_{therm} has occurred)

(8) Repeat steps (2)–(7) until a sufficient number of measurement steps N_{meas} has been performed

2.3. Hybrid Monte Carlo

An alternative approach to simulating the Holstein model is to use Hybrid Monte Carlo (HMC), which is particularly useful for sampling continuous variables such as phonon displacements [25,26]. In DQMC, the computational time to perform a full update scales at βN^3 which is due to the evaluation of the ratio of matrix determinants. Restricting to local updates to the phonon field can also lead to long autocorrelation times in DQMC, most pronounced at small phonon frequencies ω_0. HMC avoids any explicit calculation of $\det \bar{M}$ and instead has a near-linear scaling with system size, and for large systems (i.e. $N \gtrsim 100$) it has been shown to be more computationally efficient than DQMC for electron-phonon simulations. In Chapter 4 we will provide additional details on implementing HMC for the Holstein model, however here we will present a brief general overview of the method.

We can make use of the following result to express the magnitude of $\det \bar{M}$ in terms of a multidimensional Gaussian integral. We can write

$$|\det \bar{M}| \propto \int \mathcal{D}\Phi \; e^{-\frac{1}{2}\Phi^T(\bar{M}^T\bar{M})^{-1}\Phi}, \tag{2.27}$$

where Φ is a vector and each component is integrated over the real line. The expression we previously obtained in Eq. 2.24 for the partition function of the Holstein model can now be expressed as

$$Z \propto \int \mathcal{D}\Phi_\uparrow \mathcal{D}\Phi_\downarrow \mathcal{D}x \; e^{-S(x,\Phi_\sigma)}, \tag{2.28}$$

where

$$S(x,\Phi_\sigma) = S_B(x) + S_F(x,\Phi_\sigma), \tag{2.29}$$

$$S_F(x,\Phi_\sigma) = \frac{1}{2}\sum_\sigma \Phi_\sigma^T (M^T M)^{-1}\Phi_\sigma, \tag{2.30}$$

and $S_B(x)$ is the bosonic action as defined previously. We now have a fermionic component $S_F(x,\Phi_\sigma)$ in the total action, and we have introduced auxiliary fields $\Phi_{\{\uparrow,\downarrow\}}$ which must also be

sampled in addition to the phonon field x. We can sample Φ_σ at fixed x by drawing a random Gaussian vector R_σ and constructing $\Phi_\sigma = M^T R_\sigma$.

A key difference between HMC and DQMC is the manner in which updates to the phonon field are proposed. In HMC, a fictitious dynamics is introduced where we have a momentum $p_{i,\tau}$ that is dynamically conjugate to the phonon displacement variables $x_{i,\tau}$. The following Hamiltonian can then be constructed:

$$H(x,p) = S(x,\Phi) + \frac{p^T \mathcal{M}^{-1} p}{2}, \tag{2.31}$$

where the first term is the total action given by Eq. 2.29, and the second term can be interpreted as a 'kinetic energy' term where $\mathcal{M}$ is a dynamical mass matrix. $\mathcal{M}$ can be any positive-definite matrix and has no dependence on x or p. Starting from some initial configuration of the phonon field x_i and fictitious momentum p_i, the system then evolves according to Hamilton's equations of motion along a trajectory in phase space, i.e.

$$\dot{p} = -\frac{\partial H}{\partial x} = -\frac{\partial S}{\partial x}, \tag{2.32}$$

$$\dot{x} = \frac{\partial H}{\partial p} = \mathcal{M}^{-1} p. \tag{2.33}$$

This is a discrete-time process that occurs for a certain number of steps N_t, each of length Δt. At the end of the trajectory, the final position in phase space (x_f, p_f) serves as the proposed new configuration of the system. This is accepted or rejected according to the Metropolis criterion, i.e. with probability $P = \min\left(1, e^{-[H(x_f,p_f)-H(x_i,p_i)]}\right)$. This process is repeated, with a large number of complete trajectories (each comprising one update) performed during a simulation.

The first step of an HMC update is to a sample the vector p. To sample momentum in equilibrium (i.e. from the Boltzmann distribution $\propto \exp\left[-p^T \mathcal{M}^{-1} p/2\right]$) one can sample a Gaussian vector R and then calculate $p = \mathcal{M}^{1/2} R$. To evolve the phonon field and momentum variables along the trajectory in phase space, i.e. at each timestep obtain p_{t+1} and x_{t+1} given p_t and x_t, a numerical integration method is used. We employ leapfrog integration which is valid for constant timestep Δt, and is described below. The following steps outline a basic implementation of a single HMC update for the Holstein model:

(1) Record initial phonon field x_i

(2) Sample auxiliary field using $\Phi_\sigma = M^T(x_i)R_\sigma$

(3) Sample momentum via $p_i = \sqrt{\mathcal{M}}R$

(4) Calculate the initial energy $H_i(x_i, p_i)$

(5) For N_t timesteps of size Δt, evolve the momentum and phonon field variables via leapfrog integration, which consists of the following three updates in this order:

1. $p := p - \frac{\Delta t}{2}\frac{\partial S}{\partial x}$
2. $x := x + \Delta t \mathcal{M}^{-1} p$
3. $p := p - \frac{\Delta t}{2}\frac{\partial S}{\partial x}$

(6) Calculate the final energy $H_f(x_f, p_f)$ at the end of the trajectory

(7) Calculate the acceptance probability $P = \min\left(1, e^{-[H(x_f,p_f)-H(x_i,p_i)]}\right)$

(8) Generate a random number r with $0 < r < 1$ and accept the new phonon configuration x_f if $r < P$, otherwise reject the proposed move

There are also many refinements to the HMC algorithm which can be made, for example timestep splitting, where two separate timesteps Δt and $\Delta t'$ are employed to integrate the bosonic and fermionic forces ($-\partial S_B/\partial x$ and $-\partial S_F/\partial x$) separately. This will be discussed in further detail in Chapter 4, where we present an HMC study of the Holstein model on the kagome lattice.

2.4. Exact Diagonalization and Lanczos Method

Given a Hamiltonian H in matrix form, exact diagonalization is the process of finding the eigenstates of the system and corresponding energy eigenvalues (or a subset thereof), typically using a linear algebra library such as LAPACK or numpy.linalg. We can illustrate the procedure by considering the spin-1/2 Heisenberg model. For N sites the number of possible states is 2^N, giving the dimension of the Hilbert space. An explicit example is useful to consider: if we look at just a two-site cluster, we can easily solve for the eigenstates and eigenvalues by hand. In this case the Hamiltonian is simply $H = J\vec{S_1} \cdot \vec{S_2}$, where $\vec{S} = \frac{1}{2}\vec{\sigma}$, with $\vec{\sigma}$ a vector of Pauli matrices (we set $\hbar = 1$ here). The possible states are $\{|\uparrow\uparrow\rangle, |\uparrow\downarrow\rangle, |\downarrow\uparrow\rangle, |\downarrow\downarrow\rangle\}$, which will form the basis for writing H in matrix form. First note that we can rewrite the dot product between spins as

$$\vec{S_1} \cdot \vec{S_2} = S_1^z S_2^z + \frac{1}{2}\left(S_1^+ S_2^- + S_1^- S_2^+\right), \tag{2.34}$$

where $S^{\pm} = S_x \pm iS_y$ are spin raising and lowering operators. The $S_1^z S_2^z$ term will give diagonal elements along H, equal to $\frac{J}{4}$ if the corresponding basis state has two identical spins ($|\uparrow\uparrow\rangle$ and $|\downarrow\downarrow\rangle$), and equal to $-\frac{J}{4}$ if the corresponding basis state has two opposite spins ($|\uparrow\downarrow\rangle$ and $|\downarrow\uparrow\rangle$). The second term will give non-zero matrix elements only if the pair of basis states involved (corresponding to the row and column of H) are $|\uparrow\downarrow\rangle$ and $|\downarrow\uparrow\rangle$, giving two off-diagonal elements equal to $\frac{J}{2}$. The 4×4 Hamiltonian in matrix form is thus given by

$$H = \begin{pmatrix} \frac{J}{4} & 0 & 0 & 0 \\ 0 & -\frac{J}{4} & \frac{J}{2} & 0 \\ 0 & \frac{J}{2} & -\frac{J}{4} & 0 \\ 0 & 0 & 0 & \frac{J}{4} \end{pmatrix} \tag{2.35}$$

from which we can obtain the eigenvectors and eigenvalues. We find a triplet of states with energy $E = \frac{J}{4}$: $|\uparrow\uparrow\rangle$, $|\downarrow\downarrow\rangle$, and $\frac{1}{\sqrt{2}}(|\uparrow\downarrow\rangle + |\downarrow\uparrow\rangle)$, as well as a singlet state with energy $E = \frac{3J}{4}$: $\frac{1}{\sqrt{2}}(|\uparrow\downarrow\rangle - |\downarrow\uparrow\rangle)$.

In this example, the Hilbert space is small enough that all eigenstates and energies can be found by hand. However, this quickly becomes infeasible for larger systems since we require diagonalization of the $2^N \times 2^N$ matrix H. However, we can still easily construct this matrix. For a spin-1/2 Heisenberg model with N sites, there will be 2^N basis states which correspond to each particular row/column of H, which we can label in order as $1, 2, \ldots, 2^N$. Now, a natural way to represent each possible configuration of spins e.g. $|\uparrow\uparrow\downarrow\uparrow\downarrow\downarrow \ldots\rangle$ is by a bitstring of ones and zeros, with $\uparrow \equiv 0$ and $\downarrow \equiv 1$. Then after converting this binary number to base-10, we obtain the label of the row/column corresponding to this basis state.

For a nearest-neighbor Heisenberg model, we can use the following rules to obtain the matrix elements of H. To get the diagonal elements (each corresponding to a particular basis state), we count the number of parallel nearest-neighbor pairs n_p and the number of opposite nearest-neighbor pairs n_o for that basis state. The diagonal element is then given by $\frac{J}{4}(n_p - n_o)$. The off-diagonal elements of H will only be non-zero if the two basis states involved (corresponding to the row and column of H) are related to each other through flipping a single pair of adjacent opposite spins. If this is the case, the off-diagonal element will equal $\frac{J}{2}$, otherwise it will be zero. Since we now

have a mapping between the label assigned to each row/column, and a particular configuration of N spins, it is straightforward to write a program to construct H. Then a linear algebra library can be used to compute its eigenvectors and eigenvalues.

However, exact diagonalization as described above is still constrained to relatively small system sizes due to limitations on computer memory. The available RAM on a single computer may be of order $\sim 10^{11}$ bytes $= 100\,\text{GB}$ at most. If our matrix stores double-precision numbers (8 bytes) we can store $\sim 10^{10}$ real numbers, i.e. the maximum size of our square matrix H is approximately $10^5 \times 10^5$. This means that finding the complete set of eigenstates and energies becomes infeasible if the dimension of the Hilbert space exceeds $\sim 10^5$. For the spin-1/2 Heisenberg model means that for systems with $N \gtrsim 16$ sites it becomes difficult to perform exact diagonalization in the manner described above. It should be noted that exploiting symmetries or conservation laws can help increase the maximum N for which we can perform a complete diagonalization, e.g. using conservation of $\sum_i S_i^z$ in the spin-1/2 Heisenberg model can increase this to $N \approx 20$.

In practice, we are often interested in only the lowest energy states of the system. In this case, it suffices to find the m smallest eigenvalues and eigenvalues of an $n \times n$ matrix H, where $m \ll n$. To do this we can use the Lanczos method [27], which is an iterative algorithm to find the m lowest eigenvectors x_i $(i = 1, \ldots, m)$. We begin by generating a random normalized starting vector x_1, and then construct a new vector x_2 which is orthogonal to x_1 by carrying out the following steps:

(1) Generate a random normalized $n \times 1$ vector x_1

(2) $w_1' = Hx_1$

(3) $a_1 = w_1'^* x_1$

(4) $w_1 = w_1' - a_1 x_1$

and normalizing this we obtain x_2:

(5) $b_2 = \|w_1\|$

(6) $x_2 = \frac{w_1}{b_2}$

We can now construct another normalized vector x_3 which is orthogonal to both x_1 and x_2 in the following way:

(7) $w_2' = Hx_2$

(8) $a_2 = w_2'^* x_2$

(9) $w_2 = w_2' - a_2 x_2 - b_2 x_1$

(10) $b_3 = \|w_2\|$

(11) $x_3 = \frac{w_2}{b_3}$

We can now repeat this process until we have obtained m Lanczos vectors $\{x_1, x_2, \ldots x_m\}$. For the construction of each new vector we only need the previous two states, i.e. after x_j is obtained, we continue the above procedure to get x_{j+1} as follows:

$$w_j' = H x_j \tag{2.36}$$

$$a_j = w_j'^* x_j \tag{2.37}$$

$$w_j = w_j' - a_j x_j - b_j x_{j-1} \tag{2.38}$$

$$b_{j+1} = \|w_j\| \tag{2.39}$$

$$x_{j+1} = \frac{w_j}{b_{j+1}} \tag{2.40}$$

An $n \times m$ matrix V can subsequently be constructed where each column is a Lanczos vector x_i, and the Hamiltonian in the basis of Lanczos vectors becomes tridiagonal. Storing the a and b coefficients at each iteration, the Lanczos method gives us this tridiagonal matrix $T = V^* H V$ which has dimensions $m \times m$:

$$T = \begin{pmatrix} a_1 & b_2 & & & & \\ b_2 & a_2 & b_3 & & & \\ & b_3 & a_3 & b_4 & & \\ & & \ddots & \ddots & \ddots & \\ & & & b_{m-1} & a_{m-1} & b_m \\ & & & & b_m & a_m \end{pmatrix} \tag{2.41}$$

Since $m \ll n$ it is computationally inexpensive to compute all the eigenvectors and eigenvalues of T, which will give the m lowest energies of H. Typically it is sufficient to use a number of Lanczos iterations m of a few tens or hundreds, after which the ground state energy will converge to the true value [27]. In practice, one can systematically increase m until the ground state energy (corresponding to the smallest eigenvalue) converges to a single value to sufficient precision.

CHAPTER 3

Superconductivity and Charge Density Wave Order in the Two-Dimensional Holstein Model

3.1. Chapter Summary

The Holstein Hamiltonian describes fermions hopping on a lattice and interacting locally with dispersionless phonon degrees of freedom. In the low density limit, dressed quasiparticles, polarons and bipolarons, propagate with an effective mass. At higher densities, pairs can condense into a low temperature superconducting phase and, at or near commensurate filling on a bipartite lattice, to charge density wave (CDW) order. CDW formation breaks a discrete symmetry and hence occurs via a second order (Ising) transition, and therefore at a finite $T_{\rm cdw}$ in two dimensions. Quantum Monte Carlo calculations have determined $T_{\rm cdw}$ for a variety of geometries, including square, honeycomb, and Lieb lattices. The superconducting transition, on the other hand, in $d = 2$ is in the Kosterlitz-Thouless (KT) universality class, and is much less well characterized. In this chapter we determine $T_{\rm sc}$ for the square lattice, for several values of the density ρ and phonon frequency ω_0. We find that quasi-long range order sets in at $T_{\rm sc} \lesssim t/20$, where t is the near neighbor hopping amplitude, consistent with previous rough estimates from simulations which only extrapolated to the temperatures we reach from considerably higher T. We also show evidence for a discontinuous evolution of the density as the CDW transition is approached at half-filling.

This chapter is based on the following publication [28]:

O. Bradley, G. G. Batrouni, and R. T. Scalettar, *Superconductivity and charge density wave order in the two-dimensional Holstein model*, Phys. Rev. B **103**, 235104 (2021).

3.2. Introduction

The interactions of electrons with lattice degrees of freedom (phonons) underlie many of the fundamental properties of solid state materials. The many-body nature of the problem, however,

poses significant challenges to analytic investigation. Hence, over the last several decades, increasingly sophisticated computational methods have been exploited to gain quantitative insight. Early quantum Monte Carlo (QMC) work on electron-phonon models focused on the dilute limit. As an electron moves through a material, the polarization of the underlying medium causes a cloud of phonons to follow. Simulations studied the resulting "single electron polaron", identifying its size and effective mass as functions of the electron-phonon coupling and phonon frequency [29, 30, 31, 32, 33, 34, 35, 36, 37]. If the interaction is sufficiently large, it was shown that it is possible for two polarons to pair. The size, dispersion, and stability of the resulting bipolarons was evaluated [38, 39, 40], as well as bipolaron physics across a range of fillings [41].

As the density of these dressed quasiparticles increases, they can condense into phases with long range order (LRO). One possibility is off-diagonal quasi-long range order, i.e. superconductivity (SC). At, and close to, special commensurate densities, on a bipartite lattice, diagonal LRO, i.e. charge density wave (CDW) states, are another possibility. The competition between these two low temperature phases is a fundamental feature of both materials [42, 43, 44] and of simplified models of the electron-phonon interaction.

One such model is the Holstein Hamiltonian [2], which describes electrons hopping on a lattice and interacting locally with dispersionless phonon degrees of freedom. At commensurate filling on bipartite lattices, it exhibits a transition to CDW order at a finite T_{cdw} in two dimensions. Early QMC studies of the Holstein model examined the competition between CDW and SC on square lattices of up to 8×8 sites, observing the enhancement of SC correlations and a simultaneous reduction in the CDW structure factor as the system is doped away from half-filling [3, 4, 45]. Early estimates of T_{cdw} were obtained using a finite-size scaling approach, although computational constraints on lattice size limited their accuracy.

The SC transition believed to occur away from half-filling (in two dimensions) belongs to the Kosterlitz-Thouless (KT) universality class. Although similar attempts were made to quantify its appearance, it remains much less well characterized. Vekić et. al [3] provided estimates for T_{sc} based on a finite-size scaling of QMC data for the same lattices of up to 8×8 sites, as were analyzed for the CDW transition, but only reached inverse temperatures $\beta \leq 12/t$. The computational limitations on both temperature and lattice size which restricted simulations to these ranges prevented an

accurate finite-size scaling to be performed. For phonon frequencies $\omega_0/t = 1$, it was estimated that the SC transition occurs within an approximate range $\beta_{\rm sc} = 30$–40, more than a factor of two colder than the lowest temperatures simulated. Finite-size scaling estimates of the critical temperature at higher phonon frequencies, which would tend to have higher, and hence more accessible, $T_{\rm sc}$ were also limited in accuracy.

More recent studies of the Holstein model have refined estimates of $T_{\rm cdw}$ at half-filling on the square lattice [46,47,48], and studied the interplay between SC and CDW order as electron-phonon coupling is varied [49]. The influence of phonon dispersion on both SC and CDW ordering has also been studied [48], with strong evidence found for the onset of SC at half-filling when phonon dispersion is present. A finite-size scaling analysis obtained $T_{\rm sc} \approx t/26$ at a phonon frequency $\omega_0/t = 4$, simulating lattices of up to 12×12 sites. Recently, the CDW transition in the Holstein model has also been investigated for both the honeycomb and π-flux geometries [50, 51, 52], as well as for the square lattice with anisotropic hopping amplitudes [53]. These studies focused on the half-filled case only and hence did not advance our understanding of $T_{\rm sc}$. Recent work on the triangular lattice Holstein model [54] has shown that frustrating the charge order via a non-bipartite lattice can enhance SC, and an estimate of $T_{\rm sc} \approx t/10$ was obtained at a phonon frequency $\hbar\omega/E_F = 0.3$ (where E_F is the Fermi energy). This estimate was obtained at half-filling through a finite-size scaling analysis, using lattices up to 12×12 sites. However, in the work of [54], no analogous evidence of the SC transition was observed for the square lattice for the parameters studied.

In the present paper, we resolve this situation by determining $T_{\rm sc}$ for the square lattice for several values of the phonon frequency ω_0 and electron density ρ away from half-filling. We perform QMC simulations of lattices up to 12×12 sites, at inverse temperatures up to $\beta = 28/t$. Through a finite-size scaling analysis we find that SC sets in close to the lowest temperatures simulated. That is, our study does not rely on an extrapolation from temperatures much higher than $T_{\rm sc}$. We also investigate the variation of the CDW structure factor with wave vector as the system is doped away from half-filling, finding evidence for a possible incommensurate CDW phase at low temperature.

We note that, in addition to the computational literature cited above, considerable effort has gone into the analytic solution of the Holstein Hamiltonian. The Migdal-Eliashberg (ME) equations

[55, 56] form the basis for much of the analytic work on strongly coupled electron-phonon models, but disagree with exact QMC simulations [3, 4, 45, 57, 58], especially as the temperature is lowered at densities in the vicinity of half-filling where competing CDW formation occurs. This comparison can be improved somewhat with 'renormalized ME' theory in which the phonon propagator is dressed by electron-hole bubbles [59]. Recently, there has been renewed interest in examining the limits of ME theory and when it breaks down [60, 61, 62, 63, 64]. Indeed, it has been shown that ME can work well for $\omega_0 << E_F$ provided the electron phonon coupling is not too large, enabling estimates of T_{SC} to be made by extrapolating DQMC results down to lower temperatures using ME calculations [60]. However, we note that several of the parameter sets we study in this work are outside the limits of ME theory.

3.3. Model and Methods

The Holstein model is a tight-binding Hamiltonian which describes the interaction between electrons and local phonon modes in a lattice [2],

$$\hat{H} = -t \sum_{\langle \mathbf{i},\mathbf{j} \rangle,\sigma} \left(\hat{c}^{\dagger}_{\mathbf{i}\sigma} \hat{c}_{\mathbf{j}\sigma} + h.c. \right) - \mu \sum_{\mathbf{i}\sigma} \hat{n}_{\mathbf{i}\sigma} + \frac{1}{2} \sum_{\mathbf{i}} \hat{P}^2_{\mathbf{i}} + \frac{\omega_0^2}{2} \sum_{\mathbf{i}} \hat{X}^2_{\mathbf{i}} + \lambda \sum_{\mathbf{i}\sigma} \hat{n}_{\mathbf{i}\sigma} \hat{X}_{\mathbf{i}} \; . \tag{3.1}$$

Here $\hat{c}^{\dagger}_{\mathbf{i}\sigma}(\hat{c}_{\mathbf{i}\sigma})$ are creation (destruction) operators for an electron at site $\mathbf{i}$ with spin σ, μ is the chemical potential, and $\hat{n}_{\mathbf{i}\sigma} = \hat{c}^{\dagger}_{\mathbf{i}\sigma} \hat{c}_{\mathbf{i}\sigma}$. The first sum is taken over all nearest neighbor pairs $\langle \mathbf{i}, \mathbf{j} \rangle$ of a two-dimensional square lattice. t is the nearest-neighbor hopping parameter which sets the energy scale ($t = 1$), with the electronic bandwidth given by $W = 8t$. At each site are local harmonic oscillators of frequency ω_0, with independent degrees of freedom $\hat{X}_{\mathbf{i}} = \sqrt{\frac{1}{2\omega_0}} \left(\hat{a}^{\dagger}_{\mathbf{i}} + \hat{a}_{\mathbf{i}} \right)$ and $\hat{P}_{\mathbf{i}} = \sqrt{\frac{\omega_0}{2}} \left(\hat{a}^{\dagger}_{\mathbf{i}} - \hat{a}_{\mathbf{i}} \right)$, where $\hat{a}^{\dagger}_{\mathbf{i}}(\hat{a}_{\mathbf{i}})$ are phonon creation (destruction) operators at site $\mathbf{i}$. The electron density $\hat{n}_{\mathbf{i}\sigma}$ couples to the displacement $\hat{X}_{\mathbf{i}}$ through a local electron-phonon coupling λ. In this work we measure the electron-phonon coupling in terms of the dimensionless quantity $\lambda_D = \lambda^2 / \omega_0^2 W$.

We study the Holstein model using determinant quantum Monte Carlo (DQMC) simulations [20, 65]. In DQMC, the inverse temperature is expressed as $\beta = L_t \Delta\tau$, where L_t denotes the number of intervals along the imaginary time axis with discretization $\Delta\tau$. The partition function $Z = \mathrm{Tr}\, e^{-\beta \hat{H}} = \mathrm{Tr}\, e^{-\Delta\tau \hat{H}} e^{-\Delta\tau \hat{H}} \ldots e^{-\Delta\tau \hat{H}}$ can then be evaluated by inserting complete sets of

phonon position states $|\{x_{i,\tau}\}\rangle$ at each imaginary time slice. Since the Hamiltonian is quadratic in fermionic operators, these can be traced out, giving

$$Z = \int d\{x_{i,\tau}\} e^{-S_{Bose}} [\det(M(\{x_{i,\tau}\}))]^2 \tag{3.2}$$

where

$$S_{Bose} = \Delta\tau \left[\frac{\omega_0^2}{2} \sum_{\mathbf{i},\tau} x_{\mathbf{i},\tau}^2 + \sum_{\mathbf{i},\tau} \left(\frac{x_{\mathbf{i},\tau+1} - x_{\mathbf{i},\tau}}{\Delta\tau} \right)^2 \right]. \tag{3.3}$$

The harmonic oscillator terms in Eq. (3.1) yield the 'bosonic action' term given by Eq. (3.3). The partition function also includes the product of the determinant of two matrices $M_\sigma(\{x_{\mathbf{i},\tau}\})$, one for each spin species $\sigma = \{\uparrow, \downarrow\}$. These matrices depend on the phonon field $\{x_{\mathbf{i},\tau}\}$ only. However, since $\hat{X}_\mathbf{i}$ couples in the same manner to the two species, the matrices M_σ are identical, giving the square of a determinant. An important consequence is the absence of a sign problem at any electronic filling. Physical quantities can be measured via Monte Carlo sampling of the phonon field $\{x_{\mathbf{i},\tau}\}$ and accumulating appropriate combinations of the fermion Green's function $G_{\mathbf{ij}} = \langle c_{\mathbf{i}\sigma} c_{\mathbf{j}\sigma}^\dagger \rangle = [M^{-1}]_{\mathbf{ij}}$. In our work we take $\Delta\tau = 0.125$. Trotter errors arising from the discretization of the imaginary time axis are less than the statistical errors associated with the Monte Carlo sampling for the charge and pair correlations given below.

The electron-phonon coupling term gives rise to an effective attractive electron-electron interaction $U_{\text{eff}} = -\lambda^2/\omega_0^2$ which promotes the formation of local pairs. On bipartite lattices this leads to CDW order at half-filling ($\langle \hat{n}_{\mathbf{i}\uparrow} + \hat{n}_{\mathbf{i}\downarrow} \rangle = 1$) with alternating doubly occupied and empty sites favored. This occurs at $\mu = -\lambda^2/\omega_0^2$, which can be shown via a particle-hole transformation. When the system is doped away from half-filling, superconductivity can arise at sufficiently low temperature due to the electron pairs becoming increasingly mobile. In this work we study the competition between CDW and SC as electron density is varied using DQMC, for a range of inverse temperatures $\beta = T^{-1}$ as low as $\beta = 28$. We fix $\lambda_D = 0.25$ and study two fixed frequencies $\omega_0 = 1$ and $\omega_0 = 4$ for lattices sizes with linear dimension up to $L = 12$.

We characterize the nature of the charge ordering by calculating the real-space, equal time, charge density correlation function $C(\mathbf{r})$, given by

$$C(\mathbf{r}) = \langle (\hat{n}_{\mathbf{i}\uparrow} + \hat{n}_{\mathbf{i}\downarrow})(\hat{n}_{\mathbf{i}+\mathbf{r}\uparrow} + \hat{n}_{\mathbf{i}+\mathbf{r}\downarrow}) \rangle, \tag{3.4}$$

and its Fourier transform $S(\mathbf{q})$, the CDW structure factor

$$S(\mathbf{q}) = \frac{1}{N} \sum_{\mathbf{i},\mathbf{j}} e^{i\mathbf{q}\cdot(\mathbf{i}-\mathbf{j})} \langle \hat{n}_{\mathbf{i}} \hat{n}_{\mathbf{j}} \rangle. \tag{3.5}$$

In the CDW ordered phase, $C(\mathbf{r})$ becomes long ranged and $S(\mathbf{q})$ grows in proportion to the lattice size $N = L^2$ at the appropriate ordering wavevector $\mathbf{q} = (q_x, q_y)$. In the absence of CDW order, the charge density correlations are short ranged and $S(\mathbf{q})$ should exhibit no lattice size dependence. The superconducting response of the system is analyzed by the s-wave pair susceptibility

$$P_s = \frac{1}{N} \int_0^\beta \langle \Delta(\tau) \Delta^\dagger(0) \rangle d\tau, \tag{3.6}$$

where $\Delta(\tau) = \sum_{\mathbf{i}} c_{\mathbf{i}\downarrow}(\tau) c_{\mathbf{i}\uparrow}(\tau)$. Similarly, an enhancement in the pair susceptibility and the observation of lattice size dependence in P_s as the temperature is lowered can be used to detect the onset of SC order. We use the susceptibility to study SC, as opposed to an equal time structure factor, because it provides a more robust signal which is useful for exploring off-diagonal long range order of the KT type.

3.4. Results and Discussion

At half-filling, i.e. $\rho = \langle \hat{n}_{\mathbf{i}\uparrow} + \hat{n}_{\mathbf{i}\downarrow} \rangle = 1$, it is known that checkerboard CDW order dominates on the square lattice with ordering wavevector $\mathbf{q} = (\pi, \pi)$. This occurs above the inverse critical temperature $\beta_{\text{cdw}} = 6.0 \pm 0.1$ for $\omega_0 = 1$ and $\beta_{\text{cdw}} \approx 13$ for $\omega_0 = 4$, with $\lambda_D = 0.25$ in both cases [48]. By varying the chemical potential, we dope the system away from half-filling and study the behavior of both $S(\pi, \pi)$ and P_s as a function of electron density, as shown in Figs. 3.1(a)–(d) for $\omega_0 = 1$ and $\omega_0 = 4$ at $\lambda_D = 0.25$. In both cases, $S(\pi, \pi)$ is significantly enhanced at $\rho = 1$ when the inverse temperature approaches β_{cdw}, but rapidly falls off when doped away from half-filling, and is highly suppressed below $\rho \approx 0.75$ for $\omega_0 = 1$. Simultaneously, the s-wave pair susceptibility becomes enhanced away from half-filling, reaching a maximum within the density range $\rho = 0.6$–0.7. When the phonon frequency is increased to $\omega_0 = 4$, P_s increases in magnitude, while $S(\pi, \pi)$ is diminished and becomes highly suppressed at a density closer to half-filling, at approximately $\rho \approx 0.85$.

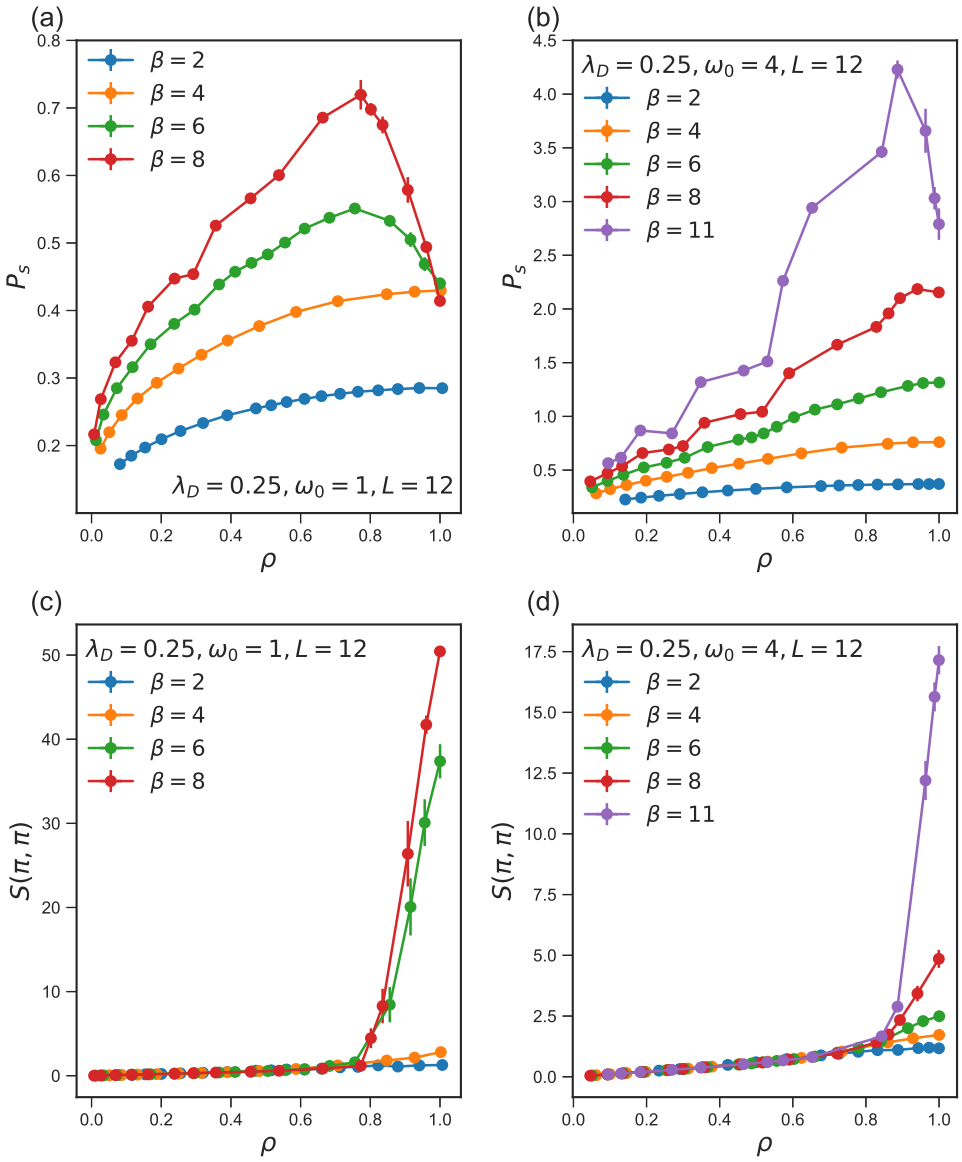

FIGURE 3.1. (a) S-wave pair susceptibility P_s as a function of electron density ρ for $\omega_0 = 1$ and $\lambda_D = 0.25$. (b) P_s vs. ρ for $\omega_0 = 4$ and $\lambda_D = 0.25$. (c) CDW structure factor $S(\pi, \pi)$ as a function of electron density ρ for $\omega_0 = 1$ and $\lambda_D = 0.25$. (d) $S(\pi, \pi)$ vs. ρ for $\omega_0 = 4$ and $\lambda_D = 0.25$. Data are shown for a 12×12 lattice for inverse temperatures $\beta = 2$, 4, 6, 8 and 11.

The CDW ordering which occurs at half-filling above β_{cdw} on the square lattice is a checkerboard pattern of alternating doubly occupied and empty sites. This becomes evident by plotting the real-space charge density correlation function $C(\mathbf{r})$ against site separation, as shown in Fig. 3.2 for a

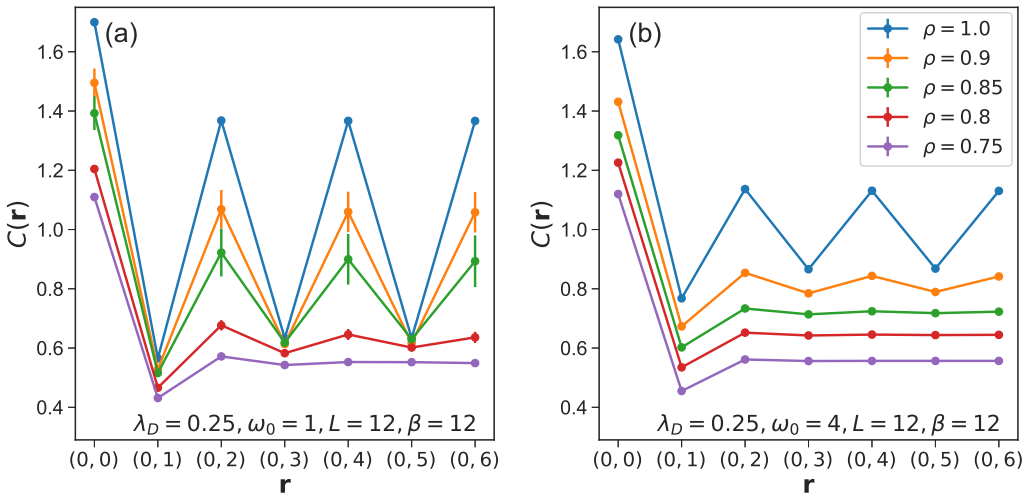

FIGURE 3.2. (a) Charge density correlation function $C(\mathbf{r})$ as a function of site separation $\mathbf{r}$, for a 12×12 lattice at $\beta = 12$, with $\mathbf{r} = (0,1) - (0,6)$ in units of the lattice spacing. Results are shown for $\omega_0 = 1$ and $\lambda_D = 0.25$ for fixed electron densities: $\rho = 1$, 0.9, 0.85, 0.8 and 0.75. (b) $C(\mathbf{r})$ vs. $\mathbf{r}$ for $\omega_0 = 4$ and $\lambda_D = 0.25$.

12×12 lattice at $\beta = 12$, for (a) $\omega_0 = 1$ and (b) $\omega_0 = 4$. The alternating high and low correlations at $\rho = 1$ are smoothed out as the density is lowered, with $C(\mathbf{r})$ becoming flat around $\rho \lesssim 0.75$ for $\omega_0 = 1$ and $\rho \lesssim 0.85$ for $\omega_0 = 4$. Increasing the phonon frequency inhibits CDW order, which is reflected by the smaller charge density correlations (at $\beta = 12$) for $\omega_0 = 4$, and the fact that the alternating CDW pattern is more rapidly suppressed for this frequency when doped away from half-filling.

At half-filling the square lattice exhibits perfect Fermi surface nesting (FSN) at $\mathbf{q} = (\pi, \pi)$ in the absence of any next-nearest neighbor hopping term, resulting in a peak in $S(\mathbf{q})$ at this wavevector. However when doped away from half-filling, the Fermi surface becomes distorted and perfect FSN no longer occurs. In Figs. 3.3(a)–(h) we show the variation of $S(\mathbf{q})$ with wavevector $\mathbf{q} = (q_x, q_y)$, taken on a triangular path through the Brillouin zone, for a 12×12 lattice at $\beta = 4$, 8, 16 and 24, for $\lambda_D = 0.25$, $\omega_0 = 1$. Results are shown for a range of electron densities from $\rho = 0.3$–1.0. $S(\mathbf{q})$ is not shown for small dopings away from half-filling. This will be further discussed in the interpretation of $\rho(\mu)$ shown in Fig. 3.7. Away from half-filling the peak magnitude of $S(\pi, \pi)$ is rapidly suppressed, reduced by a factor of 10 by $\rho \approx 0.8$, and falling by another order of magnitude by $\rho \approx 0.5$ (note the vertical scale of each plot).

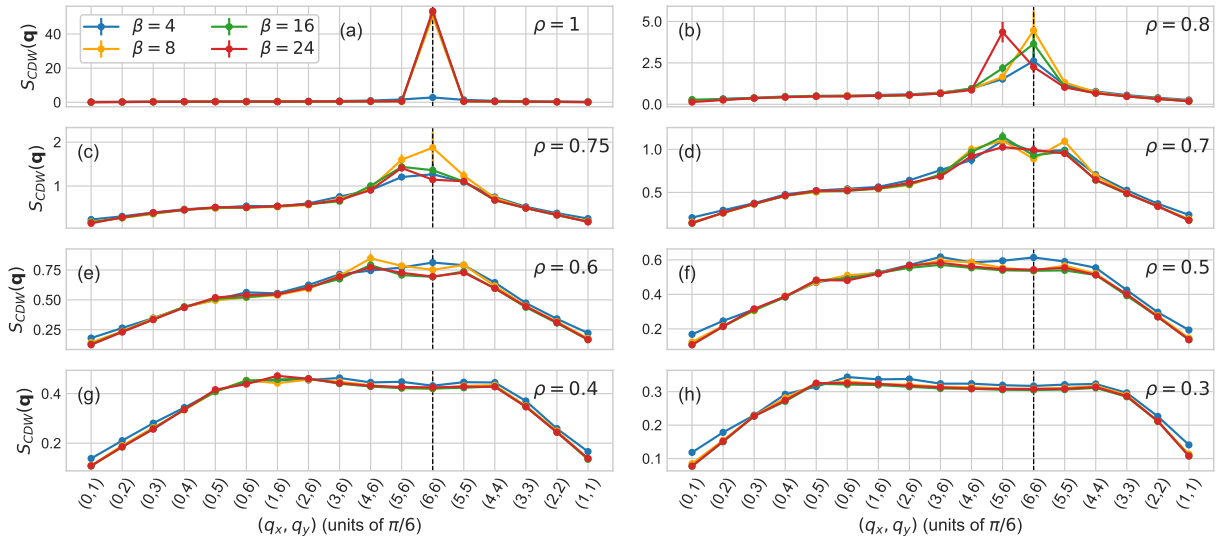

FIGURE 3.3. Variation of $S(\mathbf{q})$ with wavevector $\mathbf{q}$ for a 12×12 lattice, for $\omega_0 = 1$, $\lambda_D = 0.25$. A triangular path through the Brillouin zone is taken from $\mathbf{q} = (0, \pi/6)$ to $(0, \pi)$ to (π, π) to $(\pi/6, \pi/6)$. Results are shown for inverse temperatures $\beta = 4, 8, 16$ and 24 for electron densities in the range $\rho = 0.3 - 1.0$, specified in the upper-right corner of plots (a)–(h). In each plot the dashed line indicates the location of $\mathbf{q} = (\pi, \pi)$.

There is an important comment to make concerning the behavior at $\rho \approx 0.8$, where the location of the peak appears to shift to the wavevector nearest to (π, π), i.e. $\mathbf{q} = (5\pi/6, \pi)$ as shown in Fig. 3.3(d), with the shift occurring at low temperature ($\beta \approx 24$). The magnitude of $S(5\pi/6, \pi)$ at $\rho \approx 0.8$ grows as the temperature is lowered, becoming substantially enhanced at $\beta = 24$. Although this suggests the *possible* existence of an incommensurate CDW phase at $\rho \approx 0.8$, the rather coarse discrete momentum grid $q = \frac{2\pi}{L}\{0, 1, \cdots L\}$ precludes any conclusive statement.

When the system is doped even further from half-filling, as in Figs. 3.3(c)–(h), we do not observe any significant enhancement in $S(\mathbf{q})$ at any wavevector as the temperature is lowered from $\beta = 4$ to $\beta = 24$. The magnitude of $S(\mathbf{q})$ remains approximately constant over this temperature range for all values of $\mathbf{q}$, as shown in Figs. 3.3(c)–(h) for $\rho \leq 0.75$. In particular, within the density range $\rho = 0.6$–0.7, for which we observe a peak in the s-wave pair susceptibility, we find no indication of a coexisting CDW phase for any ordering wavevector.

Increasing the phonon frequency to $\omega_0 = 4$, we find qualitatively similar results as shown in Figs. 3.4(a)–(i), however there is no indication of CDW ordering at any particular wavevector for

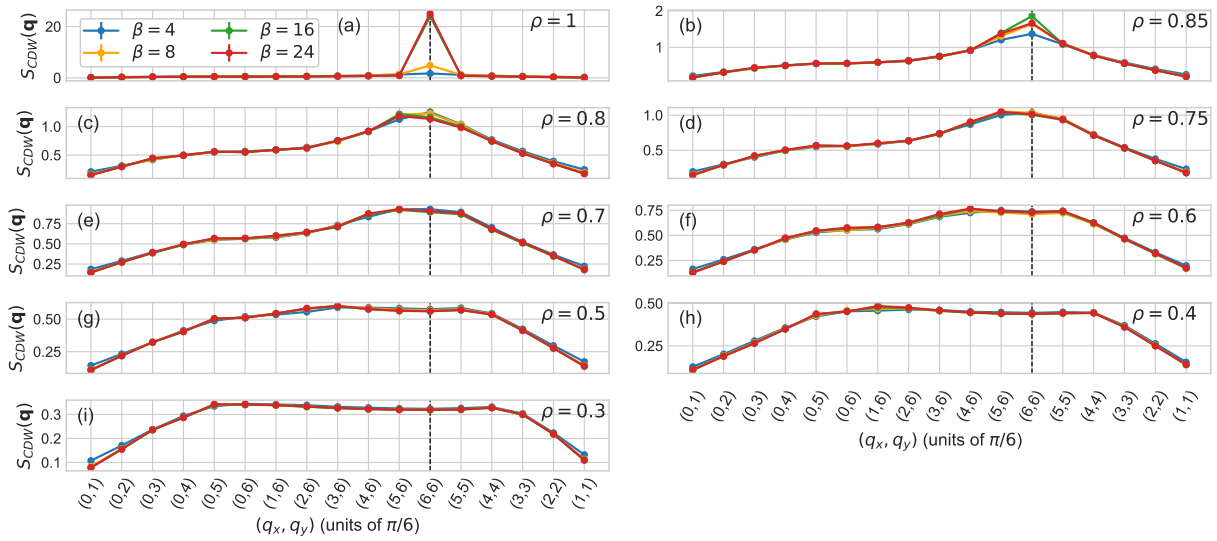

FIGURE 3.4. Variation of $S(\mathbf{q})$ with wavevector $\mathbf{q}$ for a 12×12 lattice, for $\omega_0 = 4$, $\lambda_D = 0.25$. A triangular path through the Brillouin zone is taken from $\mathbf{q} = (0, \pi/6)$ to $(0, \pi)$ to (π, π) to $(\pi/6, \pi/6)$. Results are shown for inverse temperatures $\beta = 4, 8, 16$ and 24 for electron densities in the range $\rho = 0.3 - 1.0$, specified in the upper-right corner of plots (a)–(i). In each plot the dashed line indicates the location of $\mathbf{q} = (\pi, \pi)$.

any electron density, other than at $\mathbf{q} = (\pi, \pi)$ at low temperature. The magnitude of $S(\pi, \pi)$ near half filling is also considerably suppressed compared to $\omega_0 = 1$, which is expected since increasing the phonon frequency inhibits CDW order. Although the peak in $S(\mathbf{q})$ shifts to $\mathbf{q} = (5\pi/6, \pi)$ at $\rho \approx 0.8$ as the temperature is reduced, there is no significant enhancement in the magnitude of $S(\mathbf{q})$ at this wavevector as temperature is lowered from $\beta = 4$ to $\beta = 24$, in contrast to the behavior at $\omega_0 = 1$ (Fig. 3.3).

In order to determine the critical inverse temperature β_{sc} for the SC transition, we first tune the chemical potential to achieve a fixed target density and study P_s as a function of β, for several different lattice sizes. Since P_s appears to peak in the range $\rho = 0.6$–0.7 for $\omega_0 = 1$, $\lambda_D = 0.25$, we choose to study two fixed densities $\rho = 0.6$ and $\rho = 0.7$ for this phonon frequency. For $\omega_0 = 4$, $\lambda_D = 0.25$, since CDW correlations appear highly suppressed closer to half-filling, we fix $\rho = 0.85$ and also study $\rho = 0.6$ for comparison. In Figs. 3.5(a)–(d) we show $P_s(\beta)$ for lattices of linear dimension $L = 6, 8, 10$ and 12 for these four parameter sets. For each case, we find at low β (high T), P_s is relatively small and is independent of lattice size, however as the temperature is lowered,

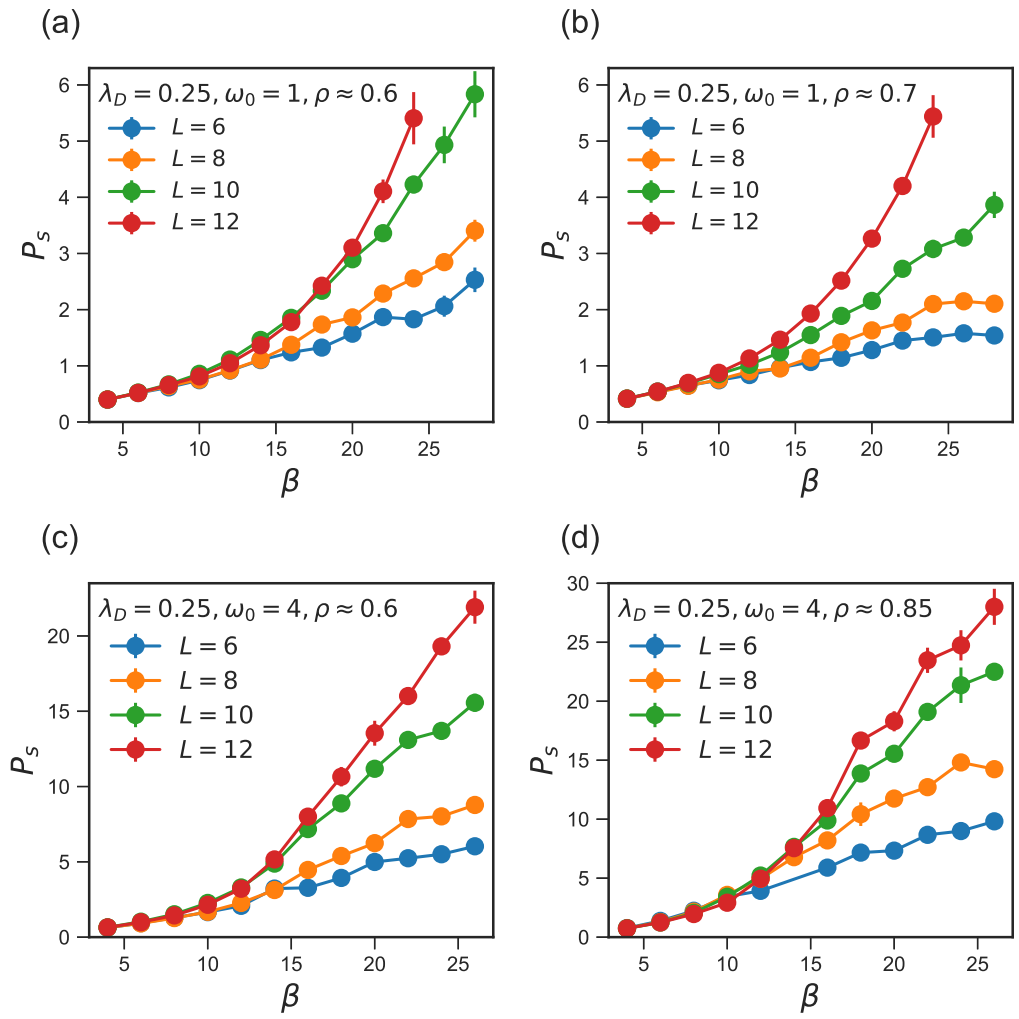

FIGURE 3.5. S-wave pair susceptibility as a function of inverse temperature β for lattice sizes of linear dimension $L = 6$, 8, 10 and 12, for the four fixed densities studied: (a) $\rho = 0.6$ and (b) $\rho = 0.7$ for $\lambda_D = 0.25$, $\omega_0 = 1$. For increased phonon frequency $\omega_0 = 4$, we fix (c) $\rho = 0.6$ and (d) $\rho = 0.85$ with the same dimensionless coupling $\lambda_D = 0.25$ and (a,b).

P_s grows and becomes dependent on L. This suggests the onset of the SC phase, because when correlations become long range they will be sensitive to the lattice size for a finite system. We can therefore apply a finite-size scaling analysis to confirm the existence of a critical inverse temperature β_{sc} for the SC transition, and determine its value.

In the two dimensional superconducting transition, the order parameter possesses $U(1)$ gauge symmetry and thus the universality class is the same as the 2D XY model. Hence we expect

a Kosterlitz-Thouless (KT) transition to a quasi-long-range ordered phase, for which the critical exponents and scaling behavior of the order parameter are known [66]. For a finite-size system of linear dimension L, we have that

$$P_s = L^{2-\eta} f\left(\frac{L}{\xi}\right) \tag{3.7}$$

with $\eta = 1/4$, and as $T \to T_{\rm sc}^+$ the correlation length ξ scales as

$$\xi \sim \exp\left[A\left(T - T_{\rm sc}\right)^{-1/2}\right] \tag{3.8}$$

where A is a constant and $T_{\rm sc}$ is the critical temperature. Therefore near $T_{\rm sc}$, plotting $P_s L^{-7/4}$ as a function of $L \exp\left[-A\left(T - T_{\rm sc}\right)^{-1/2}\right]$ for a range of lattice sizes should result in a data collapse onto a single universal curve, as shown in Figs. 3.6(a)–(d) for the four parameter sets studied. For $\lambda_D = 0.25$, $\omega_0 = 1$, we find the best data collapse occurs at $\beta_{\rm sc} \approx 28.5 \pm 1.0$ for $\rho = 0.6$ and $\beta_{\rm sc} \approx 27.5 \pm 1.0$ for $\rho = 0.7$. Keeping the dimensionless electron-phonon coupling fixed at $\lambda_D = 0.25$, increasing phonon frequency to $\omega_0 = 4$ raises the critical temperature, and we find the best data collapse at $\beta_{\rm sc} \approx 22.5 \pm 1.0$ for $\rho = 0.6$ and $\beta_{\rm sc} \approx 23.5 \pm 1.0$ for $\rho = 0.85$. Our value of $\beta_{\rm sc}$ for $\omega_0 = 1$ lies slightly below the range of $\beta_{\rm sc} = 30$–40 suggested by Vekić et al [3], although their estimate was performed using data rather far from the scaling region. Indeed, as might be expected, to obtain a precise value we find it essential to access temperatures as close as possible to T_{sc} rather than extrapolate from higher T, as discussed in the Appendix. Meanwhile, our estimate of $\beta_{\rm sc}$ for $\omega_0 = 4$ at $\rho = 0.85$ is higher than the previous $\beta_{\rm sc} \approx 12$ at $\rho = 0.8$. The larger values of L and β accessed in this study allow a more robust finite-size scaling for the KT transition. We also note that for the lower phonon frequency we study, for which the ME approximation would be more justifiable than for $\omega_0 = 4$, recent ME calculations [67] have estimated $T_{\rm sc}$ for the parameters shown in Fig. 3.5(a), yielding a value within approximately 10% our result.

We note that increasing phonon frequency simultaneously raises $T_{\rm sc}$ for the SC transition, and lowers $T_{\rm cdw}$ for the CDW transition at half-filling (from $T_{\rm cdw} \approx t/6$ at $\omega_0/t = 1$ to $T_{\rm cdw} \approx t/13$ at $\omega_0/t = 4$ [48]), illustrating the competition between SC and CDW order in the Holstein model. This is as expected since as ω_0 is lowered, the harmonic oscillators on each site become more classical, reducing quantum fluctuations. As a result, bipolarons localize more readily, enhancing CDW order [54]. Conversely, it is known that in the anti-adiabatic limit ($\omega_0 \to \infty$) the Holstein model

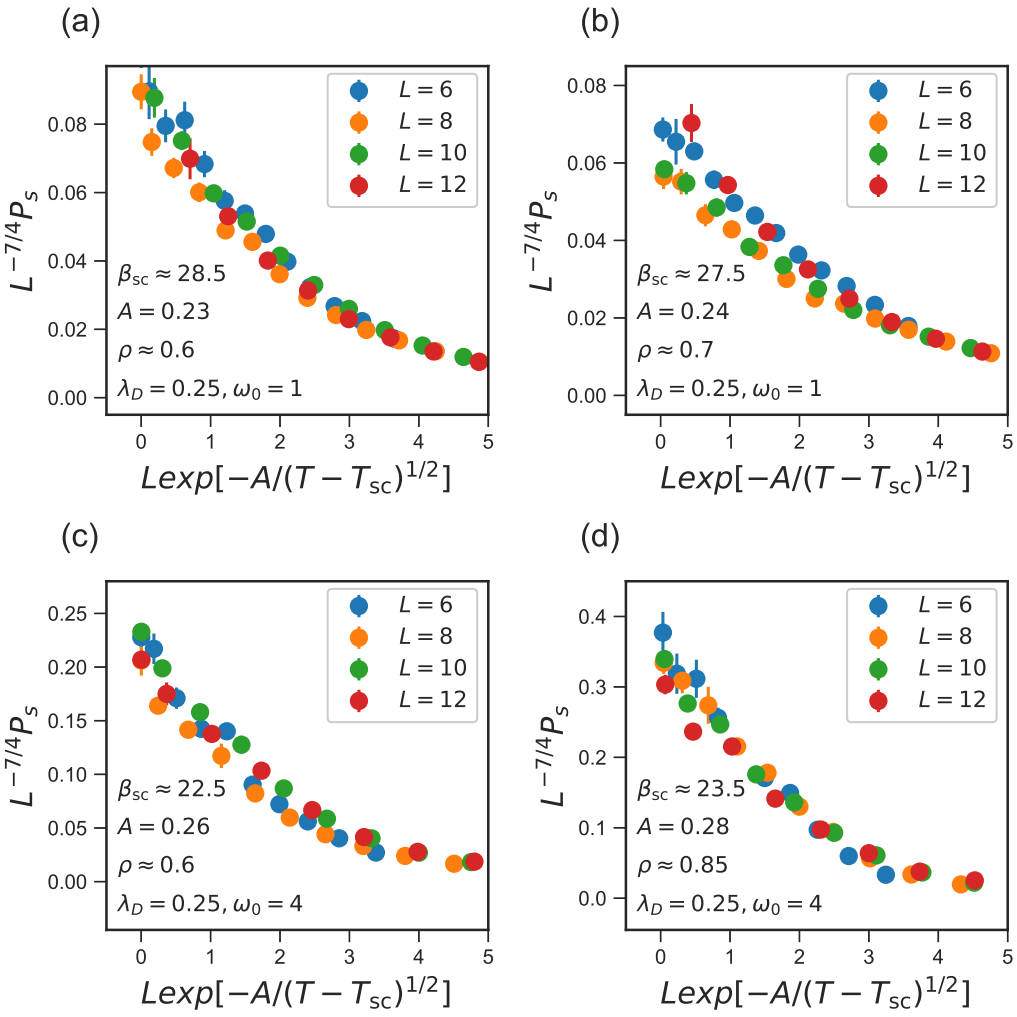

FIGURE 3.6. Finite size scaling of the s-wave pair susceptibility data obtained for the four parameter sets shown in Figs. 3.5(a)–(d). The critical inverse temperature β_{sc} and scaling factor A which yields the best data collapse is indicated in the inset of each plot.

can be mapped onto the attractive Hubbard model [3, 4, 45] with $U_{\text{eff}} = -\lambda^2/\omega_0^2 = -\lambda_D W$ [68], which has been shown to possess a finite temperature superconducting KT transition away from half-filling [69, 70, 71]. Thus one expects SC correlations to be enhanced in the Holstein model at larger values of ω_0, as we have confirmed here. Furthermore, in the attractive Hubbard model, the SC and CDW correlations are degenerate at half-filling, leading to a continuous order parameter in the Heisenberg universality class and the absence of a finite-temperature transition (i.e. $T_c = 0$)

in 2D. At half-filling, the CDW order parameter $S(\pi,\pi)$ is therefore reduced, with P_s increasing simultaneously in the limit $T \to 0$. We thus expect similar behavior in the Holstein model as $\omega_0 \to \infty$, which we have observed as an enhancement in P_s and a reduction in $S(\pi,\pi)$ at $\omega_0 = 4$ at half-filling, as shown in Figs. 3.1(a)–(d). We also note that studies of the attractive Hubbard model have found $T_{\rm sc}$ is maximal at around $U/t \approx -5$, for which $T_{\rm sc}/t \approx 0.15$ occurs at a filling $\rho = 0.7$ [72]. Since this effective coupling corresponds to a larger λ_D value than we study in this work, this suggests raising λ_D could enhance $T_{\rm sc}$ at large phonon frequencies. We have determined $T_{\rm sc}$ values for $-\lambda_D W = -2$ in this work, which one can compare to recent estimates of $T_{\rm sc}$ in the attractive Hubbard model [73]: for $U = -2.0$, $\beta_{\rm sc} = 19.0$ at $\rho = 0.7$, and $\beta_{\rm sc} = 13.5$ at $\rho = 0.87$, while for $U = -2.5$, $\beta_{\rm sc} = 23.0$ at $\rho = 0.5$. However, for $\omega_0 = 1$ and $\omega_0 = 4$, the actual on-site interaction will be smaller than in the anti-adiabatic limit (i.e. $|U| < 2$), giving a lower $T_{\rm sc}$, and the attractive Hubbard model thus provides an upper bound on $T_{\rm sc}$ in the Holstein model. Our estimates of $T_{\rm sc}$ at $\omega_0 = 1$ and $\omega_0 = 4$ are therefore quite consistent with those of the attractive Hubbard model.

We conclude the presentation of our results by noting that $\rho(\mu)$ appears to exhibit a discontinuous jump approaching the CDW transition at half-filling, as shown in Figs. 3.7(a) and (b) for $\omega_0 = 1$ and $\omega_0 = 4$. In both cases, we have that half-filling ($\rho = 1$) occurs at a chemical potential of $\mu = -\lambda^2/\omega_0^2 = -2$. Below $T_{\rm cdw}$, the formation of a plateau at $\rho = 1$ indicates the opening of the CDW gap. However, well below the transition temperature ($\beta_{\rm cdw} = 6.0 \pm 0.1$ for $\omega_0 = 1$ and $\beta_{\rm cdw} \approx 13$ for $\omega_0 = 4$) we observe a discontinuous jump in electron density as the chemical potential is varied, occurring for $\rho \gtrsim 0.8$ for $\omega_0 = 1$, and $\rho \gtrsim 0.9$ for $\omega_0 = 4$ (with $\lambda_D = 0.25$ in both cases). We note that these density ranges correspond roughly to the regions over which $S(\pi,\pi)$ grows rapidly, occurring closer to half-filling for greater ω_0, as shown previously in Figs. 3.1(c) and (d). The jump is less abrupt for $\omega_0 = 4$ but becomes apparent at $\beta = 24$, whereas a clear discontinuity emerges for $\beta \geq 16$ for $\omega_0 = 1$. This indicates finite temperature fluctuations smooth the jump more at higher frequencies.

In both cases, the jump is accompanied by an increase in the error in ρ for data close to half-filling, possibly indicating fluctuations of the system between densities on either side of the

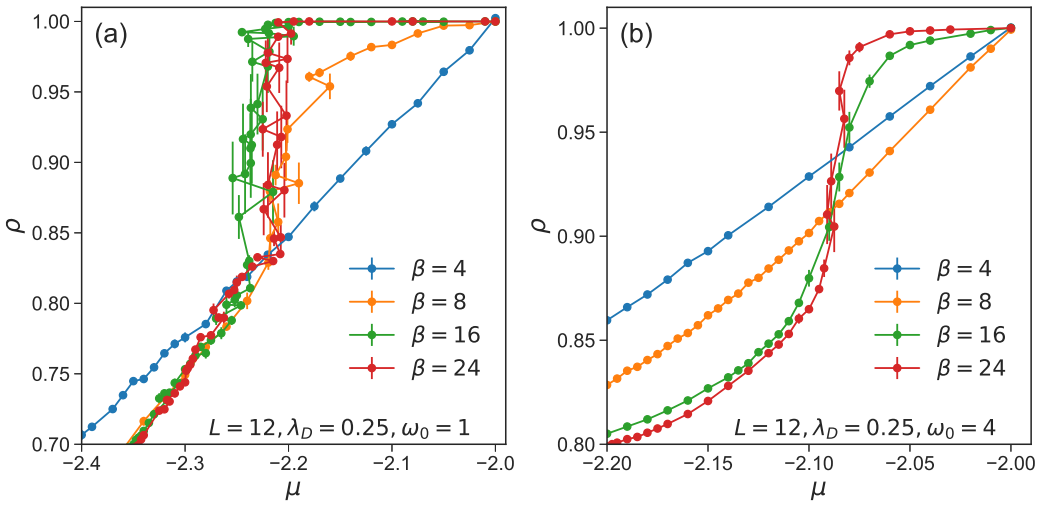

FIGURE 3.7. Density ρ as a function of chemical potential μ approaching the CDW transition at half-filling. Results shown for $L = 12$ lattices with $\lambda_D = 0.25$, for phonon frequencies (a) $\omega_0 = 1$ and (b) $\omega_0 = 4$. The data suggest a discontinuous jump prior to entry to the incompressible CDW region. Individual data points, and their large error bars, within the discontinuous jump are shown only to emphasize the difficulty of Monte Carlo sampling in this region.

discontinuity. This discontinuity may be related to the zero temperature transition from SC to commensurate CDW order, which has been observed to be first order [74].

3.5. Conclusions

In previous QMC studies, the CDW transition temperature T_{cdw} of the Holstein model at half-filling has been determined for various two-dimensional systems, including the square, honeycomb, and Lieb lattices. However, the superconducting transition away from half-filling in the square lattice has been much less well characterized, since it occurs at challengingly large values of the inverse temperature β as well as scaling in the spatial lattice size L. Moreover, away from half-filling, no analytical expression for $\rho(\mu)$ can be used to achieve a fixed target density [75], necessitating a tuning of μ for each lattice size and β. In this chapter, we have studied larger systems (up to $L = 12$) and lower temperatures (up to $\beta = 28$) than in previous work, and have determined several estimates of T_{sc} for various electron densities (fixed via tuning the chemical potential) and phonon frequencies ω_0, through a finite-size scaling analysis of pair susceptibility. We observe the onset

of SC at temperatures $T_{\rm sc} \lesssim W/160$ in each case studied. Here $W = 8\,t$ is the non-interacting bandwidth and t is the nearest neighbor hopping amplitude.

Specifically, for dimensionless electron-phonon coupling $\lambda_D = 0.25$, and phonon frequency $\omega_0/t = 1$, we estimate $T_{\rm sc} \approx W/228 = t/28.5$ for $\rho = 0.6$ and $T_{\rm sc} \approx W/220 = t/27.5$ for $\rho = 0.7$. For $\lambda_D = 0.25$, $\omega_0 = 4$, we estimate $T_{\rm sc} \approx W/180 = t/22.5$ for $\rho = 0.6$ and $T_{\rm sc} \approx W/188 = t/23.5$ for $\rho = 0.85$.

Several features illustrating the competition between CDW order and SC in the doped Holstein model emerge from our analysis. In particular, the strong checkerboard CDW order present at half-filling below $T_{\rm cdw}$ (corresponding to a peak in $S(\pi, \pi)$) is rapidly suppressed as the system is doped, with SC correlations becoming maximal in the region $\rho = 0.6$–0.7 for $\lambda_D = 0.25$, $\omega_0 = 1$. However, at an intermediate electron density of approximately $\rho \approx 0.8$, we observe evidence of a *possible* incommensurate CDW phase, with the peak in $S(\mathbf{q})$ shifting slightly from $\mathbf{q} = (\pi, \pi)$ to $\mathbf{q} = (5\pi/6, \pi)$ at low temperature. Definitive analysis of this point is precluded by the finite momentum grids currently accessible to present QMC capabilities. No evidence of a distinctly different kind of charge ordering (e.g. stripe order) is observed away from half-filling.

It is interesting to note that our estimates of $T_{\rm sc}$ in the doped Holstein model are similar in magnitude to $T_{\rm sc}$ in the half-filled case with non-zero phonon dispersion $\Delta\omega/\omega_0 = 0.1$, where DQMC simulations [48] have determined $T_{\rm sc} \approx t/26$ for $\lambda_D = 0.25$, $\omega_0 = 4$. Further, it has been proposed [76] that an upper bound on $T_{\rm sc}$ exists which is $T_{\rm sc} \lesssim \bar{\omega}/10$, where $\bar{\omega} \leq \omega_0$ is a characteristic phonon frequency no larger than the bare phonon frequency, and that for an optimal value of λ_D, $T_{\rm sc}$ should roughly saturate at this value. Since our estimates of $T_{\rm sc}$ lie below this upper bound, this suggests it may be possible to increase the transition temperature by increasing λ_D. Recently, a QMC method based on Langevin updates of the phonon degrees of freedom [77, 78] has also made studies of the cubic Holstein model amenable to simulation, and it has been found that $T_{\rm cdw}$ at half-filling is increased roughly by a factor of two compared to various two-dimensional geometries [79]. We anticipate that in future studies of the 3D Holstein model one might similarly expect higher values of $T_{\rm sc}$ away from half-filling, since the model will exhibit a more robust transition to long-ranged superconducting order, in contrast with the KT transition in two dimensions observed in this work.

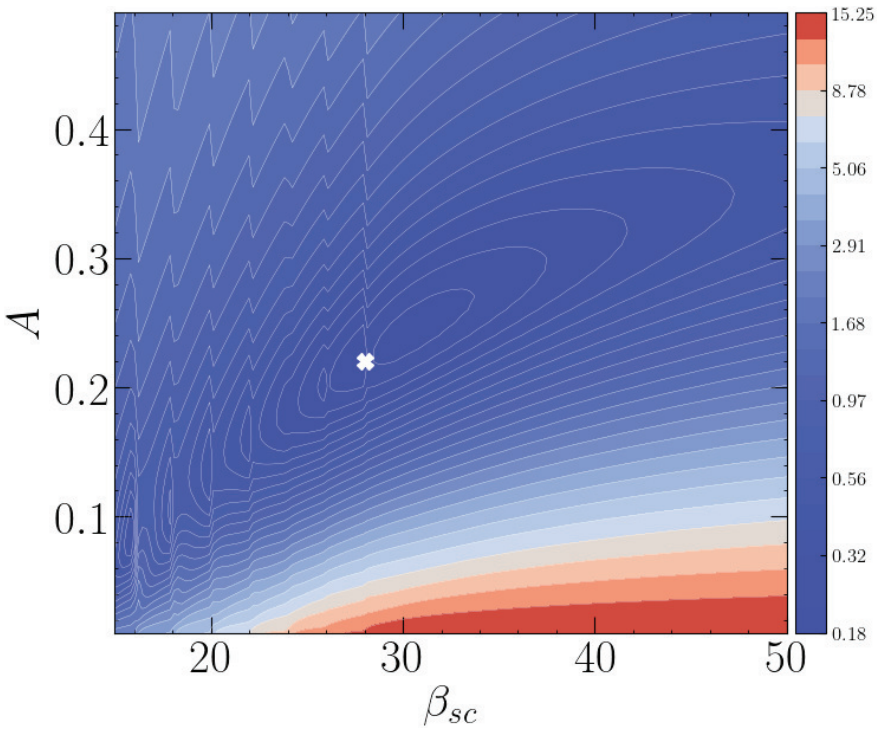

FIGURE 3.8. Finite size scaling for $\omega_0 = 1$, $\lambda_D = 0.25$, $\rho \approx 0.6$, using data up to $\min(\beta_{sc}, 28)$. Quantity shown is the sum of squared residuals for a 4^{th} order polynomial fit to $P_s L^{-7/4}$ vs. $L \exp\left[A(T - T_{sc})^{-1/2}\right]$ using low temperature data up to $\beta = 28$. The marker indicates the best fit parameters: $A \approx 0.22$ and $\beta_{sc} \approx 28.0$.

3.6. Appendix: Extrapolating T_{sc} from higher temperature

In this chapter, we have determined estimates of T_{sc} by accessing low temperatures (up to $\beta = 28$) close to the superconducting transition temperature, rather than extrapolating from higher T data as done in previous work. In [3], inverse temperatures up to $\beta = 12$ are accessed, and a broad range of $\beta_{sc} = 30$–40 is proposed (for $\omega_0 = 1$). To investigate how the determination of T_{sc} changes when one extrapolates from higher temperature, we have taken our data and excluded the lower temperature results, and performed Kosterlitz-Thouless scaling fits in order to mimic the capabilities of earlier work. Specifically, we have analyzed our data using only values $T \geq T_{\min} = 1/12$ (that is, $\beta \leq 12$).

We have fit a fourth order polynomial curve to the scaled data shown in Fig. 3.6, and determined the quality of these fits for various values of β_{sc} and A, shown in Figs. 3.8 and 3.9 above for the case $\omega_0 = 1$, $\rho = 0.6$. In each plot, the quantity shown is the sum of squared residuals for the

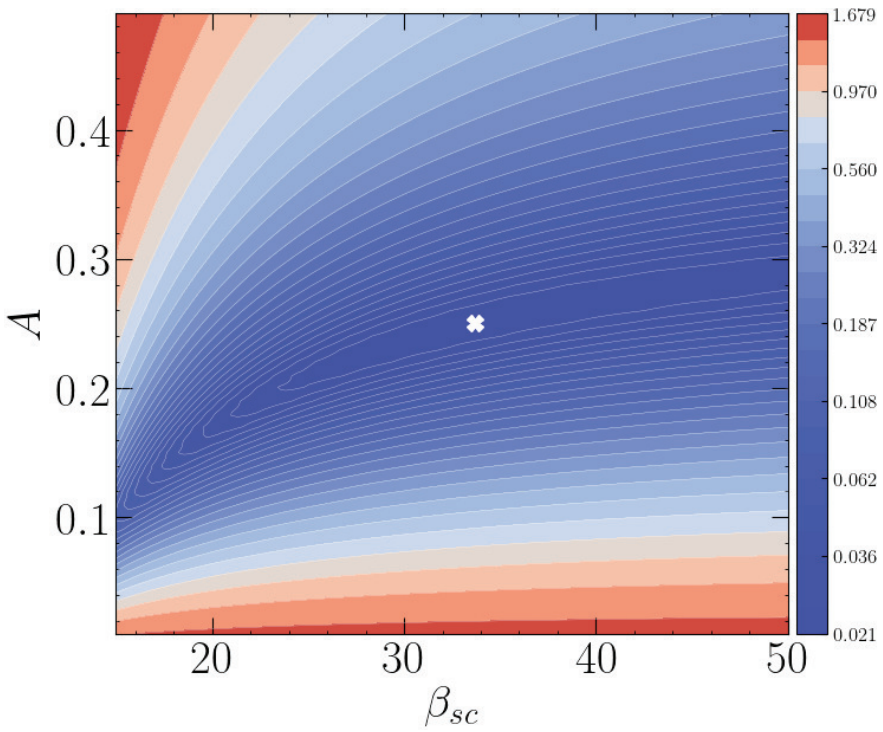

FIGURE 3.9. Finite size scaling for $\omega_0 = 1$, $\lambda_D = 0.25$, $\rho \approx 0.6$, using data up to $\min(\beta_{sc}, 12)$, which corresponds to that available in the original studies of this model. Extrapolating T_{sc} from higher temperature, we show the sum of squared residuals for a 4^{th} order polynomial fit using data up to $\beta = 12$ only. The marker indicates the best fit parameters: $A \approx 0.25$ and $\beta_{sc} \approx 33.7$.

polynomial fit, with lower values indicating a closer fit to the scaled data. In Fig. 3.8, we use all our low temperature data (up to $\beta = 28$), and Fig. 3.9 shows the results using data with $\beta \leq 12$. If one attempts the Kosterlitz-Thouless scaling using data with $\beta \leq 12$ only (Fig. 3.9), one can fit a curve to the data with relatively low error. However, in Fig. 3.5(a), we observed that P_s is completely independent of L for $\beta \lesssim 12$ (indicating the absence of quasi-long-range order since this is far from β_{sc}). Therefore plotting $P_s L^{-7/4}$ vs. $L \exp\left[A(T - T_{sc})^{-1/2}\right]$ yields a curve with an approximately exponential form with little to no overlap between the smallest and largest lattice sizes. In attempting to find T_{sc} from these data, we find the best collapse occurs at $A \approx 0.25$, $T_{sc} \approx 1/33.7$, and naively, using the $\beta \leq 12$ restricted data appears to provide a better fit. However, as shown in Fig. 3.9, the quality of the fit is essentially unchanged over a very large range of β_{sc} values (note the innermost contour which ranges from $\beta_{sc} \approx 25$ to well beyond $\beta_{sc} = 50$). We thus find it is essential to use low temperature data as close as possible to the critical temperature (as

shown in Fig. 3.8 which uses data with $\beta \leq 28$), not only to make the value of T_{sc} convincing, but to pin down the value more precisely than the broad range given in previous work [3].

Note that in Figs. 3.8 and 3.9 above, the scaling collapses are performed using data with inverse temperatures up to $\min(\beta_{sc}, 28.0)$ and $\min(\beta_{sc}, 12.0)$, respectively. This is because the Kosterlitz-Thouless scaling requires computing $(\frac{1}{\beta} - \frac{1}{\beta_{sc}})^{-1/2}$, and thus for each attempted collapse, data for temperatures lower than β_{sc} can not be used. Furthermore, the lack of smoothness to the contours in Fig. 3.8 comes from the fact that our $P_s(\beta)$ data (shown in Fig. 3.5) is relatively sparse, and so the best value of the scaling parameter A can change abruptly when additional data points are included in the collapse, which occurs as β_{sc} is increased.

CHAPTER 4

Charge Order in the Kagome Lattice Holstein Model: A Hybrid Monte Carlo Study

4.1. Chapter Summary

The Holstein model is a paradigmatic description of the electron-phonon interaction, in which electrons couple to local dispersionless phonon modes, independent of momentum. The model has been shown to host a variety of ordered ground states such as charge density wave (CDW) order and superconductivity on several geometries, including the square, honeycomb, and Lieb lattices. In this chapter, we study CDW formation in the Holstein model on the kagome lattice, using a recently developed hybrid Monte Carlo simulation method. We present evidence for $\sqrt{3}\times\sqrt{3}$ CDW order at an average electron filling of $\langle n\rangle = 2/3$ per site, with an ordering wavevector at the K-points of the Brillouin zone. We estimate a phase transition occurring at $T_c \approx t/18$, where t is the nearest-neighbor hopping parameter. Our simulations find no signature of CDW order at other electron fillings or ordering momenta for temperatures $T \geq t/20$.

This chapter is based on the following paper [80]:

O. Bradley, B. Cohen-Stead, S. Johnston, K. Barros, and R. T. Scalettar, *Charge order in the kagome lattice Holstein model: A Hybrid Monte Carlo study*, npj Quantum Materials **8**, 21 (2023).

The Hybrid Monte Carlo algorithm [26] and the chemical potential tuning method [75] used in this chapter are discussed in the following publications:

B. Cohen-Stead, **O. Bradley**, C. Miles, G. Batrouni, R. Scalettar, and K. Barros, *Fast and scalable quantum Monte Carlo simulations of electron-phonon models*, Phys. Rev. E **105**, 065302 (2022).

C. Miles, B. Cohen-Stead, **O. Bradley**, S. Johnston, R. Scalettar, and K. Barros, *Dynamical tuning of the chemical potential to achieve a target particle number in grand canonical Monte Carlo simulations*, Phys. Rev. E **105**, 045311 (2022).

4.2. Introduction

The interaction between electrons in a solid and the vibrations of its nuclei (phonons) can induce a variety of ordered phases [42, 43, 55, 56, 81, 82]. This electron-phonon coupling modifies the effective mass of itinerant electrons, and the resulting dressed quasiparticles (polarons) can pair and condense into a superconducting (SC) phase or form a periodic modulation of electron density, i.e. CDW order. At low temperatures these various phases can compete or potentially coexist. Over the past several decades, studies of model Hamiltonians describing electron-phonon coupling have attempted to capture the interplay between their emergent ordered phases. In particular, the Holstein model [2] has been subject to much numerical and analytical study because it incorporates a simplified electron-phonon interaction into a straightforward tight-binding Hamiltonian, yet exhibits a variety of competing ordered ground states.

A key feature of the Holstein model is an on-site momentum-independent electron-phonon coupling, which leads to an effective electron-electron attraction. Phonons are modeled as quantum harmonic oscillators of fixed frequency ω_0 situated on each site of a lattice, with their motion independent of their neighbors. At low temperatures and at particular electron filling fractions, numerical studies have revealed the emergence of CDW order on square [3, 4, 28, 45, 48, 53, 57, 59, 60, 63, 64, 83, 84, 85, 86], triangular [54], cubic [79], and honeycomb lattices [50, 51], with the transition temperature being sensitive to lattice geometry and dimensionality. A recent study of the Lieb lattice has also established the existence of CDW order in the Holstein model in a flat band system [87].

In recent years, kagome lattices have attracted attention as a host of exotic phases owing to their high degree of geometrical frustration, and the presence of a flat band. The spin-1/2 kagome lattice Heisenberg antiferromagnet (KHAF) with nearest-neighbor interactions lacks any magnetic ordering, but the exact nature of the ground state been subject to much debate, with several candidates such as the Dirac spin-liquid, Z_2 spin-liquid, and valence bond crystal proposed [88, 89, 90, 91]. A recent study of the KHAF in the presence of spin-lattice coupling has shown that introducing Einstein phonons on each site can induce a magnetically ordered phase [92]. For example, a $\sqrt{3}\times\sqrt{3}$ ordered phase with a 1/3-magnetization plateau emerges in weak magnetic field, breaking a Z_3 symmetry, with the transition belonging to the 3-state Potts model universality class.

The ordering wavevector for this phase lies at the K-points, i.e. corners, of the hexagonally-shaped Brillouin zone.

The ground state properties of the half-filled kagome lattice Hubbard model are also debated. Dynamical mean field theory (DMFT) and determinant quantum Monte Carlo (DQMC) studies have identified a metal-insulator transition (MIT) in the range $U_c/t \sim$ 7–9 [93, 94, 95], while variational cluster approximation (VCA) calculations estimate $U_c/t \sim$ 4–5 [96]. Recent density-matrix renormalization group (DMRG) calculations find a MIT at $U_c/t \sim 5.4$, along with strong spin-density wave fluctuations in the translational symmetry breaking insulating phase, signaled by an enhancement in the spin structure factor at the K-points of the Brillouin zone [97]. CDW formation on the kagome lattice has also been observed in the extended Hubbard model. At an average electron density per site of $\langle n \rangle = 2/3$ or $4/3$, or at the van Hove filling $\langle n \rangle = 5/6$, several types of order have been observed [98, 99, 100, 101], including CDW, spin density wave, and bond ordered wave states. In particular, at large V/U (where V is the nearest-neighbor repulsion), a CDW phase with a $\sqrt{3} \times \sqrt{3}$ supercell has been proposed for $\langle n \rangle = 2/3$ and $5/6$, which has been termed CDW-III in previous studies [100, 101]. In the attractive Hubbard model, recent results [102] indicate short-ranged charge correlations at $\langle n \rangle = 2/3$ satisfying the triangle rule.

Recent experiments on kagome metals such as AV_3Sb_5 (A = K, Rb, Cs) [103, 104, 105, 106, 107, 108, 109, 110, 111, 112, 113, 114, 115] also motivate an understanding of CDW formation on this geometry. In these systems, charge ordering has been observed at the M-points, corresponding to lattice distortions that form a star-of-David or inverse star-of-David CDW pattern. This ordering wavevector coincides with saddle points in the band structure and van Hove singularities where electronic correlations are enhanced. Theoretical studies of these materials [116, 117, 118, 119, 120, 121, 122, 123, 124], including first-principles density functional theory and mean field calculations, have corroborated these findings, where CDW ordering at the M-points has been observed near the van Hove filling.

Finally, kagome lattices have also been achieved in ultracold atom experiments [125] where they have been used to examine Bose-Einstein condensation of ^{87}Rb [126], and Rydberg atoms with large entanglement entropy and topological order [127].

Although the Holstein coupling provides a paradigmatic model of the electron-phonon interaction, the properties of the Holstein model on the kagome lattice are not yet understood, and the possible existence of CDW order remains hitherto unexplored. In this chapter, we study the kagome lattice Holstein model using a scalable algorithm based upon hybrid Monte Carlo (HMC) sampling [26], and measure the charge correlations as a function of temperature, electron density, phonon frequency, and electron-phonon coupling. We present evidence for CDW order appearing at an average electron density per site of $\langle n \rangle = 2/3$, with an ordering wavevector at the K-points of the Brillouin zone, yielding a $\sqrt{3} \times \sqrt{3}$ supercell. Away from this filling, we find no signatures of CDW order at any ordering momenta for temperatures $T \geq t/20$.

4.3. Methods

The Holstein model describes electrons coupled to local dispersionless phonon modes in a lattice through an on-site electron-phonon interaction [2]. Its Hamiltonian is

$$\hat{H} = -t \sum_{\langle i,j \rangle, \sigma} \left(\hat{c}^{\dagger}_{i\sigma} \hat{c}_{j\sigma} + h.c. \right) - \mu \sum_{i\sigma} (\hat{n}_{i\sigma} - \tfrac{1}{2}) + \frac{1}{2} \sum_{i} \hat{P}_i^2 + \frac{\omega_0^2}{2} \sum_{i} \hat{X}_i^2 + \alpha \sum_{i\sigma} \hat{n}_{i\sigma} \hat{X}_i \ ,$$

where $\hat{c}^{\dagger}_{i\sigma}$ ($\hat{c}_{i\sigma}$) are creation (destruction) operators for an electron at site i with spin $\sigma = \{\uparrow\downarrow\}$, $\hat{n}_{i\sigma} = \hat{c}^{\dagger}_{i\sigma} \hat{c}_{i\sigma}$ is the electron number operator, and μ is the chemical potential, which controls the overall filling fraction. The first term describes itinerant electrons hopping between nearest-neighbor sites of the lattice, with a fixed hopping parameter $t = 1$ setting the energy scale. In the non-interacting limit, the electronic bandwidth is $W = 6$ for the kagome lattice. On each site i are local oscillators of fixed frequency ω_0, with $\hat{X}_i$ and $\hat{P}_i$ the corresponding phonon position and momentum operators, respectively, with the phonon mass normalized to $M = 1$. The local electron density $\hat{n}_{i\sigma}$ is coupled to the displacement $\hat{X}_i$ through an on-site electron-phonon interaction λ, which we report here in terms of a dimensionless parameter $\lambda_D = \lambda^2 / \omega_0^2 \, W$.

Previous finite temperature studies of the Holstein model have typically employed DQMC [20, 128]. In this method, the inverse temperature $\beta = L_t \Delta\tau$ is discretized along an imaginary time axis with L_t intervals of length $\Delta\tau$, and the partition function is expressed as $Z = \mathrm{Tr}\, e^{-\beta \hat{H}} = \mathrm{Tr}\, e^{-\Delta\tau \hat{H}} e^{-\Delta\tau \hat{H}} \ldots e^{-\Delta\tau \hat{H}}$. Since Eq. (3.1) is quadratic in fermionic operators, these can be traced out, giving an expression for Z in terms of the product of two identical matrix determinants

$\det M(x_{i,\tau})$, which are functions of the space and time-dependent phonon displacement field only. Monte Carlo sampling using local updates to the phonon field $\{x_{i,\tau}\}$ is performed and physical quantities can be measured through the fermion Green's function $G_{ij} = \langle c_i^\dagger c_j \rangle = \left[M^{-1}\right]_{ij}$. Although there is no sign problem [21] for the Holstein model, these studies have been limited for two main reasons. First, the computational cost of DQMC scales as $N_s^3 L_t$, where N_s is the total number of lattice sites, prohibiting the study of large system sizes. Secondly, the restriction to local updates results in long autocorrelation times at small phonon frequencies. This aspect has limited simulations to phonon frequencies of $\omega_0 \gtrsim t$, which is unrealistic for most real materials, and is far from the regime where CDW order in the Holstein model is typically the strongest ($\omega_0 \ll t$).

Significant efficiency gains are possible by using a dynamical sampling procedure that updates the entire phonon field at each time-step [77, 129]. In this work, we use a recently developed collection of techniques to perform finite temperature simulations on extremely large clusters [26]. Our HMC-based approach achieves a near-linear scaling with system size [25, 129, 130], allowing us to study lattices of up to $N_s = 775$ sites at temperatures as low as $T = t/24$. Our algorithm efficiently updates the phonon field simultaneously, allowing study of a realistic phonon frequency $\omega_0/t = 0.1$.

Near-linear scaling is achieved by rewriting each matrix determinant $\det M$ as a multi-dimensional Gaussian integral involving auxiliary fields Φ_σ that will also be sampled. Here, the partition function becomes

$$\mathcal{Z} \approx (2\pi)^{N_s L_\tau} \int \mathcal{D}\Phi_\uparrow \mathcal{D}\Phi_\downarrow \mathcal{D}x \, e^{-S(x,\Phi_\sigma)}, \tag{4.1}$$

where the total action is

$$S(x, \Phi_\sigma) = S_{\mathrm{B}}(x) + S_{\mathrm{F}}(x, \Phi_\sigma) \tag{4.2}$$

with the fermionic (F) and bosonic (B) contributions

$$S_{\mathrm{F}}(x, \Phi_\sigma) = \frac{1}{2} \sum_\sigma \Phi_\sigma^T \left(M^T M\right)^{-1} \Phi_\sigma \tag{4.3}$$

$$S_{\mathrm{B}}(x) = \frac{\Delta\tau}{2} \sum_{i,\tau} \left[\omega_0^2 x_{i,\tau}^2 + \left(\frac{x_{i,\tau+1} - x_{i,\tau}}{\Delta\tau} \right)^2 \right]. \tag{4.4}$$

A Gibbs sampling procedure is then adopted where Φ_σ and x are alternately updated. The auxiliary field Φ_σ may be directly sampled. Using HMC, global updates to the phonon fields x can be performed by introducing a conjugate momentum p and evolving a fictitious Hamiltonian dynamics using a symplectic integrator [26].

The kagome lattice vectors $\mathbf{a}_1 = (1, 0)$ and $\mathbf{a}_2 = (\frac{1}{2}, \frac{\sqrt{3}}{2})$ are shown in Fig. 4.1(a), with corresponding reciprocal lattice vectors $\mathbf{b}_1 = (2\pi, -\frac{2\pi}{\sqrt{3}})$ and $\mathbf{b}_2 = (0, \frac{4\pi}{\sqrt{3}})$, where we have set the lattice constant $a = 1$. There are three sites per unit cell with basis vectors $\mathbf{u}_A = (0, 0)$, $\mathbf{u}_B = (\frac{1}{2}, 0)$, and $\mathbf{u}_C = (\frac{1}{4}, \frac{\sqrt{3}}{4})$, forming a network of corner sharing triangles with three sublattices, as shown in Fig. 4.1(a). Each site i may instead be indexed by unit cell and the sublattice $\{A, B, C\}$, such that e.g. $n_{\mathbf{i},\alpha}$ denotes the electron density at the site belonging to sublattice α within the unit cell at position $\mathbf{i}$. In this work, we study finite size lattices with periodic boundary conditions, with linear dimension L (up to $L = 15$), $N = L^2$ unit cells, and $N_s = 3N$ total sites. Note that discrete momentum values are given by $\mathbf{k} = \frac{m_1}{L}\mathbf{b}_1 + \frac{m_2}{L}\mathbf{b}_2$ where m_i is an integer and $0 \leq m_i < L$.

There are multiple ways to break the sublattice symmetry of the kagome lattice. It is, therefore, important to construct an order parameter that will detect charge ordering independent of the charge distribution within the unit cell. For example, at a filling fraction of 1/3, electrons may localize by doubly occupying only one site per unit cell, breaking a Z_3 symmetry. We therefore define an order parameter ρ_{cdw} that with perfect CDW order takes on one of three values $e^{i2\pi\left(\frac{s}{3}\right)}$, where $s = \{0, 1, 2\}$ corresponds to which way this symmetry is broken. The order parameter ρ_{cdw} should also be zero in the completely disordered state, where for any unit cell $\mathbf{i}$ we have $\langle \hat{n}_{\mathbf{i},A} \rangle = \langle \hat{n}_{\mathbf{i},B} \rangle = \langle \hat{n}_{\mathbf{i},C} \rangle$. Hence we define

$$\rho_{\text{cdw}} = \frac{n_c}{2N} \sum_{\mathbf{i}} e^{-i(\mathbf{q}\cdot\mathbf{i})} \left(\langle \hat{n}_{\mathbf{i},A} \rangle + e^{i\frac{2\pi}{3}} \langle \hat{n}_{\mathbf{i},B} \rangle + e^{i\frac{4\pi}{3}} \langle \hat{n}_{\mathbf{i},C} \rangle \right) \tag{4.5}$$

where $\mathbf{i}$ is a unit cell index, N is the total number of unit cells, $\mathbf{q}$ is the ordering wavevector, and n_c is a normalization constant included to fix $|\rho_{\text{cdw}}| = 1$ in the case of perfect CDW order. A structure factor that scales with system size can then be defined as $S_{\text{cdw}}(\mathbf{q}) \propto N\langle|\hat{\rho}_{\text{cdw}}|^2\rangle$, where again a proportionality constant can be included to fix $S_{\text{cdw}}(\mathbf{q}) = N$ for the case of perfect CDW order.

For any pair of sites in the kagome lattice, we denote their density-density correlation in position space by

$$c_{\alpha,\nu}(\mathbf{r}) = \frac{1}{N}\sum_{\mathbf{i}}\langle \hat{n}_{\mathbf{i}+\mathbf{r},\alpha}\hat{n}_{\mathbf{i},\nu}\rangle, \tag{4.6}$$

where α and ν label the sublattice $\{A, B, C\}$ of the two sites, and $\mathbf{r}$ is the displacement vector between their unit cells. The Fourier transform of $c_{\alpha,\nu}(\mathbf{r})$ gives a generic charge structure factor

$$S_{\alpha,\nu}(\mathbf{q}) = \sum_{\mathbf{r}} e^{i\mathbf{q}\cdot\mathbf{r}} c_{\alpha,\nu}(\mathbf{r}), \tag{4.7}$$

which provides information about the nature of an emergent CDW phase, where $\mathbf{q}$ is a discrete momentum value within the first Brillouin zone. For an ideal CDW pattern with ordering wavevector $\mathbf{q}$, $S_{\alpha,\alpha}(\mathbf{q})$ will reach a maximal value proportional to the number of sites, while for $\alpha \neq \nu$ the structure factor will vanish.

In the following section, we show evidence of CDW ordering on the kagome lattice where electrons localize on only one site per unit cell but alternates cyclically between the $\{A, B, C\}$ sublattices from one unit cell to the next. To study the onset of this phase, we set $n_c = 1$ in Eq. (4.5) and define a charge structure factor

$$\begin{aligned} S_{\mathrm{cdw}}(\mathbf{q}) &= 3N\langle|\hat{\rho}_{\mathrm{cdw}}|^2\rangle \\ &= \frac{3}{4}\sum_{\alpha}\left(S_{\alpha,\alpha}(\mathbf{q}) - \frac{1}{2}\sum_{\nu\neq\alpha} S_{\alpha,\nu}(\mathbf{q})\right). \end{aligned} \tag{4.8}$$

Additional details are given in an appendix to this chapter. Note that we employ a μ-tuning algorithm [75] to determine the chemical potential for any desired target density.

4.4. Results and Discussion

For the kagome lattice, the noninteracting tight-binding electronic structure with $t > 0$ has three separate bands, including one flat band at the highest energy ($E = 2t$). The lower bands touch at two inequivalent Dirac points in the Brillouin zone, which we denote $K = (\frac{2\pi}{3}, \frac{2\pi}{\sqrt{3}})$ and $K' = (\frac{4\pi}{3}, 0)$. The lower band is completely occupied at an average electron density per site of $\langle n\rangle = 2/3$ (i.e. an overall filling fraction of $f = 1/3$), while the upper band is fully occupied at $\langle n\rangle = 4/3$ ($f = 2/3$). There are also saddle points in the band structure at the point $M = (\pi, \frac{\pi}{\sqrt{3}})$,

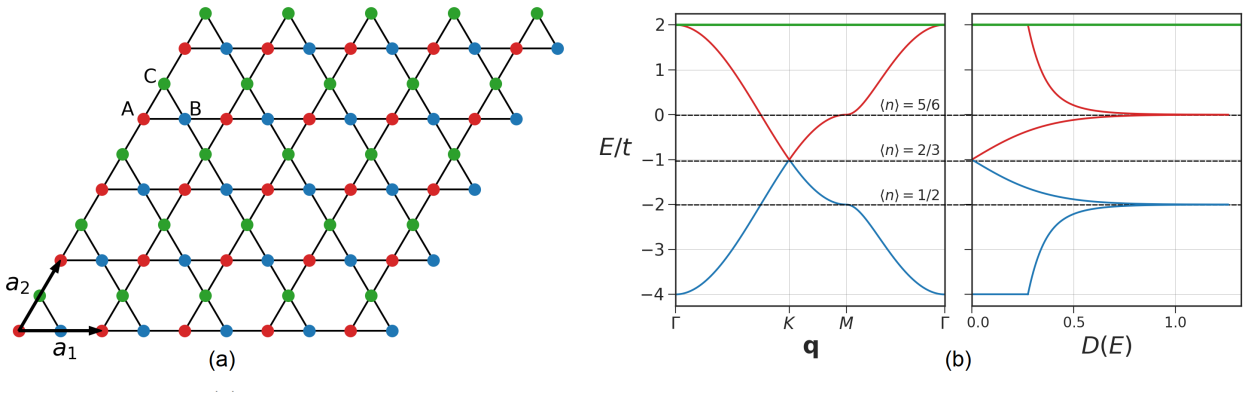

FIGURE 4.1. Kagome lattice and band structure. (a) Geometry of the kagome lattice for $L = 6$, with lattice vectors $\mathbf{a}_1 = (1, 0)$ and $\mathbf{a}_2 = (\frac{1}{2}, \frac{\sqrt{3}}{2})$. Colors denote the three triangular sublattices. (b) Left: The tight-binding electronic band structure for the kagome lattice showing the three distinct bands. Dashed lines indicate the Fermi energy at specific electron densities. Right: The non-interacting density of states $D(E)$ for the kagome lattice. A delta function at $E = 2t$ is due to the flat band.

which produce singularities in the density of states and sit at the Fermi level for average electron densities of $\langle n \rangle = 1/2$ ($f = 1/4$) and $\langle n \rangle = 5/6$ ($f = 5/12$). Fig. 4.1(b) plots the non-interacting band structure and density of states for the kagome lattice, illustrating these features.

To begin, we study the variation of local quantities as a function of electron density, at fixed ω_0 and λ_D. We set $\omega_0/t = 0.1$ to facilitate CDW ordering in the Holstein model, as bipolarons should localize more readily in the limit $\omega_0/t \to 0$ due to reduced quantum fluctuations. We also fix a moderate value of the electron-phonon coupling $\lambda_D = 0.4$. We will discuss the rationale for this choice of parameters shortly.

In Fig. 4.2(a) we show the average electron density per site $\langle n \rangle$ as a function of chemical potential μ for an $L = 12$ lattice, as the inverse temperature is varied from $\beta = 2 - 14$. We observe the formation of a plateau at $\langle n \rangle = 2/3$ as the temperature is lowered, signalling the opening of a gap. No signatures of CDW ordering is observed at fillings away from $\langle n \rangle = 2/3$ for these parameters. We also calculate the average electron kinetic energy as a function of electron density as shown in Fig. 4.2(b). We observe a sharp change at $\langle n \rangle = 2/3$, where the magnitude of the electron kinetic energy becomes maximal. This is a signature of a CDW phase transition, since a configuration of doubly occupied sites surrounded by empty nearest-neighbor sites maximizes the number of bonds

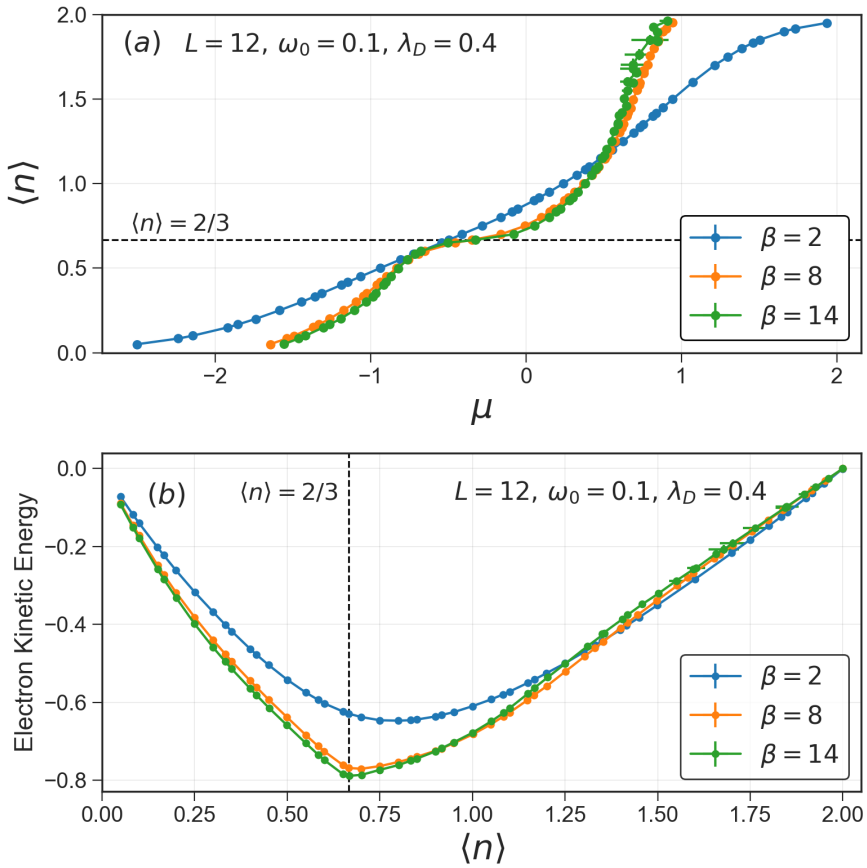

FIGURE 4.2. Electron density and kinetic energy. (a) Average electron density per site $\langle n \rangle$ as a function of the tuned chemical potential μ, for an $L = 12$ lattice with $\omega_0 = 0.1$ and $\lambda_D = 0.4$ fixed. Results are shown for $\beta = 2, 8$, and 14, with a dashed line indicating the filling $\langle n \rangle = 2/3$. (b) Electron kinetic energy as a function of the electron density $\langle n \rangle$, for the same set of parameters.

along which electron hopping is permitted (and corresponds to an average electron density per site $\langle n \rangle = 2/3$ on the kagome lattice). Note that since the kagome lattice is not bipartite, particle-hole symmetry is not present and thus both the kinetic energy and average filling are not symmetric about half-filling.

To further study the opening of a CDW gap as the temperature is lowered, we calculate the momentum integrated spectral function $A(\omega)$, which is related to the imaginary time dependent Green's function through the integral equation

$$G(\mathbf{k}, \tau) = \langle \hat{c}(\mathbf{k}, \tau) \hat{c}^\dagger(\mathbf{k}, \tau) \rangle = \int d\omega A(\mathbf{k}, \omega) \frac{e^{-\omega\tau}}{1 + e^{-\beta\omega}}, \tag{4.9}$$

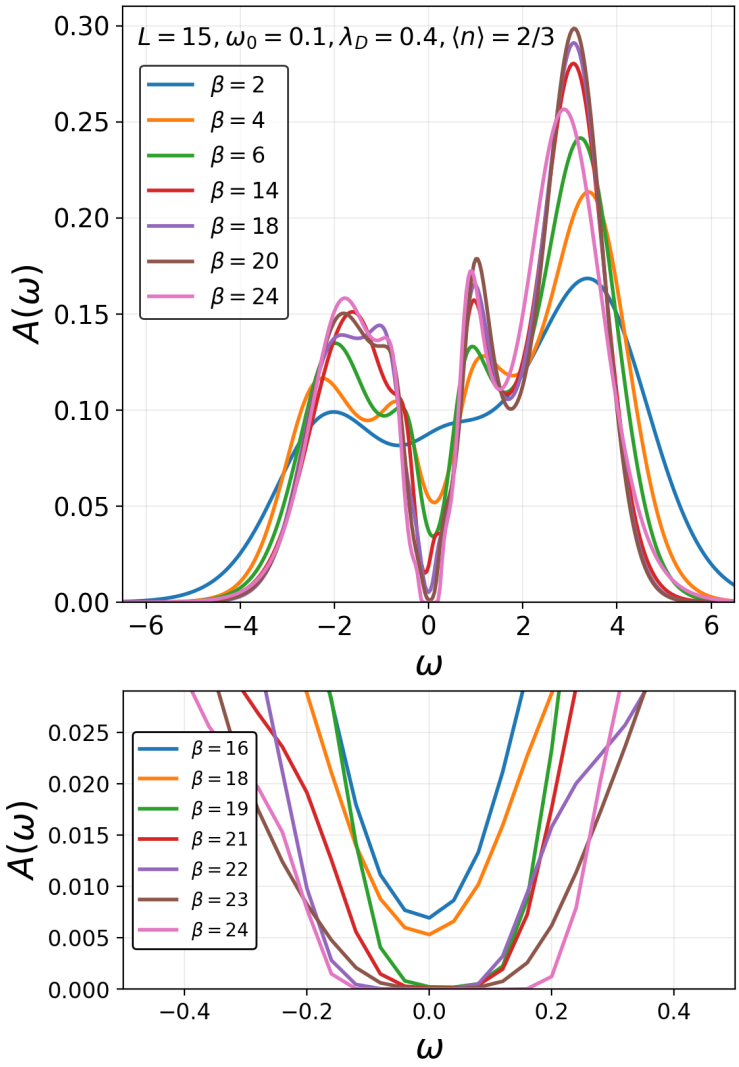

FIGURE 4.3. Spectral function. Top: Momentum integrated spectral function $A(\omega)$ shown for a range of inverse temperatures from $\beta = 2$ to $\beta = 24$, at filling fraction $\langle n \rangle = 2/3$ (with $\omega_0 = 0.1, \lambda_D = 0.4$). The linear lattice dimension is $L = 15$ i.e. $N_s = 775$. Bottom: A close-up view of the finite gap opening for $\beta \gtrsim 18$ where $A(\omega) = 0$.

which we invert using the maximum entropy method to obtain $A(\omega)$ [131]. In Fig. 4.3, we show the momentum integrated spectral function for an $L = 15$ lattice ($N_s = 775$) for a range of temperatures down to $\beta = 24$, again fixing $\omega_0 = 0.1$, $\lambda_D = 0.4$, and an average electron density per site of $\langle n \rangle = 2/3$. We observe three peaks in the spectral function corresponding to the three-band structure. As the temperature is lowered, $A(\omega)$ reaches zero and a finite gap begins to open at $\beta \gtrsim 18$, as shown in the bottom panel, indicating a transition to an insulating CDW phase.

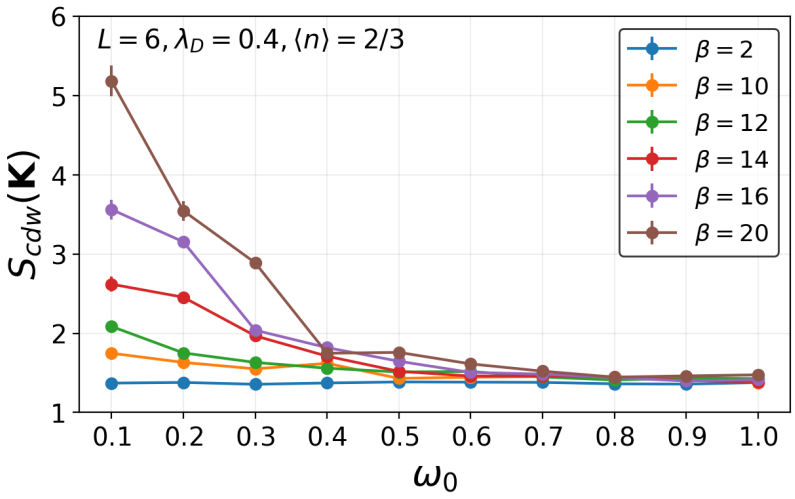

FIGURE 4.4. Charge structure factor vs. phonon frequency. Charge structure factor $S_{\text{cdw}}(\mathbf{K})$ as a function of phonon frequency, for a range of temperatures from $\beta = 2$ to $\beta = 20$. Results are shown for an $L = 6$ lattice at $\langle n \rangle = 2/3, \lambda_D = 0.4$.

At an average electron density per site of $\langle n \rangle = 2/3$, the lower energy band is completely filled and touches the upper band at the Dirac points K and K'. To study the onset of CDW order at this filling, we therefore calculate the charge structure factor S_{cdw} [Eq. (4.8)] evaluated at $\mathbf{q} = \mathbf{K}$, as a function of phonon frequency, electron-phonon coupling, and temperature.

In Fig. 4.4 we show the variation of $S_{\text{cdw}}(\mathbf{K})$ as the phonon frequency ω_0 is increased from 0.1 to 1.0. In the antiadiabatic limit ($\omega_0 \to \infty$), deformation of the lattice is weakened as sites respond more quickly to electron hopping and bipolarons do not readily localize, inhibiting the formation of a stable CDW pattern [86]. In addition, quantum fluctuations are enhanced at large ω_0, further suppressing CDW order [54]. For $\omega_0 \gtrsim 0.4$ we observe no significant growth in $S_{\text{cdw}}(\mathbf{K})$ as the temperature is lowered from $\beta = 2$ to $\beta = 20$. However, for $\omega_0 \lesssim 0.3$, the structure factor begins to increase in magnitude as the temperature is reduced, growing more rapidly with β as $\omega_0 \to 0$. We therefore fix $\omega_0 = 0.1$, and vary the dimensionless electron-phonon coupling λ_D, in order to determine the region in which CDW order at $\langle n \rangle = 2/3$ is most enhanced and subsequently estimate T_c for these parameters.

At small values of λ_D, we find no enhancement in $S_{\text{cdw}}(\mathbf{K})$ from $\beta = 2$ to $\beta = 20$ i.e. for $\lambda_D \lesssim 0.3$ there is no sign of CDW order in this temperature range, as shown in Fig. 4.5. This may be due to the critical temperature becoming exponentially suppressed as $\lambda_D \to 0$. However,

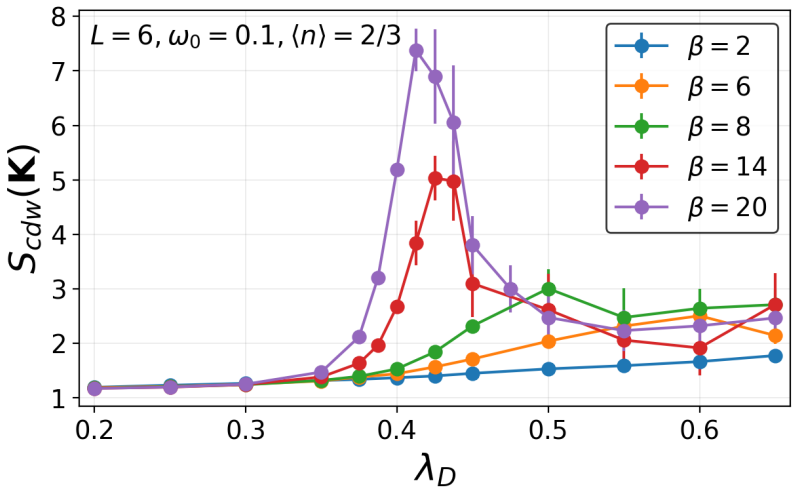

FIGURE 4.5. Charge structure factor vs. λ_D. Charge structure factor $S_{\mathrm{cdw}}(\mathbf{K})$ as a function of the dimensionless electron-phonon coupling λ_D, for a range of temperatures from $\beta = 2$ to $\beta = 20$. Results are shown for an $L = 6$ lattice at $\langle n \rangle = 2/3, \omega_0 = 0.1$.

another possibility is a finite λ_D is necessary for CDW formation, as is the case in the honeycomb lattice Holstein model at half-filling [50], which similarly has Dirac cones and a vanishing density of states at the Fermi surface. As λ_D increases, the effective electron-electron attraction is enhanced, and we observe an increase in the charge structure factor as pairs of electrons arrange themselves into a periodic CDW. As the temperature is reduced, we find that there is a maximum in $S_{\mathrm{cdw}}(\mathbf{K})$ at approximately $\lambda_D \approx 0.4$. At larger λ_D, the CDW structure factor is smaller, and eventually no significant growth is observed as the temperature is lowered from $\beta = 2$ to $\beta = 20$. This behavior might originate from the higher effective bipolaron mass at large λ_D, which will hinder their arrangement into an ordered CDW phase, as the energy barrier associated with moving from site to site is proportional to λ_D, thus promoting self-trapping. Consequently, T_c rapidly decreases as λ_D becomes much larger than its optimal value. We note that similar behavior has been observed in the honeycomb, square, and Lieb lattice Holstein models [50, 87].

The momentum dependence of $S_{\mathrm{cdw}}(\mathbf{q})$ is shown in Fig. 4.6, where the charge structure factor at $\langle n \rangle = 2/3$ is evaluated over the first Brillouin zone for an $L = 12$ lattice. An enhancement in the structure factor is observed at the Dirac points as the temperature is lowered, corresponding to the onset of an ordered CDW phase, with the magnitude of S_{cdw} increasing rapidly around $\beta \gtrsim 17$. For

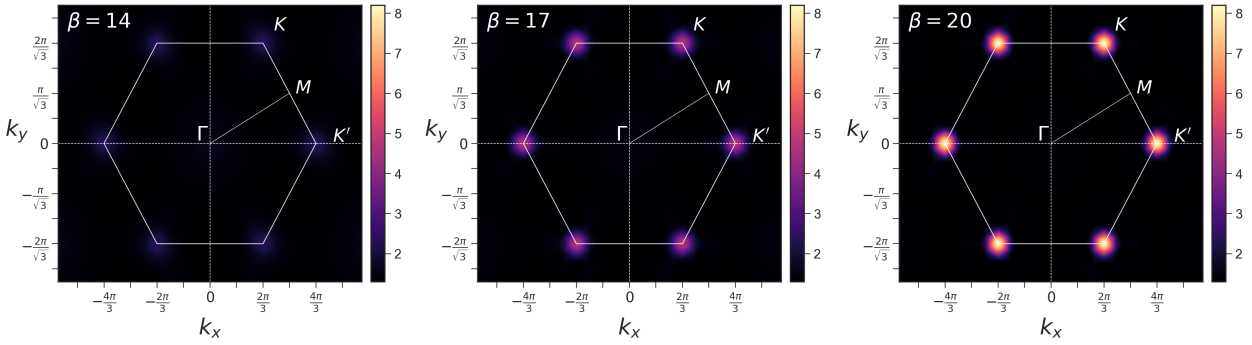

FIGURE 4.6. Charge structure factor in momentum space. Charge structure factor $S_{\mathrm{cdw}}(\mathbf{q})$ shown across the Brillouin zone of the kagome lattice with $L = 12$, shown for $\beta = 14, 17$ and 20. The locations of high-symmetry points in momentum space at $K = (2\pi/3, 2\pi/\sqrt{3})$, $K' = (4\pi/3, 0)$, $M = (\pi, \pi/\sqrt{3})$, and $\Gamma = (0, 0)$ are indicated.

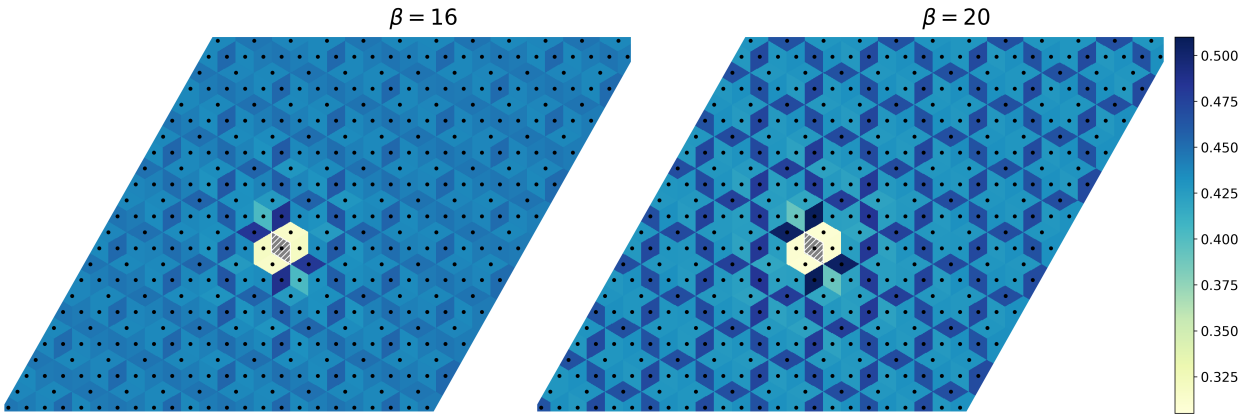

FIGURE 4.7. Real space density-density correlations. Real space density-density correlations $\langle \hat{n}(\mathbf{0})\hat{n}(\mathbf{r})\rangle$, where $\hat{n}(\mathbf{0})$ denotes the electron density at a reference site located at the origin (gray region). For each site at position $\mathbf{r}$, the color of its Voronoi cell indicates the magnitude of $\langle \hat{n}(\mathbf{0})\hat{n}(\mathbf{r})\rangle$. Results are shown for an $L = 12$ lattice with periodic boundary conditions, for $\beta = 16$ (left) and $\beta = 20$ (right) at filling $\langle n\rangle = 2/3$ (with $\lambda_D = 0.4$ and $\omega = 0.1$).

all other momentum values, including at the M and Γ-points, we find no enhancement in charge correlations with inverse temperature β, at this filling.

A real-space depiction of the CDW correlations at $\langle n\rangle = 2/3$ is shown in Fig. 4.7, which plots density-density correlations $\langle \hat{n}(\mathbf{r})\hat{n}(\mathbf{0})\rangle$ over an $L = 12$ lattice with periodic boundary conditions. Here $\mathbf{r} = 0$ is the position of a fixed reference site belonging to the A sublattice. Hence Fig. 4.7 depicts $c_{\alpha,\nu}(\mathbf{r})$ with the origin fixed at this reference site. The CDW pattern is characterized by the localization of electron pairs on only one site per unit cell, which belongs to either the A, B,

or C sublattice, alternating cyclically between these from one unit cell to the next (in both the $\mathbf{a}_1$ and $\mathbf{a}_2$ directions). The fact that $\mathbf{K}$ and $\mathbf{K}'$ are the ordering wavevectors for this pattern can be understood as follows. In terms of the reciprocal lattice vectors, we have $\mathbf{K} = \frac{1}{3}(\mathbf{b}_1 - \mathbf{b}_2)$ and $\mathbf{K}' = \frac{1}{3}(2\mathbf{b}_1 + \mathbf{b}_2)$. If the doubly-occupied sites are separated by a displacement $\mathbf{r} = n_1\mathbf{a}_1 + n_2\mathbf{a}_2$, then the Fourier transform of the density-density correlation function will have peaks at $\mathbf{K}$ or $\mathbf{K}'$ if $\mathbf{K} \cdot \mathbf{r} = 2m\pi$ or $\mathbf{K}' \cdot \mathbf{r} = 2m\pi$, where $m \in \mathbb{Z}$. This is satisfied if $(n_1 - n_2) \mod 3 = 0$ (for $\mathbf{K}$) or $(2n_1 + n_2) \mod 3 = 0$ (for $\mathbf{K}'$), which are equivalent conditions. In other words, moving along either the $\mathbf{a}_1$ or $\mathbf{a}_2$ directions, density-density correlations will repeat with a periodicity of three unit cells, i.e. for each unit cell, the site on which the electron pairs localize will alternate cyclically between the $\{A, B, C\}$ sublattices. For any given unit cell, the onset of this type of CDW order therefore breaks a Z_3 symmetry, and the phase transition should belong to the 3-state Potts model universality class.

In Fig. 4.8 we show the variation of the charge structure factor $S_{\text{cdw}}(\mathbf{K})$ with inverse temperature β, for lattices with linear dimension $L = 6, 9, 12$ and 15, for a range of temperatures down to $\beta = 24$. At high temperatures, $S_{\text{cdw}}(\mathbf{K})$ is relatively small and independent of lattice size. However, as the temperature is reduced, $S_{\text{cdw}}(\mathbf{K})$ grows and becomes dependent on the lattice size for $\beta \gtrsim 18$. This signals that correlations are becoming long-ranged and thus sensitive to system size on a finite lattice, and suggests a critical temperature of $\beta_c \approx 18$. A more accurate determination of T_c can be made by studying the correlation ratio

$$R_c = 1 - \frac{S_{\text{cdw}}(\mathbf{q} + d\mathbf{q})}{S_{\text{cdw}}(\mathbf{q})}, \tag{4.10}$$

where the ordering wavevector $\mathbf{q} = \mathbf{K}$ here, and $|d\mathbf{q}|$ is the spacing between discrete momentum values for a lattice of linear dimension L. For the kagome lattice we average over the six nearest neighbors of the K-point in momentum space to obtain $S(\mathbf{K} + d\mathbf{q})$. The correlation ratio R_c is defined such that in the CDW phase, $R_c \to 1$ as $L \to \infty$, (since $S_{\text{cdw}}(\mathbf{q})$ will diverge with L if there is long-range order), while $R_c \to 0$ if there is no long-range order. When plotted for different lattice sizes, the crossing of R_c curves gives an estimate of the critical point. In Fig. 4.9 we plot R_c for lattices with $L = 6, 9, 12$, and 15, for the same parameters as in Fig. 4.8 ($\langle n \rangle = 2/3, \omega_0 = 0.1, \lambda_D = 0.4$). There is a crossing at $\beta_c \approx 18$, which is consistent with our

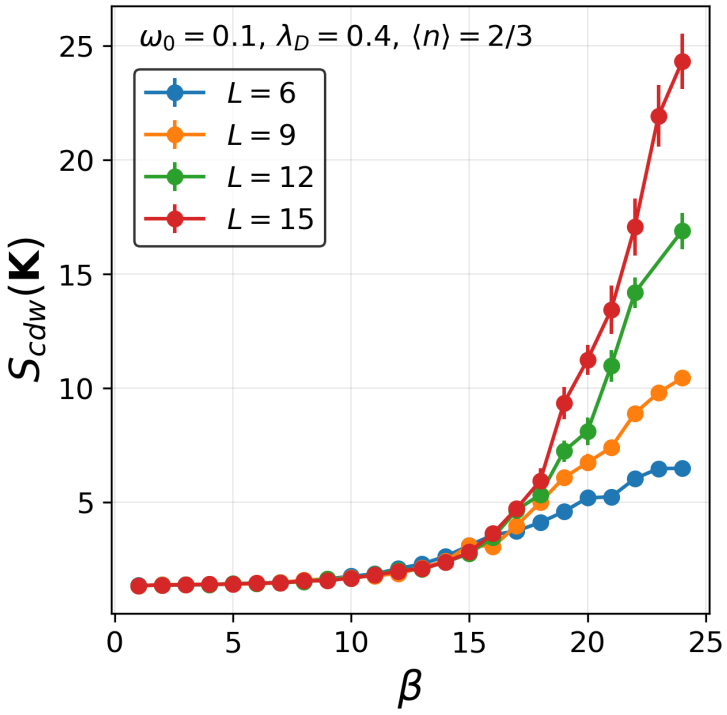

FIGURE 4.8. Charge structure factor vs. inverse temperature. Charge structure factor $S_{\mathrm{cdw}}(\mathbf{K})$ as a function of inverse temperature β, for lattice sizes $L = 6, 9, 12$ and 15, at filling $\langle n \rangle = 2/3$. A lattice size dependence in the order parameter emerges at $\beta \gtrsim 18$, indicating the onset of CDW order. Here we fix $\lambda_D = 0.4$ and $\omega_0 = 0.1$.

previous estimates of β_c obtained from observing the opening of a finite gap in $A(\omega)$, the onset of long-ranged density-density correlations, and the temperature at which S_{cdw} becomes dependent on lattice size.

Thus far we have studied the emergence of CDW order on the kagome lattice at a fixed electron density of $\langle n \rangle = 2/3$ per site. This choice was motivated by the observation of a CDW gap at $\langle n \rangle = 2/3$ and a sharp change in electron kinetic energy during sweeps of μ and $\langle n \rangle$, and the fact that this filling corresponds to a completely filled lower band, which meets the middle band at the Dirac points K and K'. However, we also considered fillings of $\langle n \rangle = 1/2$ and $\langle n \rangle = 5/6$, i.e. densities at which the saddle points in the non-interacting band structure (at the M-points) and their van Hove singularities are at the Fermi energy. We also consider $\langle n \rangle = 4/3$, which corresponds to completely filled lower and middle bands, with a quadratic touching at the Γ-point

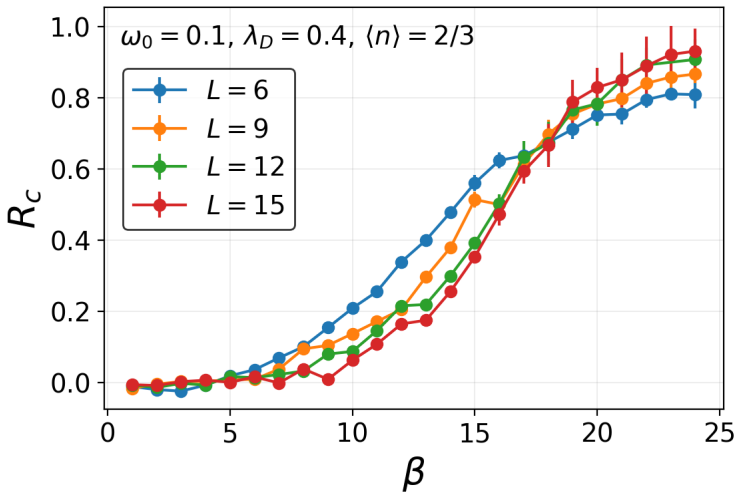

FIGURE 4.9. Correlation ratio crossing. Correlation ratio R_c as a function of β, showing a crossing at $\beta_c \approx 18$. Data is shown for lattice sizes $L = 6, 9, 12$ and 15, for the same parameters as in Fig. 4.8.

between the flat and middle bands (see Fig. 4.1). In all of these cases, we find no evidence for the formation of a CDW. For example, there are no anomalous features in components of the total energy, or any indications of a plateau in the $\langle n \rangle$ vs. μ plots near these fillings, as shown in Fig. 4.2. Moreover, as the temperature is lowered (β increases) the charge structure factor $S_{\text{cdw}}(\mathbf{q})$ does not grow significantly and remains relatively small in magnitude, as shown in Fig. 4.10 for several high-symmetry points $\mathbf{q}$ in the Brillouin zone [$\mathbf{\Gamma} = (0, 0)$, $\mathbf{K} = (\frac{2\pi}{3}, \frac{2\pi}{\sqrt{3}})$, and $\mathbf{M} = (\pi, \frac{\pi}{\sqrt{3}})$]. We fix $\omega_0 = 0.1$ here to avoid suppression of any potential CDW order, which occurs in the antiadiabatic limit. These results thus suggest an absence of any charge ordering at these fillings, at least for inverse temperatures $\beta < 20$. In other words, our results show no evidence for other varieties of CDW order in the kagome lattice Holstein model other than at the K-points at $\langle n \rangle = 2/3$.

4.5. Conclusions

We performed hybrid Monte Carlo simulations of the Holstein model on the kagome lattice on systems of up to $N_s = 775$ sites, and studied the onset of CDW order while varying the electron filling, phonon frequency, electron-phonon coupling, and temperature. Our HMC algorithm allows us to simulate larger system sizes and access lower, more realistic phonon frequencies than in previous DMQC studies of the Holstein model. We observe evidence of CDW order at an average

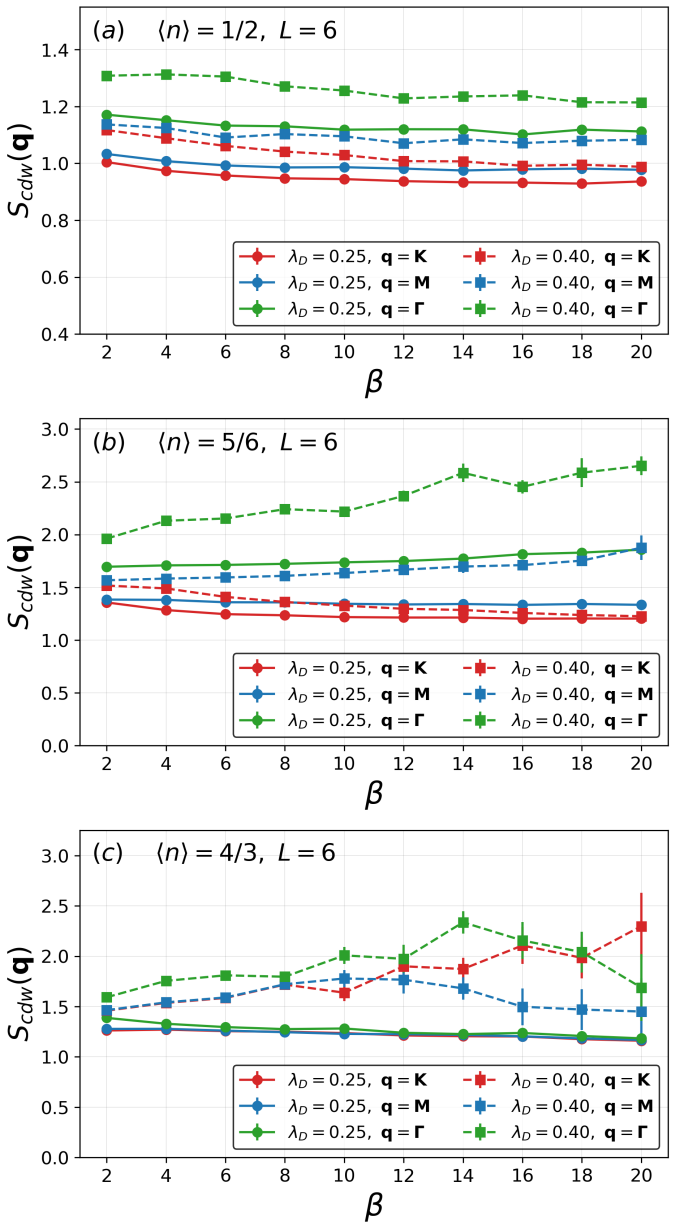

FIGURE 4.10. $S_{\mathrm{cdw}}(q)$ at $\langle n\rangle = 1/2$, 5/6, and 4/3. Charge structure factor $S_{\mathrm{cdw}}(\mathbf{q})$ as a function of inverse temperature β at several fixed electron densities: (a) $\langle n\rangle = 1/2$, (b) $\langle n\rangle = 5/6$, and (c) $\langle n\rangle = 4/3$, for an $L = 6$ lattice. Data is shown for $\lambda_D = 0.25$ (solid line) and $\lambda_D = 0.40$ (dashed line) for several momenta $\mathbf{q}$: $\mathbf{\Gamma} = (0,0)$, $\mathbf{K} = (\frac{2\pi}{3}, \frac{2\pi}{\sqrt{3}})$, and $\mathbf{M} = (\pi, \frac{\pi}{\sqrt{3}})$. The phonon frequency is fixed at $\omega_0 = 0.1$.

electron density of $\langle n\rangle = 2/3$ per site (i.e. an overall filling fraction of $f = 1/3$), signaled by the opening of a gap in $A(\omega)$ at the Fermi surface, long-ranged density-density correlations, and the

extensive scaling of the charge structure factor $S_{\mathrm{cdw}}(\mathbf{K})$ below the critical temperature. From our analysis of the correlation ration R_c, we estimate a CDW transition at $T_c \approx t/18 = W/108$, where W is the non-interacting electronic bandwidth.

This value of T_c is notably lower than the CDW transition temperatures found in the Holstein model on alternative geometries, e.g. at $\lambda_D = 0.4$, $T_c \approx t/6$ on the honeycomb and Lieb lattices, while $T_c \approx t/4$ on the square lattice [50, 87]. Moreover, the CDW order appears only for a narrow range of electron-phonon coupling strengths in the kagome lattice, peaked at $\lambda_D \approx 0.4$ (for $\omega_0/t = 0.1$). In contrast, previous Holstein model studies on square, honeycomb, and Lieb lattices have found CDW transitions across a broad range $\lambda_D \in [0.25, 1]$ [50, 86, 87]. On bipartite geometries with equal numbers of A and B sites, such as the square and honeycomb lattices, CDW formation in the Holstein model occurs at half-filling i.e. $\langle n \rangle = 1$. However, on the Lieb lattice, for which $N_A \neq N_B$, when CDW order forms the density shifts away from half-filled to either $\langle n \rangle = 2/3$ or $\langle n \rangle = 4/3$, corresponding to completely filled lower and flat bands, respectively [87]. Although the kagome lattice similarly exhibits a three-band structure, the geometry is frustrated, unlike the Lieb case, and we find that charge order emerges only at $\langle n \rangle = 2/3$ for temperatures $T \geq t/20$ with an ordering wavevector at the K-points and a $\sqrt{3} \times \sqrt{3}$ supercell. Our simulations did not reveal CDW order at other ordering momenta or electron densities, including at the van Hove filling.

The CDW order we find is analogous to the $\sqrt{3} \times \sqrt{3}$ long-range magnetic order observed in the kagome lattice Heisenberg antiferromagnet, when it is coupled to local site-phonon modes [92]. The same CDW phase has also been proposed as the ground state in certain regimes of the extended Hubbard model [100, 101], i.e. at fillings of $\langle n \rangle = 2/3$ and $\langle n \rangle = 5/6$ for large V/U, where U is the on-site Hubbard term and V is the nearest-neighbor repulsion, and has been termed CDW-III in these studies.

It should be noted that the CDW order we observe does not correspond to the star-of-David or inverse star-of-David patterns observed recently in kagome metals such as AV_3Sb_5 (A = K, Rb, Cs), which exhibit ordering at the M-points. A recent work [101] showed that such a CDW ordering is observed in the kagome lattice Hubbard model when a Su-Schrieffer-Heeger electron-phonon coupling is introduced. Here the electron-phonon coupling modulates the electron hopping

term, and is conceptually distinct from Holstein model, in which electrons and phonons interact on a single site, rather than on the bonds of the lattice.

4.6. Appendix: Derivation of CDW order parameter

For bipartite geometries such as the square lattice, checkerboard CDW order can occur in the Holstein model at half-filling. In these cases, electron pairs localize on one of the two sublattices (A or B), breaking a Z_2 symmetry, with ordering wavevector $\mathbf{q} = (\pi, \pi)$. A charge structure factor that scales with system size can be defined as $S_{\text{cdw}} = \sum_{\mathbf{r}} e^{-i(\pi,\pi)\cdot\mathbf{r}} c(\mathbf{r})$, where the sum is over all unit cells, and $c(\mathbf{r}) = \frac{1}{N}\sum_{\mathbf{i}} \langle \hat{n}_{\mathbf{i}+\mathbf{r}} \hat{n}_{\mathbf{i}} \rangle$ is the real space density-density correlation function. However, one can also express S_{cdw} in terms of an order parameter ρ_{cdw} i.e. $S_{\text{cdw}} = N\langle |\rho_{\text{cdw}}|^2 \rangle$, such that with perfect CDW order $\rho_{\text{cdw}} = \pm 1$ depending on which sublattice the electrons localize on, and $\rho_{\text{cdw}} = 0$ in the disordered phase. To detect checkerboard order on the square lattice no matter how the Z_2 symmetry is broken, we should consider the *difference* between $\langle \hat{n}_A \rangle$ and $\langle \hat{n}_B \rangle$, i.e. define

$$\begin{aligned}
\rho_{\text{cdw}} = \langle \hat{\rho}_{\text{cdw}} \rangle &= \frac{1}{2} \left(\langle \hat{n}_A \rangle - \langle \hat{n}_B \rangle \right) \\
&= \frac{1}{2} \left(\frac{2}{N} \sum_{\mathbf{i} \in A} \langle \hat{n}_{\mathbf{i}} \rangle - \frac{2}{N} \sum_{\mathbf{i} \in B} \langle \hat{n}_{\mathbf{i}} \rangle \right) \\
&= \frac{1}{N} \left(\sum_{\mathbf{i} \in A} \langle \hat{n}_{\mathbf{i}} \rangle - \sum_{\mathbf{i} \in B} \langle \hat{n}_{\mathbf{i}} \rangle \right) \\
&= \frac{1}{N} \sum_{\mathbf{i}} (-1)^{i_x + i_y} \langle \hat{n}_i \rangle \\
&= \frac{1}{N} \sum_{\mathbf{i}} e^{i(\pi,\pi)\cdot\mathbf{i}} \langle \hat{n}_{\mathbf{i}} \rangle,
\end{aligned} \tag{4.11}$$

where $\mathbf{i} = i_x \hat{\mathbf{x}} + i_y \hat{\mathbf{y}}$ are the locations of sites in a square lattice, with the lattice constant normalized to $a = 1$. Taking the squared magnitude of ρ_{cdw}, a structure factor that scales with system size

can then be expressed as

$$\begin{aligned} S_{\text{cdw}} &= N\langle|\hat{\rho}_{\text{cdw}}|^2\rangle = N\langle\hat{\rho}^\dagger_{\text{cdw}}\hat{\rho}_{\text{cdw}}\rangle \\ &= N\left\langle\left(\frac{1}{N}\sum_{\mathbf{j}} e^{-i(\pi,\pi)\cdot\mathbf{j}}\hat{n}_{\mathbf{j}}\right)\left(\frac{1}{N}\sum_{\mathbf{i}} e^{i(\pi,\pi)\cdot\mathbf{i}}\hat{n}_{\mathbf{i}}\right)\right\rangle \\ &= \frac{1}{N}\sum_{\mathbf{i},\mathbf{r}} e^{-i(\pi,\pi)\cdot\mathbf{r}}\langle\hat{n}_{\mathbf{i}+\mathbf{r}}\hat{n}_{\mathbf{i}}\rangle \\ &= \sum_{\mathbf{r}} e^{-i(\pi,\pi)\cdot\mathbf{r}}c(\mathbf{r}), \end{aligned} \tag{4.12}$$

where $\mathbf{r} = \mathbf{j} - \mathbf{i}$, i.e. the expression in Eq. (4.12) is equivalent to the Fourier transform of the real space density-density correlation function $c(\mathbf{r})$ for the square lattice.

For the kagome lattice, since each unit cell consists of three sites, we introduced a generic density-density correlation function $c_{\alpha,\nu}(\mathbf{r})$ which has Fourier transform $S_{\alpha,\nu}(\mathbf{q})$, where each lower index denotes a sublattice A, B, or C [see Eq. (4.6) and Eq. (4.7)]. Previously we discussed a CDW pattern in which electrons localize on one site per unit cell, alternating cyclically between the A, B, and C sites, as shown in Fig. 4.7. Unlike checkerboard order on the square lattice, CDW order of this type can occur in three ways, breaking a Z_3 symmetry. As in the square lattice case, we can define an order parameter ρ_{cdw} which takes on a different value depending on how the symmetry is broken, but with $|\rho_{\text{cdw}}| = 1$ in the case of perfect order and $|\rho_{\text{cdw}}| = 0$ in the disordered phase. Since a Z_3 symmetry is broken, we should have $\rho_{\text{cdw}} = e^{i2\pi\left(\frac{s}{3}\right)}$ (where $s = \{0, 1, 2\}$) in the ordered phase, and $\rho_{\text{cdw}} = 0$ in the disordered phase. However, unlike the simpler checkerboard order, the electron densities on each sublattice $\langle\hat{n}_A\rangle$, $\langle\hat{n}_B\rangle$, and $\langle\hat{n}_C\rangle$ will vary from unit cell to unit cell, with a periodicity set by the ordering wavevector $\mathbf{q}$. We can therefore define an order parameter

$$\rho_{\text{cdw}} = \frac{1}{2N}\sum_{\mathbf{i}} e^{-i(\mathbf{q}\cdot\mathbf{i})}\left(\langle\hat{n}_{\mathbf{i},A}\rangle + e^{i\frac{2\pi}{3}}\langle\hat{n}_{\mathbf{i},B}\rangle + e^{i\frac{4\pi}{3}}\langle\hat{n}_{\mathbf{i},C}\rangle\right), \tag{4.13}$$

which satisfies these properties, where the sum is over all unit cells. As before, we can now write a structure factor that scales with system size,

$$S_{\text{cdw}}(\mathbf{q}) = 3N\langle|\hat{\rho}_{\text{cdw}}|^2\rangle = 3N\langle\hat{\rho}^\dagger_{\text{cdw}}\hat{\rho}_{\text{cdw}}\rangle, \tag{4.14}$$

where a constant factor has been inserted to ensure $S_{\rm cdw} = N$ in the case of perfect CDW order. We can now expand the above equation to obtain an expression for $S_{\rm cdw}$ in terms of the generic structure factors $S_{\alpha,\nu}$ [Eq. (4.7)], which yields

$$S_{\rm cdw}(\mathbf{q}) = 3N\Bigg\langle \frac{1}{2N}\sum_{\mathbf{j}}\Big[(\hat{n}_{\mathbf{j},A} + e^{-i\frac{2\pi}{3}}\hat{n}_{\mathbf{j},B} + e^{-i\frac{4\pi}{3}}\hat{n}_{\mathbf{j},C})e^{i\mathbf{q}\cdot\mathbf{j}}\Big] \times \frac{1}{2N}\sum_{\mathbf{i}}\Big[(\hat{n}_{\mathbf{i},A} + e^{i\frac{2\pi}{3}}\hat{n}_{\mathbf{i},B} + e^{i\frac{4\pi}{3}}\hat{n}_{\mathbf{i},C})e^{-i\mathbf{q}\cdot\mathbf{i}}\Big]\Bigg\rangle \tag{4.15}$$

$$= \frac{3}{4N}\sum_{\mathbf{j},\mathbf{i}}\Big[\Big\langle \hat{n}_{\mathbf{j},A}\hat{n}_{\mathbf{i},A} + e^{i\frac{2\pi}{3}}\hat{n}_{\mathbf{j},A}\hat{n}_{\mathbf{i},B} + e^{i\frac{4\pi}{3}}\hat{n}_{\mathbf{j},A}\hat{n}_{\mathbf{i},C} + e^{-i\frac{2\pi}{3}}\hat{n}_{\mathbf{j},B}\hat{n}_{\mathbf{i},A} + \hat{n}_{\mathbf{j},B}\hat{n}_{\mathbf{i},B} + e^{i\frac{2\pi}{3}}\hat{n}_{\mathbf{j},B}\hat{n}_{\mathbf{i},C} + e^{-i\frac{4\pi}{3}}\hat{n}_{\mathbf{j},C}\hat{n}_{\mathbf{i},A} + e^{-i\frac{2\pi}{3}}\hat{n}_{\mathbf{j},C}\hat{n}_{\mathbf{i},B} + \hat{n}_{\mathbf{j},C}\hat{n}_{\mathbf{i},C}\Big\rangle e^{i\mathbf{q}\cdot(\mathbf{j}-\mathbf{i})}\Big] \tag{4.16}$$

$$= \frac{3}{4N}\sum_{\mathbf{j},\mathbf{i}}\Big[\langle \hat{n}_{\mathbf{j},A}\hat{n}_{\mathbf{i},A} + \hat{n}_{\mathbf{j},B}\hat{n}_{\mathbf{i},B} + \hat{n}_{\mathbf{j},C}\hat{n}_{\mathbf{i},C} - \hat{n}_{\mathbf{j},A}\hat{n}_{\mathbf{i},B} - \hat{n}_{\mathbf{j},A}\hat{n}_{\mathbf{i},C} - \hat{n}_{\mathbf{j},B}\hat{n}_{\mathbf{i},C}\rangle e^{i\mathbf{q}\cdot(\mathbf{j}-\mathbf{i})}\Big] \tag{4.17}$$

$$= \frac{3}{4N}\sum_{\mathbf{j},\mathbf{i}}\Big[\Big(\langle \hat{n}_{\mathbf{j},A}\hat{n}_{\mathbf{i},A}\rangle + \langle \hat{n}_{\mathbf{j},B}\hat{n}_{\mathbf{i},B}\rangle + \langle \hat{n}_{\mathbf{j},C}\hat{n}_{\mathbf{i},C}\rangle - \frac{1}{2}\langle \hat{n}_{\mathbf{j},A}\hat{n}_{\mathbf{i},B}\rangle - \frac{1}{2}\langle \hat{n}_{\mathbf{j},B}\hat{n}_{\mathbf{i},A}\rangle - \frac{1}{2}\langle \hat{n}_{\mathbf{j},A}\hat{n}_{\mathbf{i},C}\rangle - \frac{1}{2}\langle \hat{n}_{\mathbf{j},C}\hat{n}_{\mathbf{i},A}\rangle - \frac{1}{2}\langle \hat{n}_{\mathbf{j},B}\hat{n}_{\mathbf{i},C}\rangle - \frac{1}{2}\langle \hat{n}_{\mathbf{j},C}\hat{n}_{\mathbf{i},B}\rangle\Big)e^{i\mathbf{q}\cdot(\mathbf{j}-\mathbf{i})}\Big] \tag{4.18}$$

$$= \frac{3}{4N}\sum_{\mathbf{j},\mathbf{i}}\left[\left(\sum_{\alpha}\langle \hat{n}_{\mathbf{j},\alpha}\hat{n}_{\mathbf{i},\alpha}\rangle - \frac{1}{2}\sum_{\alpha,\nu\neq\alpha}\langle \hat{n}_{\mathbf{j},\alpha}\hat{n}_{\mathbf{i},\nu}\rangle\right)e^{i\mathbf{q}\cdot(\mathbf{j}-\mathbf{i})}\right] \tag{4.19}$$

$$= \frac{3}{4}\sum_{\mathbf{r}}\left[e^{i\mathbf{q}\cdot\mathbf{r}}\left(\frac{1}{N}\sum_{\mathbf{i},\alpha}\langle \hat{n}_{\mathbf{i}+\mathbf{r},\alpha}\hat{n}_{\mathbf{i},\alpha}\rangle - \frac{1}{2N}\sum_{\mathbf{i},\alpha,\nu\neq\alpha}\langle \hat{n}_{\mathbf{i}+\mathbf{r},\alpha}\hat{n}_{\mathbf{i},\nu}\rangle\right)\right] \tag{4.20}$$

$$= \frac{3}{4}\sum_{\mathbf{r}}\left[e^{i\mathbf{q}\cdot\mathbf{r}}\left(\sum_{\alpha}c_{\alpha,\alpha}(\mathbf{r}) - \frac{1}{2}\sum_{\alpha,\nu\neq\alpha}c_{\alpha,\nu}(\mathbf{r})\right)\right] \tag{4.21}$$

$$= \frac{3}{4}\left[\sum_{\alpha}S_{\alpha,\alpha}(\mathbf{r}) - \frac{1}{2}\sum_{\alpha,\nu\neq\alpha}S_{\alpha,\nu}(\mathbf{r})\right], \tag{4.22}$$

where $c_{\alpha,\nu}(\mathbf{r})$ is the generic real space density-density correlation function defined in Eq. (4.6). This expression for $S_{\rm cdw}$ is the measure we use to detect CDW ordering in the kagome lattice, and is the quantity we show in Fig. 8 at $\langle n\rangle = 2/3$ as a function of β for different lattice sizes. For a particular CDW pattern on the kagome lattice under study, Eq. (4.22) can be multiplied by a constant factor (if necessary) to fix $S_{\rm cdw} = N$ in the case of perfect CDW order.

4.7. Appendix: The renormalized phonon energy $\Omega(\mathbf{q}, i\nu_n = 0)$

An additional signature of the CDW transition can be observed in the renormalized phonon energy $\Omega(\mathbf{q}, i\nu_n = 0)$, where a softening of the phonon dispersion is expected to occur at the ordering wavevector $\mathbf{q}_{\rm cdw}$ as the temperature is lowered. The renormalized phonon energy is given by $\Omega(\mathbf{q}, 0) = [\omega_0^2 + \Pi(\mathbf{q}, 0)]^{1/2}$, where $\Pi(\mathbf{q}, 0)$ is a function defined in terms of the momentum-space phonon Green's function $D(\mathbf{q}, \nu_n)$, through the relation

$$D(\mathbf{q}, \nu_n) = \frac{2\omega_0}{(i\nu_n)^2 - \omega_0^2 - \Pi(\mathbf{q}, \nu_n)}, \tag{4.23}$$

where $\nu_n = 2\pi n T$ (and we set $\hbar = 1$). In Fig. 4.11 we show $\Omega(\mathbf{q}, 0)/\omega_0$ along a closed triangular path Γ–K–K'–Γ within the Brillouin zone. Results are shown for an $L = 12$ lattice with electron-phonon coupling $\lambda_D = 0.4$ and bare phonon frequency $\omega_0 = 0.1$, at a filling of $\langle n \rangle = 2/3$, where we previously observed evidence of CDW ordering.

At high temperature ($\beta \ll \beta_c$) we find that the renormalized phonon dispersion is relatively flat, e.g. for $\beta = 2$, we have $\Omega(\mathbf{q}, 0)/\omega_0 \approx 0.6$ for all momenta $\mathbf{q}$. This is indicative of strong electron-phonon coupling, where the renormalized phonon frequency is uniformly suppressed relative to the bare phonon frequency even at temperatures well above T_c. This signature of strong coupling is expected behavior in the Holstein model, and has been observed in the square lattice at similarly large values of λ_D [**60**]. As the temperature is lowered, we observe a softening of the phonon dispersion at the expected ordering wavevectors K and K'. We observe sharp dips in the phonon dispersion as the temperature is reduced to $\beta \approx 18$, consistent with our estimate of β_c obtained from the crossing of R_c curves shown in Fig. 4.9. Due to an expected finite-size effect, $\Omega(\mathbf{q}, 0)$ does not reach exactly zero below T_c in our simulations [**130**].

4.8. Appendix: HMC simulation parameters

Here we provide additional details of the parameter values used in our HMC simulations, which are explained further in Ref. [**26**]. We fixed the imaginary-time discretization at $\Delta\tau = 0.05$, and performed updates to the phonon field using HMC trajectories typically of $N_t = 50$ time-steps of size $\Delta t = 0.2$. We initially thermalize our systems by performing $N_{\rm therm} = 2000$–3000 trial updates. This is followed by $N_{\rm sim} = 2500$–4000 updates, where measurements are taken at the end of each

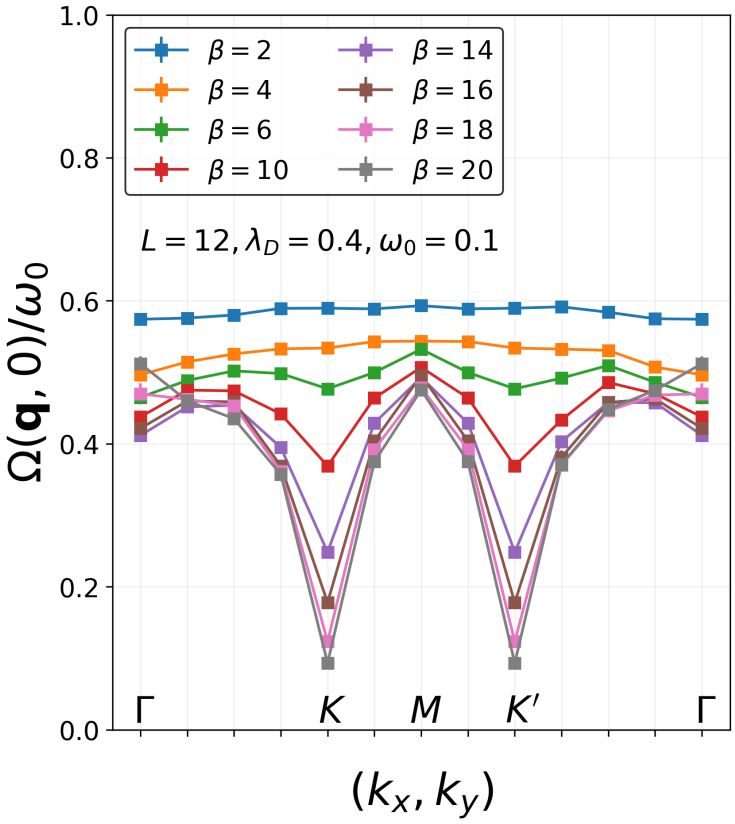

FIGURE 4.11. Renormalized phonon frequency. The renormalized phonon frequency $\Omega(\mathbf{q}, 0)/\omega_0$ at $\langle n \rangle = 2/3$ and $\lambda_D = 0.4$, shown for a range of temperatures from $\beta = 2$ to $\beta = 20$. Phonon softening at the ordering wavevectors K and K' is observed as the temperature is lowered.

trajectory. Each time-step we numerically solve for the fictitious force $\dot{p} = -\frac{\partial S}{\partial x}$ using the conjugate gradient method with a relative residual error threshold $\epsilon_{\max} = 10^{-5}$.

The forces in our HMC dynamics can be separated into fermionic and bosonic components $-\frac{\partial S_F}{\partial x}$ and $-\frac{\partial S_B}{\partial x}$ (see Eqs. 4.3 and 4.4), where the bosonic part is much less expensive to calculate. We thus employ time-step splitting where trajectories evolve with time-step $\Delta t' = \Delta t / n_t$ with $n_t = 10$ using the bosonic force alone, followed by a single step of size Δt using the fermionic force. We also use Fourier acceleration via a dynamical mass matrix with regularization parameter $m_{\text{reg}} = \omega_0$ to further reduce autocorrelation times.

CHAPTER 5

Instabilities of Spin-1 Kitaev Spin Liquid Phase in Presence of Single-Ion Anisotropies

5.1. Chapter Summary

We study the spin-one Kitaev model on the honeycomb lattice in the presence of single-ion anisotropies. We consider two types of single ion anisotropies: A D_{111} anisotropy which preserves the symmetry between X, Y, and Z bonds but violates flux conservation and a D_{100} anisotropy that breaks the symmetry between X, Y, and Z bonds but preserves flux conservation. We use series expansion methods, degenerate perturbation theory, and exact diagonalization to study these systems. Large positive D_{111} anisotropy leads to a simple product ground state with conventional magnon-like excitations, while large negative D_{111} leads to a broken symmetry and degenerate ground states. For both signs there is a phase transition at a small $|D_{111}| \approx 0.12$ separating the more conventional phases from the Kitaev spin liquid phase. With large D_{100} anisotropy, the ground state is a simple product state, but the model lacks conventional dispersive excitations due to the large number of conservation laws. Large negative D_{100} leads to decoupled one-dimensional systems and many degenerate ground states. No evidence of a phase transition is seen in our numerical studies at any finite D_{100}. Convergence of the series expansion extrapolations all the way to $D_{100} = 0$ suggests that the nontrivial Kitaev spin-liquid is a singular limit of this type of single-ion anisotropy going to zero, which also restores symmetry between the X, Y, and Z bonds.

This chapter is based on the following publication [132]:

O. Bradley and R. R. P. Singh, *Instabilities of spin-1 Kitaev spin liquid phase in presence of single-ion anisotropies*, Phys. Rev. B. **105**, L060405 (2022).

5.2. Introduction

Kitaev's spin-half honeycomb lattice model [16] provides a remarkable example of an exactly soluble emergent behavior with a quantum spin liquid ground state and Majorana fermion excitations [17, 133, 134, 135, 136, 137, 138, 139, 140, 141, 142, 143]. The search for such quantum spin liquid phases in spin-half materials remains a major focus of current research [144, 145, 146, 147, 148, 149, 150, 151]. Larger spin Kitaev models share some exotic properties of the spin-half models, namely they have conserved fluxes through each hexagon and no spin-spin correlations beyond nearest neighbors [19, 152, 153]. Yet, they are different in other key respects. As first proposed by Baskaran, Sen and Shankar [19] integer spin systems are unlikely to have Majorana fermions. The difference between integer and half integer spins is also highlighted in the work of Minakawa *et al.* [154], who found that introducing large anisotropy between X, Y, and Z bonds leads to a very different type of ground state in integer spin systems with no long-range entanglement as compared with half-integer spin systems where similar anisotropy maps on to the well known Toric code model [133]. Numerical studies have found further evidence of a gap in the excitation spectra for integer spins and for field induced spin-liquid phases [18, 152, 153, 155, 156, 157, 158, 159, 160, 161, 162, 163] as well as of large nearly degenerate subspaces giving rise to entropy plateaus [152, 153, 164, 165]. In a very recent paper, Chen *et al.* [166] have shown the existence of emergent Z_2 spin liquid phase in the spin-one system with exotic deconfined anyonic excitations which are not Majorana fermions.

In this chapter we study the spin-one Kitaev model with two different types of single-ion anisotropies. The first model is given by:

$$\mathcal{H}_1 = \mathcal{H}_K + \frac{D_{111}}{3}\sum_i (S_i^x + S_i^y + S_i^z)^2, \tag{5.1}$$

while the second model is:

$$\mathcal{H}_2 = \mathcal{H}_K + D_{100}\sum_i (S_i^z)^2, \tag{5.2}$$

where $\mathcal{H}_k$ is the pure spin-one Kitaev honeycomb model Hamiltonian given by

$$\mathcal{H}_K = K\left(\sum_{\langle i,j\rangle} S_i^x S_j^x + \sum_{(i,k)} S_i^y S_k^y + \sum_{[i,l]} S_i^z S_l^z\right). \tag{5.3}$$

Here the X, Y, and Z couplings are on nearest neighbors of the honeycomb lattice pointing along the three sets of bond directions (see Fig. 5.1).

It is evident that D_{111} preserves the symmetry between X, Y, and Z bonds whereas D_{100} does not. For each hexagon in the lattice (with sites labeled $1, \ldots, 6$ as shown in Fig. 5.1) one can define the plaquette flux operator

$$W_p = e^{i\pi(S_1^z+S_2^y+S_3^x+S_4^z+S_5^y+S_6^x)}. \tag{5.4}$$

As shown in Ref. [19], the W_p operators both commute with the Kitaev couplings and each other and have eigenvalues equal to ± 1. Hence the model, in the absence of single-ion anisotropy, has conserved Z_2 flux variables on each hexagonal plaquette of the honeycomb lattice. One can show that D_{100} term commutes with all the flux variables whereas D_{111} term does not.

For either type of anisotropy, large positive D leads to a simple product ground state that can be studied by non-degenerate perturbation theory and high order series expansions. For large negative D, one can study the system by degenerate perturbation theory. For D_{111} the phases at large positive or negative D_{111} are conventional phases. We find in our numerical studies that these phases are separated from $D_{111} = 0$ by phase transitions. However, no such transition is evident with D_{100} anisotropy. In this case even though the large $|D_{100}|$ ground states lack long-range entanglement, the phases remain exotic, either characterized by absence of conventional dispersive excitations or by a large number of ground states. Our study suggests that any long-range entangled quantum spin-liquid ground state depends crucially on the D_{100} anisotropy going to zero.

A nonzero D_{100} cannot arise in a system with full symmetry of the honeycomb lattice where X, Y, and Z bonds are equivalent but D_{111} must always be present. Our study implies that experimental realizations of a Kitaev spin-liquid phase are possible in an undistorted honeycomb structure with D_{111} single ion anisotropy, up to some moderate value of either sign. However, lattice distortions which allow D_{100} terms to arise may immediately destabilize any phase with long range entanglement.

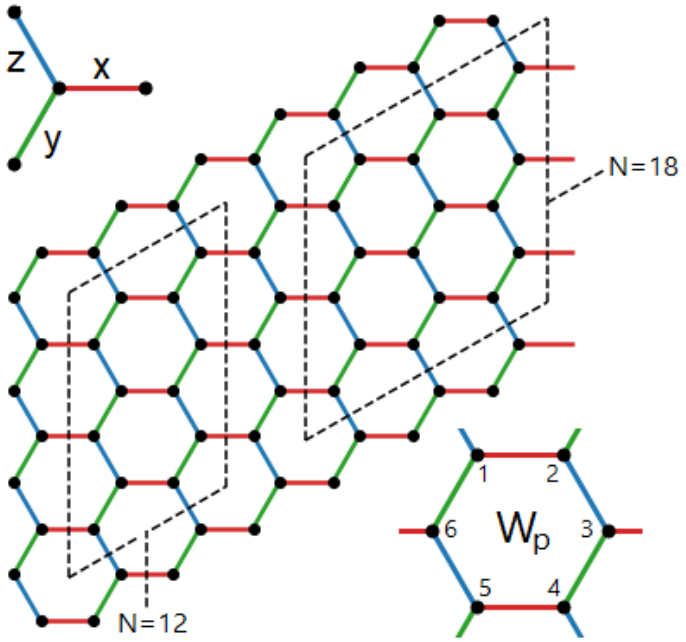

FIGURE 5.1. Geometry of the honeycomb lattice, with the x, y, and z bond directions indicated. The $N = 12$ and $N = 18$ site clusters studied using exact diagonalization are shown within dashed lines (with periodic boundary conditions). For each hexagonal plaquette (with sites labeled $1, \ldots, 6$ as shown), one can define the flux operator W_p given by Eq. (5.4).

5.3. Model and Perturbation Theories

It is convenient to work in the $|x\rangle$, $|y\rangle$, $|z\rangle$ basis introduced by Koga *et al.* [152], which can be expressed in terms of the S^z basis as follows:

$$|x\rangle = -\frac{1}{\sqrt{2}}\left(|m_s = 1\rangle - |m_s = -1\rangle\right) \tag{5.5}$$

$$|y\rangle = \frac{i}{\sqrt{2}}\left(|m_s = 1\rangle + |m_s = -1\rangle\right) \tag{5.6}$$

$$|z\rangle = |m_s = 0\rangle\,. \tag{5.7}$$

In this basis the spin operators are given by

$$S^\alpha\,|\beta\rangle = i\epsilon_{\alpha\beta\gamma}\,|\gamma\rangle\,. \tag{5.8}$$

The ground state at large positive D_{111} is given by

$$|\psi_g\rangle = \prod_i |0_i\rangle\,, \tag{5.9}$$

where the state $|0\rangle$ at a site is given by

$$|0\rangle = \frac{1}{\sqrt{3}}(|x\rangle + |y\rangle + |z\rangle), \tag{5.10}$$

i.e. the eigenvector of the 3×3 matrix $(S^x + S^y + S^z)^2$ with an eigenvalue of zero. To study this anisotropy we construct two states orthogonal to $|0\rangle$. In particular, we choose the states

$$|1\rangle = \frac{1}{\sqrt{2}}(|x\rangle - |y\rangle), \tag{5.11}$$

and,

$$|2\rangle = \frac{1}{\sqrt{6}}(|x\rangle + |y\rangle - 2\,|z\rangle). \tag{5.12}$$

The single-ion anisotropies are diagonal in this basis as are the flux variables.

For large positive D_{111}, ground state properties can be obtained by nondegenerate perturbation theory which can be calculated by the linked-cluster method [**167**, **168**, **169**]. The linked-cluster method states that a ground state property per site, P, can be expanded as a sum over all linked clusters c as

$$P = \sum_c L(c) \times W_P(c), \tag{5.13}$$

where $L(c)$, called the lattice constant, is the number of ways the linked-cluster c can be embedded in the lattice per lattice site. The quantity $W_P(c)$, called the weight of the cluster associated with the property P, is defined entirely by the property on the cluster and on its sub-clusters s that can be embedded in c. It is defined as

$$W_P(c) = N_c P(c) - \sum_{s \subset c} W_P(s), \tag{5.14}$$

where $P(c)$ is the property calculated for the finite cluster and N_c is number of sites in the cluster. One can show that the weight of a cluster with N_b bonds only contributes in order N_b or higher. Thus including all clusters with up to N bonds in Eq. 5.13 guarantees that one has the correct expansion in the thermodynamic limit to order N.

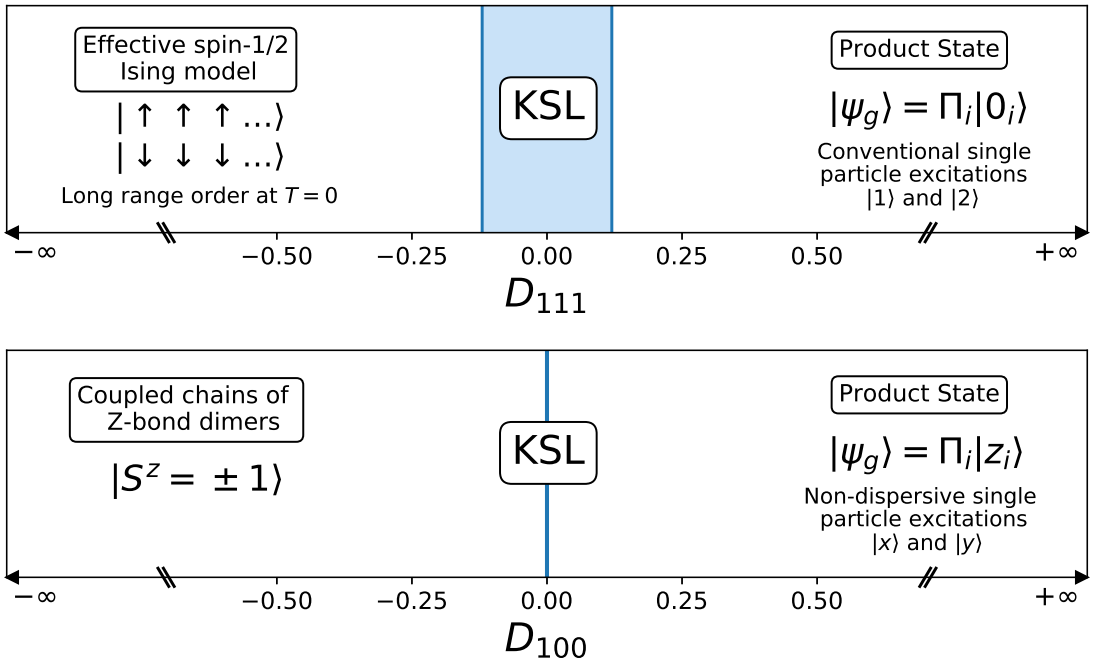

FIGURE 5.2. Phase diagram of the spin-one Kitaev model in the presence of D_{111} (top panel) and D_{100} (bottom panel) single-ion anisotropy. The ground states observed in the limits of both large positive and large negative anisotropy, and the intermediate Kitaev spin liquid (KSL) region are indicated.

For the expansion around the large positive D_{111} we work in the basis of direct product of states $|0\rangle$, $|1\rangle$ and $|2\rangle$. In this basis the D_{111} term is diagonal. It is useful to predetermine the 9×9 perturbation matrix for the Kitaev couplings in the product basis of two sites. Once the matrix elements of the unperturbed Hamiltonian and the perturbation are known, perturbation theory for a finite system is reduced to simple recursion relations [**167**, **168**, **169**], which can be carried out through automated computer programs.

We obtain the ground state energy as

$$E_g/D_{111} = \sum_n a_n (K/D_{111})^n. \tag{5.15}$$

The occupation probability of the single-spin excited states $|1\rangle$ or $|2\rangle$ at a site in the ground state is given by

$$n_{12} = \sum_n b_n (K/D_{111})^n. \tag{5.16}$$

The coefficients a_n and b_n up to $n = 10$ are available at [170]. Numerical results will be presented in the next section when we compare with exact diagonalization.

For $K = 0$ there are $2N$ single particle excitations corresponding to state $|1\rangle$ or $|2\rangle$ on a site. It is straightforward to construct the leading order in K tight-binding hopping model for these excitations. The system clearly has conventional single-particle excitations.

For large negative D_{111} the states $|1\rangle$ and $|2\rangle$ provide degenerate on-site ground states. In this 2^N dimensional Hilbert space one can obtain the effective Hamiltonian by degenerate perturbation theory. Remarkably, in this reduced subspace, S^x, S^y, and S^z become identical off-diagonal operators and the system maps on to an effective spin-half Ising model, with commuting terms, that has two degenerate ground states with long-range order.

For the case of large D_{100} the ground state is given by

$$|\psi_g\rangle = \prod_i |z_i\rangle \,. \tag{5.17}$$

One can study its properties by non-degenerate perturbation theory using the linked-cluster method [167, 168, 169]. The ground state energy series is

$$E_g/D_{100} = \sum_n c_n (K/D_{100})^{2n}. \tag{5.18}$$

This model is invariant under a change of sign of the Kitaev couplings and hence the properties depend only on $(K/D_{100})^2$.

The occupation probability of the single-spin excited states $|x\rangle$ or $|y\rangle$ at a site in the ground state is given by

$$n_{xy} = \sum_n d_n (K/D_{100})^{2n}. \tag{5.19}$$

The coefficients c_n and d_n up to $n = 12$ are available at [170]. Numerical results will be presented in the next section when we compare with exact diagonalization.

Note that despite the product ground state, this system remains unconventional. Due to various conservation laws, single-particle states remain confined to single bonds, an $|x\rangle$ excitation is confined to a single Y bond, where as a $|y\rangle$ excitation is confined to a single X bond. Only states in the zero-flux sector can be delocalized [171].

At large negative D_{100}, we need to carry out a degenerate perturbation theory in the space of states $|x\rangle$ and $|y\rangle$ on the different sites. In this case, it is easier to go back to the S^z basis. In the degenerate 2^N dimensional Hilbert space given by $|S^z = \pm 1\rangle$, the system at first breaks into decoupled dimers along the Z bonds. Depending on the sign of the Kitaev couplings, in first-order perturbation theory, the lower energy state corresponds to parallel or antiparallel spins on each dimer. This still leaves $2^{N/2}$ degenerate states. A higher order degenerate perturbation theory in this subspace is needed. In the 4^{th} order, the system breaks into coupled chains of Z-bond dimers. The Z-bond dimers in a row are coupled by a transverse Ising exchange coupling between effective spin-half degrees of freedom on neighboring dimers. Thus, there are two degenerate ground states for each such chain of Z-bond dimers and the system has large but nonextensive ground state degeneracy. In Fig. 5.2 we show a phase diagram illustrating the ground states observed for both D_{111} and D_{100} anisotropy.

To study the model near $D = 0$ it is essential to perform numerical studies.

5.4. Numerical Studies

We study the ground states of the model with different values of the anisotropy using Lanczos exact diagonalization of 12 and 18 site clusters for both D_{111} and D_{100} anisotropy. The larger system size study is enabled in the latter case by the conserved fluxes, which reduce the connected Hilbert space size, and hence the ground state is always found in the zero flux sector. For D_{111} anisotropy the fluxes are not conserved, however, the translational symmetries of the 18-site cluster (along with an inversion symmetry) give a reduced Hilbert space dimension $\sim \frac{3^{18}}{18}$, enabling Lanczos exact diagonalization of this larger system size.

We show below results of ground state energy and its second derivative, on-site occupation probabilities, entanglement entropy when the system is divided into two equal halves, and fidelity susceptibility defined as

$$\chi_F = \frac{2\left[1 - |\,\langle\psi_g(x)|\psi_g(x+dx)|\psi_g(x)|\psi_g(x+dx)\rangle\,|\right]}{dx^2}. \tag{5.20}$$

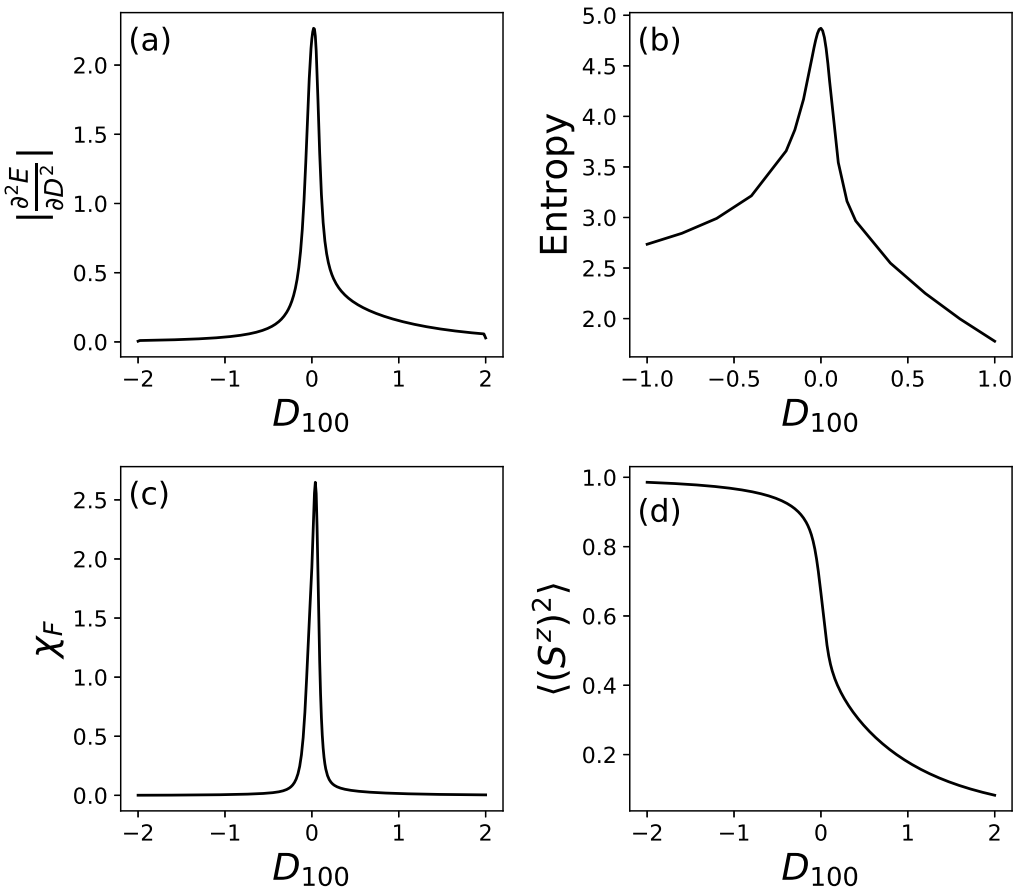

FIGURE 5.3. Exact diagonalization results for a $N = 18$ site cluster with D_{100} anisotropy, with $|K| = 1$. We show (a) the second derivative of ground state energy (arbitrary units), (b) entanglement entropy, (c) fidelity susceptibility (arbitrary units), and (d) $\langle (S^z)^2 \rangle$ as a function of D_{100}. Note that $\langle (S^z)^2 \rangle$ is equivalent to n_{xy} as defined in Eq. (5.19).

In Fig. 5.3 the results for various ground state properties with the D_{100} anisotropy from Lanczos diagonalization of the 18-site cluster are shown. In Fig. 5.4 the results are shown for the corresponding study of the 18-site cluster with D_{111} anisotropy.

It is evident from the figures that the D_{111} model undergoes a phase transition as the $D_{111} = 0$ limit is approached. For the 18-site cluster we find no significant difference in behavior for ferromagnetic and antiferromagnetic Kitaev couplings. Peaks in the second derivative of the energy and fidelity susceptibility occur at $D_{111} \approx \pm 0.12$, along with a region of maximum entanglement entropy between these values. The value of the anisotropy at which the transition occurs is similar

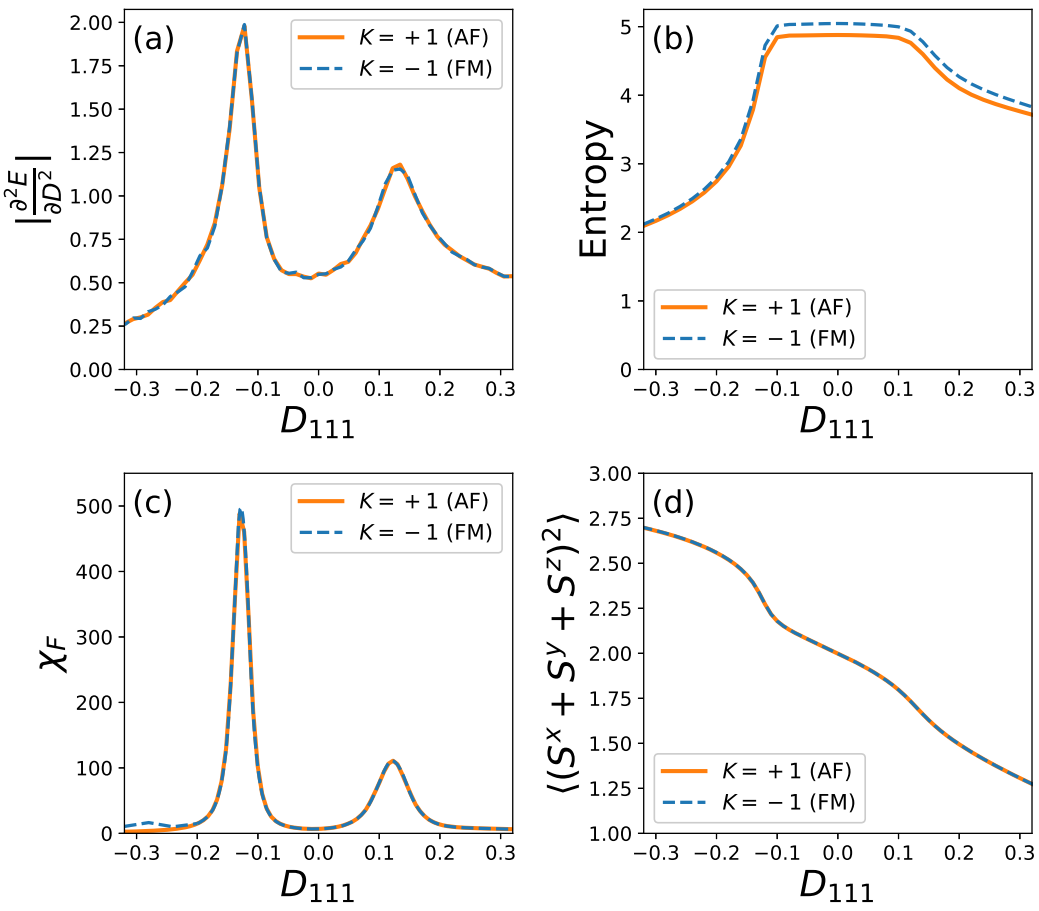

FIGURE 5.4. Exact diagonalization results for a $N = 18$ site cluster with D_{111} anisotropy, for both ferromagnetic (FM) and antiferromagnetic (AF) Kitaev couplings. We show (a) the second derivative of ground state energy (arbitrary units), (b) entanglement entropy, (c) fidelity susceptibility (arbitrary units), and (d) $\langle (S^x + S^y + S^z)^2 \rangle$ as a function of D_{111}. Note that $\frac{1}{3}\langle (S^x + S^y + S^z)^2 \rangle$ is equivalent to n_{12} as defined in Eq. (5.16).

in the two cases. The average plaquette flux $\langle W_p \rangle$ approaches 1 as the $D_{111} = 0$ limit is approached as expected, changing rapidly in the transition region and falling to zero in the limit of large negative or large positive D_{111} anisotropy, as shown in Fig. 5.5(a).

In contrast, for the D_{100} anisotropy the sharpest changes occur at $D_{100} = 0$. The entanglement entropy, fidelity susceptibility, and second derivative of ground state energy are all sharply peaked very near $D_{100} = 0$. In the finite system the peaks are not strictly at $D_{100} = 0$, but they are also system size dependent and consistent with the singularity being right at $D_{100} = 0$. The transition

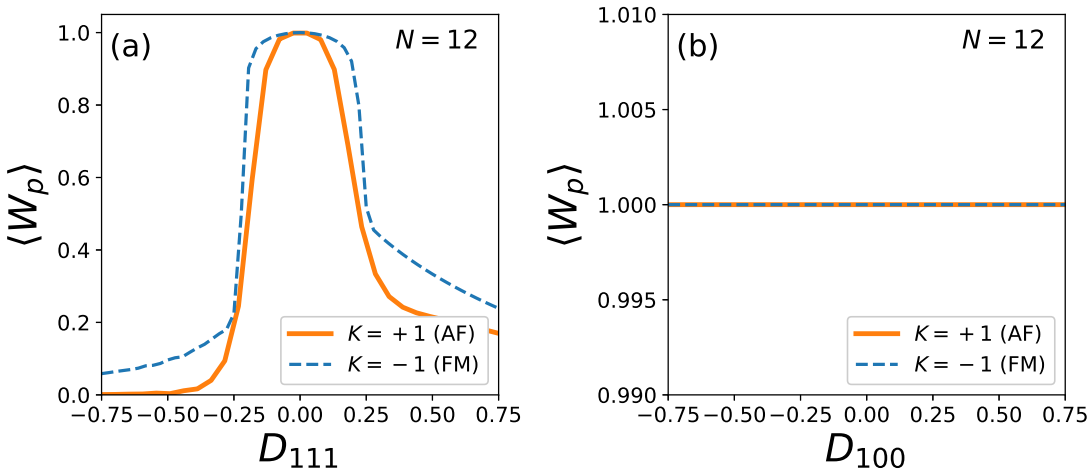

FIGURE 5.5. Average value of the plaquette flux operator W_p as a function of (a) D_{111} anisotropy and (b) D_{100} anisotropy, for both ferromagnetic (FM) and antiferromagnetic (AF) Kitaev couplings. Exact diagonalization results are shown for a $N = 12$ site cluster.

at $D_{100} = 0$ is further supported by comparison with the series analysis, which is done in the thermodynamic limit, presented in the next section. Since the ground state is always in the zero flux sector, we have $\langle W_p \rangle = 1$ for all values of D_{100} as shown in Fig. 5.5(b).

5.5. Comparison with Series Expansion and Discussion

A direct comparison of the energy and state occupation n_{xy} for positive D_{100} are shown in Fig. 5.6. For the D_{100} anisotropy the series are in powers of $(K/D_{100})^2$. One can estimate the ground state energy in the large K/D_{100} limit by using Padé extrapolation. Since the energy in this limit must go as K, we first square the energy series. The resulting series are analyzed by $[n/n-1]$ Padé approximants. This ensures the correct large K/D_{100} behavior. The series results for different Padé approximants are shown. One can see that the range of convergence is improving as more terms are added. However, the convergence slows down as D_{100} goes to zero. The extrapolated values at $K/D_{100} \to \infty$ from $[n/n-1]$ Padé are then further extrapolated as a function of $1/n$ in Fig 5.7. The linear fit to $1/n$ gives ground state energy at $D_{100} = 0$ of $E/K = -0.656$, which is close to the value $E/K \sim -0.65$ obtained from previous numerical studies of finite-size clusters [**152**, **155**]. The success of this extrapolation is evidence that the transition to a long-range entangled state happens very close to $D_{100} = 0$, likely right at $D_{100} = 0$. Also, the

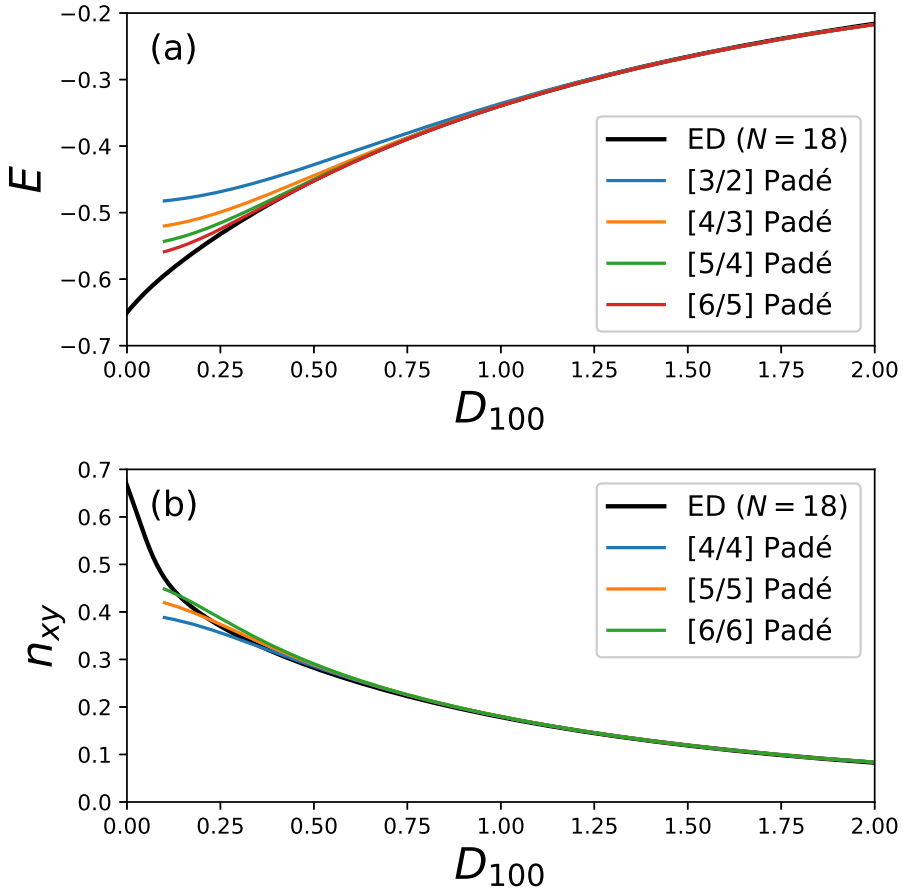

FIGURE 5.6. (a) Ground state energy per site and (b) local occupation of excited states as a function of D_{100}. Exact diagonalization results are shown for a $N = 18$ site cluster, along with Padé approximants to each series expansion.

need to extrapolate Padé results with $1/n$ suggests that $D_{100} = 0$ is a singular limit. Thus, for any nonzero $D_{100} > 0$, the ground state is adiabatically connected to the product state at large D_{100} and hence lacks long-range entanglement.

For the D_{111} case also the series expansion converges well at large D_{111} values until the transition region is reached beyond which the series expansion disagrees sharply with the exact diagonalization results, as shown in Fig. 5.8. No meaningful estimate of the properties in the $D_{111} \to 0$ limit can be obtained from the series. This is consistent with the existence of a phase transition in the model at finite D_{111}.

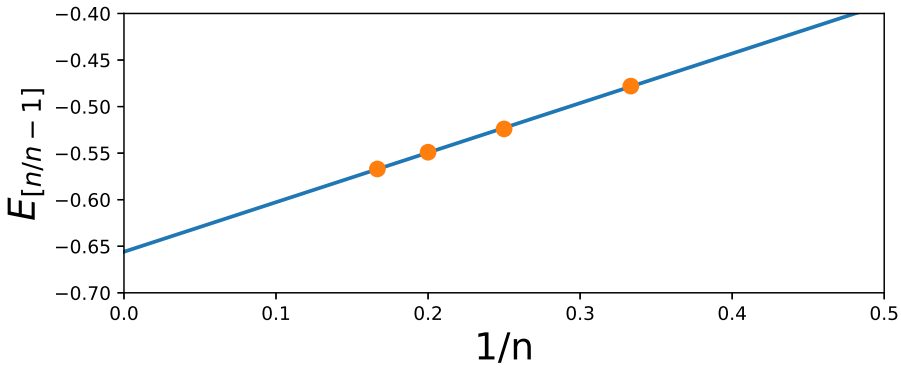

FIGURE 5.7. Asymptotic $K/D_{100} \to \infty$ value of ground state energy from $[n/n-1]$ Padé approximant for the ground state energy series is further extrapolated as a function of $1/n$ to get an estimate for the $D_{100} = 0$ ground state energy. It is found to be approximately $E/K = -0.656$.

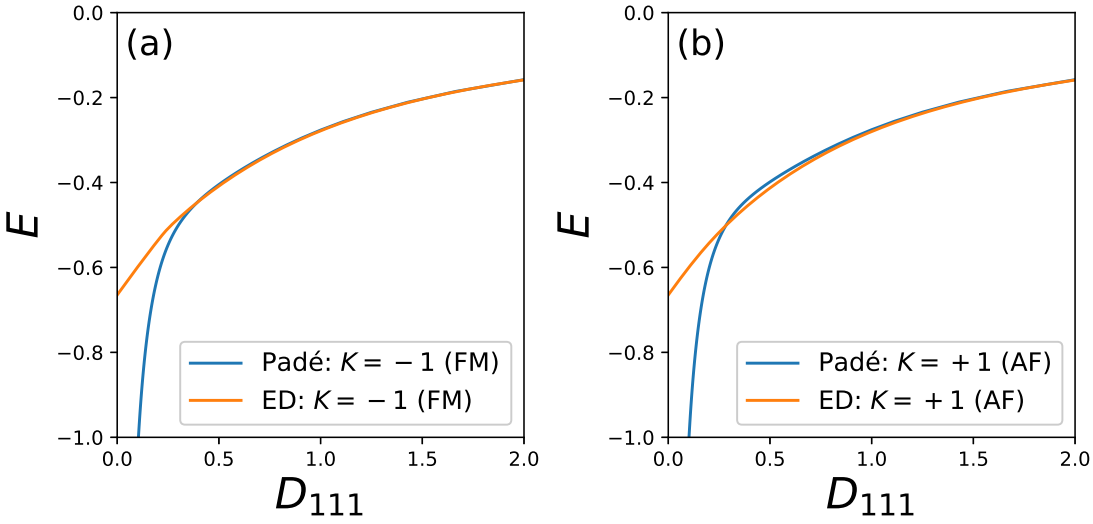

FIGURE 5.8. Ground state energy per site as a function of D_{111} anisotropy, for both (a) ferromagnetic and (b) antiferromagnetic Kitaev couplings. Results are shown comparing exact diagonalization data for a $N = 12$ site cluster and a Padé approximant of series expansion data.

We note that within perturbation theory the ferromagnetic and antiferromagnetic Kitaev models are identical in first few orders. The difference first arises in the order $(K/D_{111})^7$. Similarly, the leading effective Hamiltonian at large negative D_{111} and the selection of order does not depend on the sign of Kitaev exchange couplings. Thus any difference between ferromagnetic

and antiferromagnetic Kitaev couplings is a higher-order process and comparison with the exact diagonalization suggests that it is numerically not very significant. We note that the addition of other exchange couplings (such as Heisenberg and Gamma couplings) and magnetic fields to the Kitaev Hamiltonian causes sharp differences between ferromagnetic and antiferromagnetic Kitaev models in both the spin-half and spin-one cases [18, 146, 155, 156, 157, 158] and these deserve further attention in the presence of single-ion anisotropies.

5.6. Conclusions

In this chapter we have studied the spin-one Kitaev model with two types of single-ion anisotropies using a variety of perturbative and numerical methods. We find that the D_{111} anisotropy, which preserves the symmetry between X, Y, and Z bonds but violates flux conservation, leads to conventional phases and excitations at large anisotropy values. There is a phase transition at a modest value of $D_{111}/K \approx 0.12$ that separates these conventional phases from the Kitaev spin liquid. In contrast, for large D_{100} anisotropy, even though the ground states are simple and lack long-range entanglement the system remains exotic at both large negative and positive D_{100} values. For positive D_{100} there is a non-degenerate ground state but no conventional dispersive quasiparticle excitations. For negative D_{100}, the system decouples into chains of Z-bond dimers that are coupled by an effective Ising coupling along the chain. Thus there are two degenerate ground states for each such chain. No signature of a phase transition is seen in our study as a function of D_{100}. The fidelity, second derivative of free energy and entanglement entropy are all sharply peaked near $D_{100} = 0$ suggesting that the Kitaev spin liquid emerges only upon D_{100} going to zero and restoration of symmetry between X, Y, and Z bonds. We emphasize that the Kitaev spin-liquid becomes immediately unstable in the presence of D_{100} anisotropy.

Candidate materials for spin-one Kitaev spin liquids and underlying exchange mechanisms have been recently proposed [18]. Real spin-one materials are known to always have some single-ion anisotropies. A material with the full symmetry of the honeycomb lattice will likely have only D_{111} anisotropy. Our work shows that the anisotropy value must be small compared to Kitaev couplings to realize a Kitaev spin liquid ground state. However, distortions which can allow nonzero D_{100} anisotropy may be particularly destabilizing to the long-range entangled spin-liquid phase.

In future, it may be useful to study the nature of the phase transitions for D_{111} anisotropy. Density matrix renormalization group or tensor network studies on larger system sizes may be helpful in this respect [**166**]. For a positive sign of D_{111} the two phases on either side of the transition have no broken symmetries, hence we speculate that the transition may be purely topological in nature, although the transition could be first order. It would also be interesting to better elucidate the mechanism for loss of long-range entanglement with D_{100} anisotropy, which should also throw further light on the nature of the spin-liquid phase.

CHAPTER 6

Thermodynamic Behavior of Modified Integer-Spin Kitaev Models on the Honeycomb Lattice

6.1. Chapter Summary

We study the thermodynamic behavior of modified spin-S Kitaev models introduced by Baskaran, Sen, and Shankar [Phys. Rev. B **78**, 115116 (2008)]. These models have the property that for half-odd-integer spins their eigenstates map on to those of spin-1/2 Kitaev models, with well-known highly entangled quantum spin-liquid states and Majorana fermions. For integer spins, the Hamiltonian is made out of commuting local operators. Thus, the eigenstates can be chosen to be completely unentangled between different sites, though with a significant degeneracy for each eigenstate. For half-odd-integer spins, the thermodynamic properties can be related to the spin-1/2 Kitaev models apart from an additional degeneracy. Hence we focus here on the case of integer spins. We use transfer matrix methods, high-temperature expansions, and Monte Carlo simulations to study the thermodynamic properties of ferromagnetic and antiferromagnetic models with spin $S = 1$ and $S = 2$. Apart from large residual entropies, which all the models have, we find that they can have a variety of different behaviors. Transfer matrix calculations show that for the different models, the correlation lengths can be finite as $T \to 0$, become critical as $T \to 0$ or diverge exponentially as $T \to 0$. The Z_2 flux variable associated with each hexagonal plaquette saturates at the value $+1$ as $T \to 0$ in all models except the $S = 1$ antiferromagnet where the mean flux remains zero as $T \to 0$. We provide qualitative explanations for these results.

This chapter is based on the following publication [172]:

O. Bradley, J. Oitmaa, D. Sen, and R. R. P. Singh, *Thermodynamic behavior of modified integer-spin Kitaev models on the honeycomb lattice*, Phys. Rev. E. **103**, 022109 (2021).

6.2. Introduction

In the study of quantum spin systems [134], Kitaev materials have emerged as a very active field of research [17, 146, 147, 148, 149]. Following Kitaev's introduction of the honeycomb lattice model with bond-dependent Ising interactions for different spin components [16] and subsequent theoretical work [135, 136, 137, 138, 139, 173, 174, 175, 176, 177], Jackeli and Khaliullin showed how such exchanges can be realized in real materials [144]. Since then, a number of materials have been proposed where such interactions are dominant [147, 148, 149]. Possible observation of fractionally quantized thermal Hall effect [145] has made these systems central in the search for quantum spin-liquid phases of matter.

While much interest has justifiably focused on spin-1/2 Kitaev materials, it has been shown that Kitaev models with arbitrary spin retain many interesting properties [18, 19, 152, 153, 154, 155, 178, 179, 180, 181, 182]. For arbitrary spin, the system is a classical spin-liquid at intermediate temperatures, with only very short-range spin correlations and an extensive classical degeneracy. There are conserved flux variables associated with each elementary hexagonal plaquette. The lack of exact solubility of the models for spin greater than half means that the ground state is not known. One very interesting issue is the possibility that the property of half-odd-integer and integer spins can be very different at low temperatures. Like the famous Haldane chain problem in one dimension, half-odd-integer spin models may have gapless excitations while integer spins may be gapped. Increasingly, many studies have focused on material realization of higher-spin Kitaev models [18, 156, 182].

In Ref. [19], Baskaran, Sen, and Shankar (BSS) introduced a simpler model which we call a modified Kitaev model. This model shares some key features with the Kitaev model. It is defined by replacing the spin operators S_i^α in the Kitaev model by the operators $\tau_i^\alpha = e^{i\pi S_i^\alpha}$. The model has Ising couplings between different components of the τ variables on different bonds, just like in the Kitaev model. This model continues to have conserved local flux variables on each hexagonal plaquette of the honeycomb lattice. For each half-odd-integer spin, the model is equivalent to many copies of the spin-1/2 Kitaev model. Thus its eigenstates are highly entangled and support Majorana fermion excitations. In contrast, for integer-spins, the basic τ operators at a site commute with each other. Thus all eigenstates can be chosen to be a product state from site to site with

no intersite entanglement. However, the system remains highly degenerate, which leaves open the possibility of constructing entangled eigenstates via superposition of the many degenerate states. The modified Kitaev model is an interesting statistical model in its own right and the goal of this paper is to understand its thermodynamic behavior.

The Hamiltonian for the modified Kitaev model is [19]:

$$H = J\left(\sum_{\langle i,j\rangle}\tau_i^x\tau_j^x + \sum_{(i,k)}\tau_i^y\tau_k^y + \sum_{[i,l]}\tau_i^z\tau_l^z\right), \tag{6.1}$$

where $\tau_i^\alpha = e^{i\pi S_i^\alpha}$ and $\langle i,j\rangle$, (i,k), and $[i,l]$ denote nearest-neighbor pairs which have a bond pointing along the x, y, and z bond directions of the honeycomb lattice, respectively. S_i^α ($\alpha = x,y,z$) are the spin operators (defined at each site i) which are $(2S+1)\times(2S+1)$ matrices. Since the spin operators S^x, S^y, and S^z satisfy $e^{i\pi S^a}e^{i\pi S^b} = (-1)^{2S}e^{i\pi S^b}e^{i\pi S^a}$ (for $a \neq b$), for integer spins the τ^α operators commute and hence can be simultaneously diagonalized. As shown in Appendix A, the resulting matrices have diagonal elements ± 1, and the model becomes a classical statistical model.

In this work we study the integer spin BSS models using high-temperature expansions, transfer matrices, and Monte Carlo simulations. We find a very rich finite-temperature thermodynamic behavior, which can be contrasted with the known results for the Kitaev model. In the Kitaev model, the intermediate temperature physics is dominated by an entropy plateau at exactly half the maximum entropy regardless of the spin and ferromagnetic vs antiferromagnetic coupling in the model. The existence of such plateaus is an important indicator of a low-energy subspace from which the quantum spin-liquid states emerge. In Appendix B, we provide a semiclassical explanation for this residual entropy of large-spin Kitaev models. In contrast to the Kitaev model, for the BSS model ferromagnetic and antiferromagnetic models behave very differently, and between the $S = 1$ and $S = 2$ ferromagnetic and antiferromagnetic cases, we find several classes of behaviors. For the $S = 1$ antiferromagnet, the system stays disordered as $T \to 0$ with zero net flux and a short correlation length. The $S = 2$ antiferromagnet appears to have an exponentially diverging correlation length as $T \to 0$ on finite-width cylinders. It is known that in the one-dimensional transverse field Ising model, as the magnetic field is varied (near $T = 0$) there is analogous behavior

of the correlation length in the low and high field regimes. There is a disordered gapped phase at $T = 0$ with short-range correlations at high fields, and an ordered gapped phase in which the correlation length becomes exponentially large as $T \to 0$. In this sense, the antiferromagnetic models for $S = 1$ and $S = 2$ appear to be gapped and on two sides of a $T = 0$ order-disorder transition. In contrast the $S = 1$ and $S = 2$ ferromagnetic models appear critical with correlation length scaling with the width of the cylinder, presumably implying critical correlations and gapless excitations in the thermodynamic limit. This shows that the modified Kitaev models have a wide variety of thermodynamic behavior at intermediate temperatures.

In Sec. 6.3 we discuss the τ operators for $S = 1$ and $S = 2$ and some general properties of our model. In Sec. 6.4 we discuss the transfer matrix method for a finite-width cylindrical strip, our Monte Carlo simulations, and the method of high-temperature series expansions. In Sec. 6.5 the numerical results for the model are presented and we discuss some analytical insights into these results. We consider the integer-spin models only in this work. Finally in Sec. 6.6 we present our conclusions, open questions and the relevance of these studies to the Kitaev family of materials.

6.3. Modified Kitaev Model

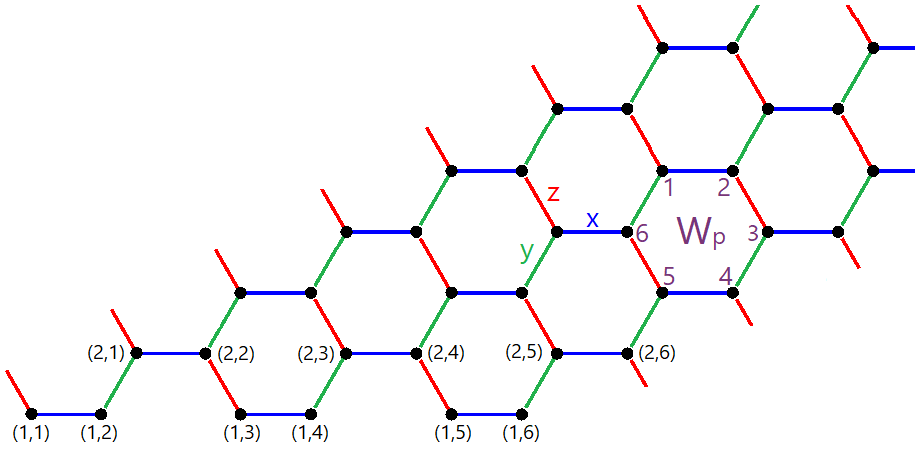

FIGURE 6.1. Geometry of the honeycomb lattice (shown for a semi-infinite lattice $n = 6$ sites in width), with the x, y, and z bond directions indicated. Each site may be labeled (α, β) where α denotes the row number and $\beta = 1, \ldots, n$ denotes the position of the site along its row.

For each hexagon in the lattice (with sites labeled $1, \ldots, 6$ as shown in Fig. 6.1) one can define the plaquette flux operator

$$W_p = e^{i\pi(S_1^z+S_2^y+S_3^x+S_4^z+S_5^y+S_6^x)} = \Pi_{i=1}^6 \tau_i^{\alpha_{out}}, \tag{6.2}$$

where α_{out} is the direction pointing out of the loop at site i. As shown in Ref. [19], the W_p operators both commute with the Hamiltonian and each other and have eigenvalues equal to ± 1. Hence the model has conserved Z_2 flux variables on each hexagonal plaquette of the honeycomb lattice. For integer spin, this conservation is trivial as each τ_i commute with each other. Nevertheless, the thermal expectation value of these flux variables is strongly correlated with the thermodynamic behavior of the model, as we will show here, resembling that in the original Kitaev models. This suggests that the modified Kitaev models preserve some aspects of the Kitaev model thermodynamics despite their simplicity.

The τ^α ($\alpha = x, y, z$) operators can be simultaneously diagonalized, giving three diagonal matrices of dimension $(2S+1) \times (2S+1)$. As shown in Appendix A, for $S = 1$ this gives three possibilities for (τ^x, τ^y, τ^z) at each site: $(1, -1, -1)$, $(-1, 1, -1)$, and $(-1, -1, 1)$. For $S = 2$, the diagonalized tau operators yield five possibilities for (τ^x, τ^y, τ^z) per site, which have $(\tau^x, \tau^y, \tau^z) = (-1, -1, 1)$, $(-1, 1, -1)$, $(1, 1, 1)$, $(1, -1, -1)$, and $(1, 1, 1)$. Note that the five triplets contain those found for $S = 1$, plus an additional pair for which $\tau^x = \tau^y = \tau^z = 1$.

6.3.1. Zero-temperature entropy for the spin-1 ferromagnetic model

We will derive here an exact result for the ground-state entropy per site for the spin-1 ferromagnetic model where the nearest-neighbor interactions are taken to be of the form $\tau_m^a \tau_n^a$, where $\tau_m^a = e^{i\pi S_m^a}$ at site m. For the spin-1 case, we find that

$$\tau_m^x \; \tau_m^y \; \tau_m^z \;\; = \;\; 1, \tag{6.3}$$

for each m, and the three possible states at each site have $(\tau^x, \tau^y, \tau^z) = (1, -1, -1)$, $(-1, 1, -1)$, and $(-1, -1, 1)$ in a suitably defined basis.

The Hamiltonian of the model is given by

$$H \;=\; J \sum_{mn} \tau_m^a \; \tau_n^a, \tag{6.4}$$

where the sum goes over nearest-neighbor pairs of sites (mn) of the honeycomb lattice, and a depends on the direction of the bond joining (mn). The ferromagnetic case corresponds to $J < 0$. Now, each state at site m has one of the τ_m^a's equal to $+1$; hence the ground state for the bond involving $\tau_m^a = +1$ must have its neighboring τ_n^a also equal to $+1$. Let us call this bond a dimer. All the nondimer bonds have both τ_m^a and τ_n^a equal to -1, which is also the ferromagnetic ground state of those bonds. The total number of ground states of the ferromagnetic model is therefore given by the number of dimer coverings of the honeycomb lattice. In the thermodynamic limit in which the number of sites $N \to \infty$, it is known [**183**, **184**, **185**] that the number of dimer coverings is given by $(1.381)^{N/2}$. Hence the ground-state entropy per site is given by $(1/2)\ln(1.381) \simeq 0.161$.

6.3.2. Ground state energy per site equal to $-3/2$ implies that the flux per hexagon is $+1$

The identity in Eq. (6.3) holds for both spin-1 and spin-2 models. For the cases of spin-1 ferromagnet, spin-2 ferromagnet, and spin-2 antiferromagnet, it is found that the ground-state energy per site is equal to $-3/2$ (for $|J| = 1$). This means that every bond simultaneously has minimum energy. We will now show that in all these cases, the flux in each hexagon must be equal to $+1$. The flux is defined as

$$W_p \;=\; \tau_1^z \; \tau_2^y \; \tau_3^x \; \tau_4^z \; \tau_5^y \; \tau_6^x \tag{6.5}$$

(see Fig. 6.1). Equation (6.3) implies that $\tau_1^z = \tau_1^x \tau_1^y$, and so on. Hence Eq. (6.5) can be re-written as

$$W_p \;=\; (\tau_1^x \tau_2^x)\; (\tau_2^z \tau_3^z)\; (\tau_3^y \tau_4^y)\; (\tau_4^x \tau_5^x)\; (\tau_5^z \tau_6^z)\; (\tau_6^y \tau_1^y)\;. \tag{6.6}$$

Each of the terms in parentheses in Eq. (6.6) corresponds to one of the interaction terms in the Hamiltonian, and each such term is equal to $+1$ or -1 in the ground state depending on whether the model is ferromagnetic or antiferromagnetic, provided that the ground-state energy per spin

attains the value $-3/2$. We therefore see that W_p must be equal to $+1$ in every hexagon in such ground states.

6.4. Methods

6.4.1. Transfer Matrix Method

One approach we employ to study the thermodynamic properties of our model is the transfer matrix method, which we now describe in detail. For spin-1, each site has three possible spin states $\sigma = \{1, 2, 3\}$, and we have $(\tau_i^x, \tau_i^y, \tau_i^z) = (1, -1, -1)$, $(-1, -1, 1)$ or $(-1, -1, 1)$ if site i is in state 1, 2, or 3 respectively. Consider a honeycomb lattice formed by stacking N rows, each consisting of n sites. There are 3^n possible configurations on each row. The total energy of the lattice obtained by Eq. (6.1) is denoted $E\{\sigma_i\}$, which depends on the state at each site. The partition function is given by

$$Z = \sum_{\{\sigma_i\}} e^{-\beta E\{\sigma_i\}}, \tag{6.7}$$

where the sum is over all possible spin states at each site. Labeling the rows as $1, 2, \ldots, N$, this can be written as

$$Z = \sum_{\{\sigma_1\}} \sum_{\{\sigma_2\}} \cdots \sum_{\{\sigma_N\}} e^{-\beta E(\{\sigma_1\},\{\sigma_2\},\ldots,\{\sigma_N\})}, \tag{6.8}$$

where $\sum_{\{\sigma_1\}}$ denotes a sum over all 3^n configurations of row 1, etc. The transfer matrix method relies on the fact that one can construct a particular matrix T such that the partition function can be written as

$$Z = \sum_{\{\sigma_1\}} \sum_{\{\sigma_2\}} \cdots \sum_{\{\sigma_N\}} T_{1;2} T_{2;3} T_{3;4} \ldots T_{N-1;N} T_{N;1}, \tag{6.9}$$

where $T_{A;B}$ is a $3^n \times 3^n$ matrix containing contributions to the total energy arising from a *pair* of rows (labeled A and B), with row B directly above row A, and we have assumed periodic boundary conditions by writing $T_{N;1}$. The partition function now becomes

$$Z = \sum_{\{\sigma_1\}} T_{1;1}^N = \mathrm{Tr}\big(T^N\big), \tag{6.10}$$

where T is a $3^n \times 3^n$ matrix. The elements of T are given by

$$T(i,j) = \exp[-\beta(E_1 + E_2 + E_3 + E_4)], \tag{6.11}$$

where the energy terms are as given in Eqs. (6.12)–(6.15) below. To find the matrix element $T(i,j)$ we consider a pair of rows labeled 1 and 2, with row 2 directly above row 1. Let rows 1 and 2 have configurations i and j, respectively, where i and j denote one of 3^n possible row configurations. For clarity, let us label each lattice site by (α, β), where α denotes the row number of the site, and $\beta = 1, 2, \ldots, n$ denotes the position of the site along its row as shown in Fig. 6.1. The energy terms in Eq. (6.11) are then given by

$$E_1 = \frac{1}{2}\left(\tau^x_{1,1}\tau^x_{1,2} + \tau^x_{1,3}\tau^x_{1,4} + \ldots + \tau^x_{1,n-1}\tau^x_{1,n}\right), \tag{6.12}$$

$$E_2 = \frac{1}{2}\left(\tau^x_{2,1}\tau^x_{2,2} + \tau^x_{2,3}\tau^x_{2,4} + \ldots + \tau^x_{2,n-1}\tau^x_{2,n}\right), \tag{6.13}$$

$$E_3 = \tau^y_{1,2}\tau^y_{2,1} + \tau^y_{1,4}\tau^y_{2,3} + \tau^y_{1,6}\tau^y_{2,5} + \ldots + \tau^y_{1,n}\tau^y_{2,n-1}, \tag{6.14}$$

$$E_4 = \left(\tau^z_{1,3}\tau^z_{2,2} + \tau^z_{1,5}\tau^z_{2,4} + \ldots + \tau^z_{1,n-1}\tau^z_{2,n-2}\right) + \tau^z_{1,1}\tau^z_{2,n}, \tag{6.15}$$

The factors of $1/2$ in E_1 and E_2 are included to avoid double counting interactions from the x bonds. The last term in E_4 is included due to the periodic boundary condition.

Since the trace of T^N is independent of the basis used, if we consider the basis where T is diagonal, then $T^N = \mathrm{diag}(\lambda_1^N, \lambda_2^N, \lambda_3^N, \ldots, \lambda_{3^n}^N)$, where λ_i are the eigenvalues of T. Letting λ_1 denote the largest eigenvalue, the partition function can now be written as

$$Z = \lambda_1^N + \lambda_2^N + \lambda_3^N + \ldots \tag{6.16}$$

$$= \lambda_1^N \left[1 + \left(\frac{\lambda_2}{\lambda_1}\right)^N + \left(\frac{\lambda_3}{\lambda_1}\right)^N + \ldots\right]. \tag{6.17}$$

In the limit $N \to \infty$ (i.e., a semi-infinite lattice) we therefore have $Z = \lambda_1^N$. The free energy can then be found from $F = -k_B T \ln Z = -k_B T N \ln(\lambda_1)$, and since the total number of sites is $N_{tot} = N \times n$, the free energy per site is given by

$$f = \frac{F}{N_{tot}} = -k_B T \, \frac{\ln(\lambda_1)}{n}. \tag{6.18}$$

Thermodynamic quantities such as entropy, specific heat, and internal energy can then be obtained by taking suitable derivatives of the free energy. The correlation length can also be found from the ratio of the two largest eigenvalues of the transfer matrix

$$\xi = \frac{1}{\ln(\lambda_1/\lambda_2)}. \tag{6.19}$$

6.4.2. Monte Carlo Method

We also employ a Monte Carlo procedure to study the thermodynamic properties of the model. This allows us to verify our transfer matrix and high-temperature series expansion results and also investigate the thermodynamic behavior of the flux variable W_p defined previously. For both the spin-1 and spin-2 cases, the τ^α operators commute and can be simultaneously diagonalized with diagonal entries equal to ± 1. Thus for integer spin, our model is akin to an Ising spin model which can be studied using classical Monte Carlo methods.

For spin-1, there are three possible states per site, whereas for spin-2 there are five possible states. We use the Metropolis-Hastings algorithm to perform local updates of these states. That is, for each Monte Carlo sweep, a change in the state at each site is proposed in sequence, and one accepts the move if the energy difference $\Delta E < 0$, otherwise the move is accepted with probability $e^{-\beta \Delta E}$. Simulations were performed for honeycomb lattices with periodic boundary conditions for systems with up to 40×40 sites. We present Monte Carlo results for both the mean energy and specific heat per site, and also the mean flux per plaquette as a function of temperature, which is evaluated by averaging the mean flux over sampled configurations, i.e.,

$$\langle W_p \rangle = \frac{1}{N_{meas}} \frac{1}{N_p} \sum_{i=1}^{N_{meas}} \sum_{p=1}^{N_p} W_p, \tag{6.20}$$

where N_{meas} is the number of measurement sweeps performed (at least $10,000$ in our simulations), and $N_p = N/2$ is the number of hexagonal plaquettes in the lattice, which is equal to half the total number of sites.

We also compute a second moment correlation length ξ_2 corresponding to state-state correlations, defined by

$$\xi_2^2 = \frac{1}{2d} \frac{\sum_{ij} r_{ij}^2 (\langle \sigma_i \sigma_j \rangle - \langle \sigma_i \rangle \langle \sigma_j \rangle)}{\sum_{ij} (\langle \sigma_i \sigma_j \rangle - \langle \sigma_i \rangle \langle \sigma_j \rangle)}, \tag{6.21}$$

where σ_i denotes the state at site i, r_{ij} is the distance between two sites in the lattice, and $d = 2$ is the number of dimensions. We map the states onto vectors in two dimensions, i.e., for spin-1 the three states are mapped to $(1, 0)$, $(-1/2, \sqrt{3}/2)$, and $(-1/2, -\sqrt{3}/2)$. The correlation $\sigma_i \sigma_j$ is then defined as the scalar product of the vectors corresponding to the states at sites i and j, and our assignment is symmetric between the three possible states.

6.4.3. High Temperature Series Expansion Method

The partition function for any interacting many-particle system is given by

$$Z = \mathrm{Tr}\{e^{-\beta H}\}. \tag{6.22}$$

The quantity

$$A \equiv (1/N) \ln Z \tag{6.23}$$

can be obtained via a linked-cluster method as

$$A_{bulk} = \Sigma_g c_g \tilde{A}_g \tag{6.24}$$

where the sum is over a set $\{g\}$ of finite clusters of increasing size, c_g is an embedding constant, and $\tilde{A}_g$ is the "reduced" value of $\ln Z$ for cluster g, with all of the subcluster contributions subtracted off. Technical details are explained in Ref. [**167**]. In the present classical case, where all operators commute, we can use the simpler form,

$$Z = \Sigma_n e^{-\beta E_n} = \Sigma_r g_r e^{-\beta E_r} \tag{6.25}$$

where the first sum is over all states $\{n\}$, which can be grouped into a sum over distinct eigenstates $\{r\}$ with g_r being the degeneracy. For any finite cluster g the partition function is then a finite, fairly small, sum of weighted exponentials, which can be expanded to give a series in powers of $\beta = 1/k_B T$, from which $\ln Z$ is easily obtained. The bulk series will then be correct to an order

determined by the number of bonds in the largest cluster. For $S = 1$ we have computed a series to order β^{16}, using a set of 17060 clusters with up to 16 bonds. For $S = 2$ a series to order β^{14} was obtained, requiring 3453 distinct clusters. We do not list the series coefficients here, but they are available in Supplemental Material [186]. From the series for $(1/N)\ln Z$ we obtain series for entropy, energy and specific heat using standard thermodynamic relations. The series are then evaluated using standard Padé approximant methods.

6.5. Results and Discussion

6.5.1. Thermodynamics of Spin-1 model

In this chapter we study the thermodynamic properties of the modified Kitaev model for $S = 1$ and $S = 2$, for both ferromagnetic ($J < 0$) and antiferromagnetic ($J > 0$) couplings, using high-temperature series expansions, transfer matrices, and Monte Carlo simulations (note that we take $|J| = 1$ throughout). We first present results for the entropy, specific heat, energy and correlation length for the ferromagnetic $S = 1$ case. Since the transfer matrix procedure involves finding the eigenvalues of a $3^n \times 3^n$ matrix we are computationally limited to studying lattices infinite in one direction but no more than $n = 8$ sites wide. Figure 6.2(b) shows the entropy per site calculated using the transfer matrix method for systems of width $n = 4$, 6 and 8. There is a nonzero residual entropy as the temperature approaches zero, resulting from the large degeneracy of the ground state. With increasing lattice size, the residual entropy per site approaches $(1/2)\ln(1.381) \approx 0.161$ as $T \to 0$, which is directly related to the number of dimer coverings of the honeycomb lattice as discussed in Sec. 6.3.1. We also observe a plateau in $S(T)$ at the value of the residual entropy for $T \lesssim 0.3$ and find that the entropy per site approaches $\ln(3)$ in the high-temperature limit, as expected. We also plot the HTE result for the entropy for comparison. There is a close agreement between the transfer matrix and HTE data at high temperature, indicating that our result is accurate in the thermodynamic limit. However the HTE convergence breaks down before the onset of the low-temperature entropy plateau.

The specific heat shows a single broad peak, with the HTE result in close agreement with the $n = 8$ transfer matrix result in this region as shown in Fig. 6.2(c). In addition, our transfer matrix

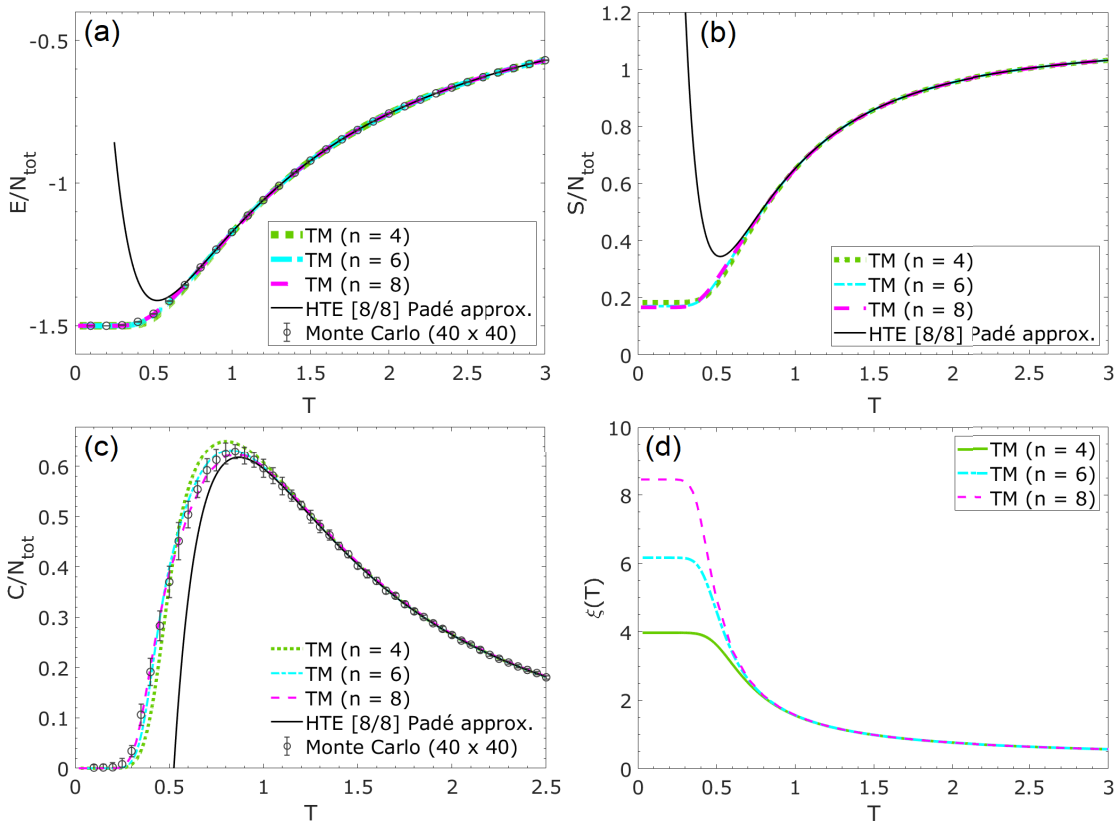

FIGURE 6.2. $S = 1$ ferromagnetic model ($J < 0$): Transfer matrix (TM), high-temperature expansion (HTE) and Monte Carlo results are shown for (a) energy per site, (b) entropy per site, (c) specific heat per site, and (d) correlation length, as a function of temperature. TM results are shown for systems $n = 4$, 6, and 8 sites wide, and HTE data are extrapolated using a Padé approximant of order $[8, 8]$. Monte Carlo data are shown for lattices of size 40×40.

result for $C(T)$ agrees well with Monte Carlo data obtained for 40×40 lattices. Figure 6.2(a) shows the ground-state energy per site is equal to $-3/2$, which corresponds to all bonds of the honeycomb lattice becoming satisfied as $T \to 0$. We also use Eq. (6.19) to find the correlation length ξ from the ratio of the two largest eigenvalues of the transfer matrix. For the ferromagnetic $S = 1$ case, ξ scales with the lattice width as $T \to 0$ indicating critical behavior, as shown in Fig. 6.2(d).

For the antiferromagnetic $S = 1$ case, there are several notable differences in the thermodynamic behavior compared to the ferromagnetic model, as shown in Fig. 6.3. Firstly, there is a much larger residual entropy of approximately 0.837, with a plateau present for $T \lesssim 0.5$. Since there is no configuration for which all antiferromagnetic couplings in the lattice are satisfied, the ground-state

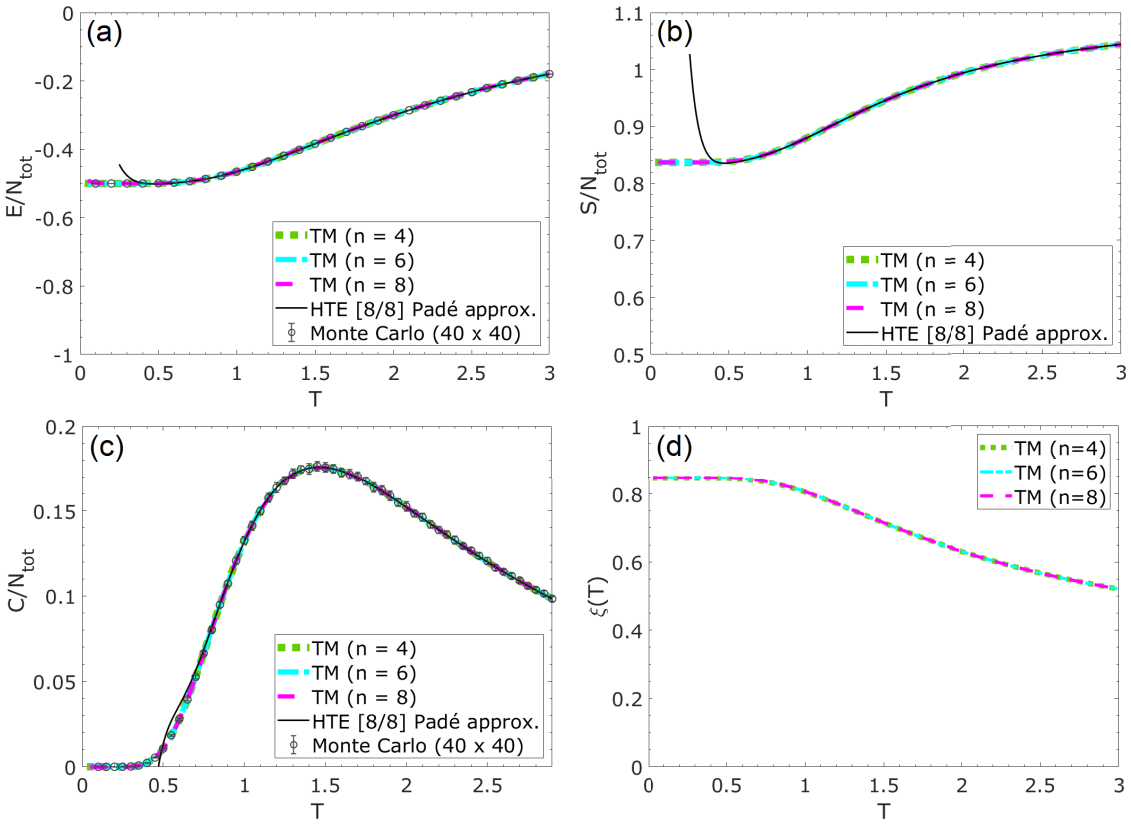

FIGURE 6.3. The $S = 1$ antiferromagnetic model ($J > 0$): TM, HTE, and Monte Carlo results are shown for (a) energy per site, (b) entropy per site, (c) specific heat per site, and (d) correlation length, as a function of temperature. TM results are shown for systems $n = 4$, 6 and 8 sites wide, and HTE data are extrapolated using a Padé approximant of order $[8, 8]$. Monte Carlo data are shown for lattices of size 40×40.

energy per site is also greater and attains the value $-1/2$. Thus the system remains disordered as $T \to 0$. This energy per site corresponds to having $2/3$ of the bonds in the lattice satisfied and $1/3$ unsatisfied (e.g., those in a particular bond direction x, y, or z) in the ground state. In contrast to the ferromagnetic case, our transfer matrix results exhibit almost no dependence on the system width n for any of the lattice sizes studied, and there is a closer agreement with HTE data for specific heat at temperatures below the peak. The correlation length also remains short as $T \to 0$ independent of n, and does not scale with system width. As in the ferromagnetic case, our transfer matrix results for $E(T)$ and $C(T)$ agree well with Monte Carlo simulations on 40×40 lattices, indicating that the finite-width cylinders studied yield quite accurate results for our purposes.

Identification of the growing correlations: The transfer matrix results do not tell us which correlation length is the largest in the system. In the Monte Carlo simulations, we have examined several correlation functions, including the spin-spin correlations involving the variable τ_i, the Z_2 flux-flux correlation functions for different hexagons and the correlation between the occupation of the (2S+1) states of the system at different sites. Only the latter grows, as temperature is lowered, in a manner similar to the correlation length found from the transfer matrix calculations. As shown in Fig. 6.4 for the $S = 1$ ferromagnet, $\xi(T)$ from transfer matrix calculations behaves similarly to the state-state correlation length ξ_2 obtained in the Monte Carlo simulations. Plotting $\ln(\xi_2)$ as a function of $1/T$ for both yields approximately straight lines of comparable slope, suggesting they have similar functional forms. We note that, at low temperatures, we found it difficult to explore

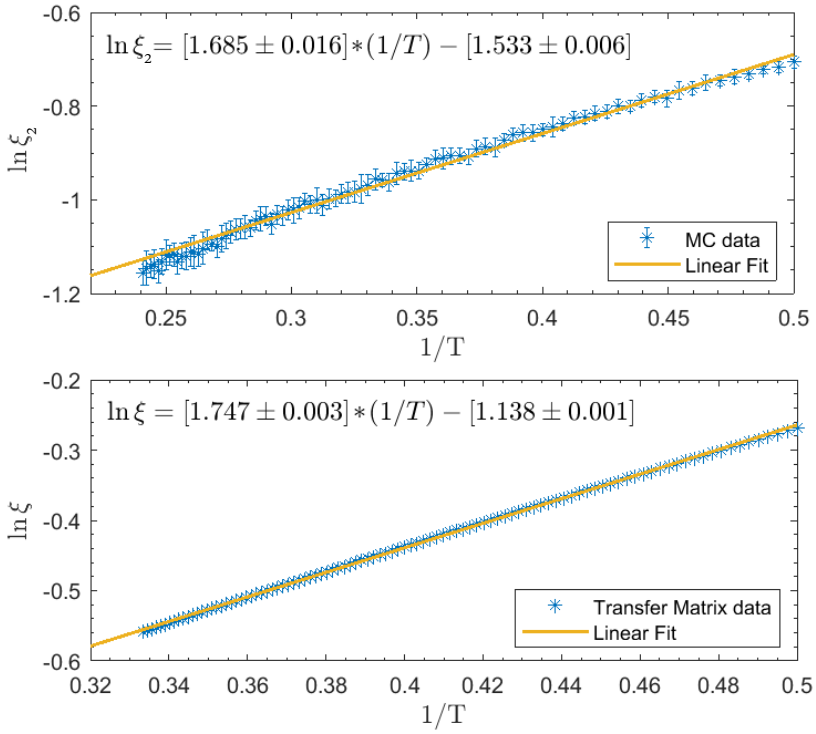

FIGURE 6.4. Top: Monte Carlo result for the state-state correlation function for the $S = 1$ ferromagnetic model (6×6 lattice). $\ln \xi_2$ is plotted as a function of $1/T$ along with a linear least-squares fit with slope 1.685 ± 0.016. Bottom: Transfer matrix result for the correlation length for a system $n = 6$ sites wide, again for the $S = 1$ ferromagnet. $\ln \xi$ is plotted as a function of $1/T$ along with a linear least-squares fit with slope 1.747 ± 0.003.

the behavior of the system with Monte Carlo simulations, even when incorporating some cluster moves which collectively change the states of sites belonging to one hexagon. Once the system enters the manifold of degenerate states, acceptance of the Monte Carlo moves goes rapidly to zero. Thus, at lower temperatures, we have to rely on the transfer matrix calculations.

6.5.2. Thermodynamics of Spin-2 model

For both the ferromagnetic and antiferromagnetic $S = 2$ models there are five possible states per site. The transfer matrix procedure thus limits us to studying finite-width cylinders no more than $n = 4$ sites wide, since the method now requires finding the eigenvalues of a $5^n \times 5^n$ matrix. Nevertheless, we find the transfer matrix results closely agree with Monte Carlo data for 40×40 clusters at low temperature, and also with high-temperature series expansion results (which are formally defined in the thermodynamic limit) down to temperatures at which the specific heat peaks.

In Fig. 6.5, we show results for the entropy, specific heat, energy, and correlation length for the ferromagnetic $S = 2$ case. As in all the models, there is a large ground-state degeneracy and a corresponding residual entropy per site as $T \to 0$, which we find to be approximately 0.707. In this model, the majority of ground states are those for which all sites have $(\tau_x, \tau_y, \tau_z) = (1, 1, 1)$; however, one can also find additional ground states by changing the state of sites belonging to closed loops in the lattice. In Sec. 6.5.3 we provide a more thorough analytical explanation of this residual entropy value. Both the ferromagnetic $S = 1$ and $S = 2$ models have a ground-state energy per site of $-3/2$ indicating that all bonds in the lattice may be satisfied. Similarly to the $S = 1$ case, the $S = 2$ ferromagnet also appears critical with the correlation length limited by the width of the system, presumably implying critical correlations in the thermodynamic limit. As shown in Fig. 6.6(b), the antiferromagnetic $S = 2$ model has a lower residual entropy per site of approximately 0.520. However, in contrast to the $S = 1$ case, it is possible to satisfy all the bonds in the lattice leading to ground-state energy of $-3/2$ per site. The $S = 2$ antiferromagnet also appears to have an exponentially diverging correlation length as the temperature is lowered. This is illustrated in Fig. 6.6(d), which shows the transfer matrix result for a semi-infinite lattice $n = 4$ sites wide.

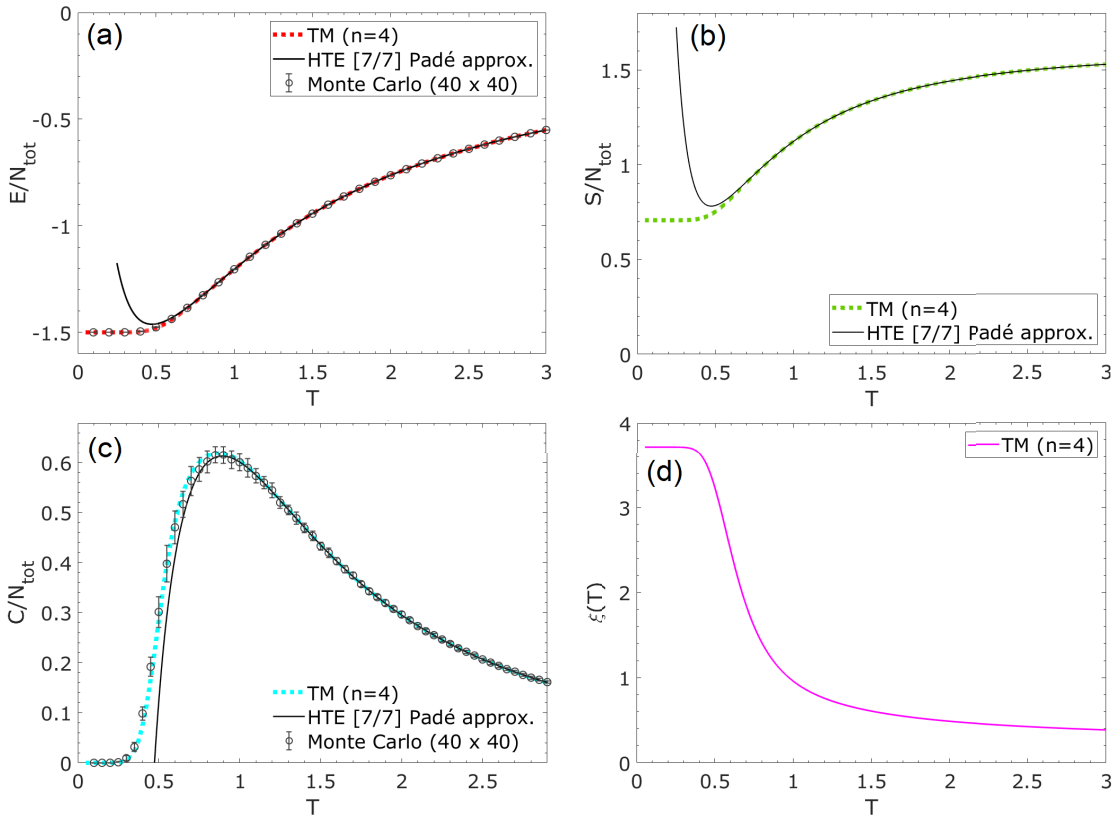

FIGURE 6.5. The $S = 2$ ferromagnetic model ($J < 0$): TM, HTE and Monte Carlo results are shown for (a) energy per site, (b) entropy per site, (c) specific heat per site, and (d) correlation length, as a function of temperature. TM results are shown for a system $n = 4$ sites wide, and HTE data are extrapolated using a Padé approximant of order $[7, 7]$. Monte Carlo data are shown for lattices of size 40×40.

6.5.3. Ground state entropy for the spin-2 ferromagnetic model

For the spin-2 case, we know that there are five states at each site in which $(\tau^x, \tau^y, \tau^z) = (1, -1, -1)$, $(-1, 1, -1)$, $(-1, -1, 1)$, $(1, 1, 1)$, and $(1, 1, 1)$ in a suitably defined basis. Note that there are two states both of which have $(\tau^x, \tau^y, \tau^z) = (1, 1, 1)$. For the ferromagnetic model, a state in which all sites have $(1, 1, 1)$ is clearly a ground state. Since this can happen in two possible ways at each site, we see that the number of ground states be at least as large as 2^N, for an N-site system. Hence the ferromagnetic model will have a ground state entropy per site which is at least as large as $\ln 2 \simeq 0.693$. We will now argue that the entropy per site is a little larger than this value.

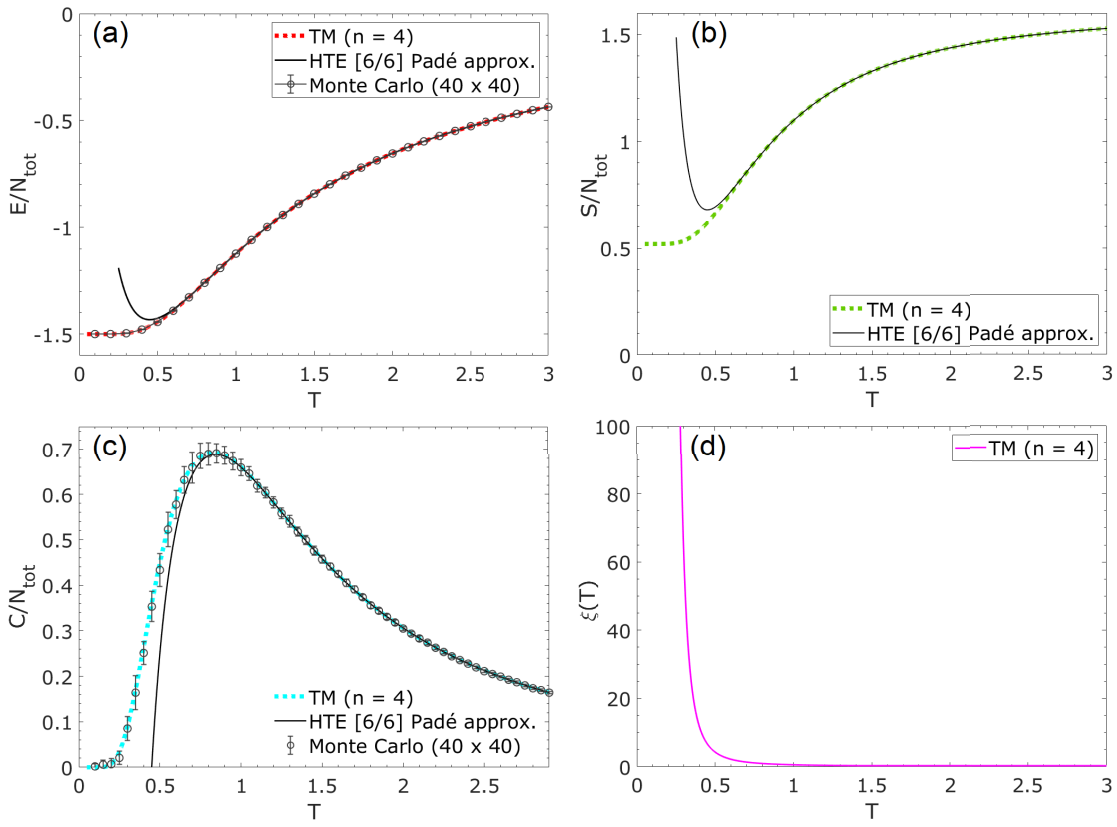

FIGURE 6.6. The $S = 2$ antiferromagnetic model ($J > 0$): TM, HTE, and Monte Carlo results are shown for (a) energy per site, (b) entropy per site, (c) specific heat per site and (d) correlation length, as a function of temperature. TM results are shown for a system $n = 4$ sites wide and HTE data are extrapolated using a Padé approximant of order $[6, 6]$. Monte Carlo data are shown for lattices of size 40×40.

Starting with one of the ground states in which all sites have $(1, 1, 1)$, suppose that we replace the states for the six sites in a particular hexagon by $(1, -1, -1)$, in which the values -1 are along the bonds going around the hexagon while the value 1 is along the bond which is directed away from the hexagon. This gives another ground state since a bond which has -1 at both ends is satisfied for a ferromagnetic interaction. The number of such states is, however, less than 2^N by a factor of 2^6, since we now have only one possible state (instead of two) at each of the sites in that hexagon. Next, let the number of such hexagons where this replacement is made be n, where n can go from zero to a maximum of $N/2$ (which is the number of hexagons for an N-site system). Actually, n should be much less than $N/2$ since we cannot make such a replacements in two neighboring hexagons; we will see below that indeed $n \ll N/2$, so that two such hexagons are unlikely to be

neighbors of each other. The number of ways n hexagons can be chosen out of $N/2$ is given by ${}^{N/2}C_n$. Hence the ground-state partition function is given by

$$Z \;=\; 2^N \sum_{n=0,1,\cdots} \frac{1}{2^{6n}}\, {}^{N/2}C_n. \tag{6.26}$$

Introducing the variable $p = n/(N/2)$, we can rewrite Eq. (6.26) as

$$Z = 2^N \int_0^1 dp\; \exp\Big[-\frac{pN}{2}\ln(2^6) \;+\; \frac{N}{2}\ln\frac{N}{2} \;-\; \frac{pN}{2}\ln\frac{pN}{2} \;-\; \frac{(1-p)N}{2}\ln\frac{(1-p)N}{2}\Big], \tag{6.27}$$

where we have used Stirling's formula for the factorial functions. We now find the maximum of the terms in the exponential in Eq. (6.27) as a function of p. This gives the condition

$$\frac{p}{1-p} \;=\; \frac{1}{2^6}. \tag{6.28}$$

Since $1/2^6 \ll 1$, this gives $p = 1/2^6$ to a good approximation. Substituting this back in Eq. (6.27), we find that

$$Z \;=\; \exp\big[N(\ln 2 \;+\; 1/2^7)\big]. \tag{6.29}$$

Hence the entropy per site is $\ln 2 + 1/2^7 \;\simeq\; 0.701$, which lies below the value of 0.707 found numerically.

The above argument was based on taking a closed loop and changing the states for each site of that loop from $(1,1,1)$ to $(1,-1,-1)$. The smallest possible closed loop forms a hexagon and this is what was assumed above. The next larger closed loop involves ten sites covering two neighboring hexagons. A similar argument as above will then give an additional contribution of $1/2^{11} \simeq 0.0005$ to the entropy per site. Larger loops will give additional contributions; however, these contributions will rapidly approach zero since a closed loop with m sites will contribute $1/2^{m+1}$. We have therefore only discussed here the contribution from the smallest closed loop which has $m = 6$.

6.5.4. Measurement of Z_2 Flux through a hexagonal plaquette

Our Monte Carlo simulations also allow us to study the thermodynamic behavior of the Z_2 flux variable defined in Eq. (6.2), which we perform on lattices of up to 40×40 sites with periodic boundary conditions. In Fig. 6.7, we show the temperature dependence of the mean flux $\langle W_p \rangle$

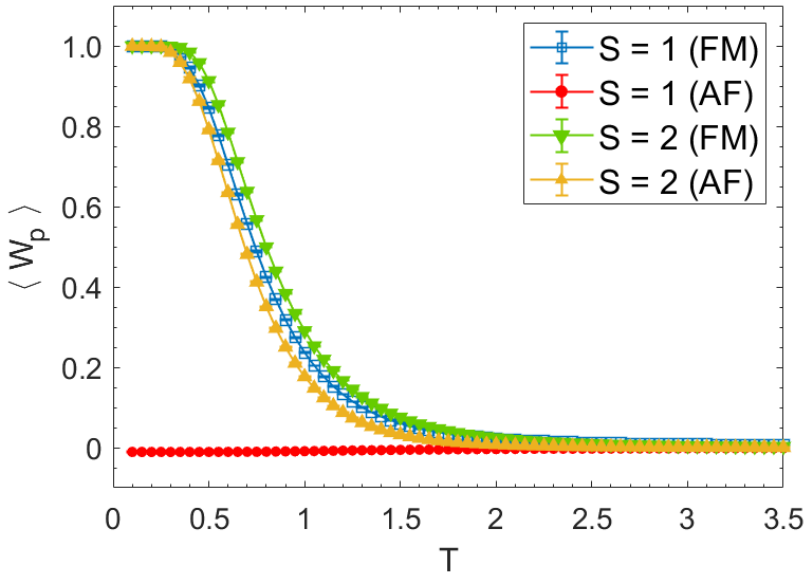

FIGURE 6.7. The mean flux per hexagonal plaquette $\langle W_p \rangle$ as defined in Eq. (6.20) is plotted as a function of temperature for the $S = 1$ ferromagnetic, $S = 1$ antiferromagnetic, $S = 2$ ferromagnetic, and $S = 2$ antiferromagnetic models. The results are obtained from Monte Carlo simulations on lattices of size 40×40.

through a hexagonal plaquette of the honeycomb lattice, for both the ferromagnetic and antiferromagnetic $S = 1$ and $S = 2$ models. In all cases, $\langle W_p \rangle \to 0$ as $T \to \infty$ as expected, since if the states at each site occur with equal likelihood, then fluxes of $+1$ and -1 occur with equal probability throughout the lattice. For the $S = 1$ ferromagnetic case, and both the $S = 2$ ferromagnetic and antiferromagnetic cases, we have seen that the ground-state energy per site is $-3/2$. As discussed in Sec. 6.3.2, this implies that the flux per hexagon must become $+1$. For these cases, we indeed find that the mean flux saturates at this value for around $T \lesssim 0.5$, which corresponds to the temperature at which the ground-state energy is attained. Moreover, in these cases, the temperature at which $\langle W_p \rangle$ grows rapidly ($T \approx 1$) coincides with the peak in specific heat, which resembles the original spin-1 Kitaev model with ferromagnetic interactions [**152**]. In contrast, the $S = 1$ antiferromagnetic model, which has a ground-state energy per site of $-1/2$, does not exhibit a crossover to $\langle W_p \rangle = 1$. Instead the mean flux remains approximately zero as the temperature is lowered. This shows that frustration can lead to a degenerate manifold, where flux variables can fluctuate strongly even as $T \to 0$.

Model	n	S_0/N_{tot}	E_{GS}/N_{tot}	$\xi_{(T\to 0)}$
$S=1$ (FM)	4	0.183	-1.5	3.974
$S=1$ (FM)	6	0.171	-1.5	6.166
$S=1$ (FM)	8	0.167	-1.5	8.452
$S=2$ (FM)	4	0.707	-1.5	3.718
$S=1$ (AF)	4	0.837	-0.5	0.846
$S=1$ (AF)	6	0.837	-0.5	0.848
$S=1$ (AF)	8	0.837	-0.5	0.848
$S=2$ (AF)	4	0.520	-1.5	Diverges

TABLE 6.1. Transfer matrix results for the $S=1$ and $S=2$ models, for both the ferromagnetic (FM) and antiferromagnetic (AF) cases. The residual entropy S_0 and ground state energy E_{GS} per site are given for each system width n studied. The low-temperature limit of the state-state correlation length is denoted $\xi_{(T\to 0)}$.

6.6. Conclusions

In this chapter we have studied the properties of a modified Kitaev model introduced by BSS [19] for integer spins. There is a fundamental differences between half-integer and integer spin cases: for half-integer spins, the modified model is equivalent to many copies of the original spin-1/2 Kitaev model. For example, for $S=3/2$, the 4^N-dimensional Hilbert space decomposes into 2^N copies of 2^N-dimensional Hilbert spaces, each representing a spin-half Kitaev model. Consequently, the partition function for the $S=3/2$ modified Kitaev model (and for half-integer spin in general) is equal to the partition function for the original $S=1/2$ Kitaev model multiplied by a constant. Thermodynamic quantities such as specific heat are therefore identical, with the entropy differing by just an additive temperature independent constant. But for integer spins, the eigenstates of our modified Kitaev model can be chosen to be a product state from site to site with no entanglement. The large degeneracy of these models, which we have explored in this work through examinations of the residual entropy, thus allows for the possibility of constructing entangled states through a superposition of the many degenerate states.

Residual entropy plateaus at intermediate temperatures are a generic feature of highly frustrated systems including the Kitaev systems and their experimental realizations [150, 153, 165, 187, 188, 189, 190, 191]. These represent a classical spin-liquid state [134], with a highly degenerate manifold

of configurations, which is a precursor to the quantum selection that leads to the quantum spin-liquid at still lower temperatures. Thus, the modified Kitaev models allow us to study such an intermediate temperature behavior with many variations. Since the integer-S modified Kitaev models do not have quantum fluctuations, they are, however, missing the physics of ground-state selection and quantum mechanical excitations.

Our study highlights that the modified Kitaev models do not just have a difference between half-integer and integer-spin cases. While all the half-integer models are closely related, within the integer spin models we find a rich variety of behaviors, which depends on the spin value and also on whether the coupling is ferromagnetic or antiferromagnetic. There are striking differences in their thermodynamic properties, which we have summarized in Table 6.1. In particular, the ferromagnetic models appear critical as $T \to 0$ in the two-dimensional thermodynamic limit, with transfer matrix results indicating a correlation length scaling with the system width. Our Monte Carlo simulations identify that this diverging correlation length corresponds to state-state correlation functions. In contrast to the ferromagnetic case, for the antiferromagnetic models, the correlations remain short-ranged as $T \to 0$ for $S = 1$, whereas they diverge exponentially fast for $S = 2$. This suggests that there may be an order-disorder transition at $T = 0$ for antiferromagnetic models, if we regard spin as a continuous variable, between $S = 1$ and $S = 2$.

For all but the $S = 1$ antiferromagnetic case, every bond contributes the minimum allowed energy in the ground state. With the absence of frustration in this sense, we can rigorously show that the average flux through a hexagonal plaquette goes to $\langle W_p \rangle = 1$ as $T \to 0$. This is confirmed by the Monte Carlo simulations. Similar result is known to hold for the spin-one Kitaev model with ferromagnetic interactions. The spin-1 antiferromagnet, however, is more strongly frustrated than others. In this case, all bonds do not contribute minimum possible energy of -1 to the ground state and, indeed, we find in the simulations, that the average flux through a plaquette remains close to zero even as $T \to 0$. This latter result remains to be explained analytically.

The residual entropy per site, in the models, differs for each of the integer-spin models studied. We have provided analytical insights into the residual entropy values for the two ferromagnetic cases. For the antiferromagnetic models, one can provide bounds to the residual entropies, but their exact values have not been explained. For the spin-S Kitaev models, we have given analytical

arguments why the residual entropy is $S_{max}/2$, in agreement with previous numerical results [164]. When additional terms are added to higher spin Kitaev Hamiltonian [155], there is numerical evidence that there may still be a residual entropy, but it may not have a simple value as in the pure Kitaev case.

Finally, we note that although the modified Kitaev models are not expected to describe real materials because of the special nature of the spin-spin interactions, they are motivated by a large body of current work exploring models with bond-dependent interactions. Also, their thermodynamic behavior shares features with spin-S Kitaev models at intermediate temperatures. Indeed, a double peaked structure in the heat capacity and a plateau-like feature in the entropy with varying values are being discussed as experimental signatures of Kitaev physics [150, 187, 189]. We hope that our study provides further motivation to examine higher spin Kitaev materials with both ferromagnetic and antiferromagnetic interactions [18, 182], which this model illustrates can exhibit quite distinct thermodynamic behaviors.

6.7. Appendix: Simultaneous diagonalization of the operators τ^α

For integer spins, the operators $\tau^\alpha = e^{i\pi S^\alpha}$ ($\alpha = x, y, z$) commute with each other and thus can be simultaneously diagonalized. In this section, we show that for $S = 1$ the diagonalized tau operators yield three possible states per site, which have $(\tau_x, \tau_y, \tau_z) = (1, -1, -1)$, $(-1, 1, -1)$, and $(-1, -1, 1)$. We will also show that for $S = 2$ there are five possible states per site, which have $(\tau^x, \tau^y, \tau^z) = (-1, -1, 1)$, $(-1, 1, -1)$, $(1, 1, 1)$, $(1, -1, -1)$, and $(1, 1, 1)$. Working in the S_z basis, one may exponentiate the spin matrices for $S = 1$ to obtain

$$e^{i\pi S_x} = \exp\left[i\pi \frac{1}{\sqrt{2}} \begin{pmatrix} 0 & 1 & 0 \\ 1 & 0 & 1 \\ 0 & 1 & 0 \end{pmatrix} \right] = \begin{pmatrix} 0 & 0 & -1 \\ 0 & -1 & 0 \\ -1 & 0 & 0 \end{pmatrix} \equiv A, \tag{6.30}$$

$$e^{i\pi S_y} = \exp\left[i\pi \frac{1}{\sqrt{2}i} \begin{pmatrix} 0 & 1 & 0 \\ -1 & 0 & 1 \\ 0 & -1 & 0 \end{pmatrix} \right] = \begin{pmatrix} 0 & 0 & 1 \\ 0 & -1 & 0 \\ 1 & 0 & 0 \end{pmatrix} \equiv B, \tag{6.31}$$

$$e^{i\pi S_z} = \exp\left[i\pi \begin{pmatrix} 1 & 0 & 0 \\ 0 & 0 & 0 \\ 0 & 0 & -1 \end{pmatrix} \right] = \begin{pmatrix} -1 & 0 & 0 \\ 0 & 1 & 0 \\ 0 & 0 & -1 \end{pmatrix} \equiv C. \tag{6.32}$$

Let

$$V = \begin{pmatrix} 1 & 0 & -1 \\ 0 & 1 & 0 \\ 1 & 0 & 1 \end{pmatrix}, \quad V^{-1} = \begin{pmatrix} \frac{1}{2} & 0 & \frac{1}{2} \\ 0 & 1 & 0 \\ -\frac{1}{2} & 0 & \frac{1}{2} \end{pmatrix}. \tag{6.33}$$

Then $V^{-1}AV$, $V^{-1}BV$, and $V^{-1}CV$ are all diagonal, i.e., {A,B,C} are simultaneously diagonalizable,

$$V^{-1}AV = \begin{pmatrix} -1 & 0 & 0 \\ 0 & -1 & 0 \\ 0 & 0 & 1 \end{pmatrix}, \tag{6.34}$$

$$V^{-1}BV = \begin{pmatrix} 1 & 0 & 0 \\ 0 & -1 & 0 \\ 0 & 0 & -1 \end{pmatrix}, \tag{6.35}$$

$$V^{-1}CV = \begin{pmatrix} -1 & 0 & 0 \\ 0 & 1 & 0 \\ 0 & 0 & -1 \end{pmatrix}. \tag{6.36}$$

The diagonal elements of $V^{-1}AV$, $V^{-1}BV$, and $V^{-1}CV$ yield the three states described previously (labeled $\sigma = \{1, 2, 3\}$ below)

$$\langle 1|\tau_x|1\rangle = -1, \quad \langle 1|\tau_y|1\rangle = 1, \quad \langle 1|\tau_z|1\rangle = -1, \tag{6.37}$$

$$\langle 2|\tau_x|2\rangle = -1, \quad \langle 2|\tau_y|2\rangle = -1, \quad \langle 2|\tau_z|2\rangle = 1, \tag{6.38}$$

$$\langle 3|\tau_x|3\rangle = 1, \quad \langle 3|\tau_y|3\rangle = -1, \quad \langle 3|\tau_z|3\rangle = -1. \tag{6.39}$$

Hence for $S = 1$ there are three possible states per site, which have $(\tau^x, \tau^y, \tau^z) = (1, -1, -1)$, $(-1, 1, -1)$, and $(-1, -1, 1)$. Again working in the S_z basis, one can similarly exponentiate the spin matrices for $S = 2$ to obtain $e^{i\pi S_x} \equiv A$, $e^{i\pi S_y} \equiv B$, and $e^{i\pi S_z} \equiv C$, which are now 5×5 matrices. Then one can construct the following matrix V such that $V^{-1}AV$, $V^{-1}BV$, and $V^{-1}CV$ are all

diagonal,

$$V = \begin{pmatrix} -1 & 0 & 1 & 0 & 0 \\ 0 & -1 & 0 & 1 & 0 \\ 0 & 0 & 0 & 0 & 1 \\ 0 & 1 & 0 & 1 & 0 \\ 1 & 0 & 1 & 0 & 0 \end{pmatrix}, \quad V^{-1} = \begin{pmatrix} -1 & 0 & 1 & 0 & 0 \\ 0 & -1 & 0 & 1 & 0 \\ 0 & 0 & 0 & 0 & 1 \\ 0 & 1 & 0 & 1 & 0 \\ 1 & 0 & 1 & 0 & 0 \end{pmatrix}. \tag{6.40}$$

Hence {A,B,C} are simultaneously diagonalizable,

$$V^{-1}AV = \begin{pmatrix} -1 & 0 & 0 & 0 & 0 \\ 0 & -1 & 0 & 0 & 0 \\ 0 & 0 & 1 & 0 & 0 \\ 0 & 0 & 0 & 1 & 0 \\ 0 & 0 & 0 & 0 & 1 \end{pmatrix}, \tag{6.41}$$

$$V^{-1}BV = \begin{pmatrix} -1 & 0 & 0 & 0 & 0 \\ 0 & 1 & 0 & 0 & 0 \\ 0 & 0 & 1 & 0 & 0 \\ 0 & 0 & 0 & -1 & 0 \\ 0 & 0 & 0 & 0 & 1 \end{pmatrix}, \tag{6.42}$$

$$V^{-1}CV = \begin{pmatrix} 1 & 0 & 0 & 0 & 0 \\ 0 & -1 & 0 & 0 & 0 \\ 0 & 0 & 1 & 0 & 0 \\ 0 & 0 & 0 & -1 & 0 \\ 0 & 0 & 0 & 0 & 1 \end{pmatrix}. \tag{6.43}$$

As before, the diagonal elements of $V^{-1}AV$, $V^{-1}BV$, and $V^{-1}CV$ give the following states:

$$\langle 1|\tau_x|1\rangle = -1, \quad \langle 1|\tau_y|1\rangle = -1, \quad \langle 1|\tau_z|1\rangle = 1 \tag{6.44}$$

$$\langle 2|\tau_x|2\rangle = -1, \quad \langle 2|\tau_y|2\rangle = 1, \quad \langle 2|\tau_z|2\rangle = -1, \tag{6.45}$$

$$\langle 3|\tau_x|3\rangle = 1, \quad \langle 3|\tau_y|3\rangle = 1, \quad \langle 3|\tau_z|3\rangle = 1, \tag{6.46}$$

$$\langle 4|\tau_x|4\rangle = 1, \quad \langle 4|\tau_y|4\rangle = -1, \quad \langle 4|\tau_z|4\rangle = -1, \tag{6.47}$$

$$\langle 5|\tau_x|5\rangle = 1, \quad \langle 5|\tau_y|5\rangle = 1, \quad \langle 5|\tau_z|5\rangle = 1. \tag{6.48}$$

We therefore see that for $S = 2$ there are five possible states per site, which have $(\tau^x, \tau^y, \tau^z) = (-1, -1, 1)$, $(-1, 1, -1)$, $(1, 1, 1)$, $(1, -1, -1)$, and $(1, 1, 1)$.

6.8. Appendix: Argument for zero modes from spin wave theory

In this section, we will study the large-S limit of the Kitaev model defined on a honeycomb lattice [19]. We will consider a classical spin configuration and compute the spin-wave excitations around that configuration.

We consider a closed loop formed by a string of bonds. Each bond consists of nearest-neighbor spins at sites m and n which interact with each other through a term of the form $S_m^a S_n^a$, where a can be x, y, or z; the value of a must necessarily be different for two successive bonds along the loop. Any closed loop must have an even number of sites which alternately lie on the A and B sublattices of the system.

Given that the nearest-neighbor couplings $S_m^a S_n^a$ involve different values of a for successive bonds, we can perform a unitary transformation to make $a = x, y, x, y, \cdots, x, y$ as we go around the closed loop. Given a loop formed by $2N$ sites, there are N unit cells which are labeled as j, and each unit cell has two sites labeled as $(j, 1)$ and $(j, 2)$. If the sites have spin-S, the Hamiltonian for the loop is given by

$$H = \frac{J}{S} \sum_{j=1}^{N} (S_{j,1}^x S_{j,2}^x + S_{j,2}^y S_{j+1,1}^y), \tag{6.49}$$

and we have a periodic boundary condition for i. We assume that $J > 0$. (If $J < 0$, we can change its sign by performing a unitary rotation which flips the signs of $S_{j,1}^x$, $S_{j,1}^z$, $S_{j,2}^y$, and $S_{j,2}^z$ for all values of j). A factor of $1/S$ has been introduced in Eq. (6.49) so that the ground-state energy is proportional to S in the limit $S \to \infty$.

We will now use the Holstein-Primakoff (HP) transformation [192, 193, 194] to compute the spin-wave spectrum for a closed loop. We assume that the classical spin configuration is such that the spin at a site n lying on the loop points along either the direction $+\hat{a}$ or $-\hat{a}$, where $\hat{a}$ is different from the directions of the interactions of that site with its two nearest neighbors along the loop.

For instance, if site n interacts with site $n-1$ with an interaction $S_n^x S_{n-1}^x$ and with site $n+1$ with interaction $S_n^y S_{n+1}^y$, then classically the spin at site n is given by $\vec{S}_n = \pm S\hat{z}$. Let us now consider these two cases separately.

(i) If the spin at site n points along the $\hat{z}$ direction, then we have $S_n^z = S - (p_n^2 + q_n^2 - 1)/2$, and (S_n^x, S_n^y) can be chosen in four different ways, namely, $\sqrt{S}(q_n, p_n)$, $\sqrt{S}(-q_n, -p_n)$, $\sqrt{S}(p_n, -q_n)$, and $\sqrt{S}(-p_n, q_n)$, up to the lowest order in the HP transformation. Here q_n and p_n are canonically conjugate variables which satisfy the commutation relation $[q_n, p_n] = i$.

(ii) If the spin points along the $-\hat{z}$ direction, then we have $S_n^z = -S + (p_n^2 + q_n^2 - 1)/2$, and (S^x, S^y) can be chosen in four ways, namely, $\sqrt{S}(p_n, q_n)$, $\sqrt{S}(-p_n, -q_n)$, $\sqrt{S}(q_n, -p_n)$ and $\sqrt{S}(-q_n, p_n)$.

We now compute the spin-wave spectrum for a closed loop with $2N$ sites. (The minimum value of $2N$ is 6 corresponding to a hexagon). As we go around the loop, we choose the spin variables along the loops to be q and p alternately, so that the couplings between nearest neighbors involve either (q_m, q_n) or (p_m, p_n) but not (q_m, p_n). Because of the two cases (i) and (ii) discussed above, the loop may have either periodic boundary condition (PBC) or antiperiodic boundary condition (ABC) depending on the set of classical spin directions $\vec{S}_n$ as we go around the loop. Ignoring some constants, we find the spin-wave Hamiltonian for the loop to be

$$\begin{aligned} H_{sw} &= \frac{J}{2} \sum_{n=1}^{2N} (p_n^2 + q_n^2) \\ &\quad + J \sum_{n=1}^{N-1} (p_{2n-1} p_{2n} + q_{2n} q_{2n+1}) \\ &\quad + J\, (p_{2N-1} p_{2N} \pm q_{2N} q_1), \end{aligned} \tag{6.50}$$

with either PBC or ABC for the last bond connecting sites $2N$ and 1; the sign of term $q_{2N}q_1$ term is $+$ and $-$ in the two cases, respectively. Solving for the spectrum, we find that the normal modes can be characterized by a momentum k, where $k = 0,\ 2\pi/N,\ \cdots,\ (2\pi N - 2\pi)/N$ in the case of PBC, and $k = \pi/N,\ 3\pi/N,\ \cdots,\ (2\pi N - \pi)/N$ in the case of ABC; in each case, k can take N different values. We now find the normal mode frequencies by solving the classical Hamiltonian equations of motion. (For a quadratic Hamiltonian, the frequencies turn out to be the same regardless of whether we study the problem classically or quantum mechanically). For each momentum k, we find that there are two frequencies given by 0 and $\omega_k = 2J|\cos(k/2)|$. The existence of a zero-energy

mode for each k implies a large ground-state degeneracy for the following reason. Since the total number of states of the loop is $(2S+1)^{2N}$, we can take each of the $2N$ modes to describe $2S+1$ possible states. The N zero modes therefore imply that there are $(2S+1)^N$ states all of which have zero energy and are therefore degenerate. This seems to agree well with the numerical results reported in Ref. [**164**], even for cases where S is not very large. Namely, for $S = 1, 3/2$ and 2, it is found that there is a low-energy manifold with an entropy per site given by $(1/2)\ln(2S+1)$.

CHAPTER 7

Robustness of Entropy Plateaus: A Case Study of Triangular Ising Antiferromagnets

7.1. Chapter Summary

Residual entropy is a key feature associated with emergence in many-body systems. From a variety of frustrated magnets to the onset of spin-charge separation in Hubbard models and fermion-Z_2-flux variables in Kitaev models, the freezing of one set of degrees of freedom and the establishment of local constraints are marked by a plateau in entropy as a function of temperature. Yet, with the exception of the rare-earth pyrochlore family of spin-ice materials, evidence for such plateaus is rarely seen in real materials, raising questions about their robustness. Following recent experimental findings of the absence of such plateaus in the triangular-lattice Ising antiferromagnet (TIAF) $TmMgGaO_4$ by Li et al [**195**], we explore in detail the existence and rounding of entropy plateaus in TIAF. We use a transfer matrix method to numerically calculate the properties of the system at different temperatures and magnetic fields, with further neighbor interactions and disorder. We find that temperature windows of entropy plateaus exist only when second-neighbor interactions are no more than a couple of percent of the nearest-neighbor ones, and they are also easily destroyed by disorder in the nearest-neighbor exchange variable, thereby explaining the challenge in observing such effects.

This chapter is based on the following publication [**165**]:

O. Bradley, C. Feng, R. T. Scalettar, and R. R. P. Singh, *Robustness of entropy plateaus: A case study of triangular Ising antiferromagnets*, Phys. Rev. B. **100**, 064414 (2019).

7.2. Introduction

Residual entropy is a hallmark of frustrated systems, reflecting the emergence of local constraints or new degrees of freedom distinct from the microscopic ones [134]. One of the earliest theoretical works in this direction was the calculation of residual entropy associated with the establishment of ice rules in water done by Pauling [196]. It is now well established that such a strongly constrained phase has an analog in magnetic systems known as spin-ice [197, 198, 199, 200]. Such a classical spin-liquid exhibits residual entropy [201, 202, 203] and supports magnetic-monopole excitations. Quantum fluctuations in such a system can lead to a highly resonating quantum spin-liquid phase with emergent quantum electrodynamics.

In models of geometrically frustrated magnets, such residual entropy is widespread [204]. But, how robust are they in real materials? In fact, the issue is much broader than geometric frustration. In recent years, there has been a lot of interest in Kitaev materials [144, 147, 205, 206, 207]. At a microscopic level, the honeycomb-lattice Kitaev model describes spins interacting with anisotropic bond-direction dependent exchange interactions [16]. Yet, the model can be exactly mapped onto one of Majorana fermions and Z_2-valued fluxes. As the fermions reach their degeneracy temperature or freeze-out if they have a gapped spectrum, an entropy plateau sets in [191, 208]. Indeed, some hints of entropy plateaus have been seen in experiments [209, 210]. The plateaus are far more robust than the soluble models. For example, spin-S models show even more interesting possibilities of entropy plateaus [19, 152, 164, 178]. When Kitaev couplings are the same along all three axes, there are incipient plateaus at an entropy of $\ln(2S+1)/2$, which keeps increasing with spin S. The physical mechanism behind such large entropy values at the plateau with increasing S is not well understood.

Entropy plateaus are also a prominent feature of correlated electron Hamiltonians such as the Hubbard and periodic Anderson models [211, 212, 213]. In the regime of strong on-site interaction U, there are clearly distinct charge and spin energy scales. At the higher scale, $T \sim U$, a drop in entropy occurs when doubly occupied sites are frozen out. At the lower scale, $T \sim J = 4t^2/U$, a second drop occurs that is associated with the development of antiferromagnetic (AF) correlations. Studies of the specific heat $C(T)$ in one dimension [214, 215, 216], and in infinite dimensions, i.e. within dynamical mean field theory (DMFT) [217, 218, 219], suggested the disappearance of

an entropy plateau as $U \to t$, and hence the two energy scales merge. However, quantum Monte Carlo calculations for the half-filled Hubbard model on a two-dimensional square lattice revealed that the two peak structure in $C(T)$ is robust, surviving even down to $U \sim t$. An interesting feature of this robustness was an apparent interchange in the "driving force" of the entropy reduction. At strong U, changes in the *potential energy* led to the high-T specific heat peak, while at small U, it is the changes in the *kinetic energy* that yields the peak at higher temperature.

Preservation of the entropy plateaus, in these systems, appears to be linked to the AF order. On a honeycomb lattice [220], the two peaks in $C(T)$ merge as U is reduced, with a resultant destruction of the plateau. The most natural explanation is that, unlike the square lattice where antiferromagnetism exists down to $U = 0$, the honeycomb lattice has a quantum critical point $U_c/t \sim 4$, below which antiferromagnetism disappears [213, 221].

The Ising antiferromagnet on the triangular lattice is an iconic problem in frustrated magnetism where an exact residual ground state entropy was first calculated by Wannier [13, 14]. Several materials, including $CeCd_3As_3$ [222], FeI_2 [223], and $TmMgGaO_4$ [195, 224], have been identified experimentally as triangular-lattice Ising antiferromagnet (TIAF) systems owing to the strong Ising nature of their constituent spins. Despite being of such central interest, there are few (or no) experimental systems where such residual entropy has been observed. Very recently, Li et al [195] investigated the triangular-lattice Ising antiferromagnetic material $TmMgGaO_4$. They measured the heat capacity and entropy of the system as well as the magnetization as a function of an applied magnetic field. Li et al found a complete absence of entropy plateaus and rounded magnetization plateaus, with roundings that are only partly thermal and partly reflect the presence of quenched impurities.

The TIAF has been studied over the years using a variety of analytical and numerical methods. Such studies have determined the phase diagram, minimum energy spin configurations, as well as entropy and specific heat curves for finite size clusters [225, 226, 227, 228, 229, 230]. Several numerical studies of disordered TIAF (and ferromagnetic) systems have also been performed, including investigations of random site vacancies, diluted lattices, varying bond lengths, and disorder in the applied field [231, 232, 233].

The purpose of this paper is to explore the rounding or absence of entropy and magnetization plateaus in the TIAF as a function of applied field due to further neighbor interactions and disorder. How large a perturbation can the system tolerate before the plateaus disappear altogether? We use a numerical transfer matrix based approach to calculate the thermodynamic properties. We first confirm that, in the absence of second neighbor interactions, the magnetization of the pure TIAF jumps from 0 to 1/3 in an infinitesimal field, and then at a field of $B = 6$ it jumps again to full saturation value. The transition field $B = 6$ also has a finite ground-state entropy.

We next consider antiferromagnetic second-neighbor interactions, as appropriate for the $TmMgGaO_4$ material. This interaction is shown to lead to a striped ground-state phase and a finite-temperature phase transition. The entropy plateaus are lost rapidly with a fairly small second-neighbor interaction of only a few percent. They are replaced by sharp drops in the entropy at a first-order transition. This is in contrast to the spin-ice system, where the entropy plateaus are very robust and survive even with long-range dipolar interactions [**197**, **198**, **199**, **200**] and quantum fluctuations [**234**, **235**]. If we consider only the nearest-neighbor TIAF with disorder in the exchange interactions, rounded entropy plateaus are quickly destroyed.

When the second-neighbor interaction is about 10% of the nearest-neighbor value, there are magnetization plateaus at values 0, 1/3, 1/2, and 1. Thermal rounding of the magnetization plateaus is very gradual. Despite the finite temperature, the plateaus remain extremely flat, reflecting the energy gap in the system. The rounding is much stronger with quenched disorder. We find that strong disorder is needed to obtain results that look quantitatively like the experiments, with both plateaus at magnetizations of 1/3 and 1/2 becoming significantly rounded.

The outline of this chapter is as follows: First, an overview of the model and the numerical methods is given. We then present entropy $S(T)$ and specific heat $C(T)$ results for the TIAF system with no magnetic field present, in the absence of any disorder, for various strengths of the second nearest-neighbor interaction J_2. Disorder in the nearest-neighbor interaction J_1 is then introduced and we study its influence on entropy plateaus in the TIAF. We then show the influence of an applied magnetic field on the form of $S(T)$ and $C(T)$, and we present magnetization curves for various temperatures and J_2 values. Our final set of results shows the effect of quenched disorder

in both J_1 and J_2 on the magnetization plateaus observed in the TIAF. Two disorder types—box and Gaussian—are compared. We finally present our conclusions.

7.3. Model and Methods

We study a triangular lattice of Ising spins. Both nearest-neighbor (NN) and next-nearest-neighbor (NNN) interactions are considered in an applied magnetic field B, perpendicular to the plane of the lattice. The Hamiltonian studied is thus given by,

$$H = -J_1 \sum_{\langle i,j \rangle} S_i S_j - J_2 \sum_{\langle\langle i,j \rangle\rangle} S_i S_j - B \sum_i S_i, \tag{7.1}$$

where J_1 and J_2 denote the NN and NNN coupling strengths, respectively, and $S_i = \pm 1$ is the Ising spin at site i of the lattice, which may be aligned parallel or anti-parallel to the applied field. The first sum is taken over all pairs of NN sites, and the second is a sum over all NNN pairs. Negative values of J_1 and J_2 correspond to antiferromagnetic interactions.

We employ a transfer matrix approach to obtain values of the Helmholtz free energy $F(T, B)$ for our TIAF system, which is found from the largest eigenvalue of a suitably constructed transfer matrix. We consider a long cylinder-geometry for our calculations, which implies periodic boundary conditions in the short direction. The second neighbor interactions demand that the transfer matrix involve two rows of spins at a time. This is no longer an analytically soluble problem. It also limits the sizes of systems that can be studied. Furthermore, in order for the system to have compatibility with a three-sublattice structure of the triangular-lattice and for our results not to be artificially affected by the periodic boundary conditions in the short direction, we need to have a multiple of three spins in each row. Our results are all based on six spins in a row which requires a $2^{12} \times 2^{12}$ transfer matrix. We believe that these results should be reasonably close to the thermodynamic limit, except near phase transitions or points where the correlation length becomes large. For the nearest-neighbor Ising model in zero field, the calculated entropy curves are close, though clearly not identical, to the exact answer.

Since the TIAF with nearest and second-neighbor interactions shows a first-order phase transition over a range of parameters, with a jump in the entropy of the system [**230**], there will be large finite-size effects near the transition. In a finite system, all thermodynamic functions

must be analytic and hence no jump in entropy is possible. Instead, one would have a rounded δ-function in the heat capacity per site, whose peak for an $L \times L$ system scales as L^2 and peak-width scales as $1/L^2$. In the thermodynamic limit, this becomes a δ-function, whose integral gives a jump in the entropy, per site, at the transition.

In an $L \times \infty$ transfer-matrix calculation also the largest eigenvalue of the transfer matrix must be analytic at any finite temperature and hence there can be no jump in a thermodynamic property. The correlation length in the infinite direction must be finite (set by L) and the jump in entropy must be rounded over a range of temperatures near the transition. Since the linear dimension $L = 6$ of our study is much smaller than those studied by Monte Carlo simulations of Rastelli et al [**230**], the rounding must be over a wider temperature range. However, we would not expect the transition temperature to be strongly size dependent for a first-order transition, and our conclusions regarding rounding of entropy plateaus at low temperatures should not be affected by this behavior near the transition. Comparing our data with those of Rastelli et al will allow us to quantify this effect.

Previous Monte Carlo data [**230**] are only available for a magnitude of J_2 greater than or equal to 0.1, which pushes the first order transition temperature outside the plateau region of the nearest-neighbor model. To accurately evaluate the jump in entropy ΔS for smaller J_2, we have performed further Monte Carlo simulations on up to 96×96 lattices. At small J_2, the transition temperature is very low. The transition is strongly first order, with clear evidence for hysteresis. The internal energy jumps at the transition and ΔE are easily read off from the simulations, as is the transition temperature where the sharp change in energy occurs. At the transition, we know that the two states must have equal free energy. Thus we can get the entropy jump by using the relation $\Delta S = \Delta E/T_c$. These will also be compared with the transfer matrix calculations.

Free energies per site are found for a range of temperatures (at fixed B), and over a range of magnetic field values at fixed temperature, from which the thermodynamic properties $S(T), C(T)$, and $M(B)$ can be computed easily by taking suitable derivatives. For a triangular lattice N sites wide, with $2P$ rows of spins (i.e. there are P distinct 'blocks' of two rows, each N sites in width), the partition function is given by $Z = \sum_{s_i} e^{-\beta H}$ where H is as given in Eq. (7.1) and we take k_B equal to unity, with the sum taken over all spin configurations. The method relies on the fact that a careful construction of a particular $2^{2N} \times 2^{2N}$ matrix M allows one to write the partition function

as $Z = \sum_{S_A} M^P(S_A; S_A) = Tr[M^P]$, where S_A is shorthand for a particular configuration of $2N$ spins within a block. The partition function is thus given by

$$Z = \lambda_1^P + \lambda_2^P + \lambda_3^P \ldots, \tag{7.2}$$

where λ_i are the eigenvalues of the transfer matrix M. Taking λ_1 to be the maximum eigenvalue, we have that,

$$Z = \lambda_1^P \left[1 + \left(\frac{\lambda_2}{\lambda_1}\right)^P + \left(\frac{\lambda_3}{\lambda_1}\right)^P + \ldots\right], \tag{7.3}$$

and so in the limit $P \to \infty$ (i.e. for a semi-infinite triangular lattice) we have that $Z = \lambda_1^P$. The free energy is found via $F = -T \ln Z = -T \ln\left(\lambda_1^P\right) = -TP \ln(\lambda_1)$. Since the total number of sites is $N_{tot} = 2P \times N$, the free energy per site is given by

$$f = \frac{F}{N_{tot}} = \frac{-T \ln(\lambda_1)}{2N}. \tag{7.4}$$

With this method, we also investigate the influence of disorder in J_1 and J_2. To obtain the partition function when disorder is present, we instead take the trace of the product of many transfer matrices, each one using a different set of values for J_1 and J_2. We show results for which these parameters are chosen from a uniform distribution and also a Gaussian distribution.

7.4. Results and Discussion

7.4.1. Results in zero field with no disorder

The transfer matrix method outlined above was used to obtain $S(T)$ and $C(T)$ results for the TIAF in the absence of a magnetic field, with no disorder. To investigate the effect of the NNN coupling, we calculated $S(T)$ and $C(T)$ curves for a range of J_2 values including $J_2 = 0$, i.e. NN interactions only. Fig. 7.1 shows entropy per site as a function of temperature for various antiferromagnetic NNN interaction strengths: $J_2 = 0, -0.01, -0.02, -0.05, -0.10$ and -0.25 (with $J_1 = -1$). As expected, for $J_2 = 0$ (black curve) we observe a non-zero residual entropy as the temperature tends to zero, since frustration in the triangular lattice produces a degenerate ground state when only nearest neighbor interactions are present. The presence of any non-zero next-nearest neighbor interaction removes the ground state degeneracy, giving an entropy which tends

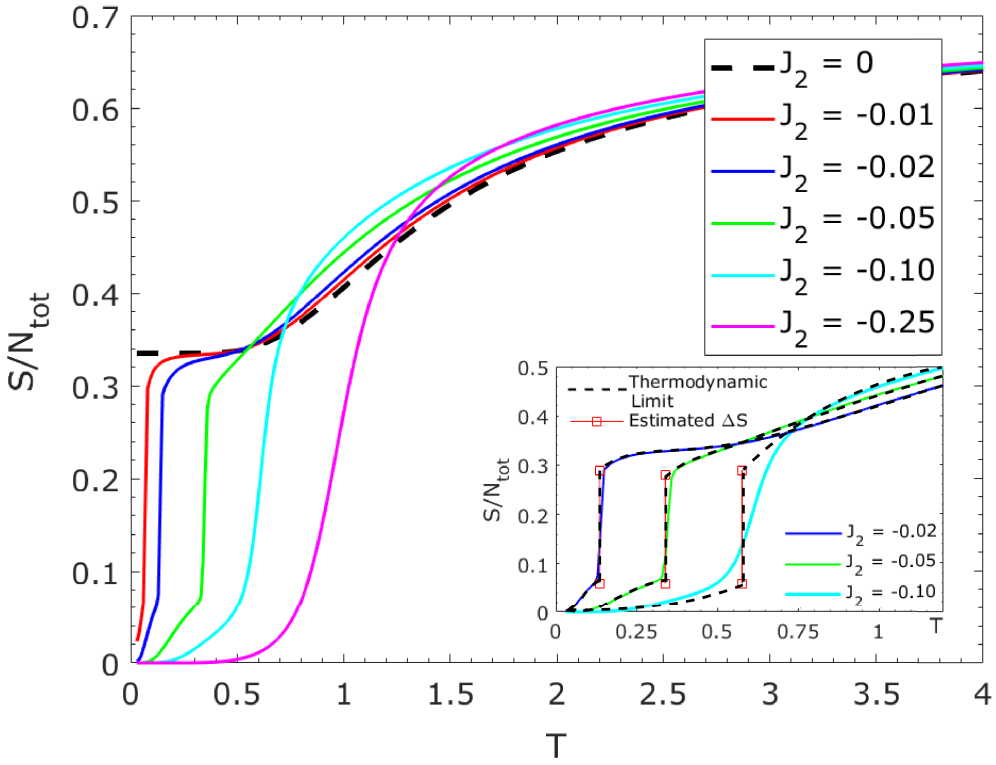

FIGURE 7.1. Entropy per site as a function of temperature for the semi-infinite TIAF geometry, calculated using the transfer matrix method. $S(T)$ curves are shown for six different values of the NNN interaction J_2, with $J_1 = -1$ fixed. At $J_2 = 0$ a residual ground state entropy is observed at zero temperature. The inset shows a comparison of our $J_2 = -0.1, -0.05$ and -0.02 entropy functions with the entropy jump expected in the thermodynamic limit. The magnitude of the jump and the transition temperatures are obtained from the hysterisis of the energy function in the Monte Carlo simulations of up to 96×96 systems.

to zero at low temperature. For small values of J_2 (e.g. $J_2 = -0.01$), a plateau in the $S(T)$ curve is observed at the value of the residual entropy for the $J_2 = 0$ case, before sharply dropping to $S = 0$ as the temperature reaches zero. As the magnitude of J_2 increases, the entropy plateau is gradually rounded, until there is no longer a plateau visible in $S(T)$ (i.e., for $|J_2| \geq 0.05$).

Finite size effects can be seen in the inset of Fig. 7.1. The entropy function can not have a jump in a finite system, instead that change in entropy will happen over a range of temperatures. The Monte Carlo study of Rastelli et al [**230**] allows us to locate the amount of the entropy jump at the transition and the transition temperature for $J_2 = -0.1$. These are indicated in the inset figure by a dashed curve. Previous Monte Carlo data [**230**] are only available for a magnitude of J_2

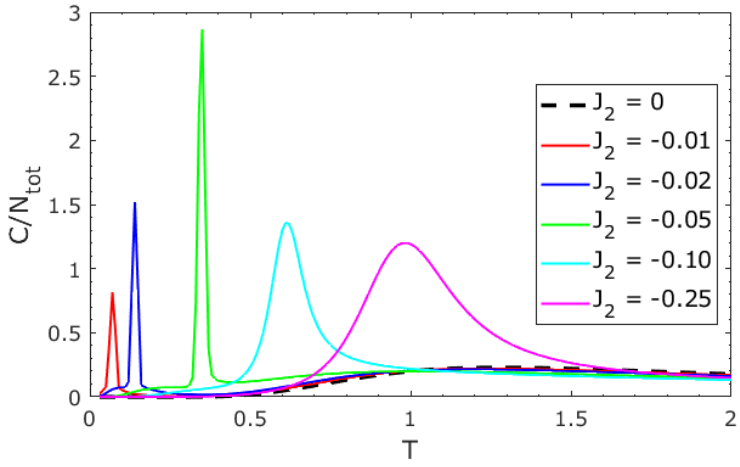

FIGURE 7.2. Specific heat as a function of temperature for six different values of J_2, obtained from our $S(T)$ calculation. Peaks in the specific heat occur at temperatures at which the corresponding $S(T)$ curve sharply drops to zero.

greater than or equal to 0.1, which pushes the first order transition temperature outside the plateau region of the nearest-neighbor model. Thus, we have developed further Monte Carlo simulations for $J_2 = -0.05$ and $J_2 = -0.02$ (and also verified the results for $J_2 = -0.1$ [**230**]) to study the entropy jump at a temperature in the plateau region of the nearest-neighbor model. These jumps are also shown in the inset. The data are consistent with the absence of an entropy plateau for $|J_2| \geq 0.05$. For $J_2 = -0.02$, we calculate an entropy jump which is consistent with the sharp change in the entropy function observed below the plateau.

The specific heat per site is found using the relation $C = T\frac{\partial S}{\partial T}$, and is shown in Fig. 7.2 for a range of J_2 values. For non-zero values of J_2, a peak in the specific heat is observed at the temperature where $S(T)$ sharply drops, indicating a transition to an ordered ground state. The $J_2 = 0$ specific heat curve (shown in black) has no peak, since ordering to a non-degenerate ground state does not occur. As the magnitude of J_2 increases, the peaks in the specific heat are shifted to higher temperature, consistent with Fig. 7.1.

The entropy and specific heat of the infinite triangular lattice (i.e. in the thermodynamic limit) were calculated exactly by Wannier [**13**, **14**]. An exact expression for $C(T)$ (with NN interactions only) for the TIAF is given in [**236**], which is plotted in Fig. 7.3. The transfer matrix result for $C(T)$ for our semi-infinite $6 \times \infty$ system is plotted for comparison, indicating our results are in

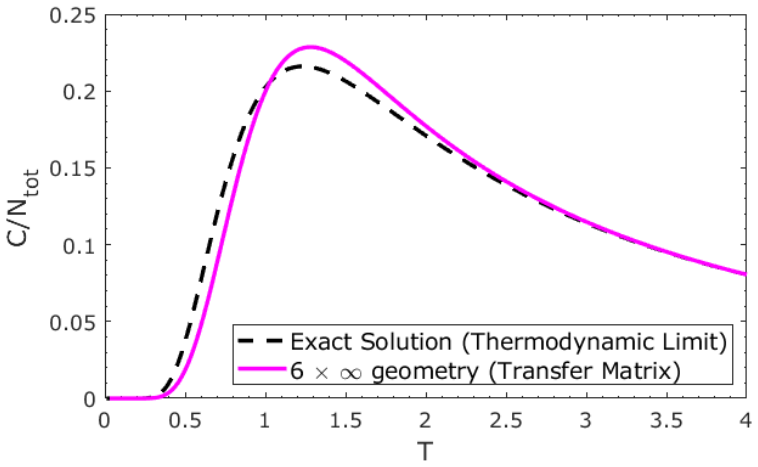

FIGURE 7.3. Comparison of $C(T)$ calculated using the transfer matrix method for our semi-infinite $6 \times \infty$ lattice with the exact result for the TIAF in the thermodynamic limit.

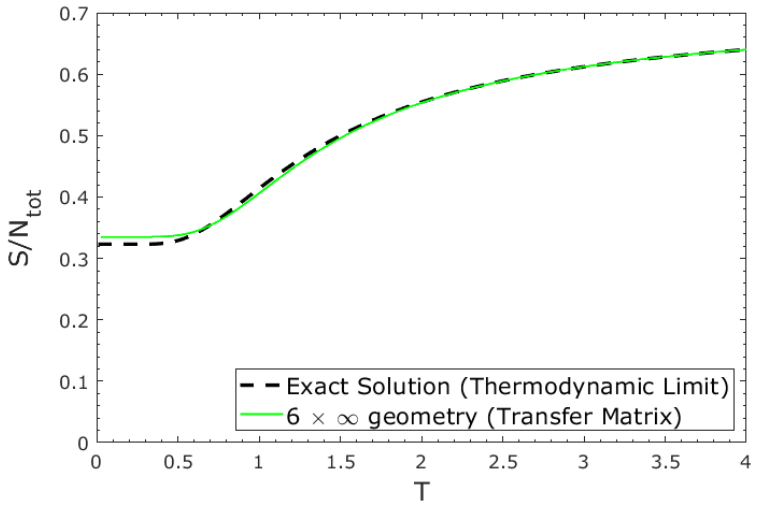

FIGURE 7.4. Comparison of $S(T)$ with the exact result in the thermodynamic limit. We obtain a residual entropy of $S(0) \approx 0.3350$ for our semi-infinite $6 \times \infty$ lattice, which is slightly greater than the exact value $S(0) \approx 0.32306$ in the thermodynamic limit.

good agreement with the exact case in the thermodynamic limit. By integrating the specific heat we also obtain the exact form of $S(T)$ in the thermodynamic limit, which is shown in Fig. 7.3. The numerical result for $S(T)$ for our semi-infinite geometry is also shown, and the agreement between the numerical and exact results is even closer than it is for specific heat. The Wannier value of the

residual entropy in the thermodynamic limit is $S(0) \approx 0.32306$ [14], and for our semi-infinite $6 \times \infty$ system we obtain $S(0) \approx 0.3350$.

7.4.2. Results in zero field with Gaussian disorder

We observe in Fig. 7.1 that in the absence of NNN interactions, $S(T)$ tends towards the residual entropy value as the temperature is reduced to zero, with a short plateau appearing at low temperature. With a non-zero J_2, we find that a plateau at the residual entropy value exists for a finite temperature window, before $S(T)$ drops to zero. As the magnitude of J_2 increases (i.e. for $|J_2| \geq 0.05$) this plateau weakens and we observe the $S(T)$ curve smoothly decreasing to zero. In order to determine the robustness of such entropy plateaus, we now consider the effect of Gaussian disorder (in the nearest-neighbor variable J_1) on the form of the $S(T)$ curve. Fig. 7.5(a) shows the effect of increasing levels of Gaussian disorder in J_1 in the absence of next-nearest-neighbor interactions. To obtain $S(T)$ values with disorder, the trace of the product of 101 transfer matrices was taken, each one containing J_1 values drawn from a Gaussian distribution for each occurrence, i.e., each individual NN coupling in the lattice has a randomly chosen interaction strength. The particular set of J_1 values used was stored and used for each temperature increment.

We label Gaussian distributions by $G(\mu, \sigma)$ where μ and σ denote the mean and standard deviation respectively. As σ is increased, the plateau at the value of the residual entropy is gradually weakened, and we eventually observe the $S(T)$ curve approaching zero with no plateau. At all temperatures, the entropy per site is lower for increasing levels of disorder, and we also find that for relatively low levels of disorder (e.g. $J_1 = G(-1, 0.02)$) an entropy plateau persists to quite low temperatures ($T \approx 0.2$). A logarithmic temperature scale emphasizes the influence of σ on the form of the entropy plateau at low values of T, as illustrated in Fig. 7.5(b). For wider distributions (i.e., $\sigma \geq 0.05$), a short plateau is no longer observed. Even in the absence of a NNN interaction, we see that the introduction of any amount of disorder in J_1 leads to a non-degenerate ground state with $S(T)$ approaching zero at $T = 0$. Moreover, the presence of weak disorder, i.e. with a standard deviation of just a few percent of the mean J_1 value, is enough to remove any sign of a plateau

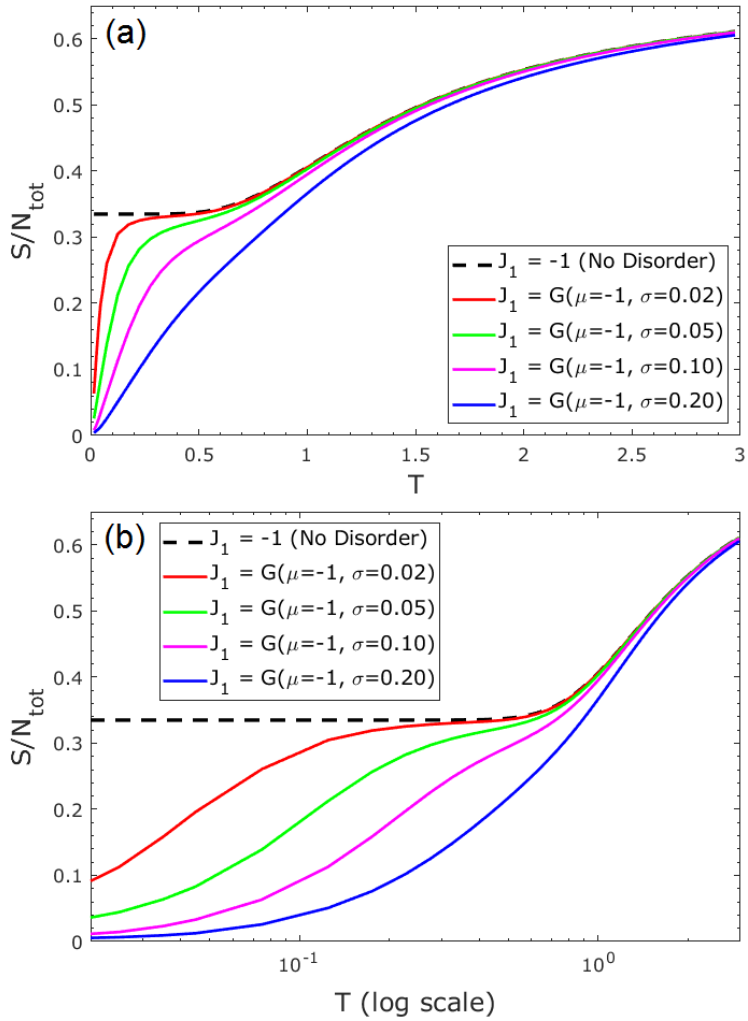

FIGURE 7.5. (a) $S(T)$ results with Gaussian disorder in J_1 are shown for various values of σ, with $J_2 = 0$. The mean of the distribution is fixed at $\mu = -1$ in each case. The entropy curve in the absence of disorder is shown in black for comparison. (b) The same $S(T)$ results as above shown on a logarithmic temperature scale, emphasizing differences in plateau rounding at low T.

at low temperatures. This suggests that for the TIAF system, the existence of entropy plateaus is highly sensitive to disorder in the nearest-neighbor interaction.

7.4.3. Results in magnetic field with no disorder

Introducing a magnetic field aligned parallel to the Ising axis, the Hamiltonian given by Eq. (7.1) now has a non-zero value of B in the final term. Using the same transfer matrix procedure with this

Hamiltonian, we again obtained $S(T)$ and $C(T)$ plots at different values of B, for various values of J_2. Fig. 7.6 shows $S(T)$ for three NNN interaction strengths: (a) $J_2 = 0$, (b) $J_2 = -0.01$ and (c) $J_2 = -0.10$. For the $J_2 = 0$ case, we again find that for $B = 0$, we have a non-zero residual entropy as the temperature tends to zero. As noted in [228], a critical field value exists for antiferromagnetic Ising lattices at $B_c = z|J_1|$, at which there is degeneracy in the ground state. Here $z = 6$ for the triangular lattice, and we take $|J_1| = 1$. Hence we observe a non-zero residual entropy again at $B = 6$. For all other magnetic field values, the entropy tends to zero at low temperature since the ground state degeneracy due to frustration is removed.

When a NNN interaction is introduced, as in Fig. 7.6(b), where $J_2 = -0.01$, there is no residual entropy even at $B = 0$ or $B = 6$, since the ground-state degeneracy is removed. For small values of J_2 we observe a rounded plateau in $S(T)$ for $B = 0$ and $B = 6$. As the magnitude of J_2 increases, we no longer observe a plateau, and the entropy per site smoothly falls from $\ln 2$ to zero as the temperature is lowered. As in the previous section, plots of the specific heat (at various magnetic field values) were obtained for $J_2 = 0, -0.01$ and -0.10, as shown in Figs. 7.7(a)–(c). Comparing the $B = 0$ case in Fig. 7.7(a) and Fig. 7.7(b), we see that introducing a small non-zero NNN interaction (i.e. $J_2 = -0.01$) produces a peak in the specific heat, indicating a transition to a non-degenerate ground state and the absence of residual entropy at $T = 0$. Similarly, we also observe a peak in $C(T)$ at low temperature for $B = 6$, when $J_2 = -0.01$. Increasing the magnitude of J_2 further, we find that the locations of the peaks are shifted to lower temperature, for all values of B between $B = 0$ and $B = 6$.

With a non-zero magnetic field, we can obtain free energies at a fixed temperature for a range of B values and obtain the magnetization (per site) using $M = -\frac{\partial F}{\partial B}$. $M(B)$ curves were obtained at $T = 0.05$, $T = 0.2$ and $T = 2$ for three different values of J_2, as shown in Fig. 7.8: (a) $J_2 = 0$, (b) $J_2 = -0.01$, and (c) $J_2 = -0.10$. We find that at relatively high temperature (i.e. $T = 2$), magnetization per site increases linearly with magnetic field, and no plateaus occur. As temperature is lowered, magnetization plateaus are observed. The plateaus become less rounded and more step-like as the temperature is lowered further. For $J_2 = 0$ and $J_2 = -0.01$, a single plateau is observed at $M = 1/3$, but for $J_2 = -0.1$ we observe another plateau at $M = 1/2$, suggesting the $M = 1/2$ plateau phase is only observed if the NNN interaction is sufficiently strong. Indeed,

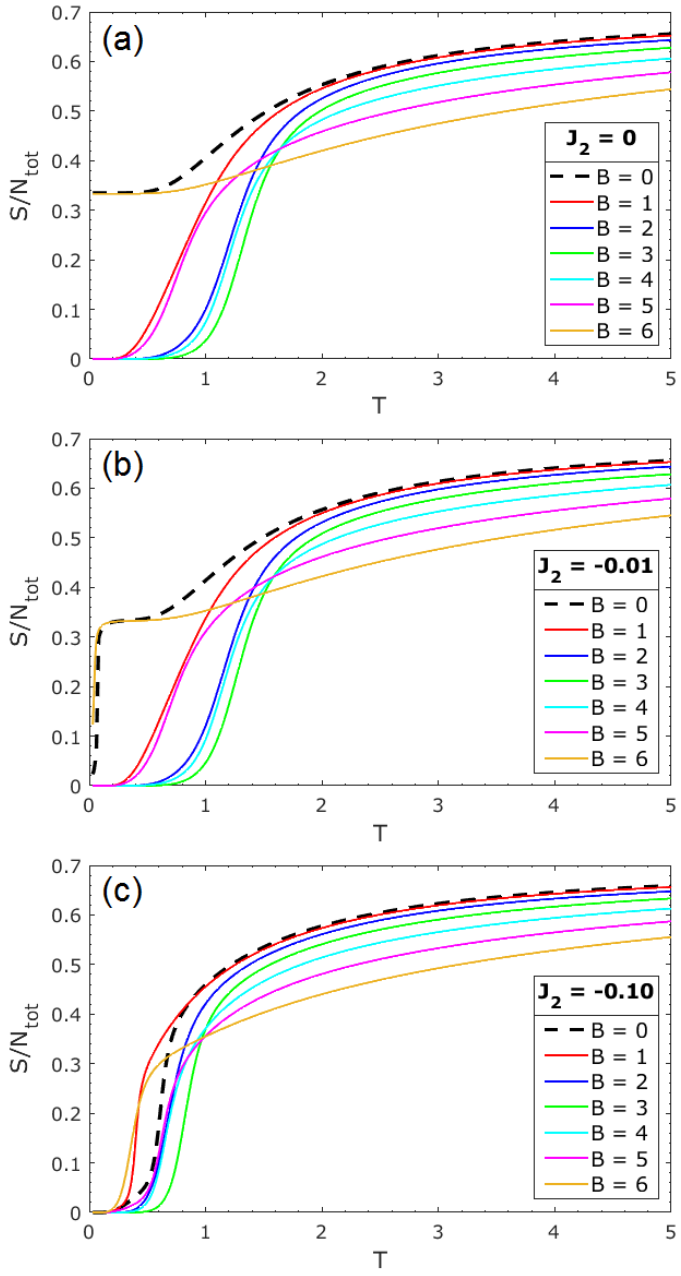

FIGURE 7.6. $S(T)$ results in the presence of a magnetic field, with no disorder. Field strengths ranging from $B = 0$ to the TIAF critical field value $B_c = 6$ are shown. The magnitude of the NN interaction strength J_1 is set to 1. Entropy curves are shown for three different J_2 values: (a) $J_2 = 0$, (b) $J_2 = -0.01$, and (c) $J_2 = -0.10$.

the J_2 dependence of the width of the $M = 1/2$ plateau at finite temperature (shown in Fig. 7.9) illustrates that a well defined plateau appears only when $|J_2|$ exceeds some threshold value, with

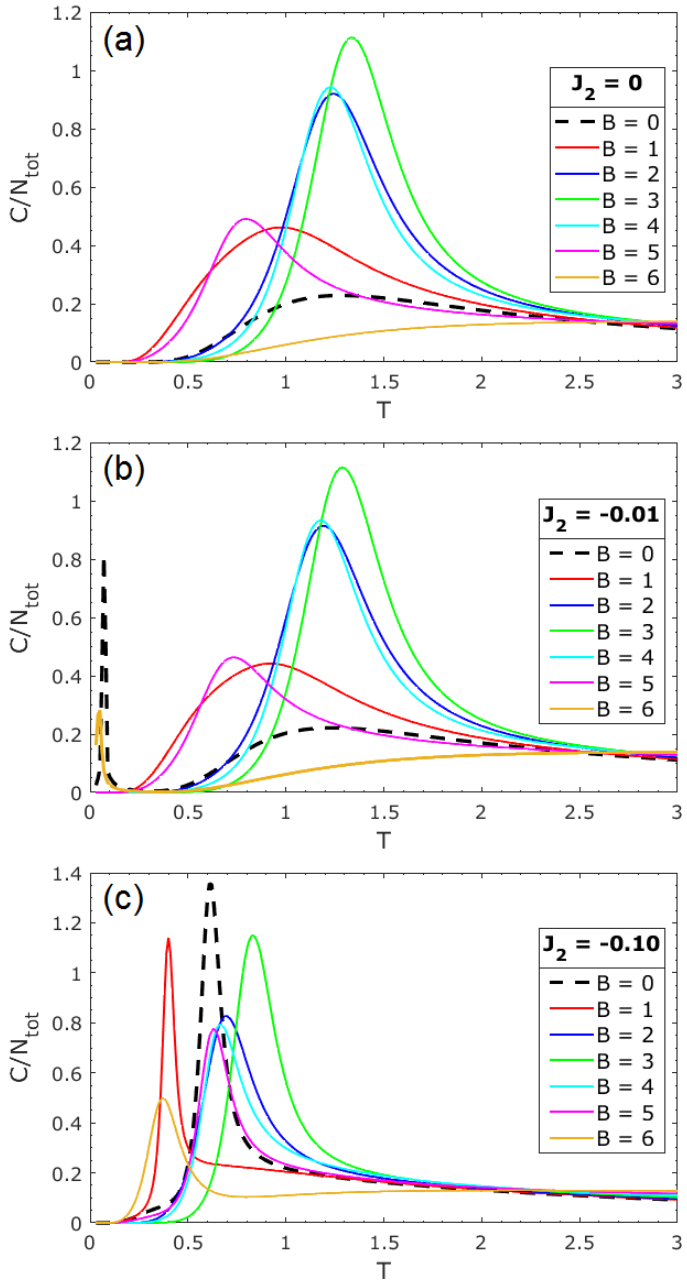

FIGURE 7.7. $C(T)$ results in the presence of a magnetic field, with no disorder. Specific heat curves are shown for three different J_2 values: (a) $J_2 = 0$, (b) $J_2 = -0.01$, and (c) $J_2 = -0.10$. Low temperature peaks in $C(T)$ are observed for both $B = 0$ and $B = 6$ when there is a small NNN interaction present, i.e. for $J_2 = -0.01$.

plateau width increasing approximately linearly with $|J_2|$ thereafter. At a temperature of $T = 0.05$, a plateau at $M = 1/2$ is apparent for $|J_2| \geq 0.04$. Decreasing the magnitude of J_2 gradually rounds

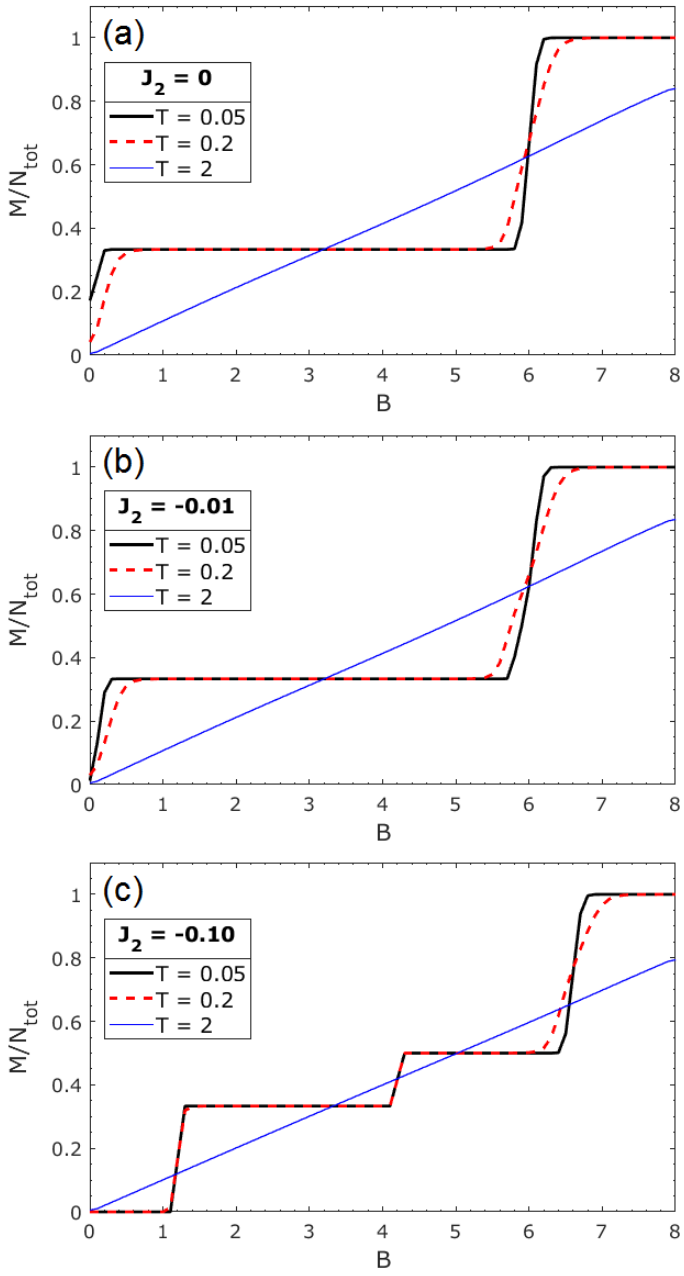

FIGURE 7.8. $M(B)$ results at finite temperature for different values of J_2: (a) $J_2 = 0$, (b) $J_2 = -0.01$, and (c) $J_2 = -0.10$, without disorder. For $J_2 = -0.10$, step-like magnetization plateaus can be seen at both $M = 1/3$ and $M = 1/2$. In each plot, $M(B)$ curves for three different temperatures are shown: $T = 0.05$, $T = 0.2$, and $T = 2$.

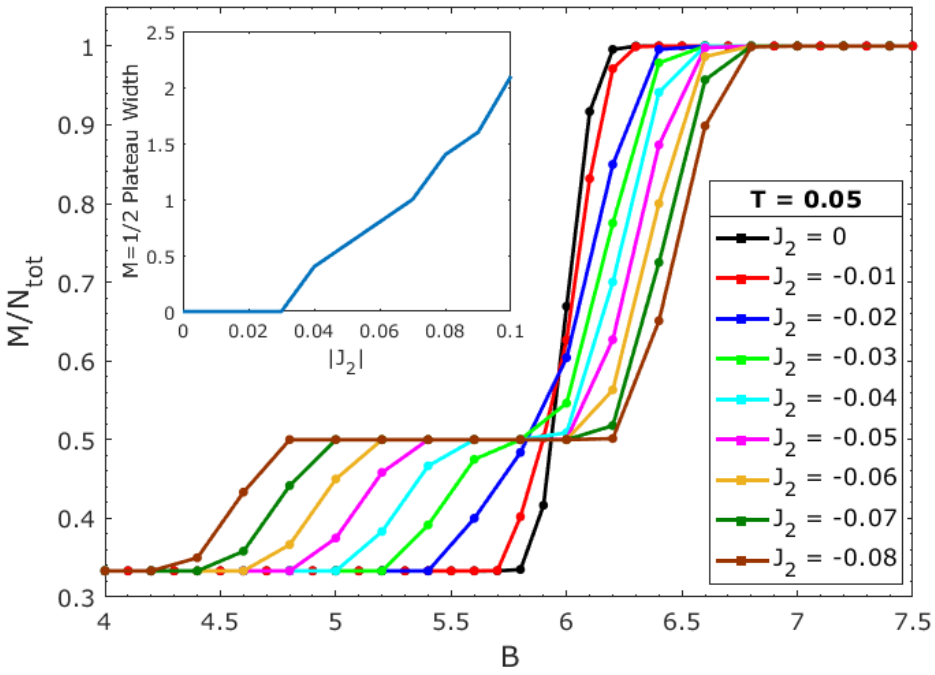

FIGURE 7.9. $M(B)$ curves around the $M = 1/2$ plateau region are shown for various values of J_2, at a fixed finite temperature of $T = 0.05$. The inset graph shows the dependence of the $M = 1/2$ plateau width (in units of B) upon the magnitude of J_2.

the plateau until it is no longer present, and the magnetization per site increases smoothly from 1/3 to full saturation. From Fig. 7.8(c) we can see that for $J_2 = -0.10$ (at $T = 0.2$), we have an $M = 0$ stripe phase for approximately $0 < B < 1$, an $M = 1/3$ plateau phase in the region $1.2 < B < 4.1$, and an $M = 1/2$ phase for $4.2 < B < 6$. Greater values of magnetic field produce a fully spin-polarized phase with $M = 1$. We also find that as the temperature increases, the rounding of the $M = 1/2$ plateau is more pronounced than at $M = 1/3$, which at $J_2 = -0.10$ and $T = 0.2$ remains step-like, as shown in Fig. 7.8(c) (red curve).

7.4.4. Results in magnetic field with uniform and Gaussian disorder

Although rounding of the magnetization plateaus in the ideal TIAF system is illustrated here at finite temperature, at $T = 0$ the magnetization per site increases in discrete steps between 0, 1/3, 1/2 and 1. However, in low-temperature measurements of TIAF materials such as $TmMgGaO_4$ [195, 224], distinct plateaus in magnetization are absent, which has been ascribed to the presence

of disorder in inter-site interactions and coupling to the magnetic field, which weakens or removes these plateaus entirely. The influence of disorder on $M(B)$ for the TIAF with both NN and NNN interactions has been studied previously for a finite 6×6 cluster by Li et al [**195**], where it was found that introducing disorder produced magnetization curves in agreement with experiment. Motivated by this work, we studied the influence of disorder strength on the form of the magnetization plateaus, and also investigated the relative importance of disorder in J_1 and J_2.

Using the transfer matrix approach to obtain $M(B)$, one introduces disorder in J_1 and J_2 by generating random values of these parameters from a chosen distribution. For a given set of J_1 and J_2 values (for all individual NN and NNN couplings in the lattice) we produce the corresponding transfer matrices as before, however the partition function is now obtained by taking the trace of the product of P transfer matrices, each one containing different parameter values. We use $P = 101$ and parameter values drawn from both a uniform distribution and a Gaussian distribution in the results presented here, with temperature fixed at $T = 0.2$. Uniform distributions are denoted by $U(J_{min}, J_{max})$ where J_{min} and J_{max} are the boundaries of the distribution, which has a width $J_{max} - J_{min}$. As shown in Fig. 7.10(a), we observe that strong plateaus at both $M = 1/3$ and $M = 1/2$ remain for $J_1 = U(-1.2, -0.8)$ and $J_2 = U(-0.16, -0.04)$, i.e. uniform distributions with mean values of $J_1 = -1$ and $J_2 = -0.1$. As the distribution width is increased, the plateaus are rounded further, and we find that both the $M = 1/2$ and $M = 1/3$ plateaus are eventually no longer observable, e.g. for $J_1 = U(-1.4, -0.6)$ and $J_2 = U(-0.2, 0)$. There is an indication that the $M = 1/3$ plateau may be more robust to disorder than the $M = 1/2$ plateau, since as the level of disorder increases, the plateau at $M = 1/2$ is lifted while a short plateau remains observable at $M = 1/3$, which can be seen for $J_1 = U(-1.3, -0.7)$ and $J_2 = U(-0.18, -0.02)$. When the disorder strength is increased further (i.e. to $J_1 = U(-1.4, -0.6)$ and $J_2 = U(-0.2, 0)$), the weak plateau at $M = 1/3$ is no longer present, and one obtains a magnetization curve quite similar to the recent experimental result for $TmMgGaO_4$ [**195**].

We also investigated introducing disorder in only one of the parameters J_1 or J_2 as shown in Fig. 7.10(b), using uniform distributions $J_1 = U(-1.4, -0.6)$ and $J_2 = U(-0.2, 0)$, again with mean values $J_1 = -1$ and $J_2 = -0.1$. We find that with disorder in J_2 only, both plateaus at $M = 1/3$ and $M = 1/2$ are present, and the magnetization curve remains similar to the zero-disorder case.

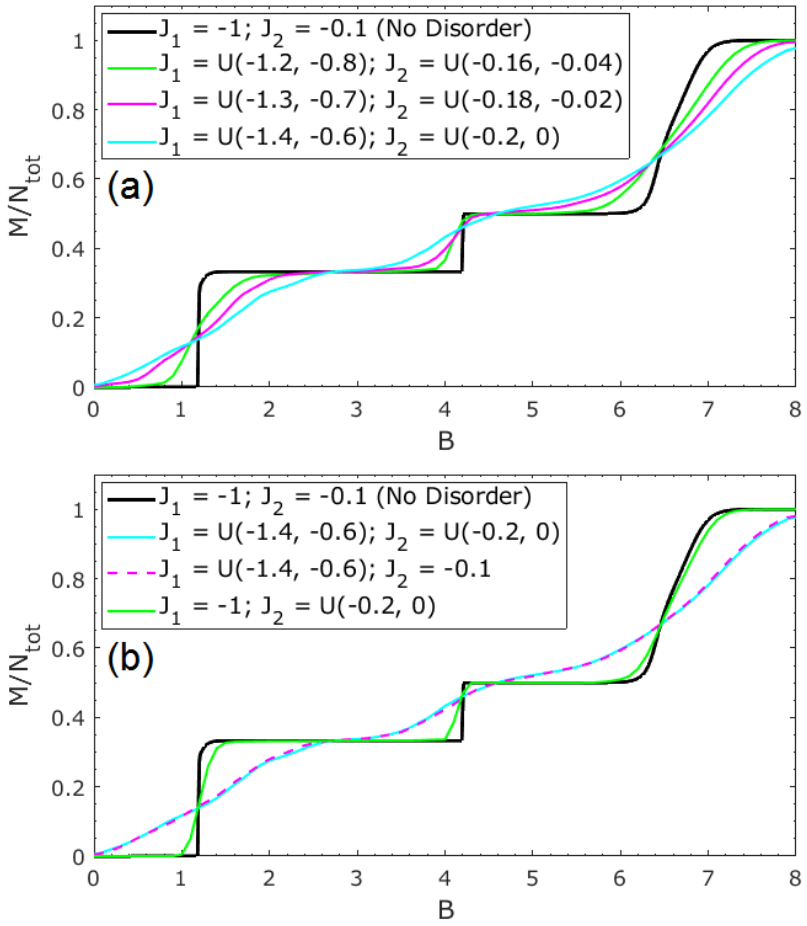

FIGURE 7.10. (a) $M(B)$ results for three different levels of uniform disorder, in both J_1 and J_2 combined, with the zero-disorder result shown in black for comparison. In each case, the uniform distributions of J_1 and J_2 used are centered at -1 and -0.1 respectively. (b) Additional $M(B)$ results are shown for uniform disorder in J_1 only ($J_1 = U(-1.4, -0.6)$ with $J_2 = -0.1$) and in J_2 only ($J_2 = U(-0.2, 0)$ with $J_1 = -1$).

With disorder in J_1 only, both plateaus are completely removed, and $M(B)$ is essentially identical to our result with disorder in both J_1 and J_2 combined. This suggests that disorder in J_1 only is sufficient to eliminate both magnetization plateaus, giving an $M(B)$ curve similar to experiment, provided $|J_1|$ exceeds $|J_2|$ by approximately an order of magnitude, as in this study. In this case, magnetization plateaus in the TIAF system are robust to disorder solely in J_2, even when the width of the parameter distribution spans $\pm 100\%$ of the mean value, i.e. for $J_2 = U(-0.2, 0)$. With disorder in J_2 only, step-like transitions between magnetization plateaus are still present, and there

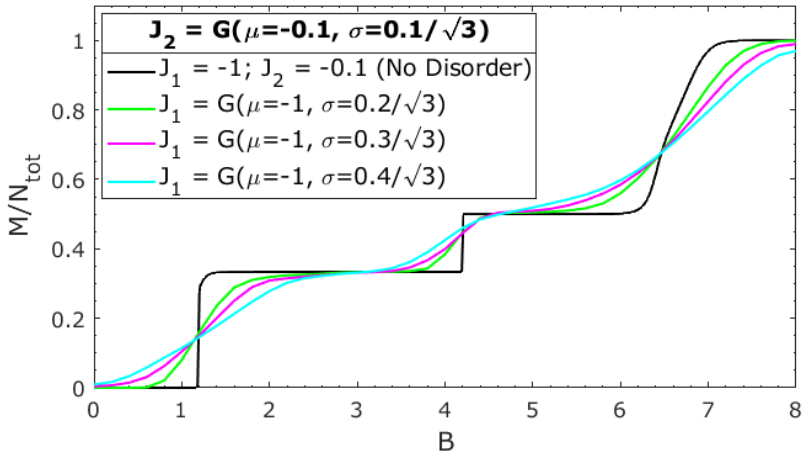

FIGURE 7.11. $M(B)$ results for three different levels of Gaussian disorder, in both J_1 and J_2 combined, with the zero-disorder result shown in black for comparison. The standard deviations of the distributions of J_1 values match those used in Fig. 7.10(a) for the case of uniform disorder.

is only a slight rounding of the magnetization curve compared to the zero-disorder case, even for $J_2 = U(-0.2, 0)$. We also find that disorder in the magnetic field is relatively insignificant, and one can obtain a result qualitatively similar to experiment with disorder in J_1 and J_2 only.

The form of the $M(B)$ curves in the presence of Gaussian disorder in J_1 and J_2 (instead of uniform disorder) was also investigated, as shown in Fig. 7.11. The Gaussian distributions for J_1 and J_2 were chosen to have mean values of -1 and -0.1 respectively, with the standard deviation of the distribution of J_2 values fixed at $\sigma = 0.1/\sqrt{3}$. The width of the distribution of J_1 values was varied and $M(B)$ results compared to the zero-disorder case. Three Gaussian distributions were used, which were chosen to have same standard deviations for J_1 as the three uniform distributions shown in Fig. 7.10(a), where we have used $\sigma = (b-a)/\sqrt{12}$ for any uniform distribution $U(a, b)$. As with uniform disorder, increasing the width of the distribution gradually weakens the magnetization plateaus at $M = 1/3$ and $M = 1/2$ until both are no longer visible, which occurs when the standard deviation of J_1 values approaches $\sigma = 0.4/\sqrt{3}$. The strong similarity between our results for uniform and Gaussian disorder indicates that the exact form of the distribution used is relatively unimportant in determining the robustness of magnetization plateaus in the TIAF system.

7.5. Conclusions

In this chapter we have studied the rounding and in some cases complete absence of entropy and magnetization plateaus for the triangular lattice antiferromagnet, with both NN and NNN interactions in a magnetic field, with and without quenched disorder. In particular, we have found that in the ideal TIAF, increasing $|J_2|$ tends to round and quickly remove the plateau in $S(T)$ near the theoretical residual entropy value at low temperature. The plateau-like feature is replaced by a sharp drop in entropy at the first-order transition. The strength of the second-nearest-neighbor interaction also determines if a magnetization plateau at $M = 1/2$ is present at finite temperature, and controls the width of the plateau. For sufficiently large J_2, a distinct plateau at $M = 1/2$ will be visible, which is gradually rounded as the magnitude of J_2 is lowered, until a plateau no longer remains.

In order to model realistic TIAF materials such as $TmMgGaO_4$, we studied the influence of disorder in J_1 and J_2 on the form of the entropy and magnetization curves. We find that with nearest-neighbor interactions alone, rounded entropy plateaus are quite sensitive to disorder in the exchange variable, and they are no longer observed when the width of the J_1 distribution exceeds $\sigma \approx 0.05J_1$. For weaker levels of disorder, a plateau at the residual entropy value persists to low temperatures (around $T = 0.2$ for $\sigma = 0.02J_1$). Consequently, we expect rounded entropy plateaus to be observable in TIAF systems at low temperatures only if the second neighbor interactions are less than a few percent and there is a significant absence of quenched disorder in the system. Our $M(B)$ results with disorder are close to recent experimental observations [**195**], confirming the presence of second-neighbor interactions and disorder in the system.

More generally, we conclude that the existence of well-defined entropy plateaus requires a fair amount of fine-tuning of the system, so whether they will be observed in a generic frustrated magnet is unclear. The spin-ice system is clearly special. The fact that a residual entropy plateau is seen in model simulations with arbitrary strength long-range dipolar interactions in addition to nearest-neighbor exchange interactions [**197**, **198**, **199**, **200**] shows their robustness. One might have expected these long-range interactions to remove the ground state degeneracy, and the corresponding zero-point entropy. But, it has been shown that a 'model dipole' interaction can be constructed that has exactly the same ground states as the nearest-neighbor model [**237**, **238**].

Remarkably, the dipolar interaction on the pyrochlore lattice has the noteworthy property of differing only slightly from this model interaction, and at short distances only. This robustness is presumably a manifestation of the emergent gauge theory.

Independent of the issue of fine-tuning, there are strong experimental challenges in looking for these entropy plateaus in real materials. The need to have clean low-disorder material and to be able to isolate the magnetic contribution to heat capacity and entropy from phonons and other degrees of freedom can be formidable. We hope our work will motivate further work on entropy plateaus in frustrated magnets and also in strongly-correlated electron systems, where a residual entropy phase may be a precursor to intertwined and competing orders [**239**].

CHAPTER 8

High-temperature Magnetization and Entropy of the Triangular Lattice Hubbard Model in a Zeeman Field

8.1. Chapter Summary

We use strong coupling expansions to calculate the entropy function $S(T,h)$, the magnetization $M(T,h)$, and the double occupancy factor $D(T,h)$ for the half-filled triangular lattice Hubbard model as a function of temperature T and Zeeman field h, for various values of the Hubbard parameter ratio U/t. These calculations converge well for temperatures larger than the exchange parameter $J = \frac{4t^2}{U}$ for moderate to large U/t values. Setting $\mu = U/2$ suffices to obtain the density of half filling within a fraction of one percent at all temperatures studied for $U/t \geq 8$. We discuss the systematic variation of properties with U/t. The temperature dependence of entropy and the double occupancy parameter shows a mapping to an antiferromagnetic Mott insulating behavior at temperatures well above $T = J$ for $U/t \geq 10$. Convergence of the series is weaker at intermediate fields implying non-monotonic variation of spin-correlations with the Zeeman field. We discuss the relevance of the Hubbard model results to the triangular-lattice antiferromagnetic materials $Lu_3Cu_2Sb_3O_{14}$ (LCSO) studied recently by Yang *et al* [240].

This chapter is based on the following paper [241]:

O. Bradley, Y. Zhang, J. Oitmaa, and R. R. P. Singh, *High-temperature magnetization and entropy of the triangular lattice Hubbard model in a Zeeman field*, arXiv 2303.03550 (2023).

8.2. Introduction

The Hubbard model serves as one of the most important paradigms for studying electronic correlations in solids [5, 242, 243]. It has played a central role in our emerging understanding of many important solid-state phenomena [239, 244, 245] including metal-insulator transitions,

quantum magnetism, the physics of intertwined orders, strange metals, and high temperature superconductivity. In recent years, the model has found additional relevance in new platforms such as cold-atoms in optical lattices [246, 247, 248] and layered Van der Waals systems such as transition-metal dichalcogenides [249] that can be manipulated to produce a plethora of exotic phases. Some advantages of these new platforms over traditional solid state systems are that the Hubbard model parameters can be controlled and well-determined, the system can be relatively free from unknown perturbations, and also engineered to exquisite detail.

The Hubbard Hamiltonian is given by

$$H = -t \sum_{\langle \mathbf{i},\mathbf{j} \rangle,\sigma} \left(c^{\dagger}_{\mathbf{i}\sigma} c_{\mathbf{j}\sigma} + c^{\dagger}_{\mathbf{j}\sigma} c_{\mathbf{i}\sigma} \right) + U \sum_{\mathbf{i}} n_{\mathbf{i}\uparrow} n_{\mathbf{i}\downarrow} - \mu \sum_{\mathbf{i}} (n_{\mathbf{i}\uparrow} + n_{\mathbf{i}\downarrow}) - \frac{h}{2} \sum_{\mathbf{i}} (n_{\mathbf{i}\uparrow} - n_{\mathbf{i}\downarrow}) \tag{8.1}$$

where $c^{\dagger}_{\mathbf{i}\sigma}(c_{\mathbf{i}\sigma})$ is a creation (destruction) operator for an electron with spin $\sigma = \{\uparrow, \downarrow\}$ at site $\mathbf{i}$ of a lattice. Here t is the nearest-neighbor hopping parameter, and the first sum is taken over all nearest neighbor pairs of sites $\langle \mathbf{i}, \mathbf{j} \rangle$. The number operator $n_{\mathbf{i}\sigma} = c^{\dagger}_{\mathbf{i}\sigma} c_{\mathbf{i}\sigma}$ gives the number of electrons at site $\mathbf{i}$ of spin σ. An on-site repulsion $U > 0$ penalizes sites which are doubly occupied, while the chemical potential μ controls the overall filling. We include a Zeeman field h which lowers the overall energy for electron spins oriented in the direction of the magnetic field.

In this paper we wish to explore properties of the half-filled triangular-lattice Hubbard model at temperatures above the exchange energy scale J. There have been many experimental studies of triangular antiferromagnets over the last few years [250, 251, 252, 253, 254, 255, 256] reporting varied phase behaviors including different types of quantum spin-liquids, yet many questions remain. We are motivated, in part, by the recent experimental study of the triangular-lattice antiferromagnetic materials $Lu_3Cu_2Sb_3O_{14}$ (LCSO) and $Lu_3CuZnSb_3O_{14}$ (LCZSO) by Yang et al [240]. These materials have an exchange energy scale J of order $10K$. However, the authors find that the molar magnetic entropy difference $\Delta S(T)$ between temperatures of $T = 0.1K$ and above $T = 20K$, where it begins to saturate as a function of temperature, was only about a third of $R \ln 2$. This is an extraordinary result implying either that at temperatures an order of magnitude below J a substantial fraction of $R \ln 2$ entropy remains in the system or that the entropy at $T = 2J$ is already reduced to only a third of $R \ln 2$.

From a theoretical point of view, the nearest-neighbor Heisenberg model on the triangular-lattice is known to retain substantially more entropy as temperature is lowered compared to the square-lattice. Using high temperature series expansions for the Heisenberg model, Elstner *et al* found [257,258] that the square-lattice entropy at $T = 0.4J$ was about ten percent of $R \ln 2$ for the square-lattice but close to fifty percent of $R \ln 2$ for the triangular lattice. However, at the lowest temperatures the triangular-lattice entropy is decreasing with reduction in temperature and one does not expect much entropy to remain [259, 260] at $T = 0.1J$. Indeed, there is overwhelming evidence that the triangular-lattice Heisenberg model has an ordered ground state [261, 262, 263, 264, 265, 266, 267, 268] and extrapolations of high temperature series that build in information about the low temperature behavior imply [259] a very small entropy at $T = 0.1J$.

Here we will study how the magnetic and thermodynamic properties of a finite-U Hubbard model differ from the Heisenberg model at temperatures of order J and higher and if the behavior of LCSO can be explained by such a finite U. To study the Hubbard model, we will use strong coupling expansions carried out at arbitrary temperatures [167, 269, 270]. These are expansions around the atomic limit in powers of βt. The Hubbard parameter U is treated non-perturbatively and enters as $\exp\{(-\beta U)\}$ and as energy denominators $1/U$. These expansions are very accurate at temperatures above t and turn into an expansion in powers of t/U or $\beta t^2/U$ at lower temperatures. As $T \to 0$, these expansions turn into degenerate perturbation theory around the atomic limit [271, 272]. We will study the crossover from high-temperatures comparable to U to the strongly correlated regime at temperatures much below U. By studying the entropy and magnetization as a function of temperature, Zeeman field h, and U/t ratio, we will explore the crossover to Heisenberg behavior and deviations from the Heisenberg behavior ultimately indicating a transition away from a Mott insulator. Note that we use Numerical Linked Cluster (NLC) expansions [273, 274] to obtain results for the triangular-lattice Heisenberg model.

Much of this physics has been studied before at low temperatures [271, 272]. However, it is difficult to establish the low temperature properties of the model in a conclusive way for lack of definitive computational tools. Our goal is to understand the intermediate temperature properties of the model where the strong coupling expansions should be well converged and provide accurate answers in the thermodynamic limit.

We also study the Maxwell's relations between $(\frac{\partial S}{\partial h})_T$ and $(\frac{\partial M}{\partial T})_h$. These are important for experimental measurements of magnetic entropy and heat capacity of solid state systems [240]. Direct experimental measurement of thermodynamic properties such as magnetic entropy and heat capacity can be difficult due to the presence of phonons and other degrees of freedom whose contributions can be hard to accurately subtract. In contrast, the magnetization measurements can be relatively free of such complications. Thus, Maxwell's relations provide a way of measuring field dependent changes in entropy. In a theoretical model study these relations also act as checks on the numerical convergence of the calculations.

We find that for $U/t \geq 16$, the zero-field molar entropy function develops a plateau as a function of temperature at a value of $R \ln 2$ and below that temperature the Heisenberg behavior is realized. In the intermediate coupling region $10 < U/t < 16$, we also see a crossover to Heisenberg behavior but there is no entropy plateau at a value of $R \ln 2$ and instead the Heisenberg behavior only sets in at an entropy value less than $R \ln 2$. Below $U/t = 8$ any resemblance to the Heisenberg behavior is lost. The study of the double occupancy parameter reinforces the result that a transition away from antiferromagnetic Mott insulator occurs in the region $8 < U/t < 10$, consistent with previous results [272,275,276]. At still smaller U/t the entropy at a temperature of $2J$ is greater than $R \ln 2$ as the system still has significant double occupancy left. Around and below $U/t = 10$, the entropy decreases rapidly with reduction in temperature around $T = 2J$ and thus smaller U/t values cannot explain the magnetic properties of these materials at all. In fact, we find that the best fits to the material behavior at high temperatures is obtained in the large-U limit, that is by a Heisenberg model.

In our study, we find that one needs a magnetic field of order J to see substantial reduction in the magnetic entropy at temperatures of $2J$ and higher. As expected, strong coupling expansions converge well for high fields at all temperatures. However, surprisingly, we find that the convergence is worse for intermediate fields $h \sim 2J$ than at $h = 0$. The extrapolations show some hints of magnetization plateaus already at temperatures of order J, though the convergence remains poor. The non-monotonic convergence suggests that spin-spin correlation length at these temperatures may be non-monotonic as a function of magnetic field, being larger at fields of order $2J$, where the

system may be developing spatial correlations associated with the onset of magnetization plateaus at lower temperatures.

The organization of this chapter is as follows: In Section 8.3, we discuss the strong coupling expansion method. In Section 8.4, the numerical results for zero-field are presented and discussed. In Section 8.5, we discuss the thermodynamic properties of the model as a function of magnetic field. In Section 8.6, we present comparisons of numerical results with the LCSO materials. In Section 8.7, we present our conclusions.

8.3. Methods

We employ finite temperature strong coupling expansions to obtain thermodynamic properties of the triangular-lattice Hubbard model. We write the Hubbard Hamiltonian Eq. (8.1) as $H = H_0 + V$, where

$$H_0 = U \sum_{\mathbf{i}} n_{\mathbf{i}\uparrow} n_{\mathbf{i}\downarrow} - \mu \sum_{\mathbf{i}} (n_{\mathbf{i}\uparrow} + n_{\mathbf{i}\downarrow}) - \frac{h}{2} \sum_{\mathbf{i}} (n_{\mathbf{i}\uparrow} - n_{\mathbf{i}\downarrow}) \tag{8.2}$$

i.e. the onsite terms form the unperturbed part of the Hamiltonian, and we treat the electron kinetic energy as a perturbation

$$V = -t \sum_{\langle \mathbf{i},\mathbf{j} \rangle, \sigma} \left(c^{\dagger}_{\mathbf{i}\sigma} c_{\mathbf{j}\sigma} + c^{\dagger}_{\mathbf{j}\sigma} c_{\mathbf{i}\sigma} \right). \tag{8.3}$$

Now, the logarithm of the grand partition function $\ln Z$ (per site) can be expressed as a perturbation expansion. Using the formalism of thermodynamic perturbation theory [**167**], we expand $\ln Z$ as

$$\ln Z = \ln z_0 + \sum_{r=1}^{\infty} \int_0^{\beta} d\tau_1 \int_0^{\tau_1} d\tau_2 \ldots \int_0^{\tau_{r-1}} d\tau_r \langle \tilde{V}(\tau_1) \tilde{V}(\tau_2) \ldots \tilde{V}(\tau_r) \rangle, \tag{8.4}$$

where z_0 is the single-site partition function, $\tilde{V}(\tau) = e^{\tau H_0} V e^{-\tau H_0}$, and the expectation value is defined as

$$\langle X \rangle = \frac{\mathrm{Tr}\, e^{-\beta H_0} X}{\mathrm{Tr}\, e^{-\beta H_0}}. \tag{8.5}$$

To each order, terms in Eq. (8.4) can be expressed in terms of clusters of sites (graphs) on the triangular lattice having N_s sites and N_r bonds. We have that

$$\ln Z = \ln z_0 + \sum_{G} L_G z_0^{N_s} (\beta t)^{N_r} X_G(\zeta, \beta U), \tag{8.6}$$

where the sum is over graphs G. Here L_G, the lattice constant for a graph G, is the extensive part of its count divided by number of sites, X_G is the reduced weight of the graph, and $\zeta = e^{\beta\mu}$ defines the fugacity of the system.

The single-site partition function can be expressed as a series in powers of ζ and $w = e^{-\beta U}$. For the SU(2) Hubbard model (in a magnetic field h) it is given by

$$z_0 = 1 + \left(e^{\beta h/2} + e^{-\beta h/2}\right)\zeta + \zeta^2 e^{-\beta U}. \tag{8.7}$$

We obtain strong coupling expansions for $\ln Z$ up to 8^{th} order in βt. We can rewrite Eq. (8.6) as a series expansion in orders βt, i.e.

$$\ln Z = \ln z_0 + \sum_{n=2}^{\infty} \frac{(\beta t)^n}{z_0^n} \sum_{t=1}^{n_t} a_t(n_1, n_2, n_3, n_4, C), \tag{8.8}$$

where each order n contributes a sum of n_t terms, and our calculations are complete to order $n_{\max} = 8$. The function a_t has the form

$$a_t = C e^{(n_2\mu + n_3 h/2 - n_4 U)} \left(\beta U\right)^{-(n-n_1)}, \tag{8.9}$$

where n_1, n_2, n_3, and n_4 take integer values, and the set of C values are the series coefficients that we have calculated complete to eighth order. Without loss of generality, we set the hopping parameter $t = 1$.

Thermodynamic properties such as the internal energy E, electron density ρ, magnetization M, double occupancy D, and entropy S, can now be obtained by taking suitable derivatives of $\ln Z$ given by Eq. (8.8). We have that

$$E = -\left(\frac{\partial}{\partial\beta} \ln Z\right)_{\zeta}, \tag{8.10}$$

$$\rho = \zeta \frac{\partial}{\partial\zeta} \ln Z \equiv \frac{1}{\beta} \frac{\partial}{\partial\mu} \ln Z, \tag{8.11}$$

$$M = \frac{1}{\beta} \frac{\partial}{\partial h} \ln Z, \tag{8.12}$$

$$D = -\frac{1}{\beta} \frac{\partial}{\partial U} \ln Z, \tag{8.13}$$

$$S = \beta E + \ln Z - \beta\rho\mu, \tag{8.14}$$

where each thermodynamic property above is a function of the four parameters β, μ, h, and U. By directly differentiating Eq. (8.8) we obtain:

$$E(\beta,\mu,h,U) = e_0 - \sum_{n=2}^{n_{\max}} \sum_{t=1}^{n_t} \frac{a_t \beta^n}{Z_0^n} \left[\frac{n_3 h}{2} - n_4 U - \frac{(n-n_1)}{\beta} + \left(\frac{n}{\beta} + n e_0 \right) \right], \tag{8.15}$$

$$\rho(\beta,\mu,h,U) = \rho_0 + \sum_{n=2}^{n_{\max}} \sum_{t=1}^{n_t} \left[\left(\frac{\beta^n}{Z_0^n} \right) (n_2 - n\rho_0) a_t \right], \tag{8.16}$$

$$M(\beta,\mu,h,U) = m_0 + \sum_{n=2}^{n_{\max}} \sum_{t=1}^{n_t} \left[\left(\frac{\beta^n}{Z_0^n} \right) \left(\frac{n_3}{2} - n m_0 \right) a_t \right], \tag{8.17}$$

$$D(\beta,\mu,h,U) = d_0 - \sum_{n=2}^{n_{\max}} \sum_{t=1}^{n_t} \left[\left(\frac{\beta^n}{Z_0^n} \right) \left(n d_0 - n_4 - \frac{(n-n_1)}{\beta U} \right) a_t \right], \tag{8.18}$$

where each expression involves a zeroth order term arising from a derivative of $\ln z_0$: $e_0 = -\frac{\partial}{\partial \beta}(\ln z_0)_\zeta$, $\rho_0 = \frac{1}{\beta}\frac{\partial}{\partial \mu}(\ln z_0)$, $m_0 = \frac{1}{\beta}\frac{\partial}{\partial h}(\ln z_0)$, and $d_0 = -\frac{1}{\beta}\frac{\partial}{\partial U}(\ln z_0)$. Note that the entropy S is subsequently obtained via the thermodynamic relation Eq. (8.14).

8.4. Thermodynamic Properties in Zero Magnetic Field

We first present results for the triangular lattice Hubbard model in zero magnetic field ($h = 0$). On bipartite lattices, fixing the chemical potential at $\mu = U/2$ ensures the system is at half-filling, i.e. an average electron density of $\rho = 1$ per site. However, this does not strictly hold for the triangular lattice, which is non-bipartite. Nevertheless, we find that fixing $\mu = U/2$ yields approximately $\rho = 1$ to sufficient accuracy across a wide range of temperatures and values of U. In Fig. 8.1, we plot $\rho(T)$ for several values of U from $U = 8$ to $U = 32$, where we fix $\mu = U/2$, and we report the temperature T in units of the exchange parameter $J = 4t^2/U$. We find that setting $\mu = U/2$ suffices to obtain half-filling to within a fraction of one percent at all temperatures studied for $U \geq 8$. We thus fix $\mu = U/2$ in the results that follow. We note that descending from high T, there is a slight positive contribution to ρ, exceeding half-filling, while at low T there is a small negative contribution yielding $\rho < 1$. This behavior can be understood by the examining the third order term in the density series [Eq. (8.13)].

In Fig. 8.2, we plot the entropy $S(T)$ as a function of temperature for several values of U from $U = 4$ to $U = 32$. One can see that for $U/t > 16$, the entropy develops a plateau at a value of $R \ln 2$ marking the onset of Mott behavior and below that temperature the entropy function is well

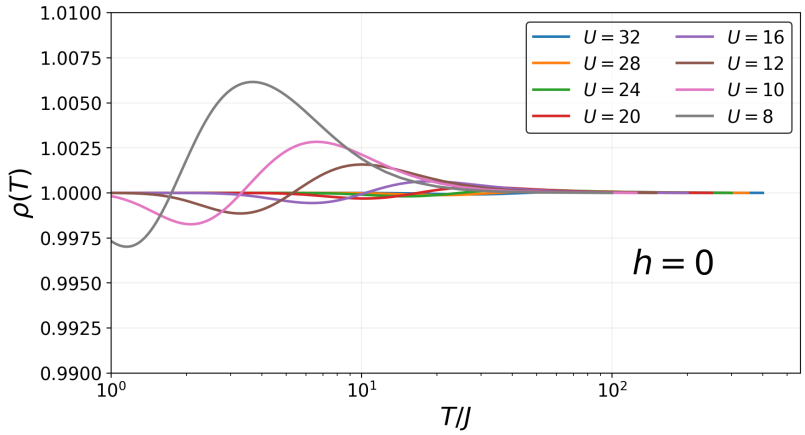

FIGURE 8.1. Electron density per site $\rho(T)$ at $h = 0$ is shown for different values of U, where we fix the chemical potential $\mu = U/2$ in each case. We find this yields half-filling on the triangular lattice to sufficient accuracy (a fraction of one percent) for $U \geq 8$.

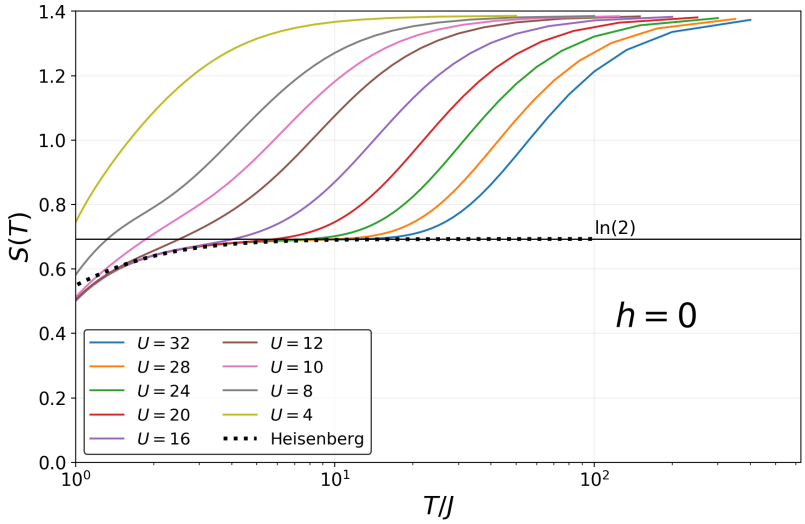

FIGURE 8.2. The entropy $S(T)$ at $h = 0$ is shown for different values of U, along with the triangular-lattice Heisenberg result (dotted line). We observe an entropy plateau at $\ln(2)$ for large U, and a high T maximum at $\ln(4)$ as expected. The deviation of $S(T)$ from the Heisenberg limit becomes apparent as U decreases.

described by that of the Heisenberg model (a 9^{th} order NLC calculation is shown). For intermediate U/t values, there is no entropy plateau but instead the crossover to Heisenberg behavior is obtained at entropy values that are successively smaller than $R \ln 2$ as U/t is lowered. This crossover happens at temperatures of only a few times J and thus there is no high-temperature Heisenberg limit. For

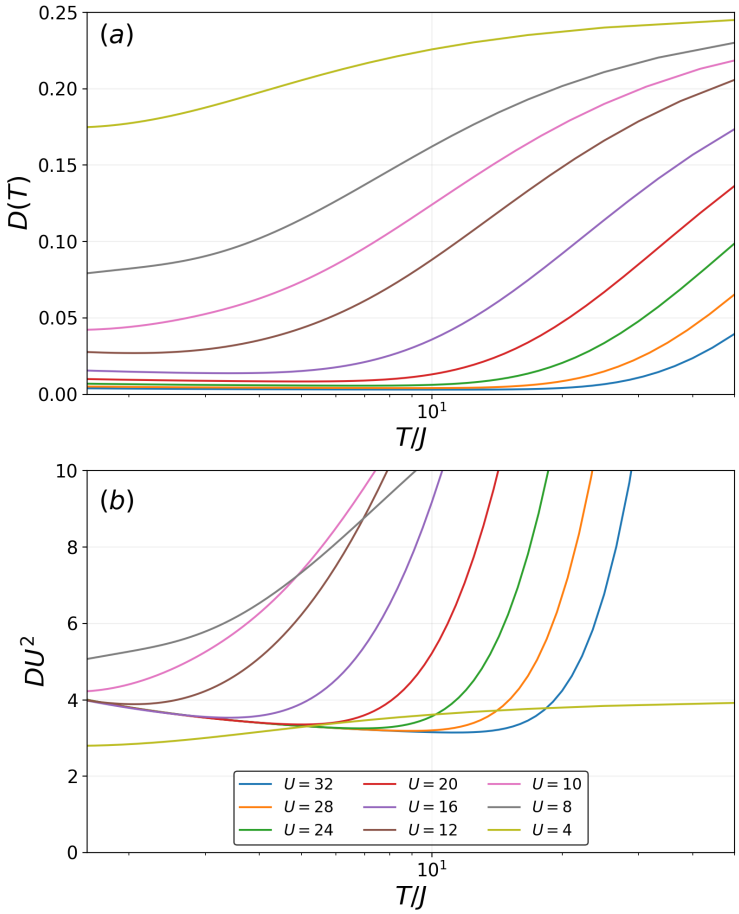

FIGURE 8.3. (a) The double occupancy factor $D(T)$ at $h = 0$ is shown for different values of U. We observe $D(T)$ goes to zero at low T more rapidly at large U, and reaches a maximum value of $1/4$ at high temperature as expected. (b) Plot of DU^2 as a function of T for different values of U, illustrating an upturn for $U \gtrsim 12$ at low T.

$U/t < 8$, the entropy is much larger than $R \ln 2$ at $T = 2J$ but drops rapidly below that temperature presumably reflecting a crossover to the metallic Fermi liquid regime.

In Fig. 8.3, we show the variation of the double occupancy factor D as a function of temperature. In Fig. 8.3(a) we plot D whereas in Fig. 8.3(b) we plot DU^2 versus T. In the large U limit double occupancy can be shown by perturbation theory to go as $1/U^2$. This virtual double occupancy is intimately related to antiferromagnetism and increases as temperature is lowered indicating a growth in antiferromagnetic configurations compared to ferromagnetic ones. We find that for $U/t > 16$, all the plots share the large U behavior at low temperatures. Down to the lowest temperature

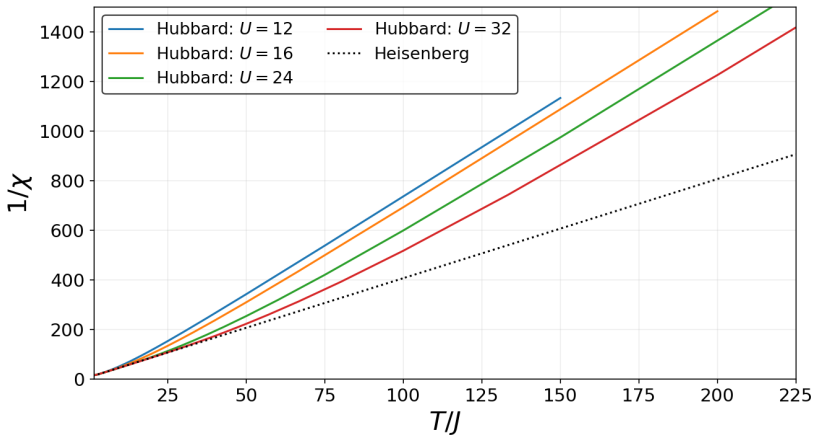

FIGURE 8.4. The zero-field inverse magnetic susceptibility $1/\chi$ for the Hubbard model is shown as a function of temperature T/J, for $U = 12, 16, 24$, and 32. The Heisenberg model result is shown as a dotted black line.

studied, $U/t = 8$ still has substantial double occupancy and it is still slowly decreasing with temperature. The behavior at $U/t = 4$ is clearly very different. In this case, the substantial double occupancy presumably remains in the Fermi liquid regime and is only enhanced by temperature.

In Fig. 8.4, we show the inverse susceptibility as a function of temperature. The dotted line is the Curie-Weiss result for the Heisenberg model from a 9^{th} order NLC calculation. One can see that the susceptibility matches on to the Heisenberg limit at temperatures much smaller than U. At temperatures above U double occupancy reduces the effective Curie constant by a factor of 2. This increases the slope of the inverse susceptibility plots by a factor of 2. For a material well described by the Hubbard model, measurements of such a crossover can be a good way to determine the U/t value.

In Fig. 8.5, we show the variation of entropy and double occupancy as a function of U/t. In Fig. 8.5(a) the entropy is plotted as a function of U/t for various temperature values. In Fig. 8.5(b) the double occupancy is plotted as a function of U/t for various temperature values. At large U/t, the entropy goes smoothly to the values obtained in the Heisenberg limit. As the temperature is lowered, the metal insulator transition should show up as a sharp increase in double occupancy. The lowest temperatures where our results are well converged is around $T = 1.5J$. At these temperatures one can see a change in behavior around $U/t = 10$, which is a rough indication of the

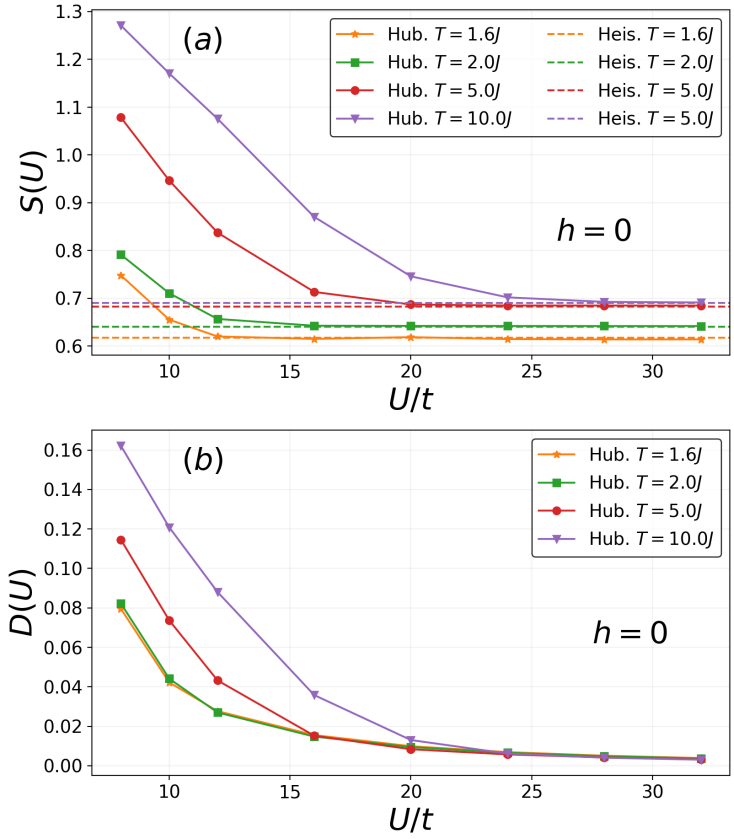

FIGURE 8.5. We show (a) entropy $S(U)$ and (b) double occupancy $D(U)$ as a function of U, in zero magnetic field. In panel (a) the corresponding entropy values in the Heisenberg model (9^{th} order NLC) are shown as dashed lines. If U is sufficiently large, S approaches the Heisenberg result, with the required U value increasing with temperature.

metal-insulator transition, which strictly occurs only at $T = 0$. All properties are smooth at finite temperatures and one cannot identify any phase transitions more precisely at these temperatures.

8.5. Thermodynamic Properties in a Magnetic Field

In this section, we discuss how the intermediate temperature properties of the Hubbard model evolve with a magnetic field. We consider a Zeeman-field only. In a quasi-two dimensional system, an in-plane magnetic field only couples to the spin degrees of freedom and acts as a Zeeman field. The application of such a field lowers double occupancy, lowers the entropy and causes the system to develop a magnetization. Thus we present results for $S(T, h)$, $M(T, h)$ and $D(T, h)$ for several

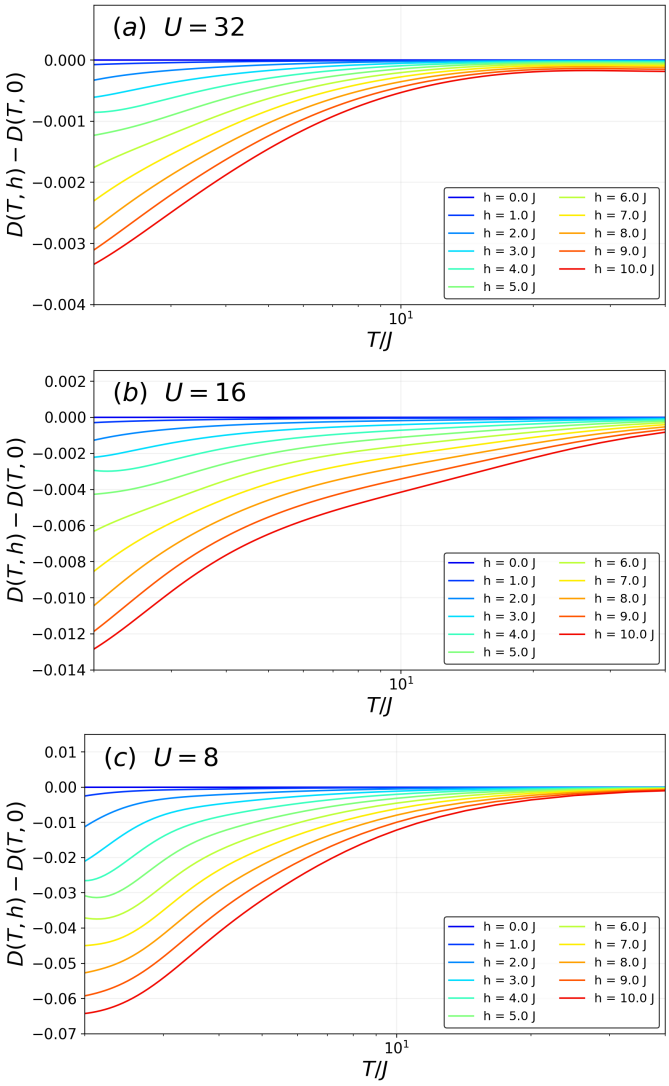

FIGURE 8.6. The double occupancy factor difference $D(T,h)-D(T,0)$ is shown for various magnetic field values h, for the Hubbard model at (a) $U=32$, (b) $U=16$, and (c) $U=8$.

different parameter ratios U/t. All plots are restricted to temperatures $T > 2J$, which is where convergence is best.

In Fig. 8.6, we show how that the double occupancy is reduced by the application of the field. We plot the difference in the double occupancy parameter in a field and in zero field at a given temperature. A negative value shows it to be reduced. This reduction at large U is related to the fact that the field favors configurations where spins are aligned with the field. Such configurations

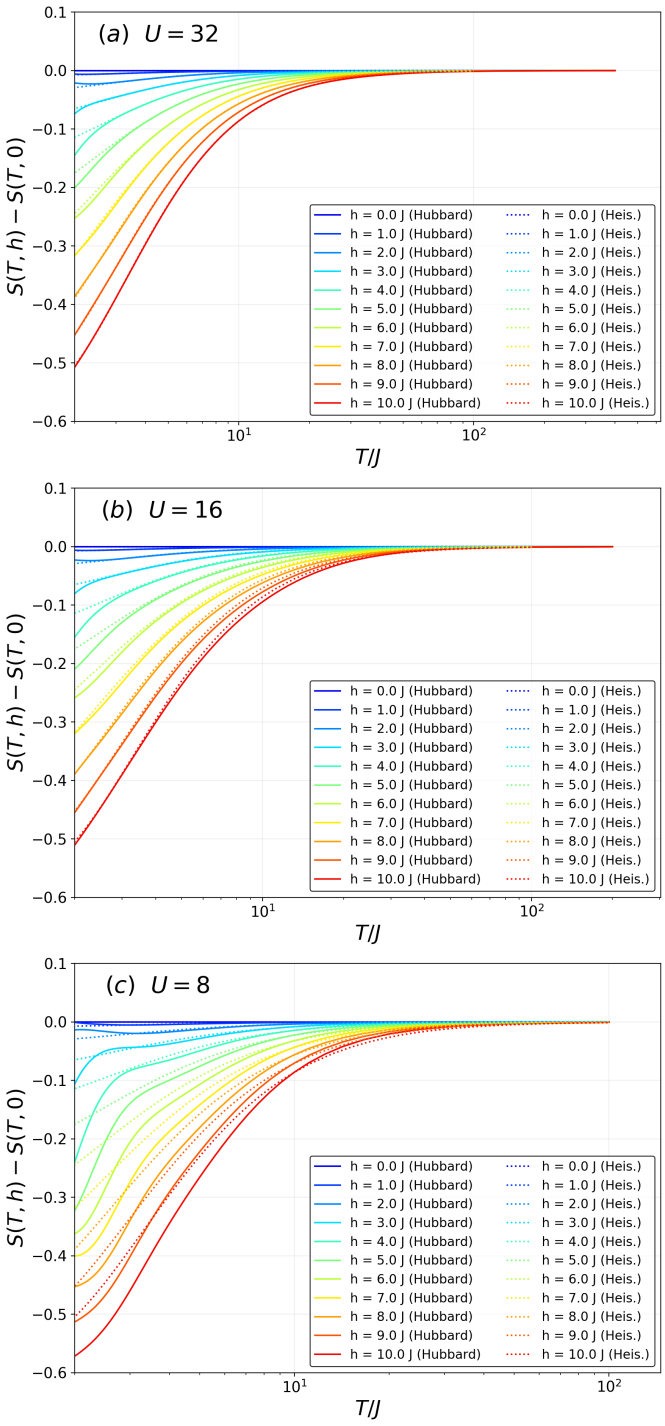

FIGURE 8.7. The entropy difference $S(T,h)-S(T,0)$ is shown for various magnetic field values h, for the Hubbard model at (a) $U=32$, (b) $U=16$, and (c) $U=8$.

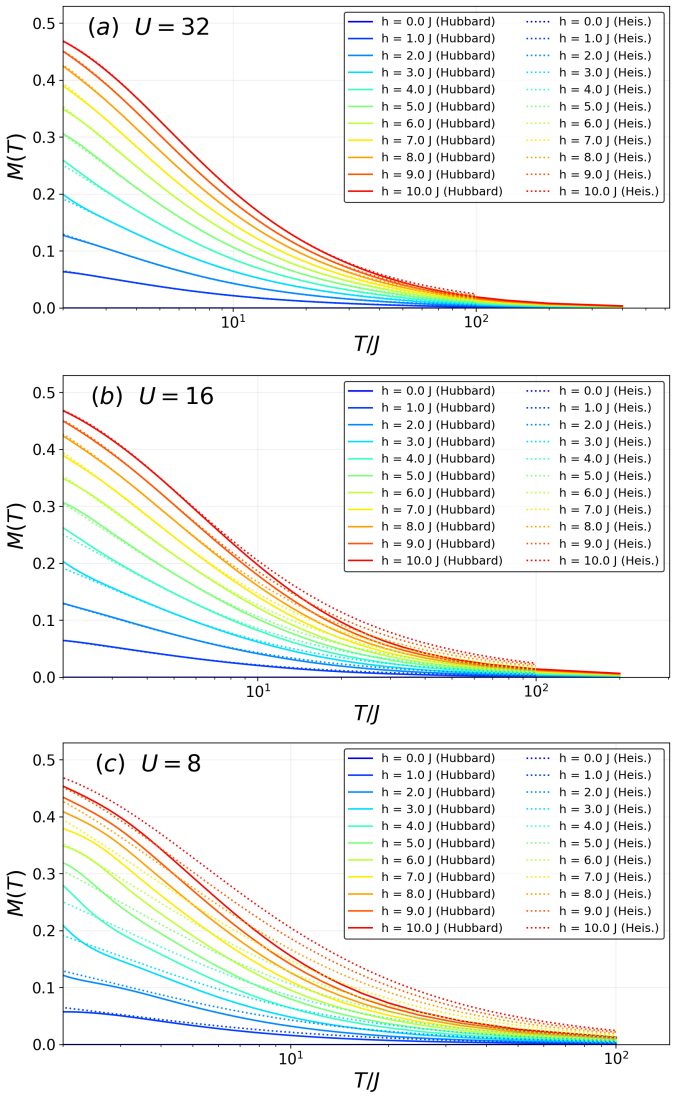

FIGURE 8.8. The magnetization $M(T)$ is shown for various magnetic field values h, for the Hubbard model at (a) $U = 32$, (b) $U = 16$, and (c) $U = 8$.

have reduced virtual mixing with doubly occupied states. In zero-field, there was an upturn in $D(T)$ at low temperatures. It goes away at large h, e.g. at $U = 32$, $D(T)$ decreases monotonically with temperature for $h/J \gtrsim 5$. As U is decreased, the field has a greater suppression of the double occupancy. This is simply related to the fact that there is more double occupancy in the system in zero field.

In Fig. 8.7, we show how the entropy function is reduced by the application of the field. We plot the difference in the entropy in a field and in zero field at a given temperature. In each panel

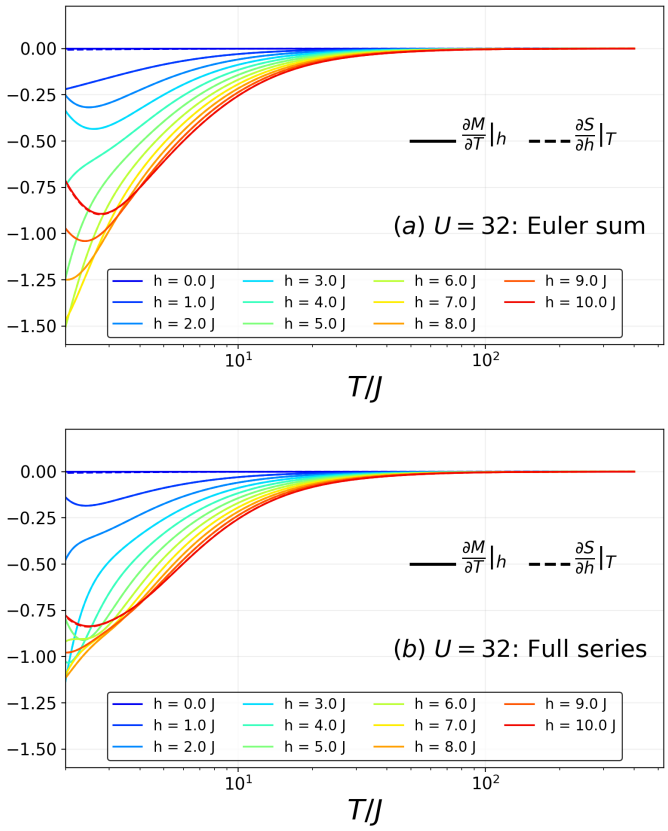

FIGURE 8.9. The partial derivatives $(\frac{\partial S}{\partial h})_T$ (dashed lines) and $(\frac{\partial M}{\partial T})_h$ (solid lines) are calculated separately and shown as a function of temperature T/J, for several magnetic field values from $h = 0$ to $h = 10J$.

the Heisenberg result (9^{th} order NLC) is shown for comparison as a dotted line. Qualitatively the results are similar for different U values. At $U = 32$, the Hubbard results agree well with the Heisenberg data. Only for $U = 8$, we observe significant deviations from the Heisenberg limit with greater deviation occurring at larger fields.

In Fig. 8.8, we show the magnetization as a function of the field. Here too, in each panel the Heisenberg result (9^{th} order NLC) is shown as a dotted line. At $U = 32$, the Hubbard results agree well with the Heisenberg data. We observe significant deviation from the Heisenberg limit by $U = 8$, again with greater deviation at larger fields.

In Fig. 8.9, The partial derivatives $(\frac{\partial S}{\partial h})_T$ (dashed lines) and $(\frac{\partial M}{\partial T})_h$ (solid lines) are shown as a function of temperature T/J, for several magnetic field values from $h = 0$ to $h = 10J$. Here we fix $U = 32$ and plot for each derivative (a) an 8^{th} order Euler sum [277] and (b) the direct sum of

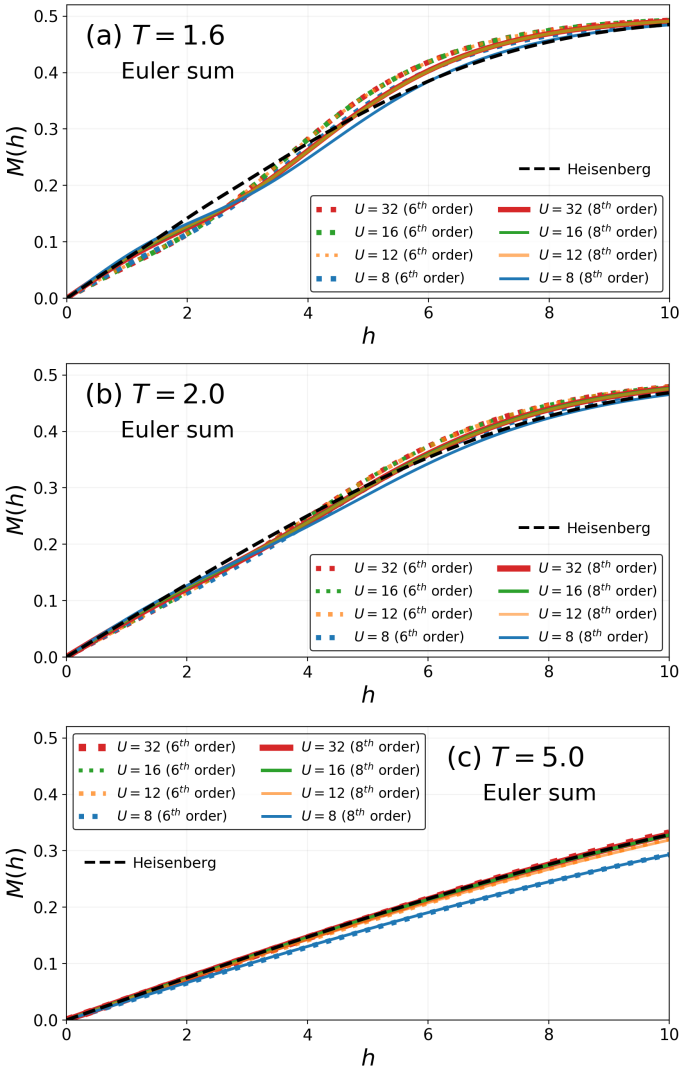

FIGURE 8.10. The magnetization $M(h)$ in the triangular lattice Hubbard model at fixed temperatures (a) $T/J = 1.6$, (b) 2.0, and (c) 5.0 is shown for various values of U. In each panel we show an Euler sum for $M(h)$, and compare 6^{th} and 8^{th} order series. In each plot the corresponding $M(h)$ curve in the triangular lattice Heisenberg model is shown for reference (black dashed line).

the 8^{th} order expansion. At large h, the magnetization saturates at 1/2 at low temperatures, thus we observe the derivatives curving upwards towards zero. Maxwell's relation $(\frac{\partial S}{\partial h})_T = (\frac{\partial M}{\partial T})_h$ are well satisfied. The comparison between results obtained from a direct sums of the series in (b) and Euler sums in (a) shows that the convergence of the direct sum starts to break down a bit above $T/J = 2$ and it becomes important to employ a convergence method such as Euler summation.

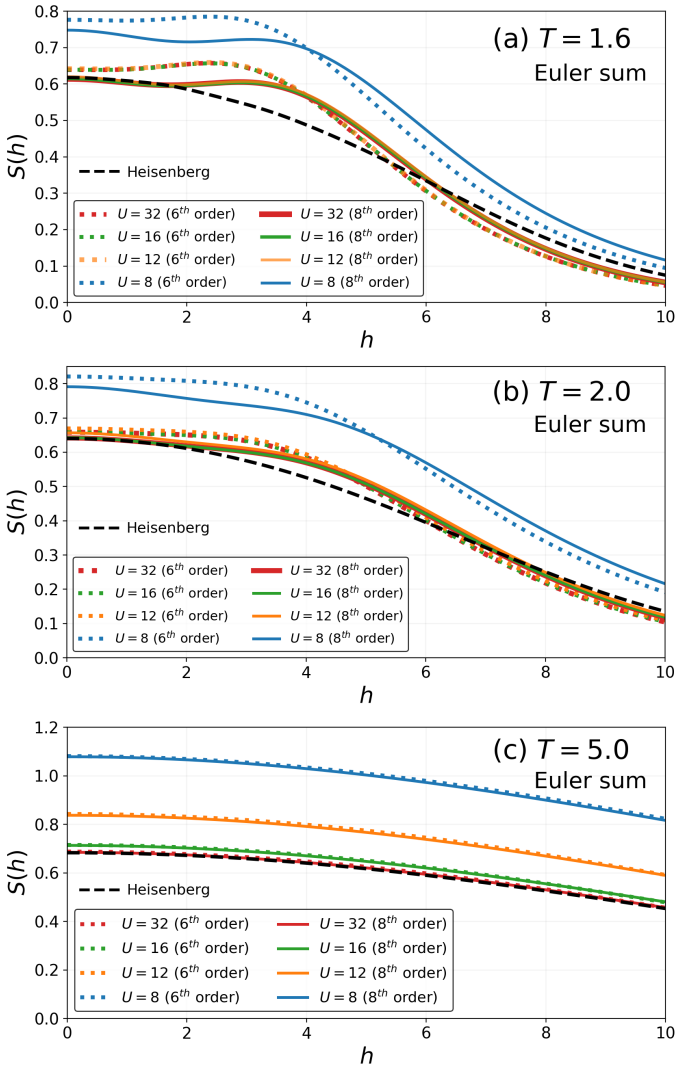

FIGURE 8.11. The entropy $S(h)$ in the triangular lattice Hubbard model at fixed temperatures (a) $T/J = 1.6$, (b) 2.0, and (c) 5.0 is shown for various values of U. In each panel we show an Euler sum for $S(h)$, and compare 6^{th} and 8^{th} order series. In each plot the corresponding $S(h)$ curve in the triangular lattice Heisenberg model is shown for reference (black dashed line).

The Euler summation improves the convergence in both NLC expansions and series expansions as it eliminates any alternating terms in the series [**235**] however the convergence cannot be pushed too far down in temperature in a reliable way. Hence for field dependent quantities, we mostly show data for $T/J > 2$.

In Fig. 8.10 and Fig. 8.11, we show plots of magnetization and entropy as a function of magnetic field for a few select values of temperature and several values of U. At $T = 5J$, the field dependence

is featureless and the magnetization is converging well towards the Heisenberg limit at large U. Here we show Heisenberg model results obtained from a 12^{th} order NLC calculation. However, there is still significant additional entropy associated with double occupancy for $U = 32$. The excess entropy at $T = 2J$ is limited to an intermediate window in the magnetic field for $U = 32$. At $T = 1.6J$, the M vs h curve begins to develop an inflection and at the same time the entropy begins to develop a minima at $h = 2J$ and there is even more extra entropy at intermediate fields. While the convergence is starting to break down at these temperatures, we believe that these are an early indication of the magnetization plateaus arising at lower temperatures which may be magnified by the finite U through the frustrating interactions generated in higher orders. This question of precursor effects of magnetization plateaus in magnetization and entropy at temperatures of order J deserves further attention.

8.6. Comparison with LCSO Experimental Data

In this section, we present comparisons of the experimental data [240] for the material $Lu_3Cu_2Sb_3O_{14}$ (LCSO) with those obtained here for the Hubbard model. We have done extensive comparisons of the magnetization data as a function of temperature and magnetic field. First, we use the high-temperature data to estimate the g-factor by comparing magnetization $M(T)$ with a second order NLC calculation [273, 274], which should be highly accurate above $T = 10J$. It is known that there are two types of spins in the system, where the exchange constant of one type is larger than the other. For simplicity we assume that one set of spins are coupled much more strongly than the other. At high temperatures only the average exchange that sets the Curie-Weiss constant matters.

We can treat the weakly coupled spin as a free spin, whose magnetization we call M_1, while the magnetization of the other will be accurately described by an expression given by a second order NLC calculation. This expression is $3M_2 - 5M_1$, where M_2 is the magnetization of a two-site Heisenberg model. An overall magnetization $M(T)$ per spin can then be calculated by averaging over the two types of spin, i.e.

$$M(T) = \frac{1}{2}\left(3M_2 - 5M_1\right) + \frac{M_1}{2}. \tag{8.19}$$

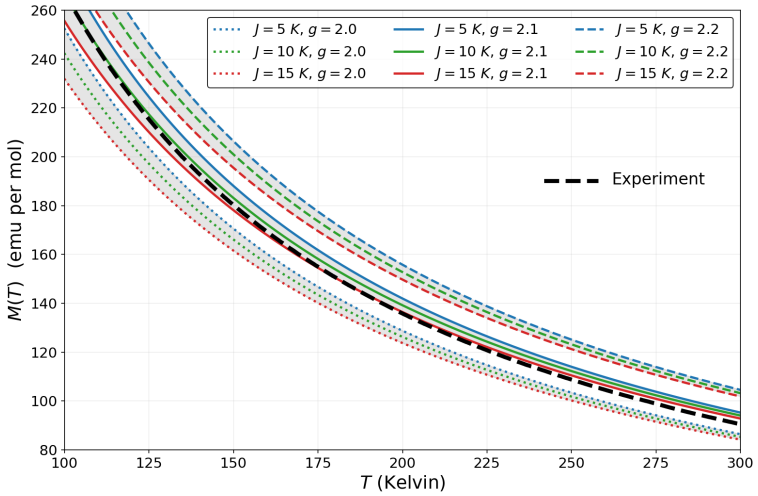

FIGURE 8.12. A fit of the very high temperature magnetization data ($T > 100K$) at a field of 7 Tesla for LCSO [240] with a Heisenberg model on the triangular lattice obtained in second order NLC. We show results with half the spins assumed to be free while the other half are exchange coupled with nearest-neighbor coupling J. Different J and g values are shown. Although the very high temperature data are better fit by a g value below 2.1, the latter value is better for fits at lower temperatures.

We plot this in Fig. 8.12 for several values of g: 2.0, 2.1, and 2.2. For each g value we show $M(T)$ for three values of J: $5K$, $10K$, and $15K$, and shade the region enclosed by these curves in gray. The experimental result for the material LCSO (at a field $h = 7$ Tesla) is shown as a black dashed line. We find that over the temperature range shown, $g \approx 2.1$ fits the data best, although we note that at higher temperatures ($T > 300K$) a smaller value $2.0 < g < 2.1$ matches the experimental results more closely. However, since $g = 2.1$ fits well over a wide temperature range, we fix g at this value in what follows.

Next, we determine the optimal value of the exchange parameter $J = 4t^2/U$, by comparing both our Hubbard model calculations (at several U values) and 9^{th} order Heisenberg NLC results to experimental $M(h)$ data. Here we have assumed that we can represent the system by a single J or single t/U for all spins. We see from Fig. 8.13 that the fits improve with increasing U and there is not much difference between $U = 32$ Hubbard model and the Heisenberg fits. The average J, assuming a single exchange constant for all the spins, is greater than $6K$ but less than $8K$. To judge the quality of the fit and allow the interactions for the two types of spins to be different, we use the quantitative measure of sum of relative least squares. Let the data points be given as y_i

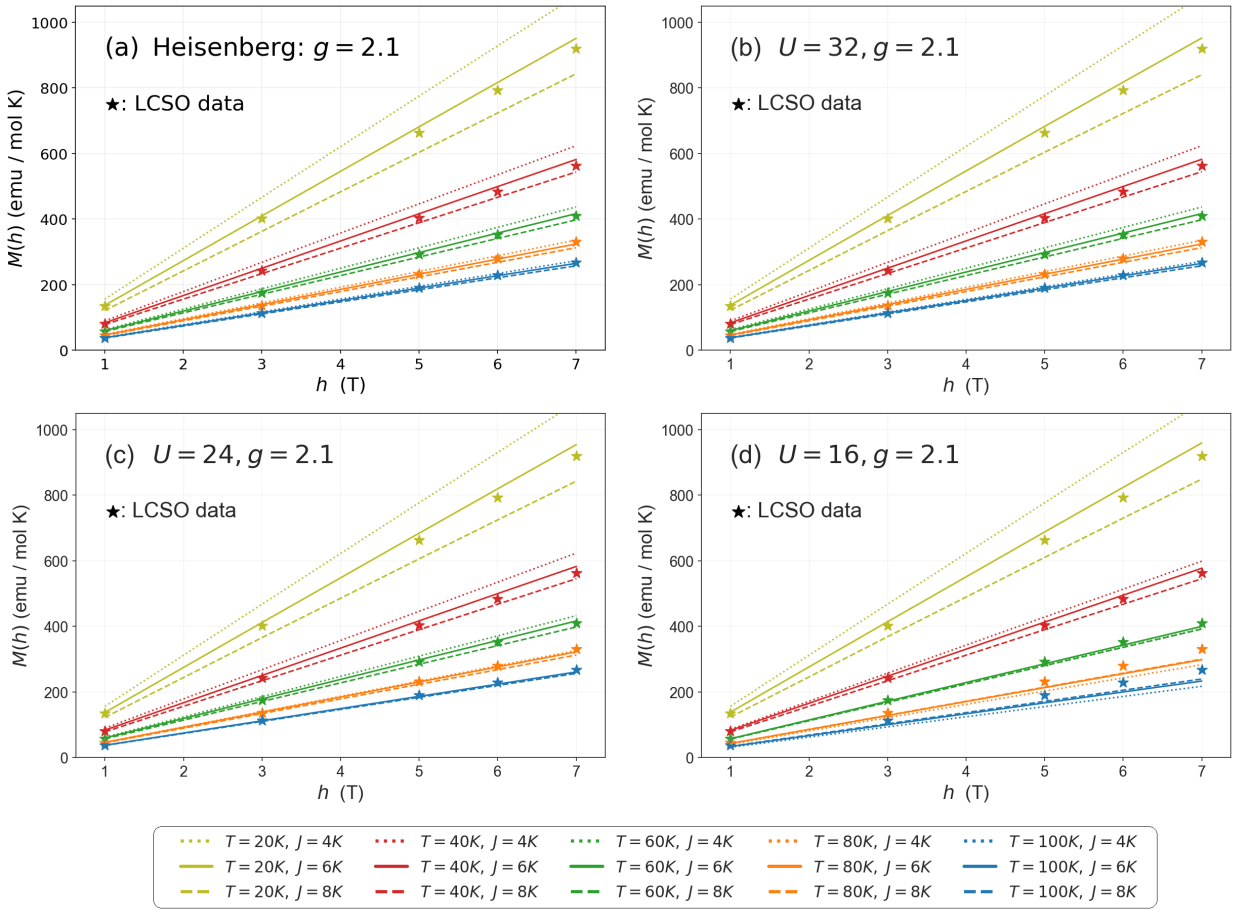

FIGURE 8.13. Comparisons of the LCSO experimental data [240] at select temperatures as a function of magnetic field with (a) Heisenberg model and (b)–(d) Hubbard models for different U/t ratios. Best fits are obtained for the Heisenberg or $U = 32$ Hubbard model whose results are barely distinguishable from that of the Heisenberg model at fields up to 7 Tesla, which is still in the linear regime. Here all spins are assumed to have the same exchange coupling.

and the corresponding calculated values f_i. We define the sum of relative least squares as

$$L = \sum_i \left(\frac{y_i - f_i}{y_i} \right)^2 , \tag{8.20}$$

and plot the logarithm of this quantity to highlight the location of the minima. Heat maps showing $\ln(L)$ for $U = 32$ Hubbard and Heisenberg models are shown in Fig. 8.14. Once again, there is not much difference between Heisenberg and $U = 32$ Hubbard model fits. We see that the data primarily

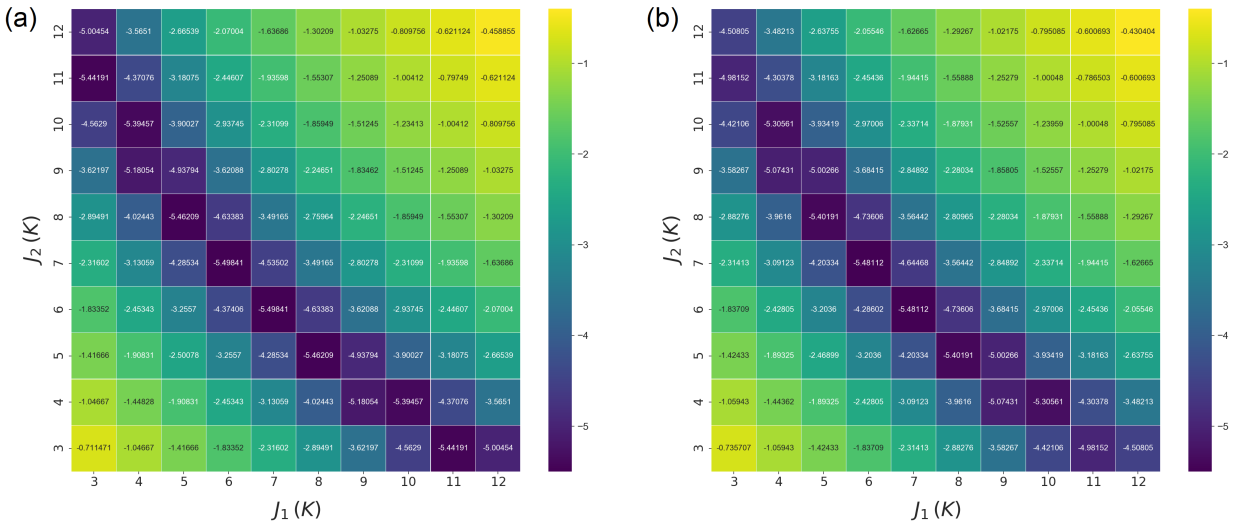

FIGURE 8.14. A heat map of the logarithm of relative least square error $\ln(L)$ defined by Eq. (8.20). Plots are shown for (a) Heisenberg and (b) $U = 32$ Hubbard model. In both cases, we assume the exchange or hopping between the two types of spins are different, giving rise to different exchange constants J_1 and J_2. The comparison strongly constraints the sum of exchange constants, which also determines the Curie-Weiss constant but not their ratio.

constrain the average of the exchange constants to be $\frac{J_1+J_2}{2} = 6.5K$. The ratio of the weaker and the stronger couplings are not well constrained by the behavior at these high temperatures.

In Fig. 8.15, we study the change in entropy $S(T) - S(T = J)$ in zero magnetic field, comparing our Hubbard model results with experimental data for LCSO. Here we have assumed that all of triangular-lattice spins have the same U and t. Results are shown for several values of the exchange parameter J, for different U/t ratios ranging from $U/t = 8$ to $U/t = 32$. As discussed in Ref. [240], the uncertainty in experimental entropy arising in subtraction of lattice entropy from a non-magnetic material can be parameterized by a scale factor η. We show experimental data for $\eta = 0$, 0.01, and 0.035 here. We find that the entropy data is best fit by $J \approx 10$–$12K$, for large U/t (i.e. $U/t = 32$), and a scale factor $\eta = 0.01$. Note that the $\eta = 0.035$ data is fit well by a smaller U/t value (i.e. $U/t = 20$) with smaller $J \approx 6K$ but only for temperatures $T \gtrsim 30K$. However, at temperatures below $T \approx 30K$, the reduction in entropy is not reflected in the Hubbard model result at these parameters.

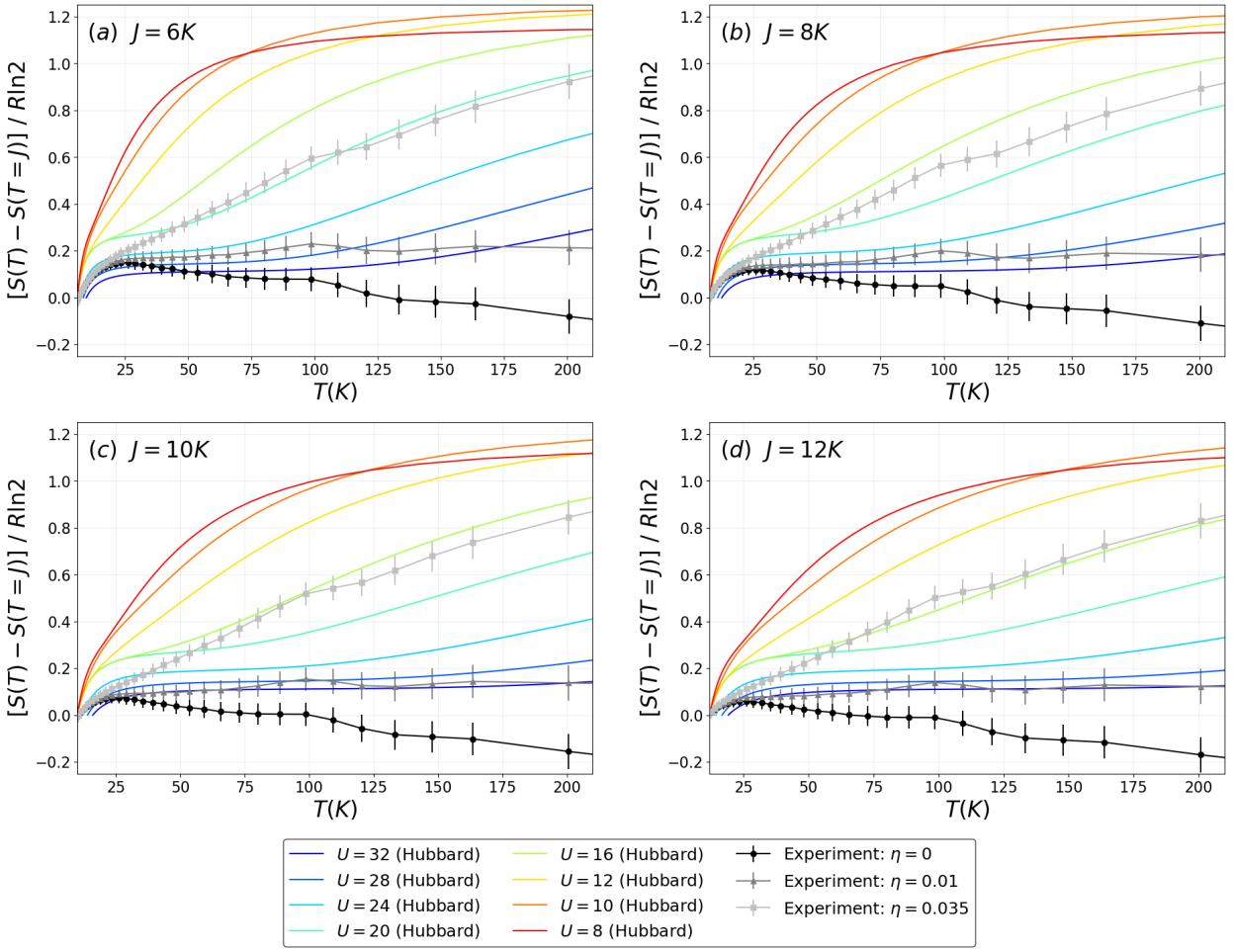

FIGURE 8.15. Comparison of the entropy difference $S(T) - S(T = J)$ in zero magnetic field with experimental data for LCSO. In panels (a)–(d) we show the results for a fixed value of the exchange parameter J ranging from $6K$ to $12K$, for several values of U/t. Experimental data is shown for three different values of the scaling parameter η discussed in Ref. [240]. The best fits come from J in the range of 10-12 K and large $U \geq 32$.

8.7. Conclusions

In this chapter we have studied the magnetization and entropy functions of the triangular-lattice nearest-neighbor Hubbard model at half filling as a function of temperature and magnetic field. These expansions are well converged at temperatures above the hopping parameter t. Below temperatures of order $U/2$ there is a crossover from the high temperature regime to the strongly

correlated regime for moderate to large values of U/t, which is characterized by a suppression of double occupancy and a change in the Curie constant by a factor of 2.

Our primary interest in this work is at temperatures below t and of order $J = \frac{4t^2}{U}$ where the large-U system crosses over to the Heisenberg model. The crossover can be seen quantitatively for all values of $U/t > 10$. Only at U/t values below 8 does the system show behavior that is qualitatively unlike the large U behavior. A strict location of the metal insulator transition cannot be determined at temperatures of order J, where our results are convergent, but they are consistent with a transition in the range $8 < (U/t)_c < 10$.

One of our motivations was to see if finite-U/t value can help explain the unusually small entropy difference between the temperatures of $2J$ and $0.1J$ seen in the LCSO materials [240] by already reducing the system entropy at temperatures above $2J$. That is not found to the case. In fact, best fits to the experimental data are obtained by the Hubbard model of $U/t = 32$ or larger, whose results in zero-field are barely distinguishable from the Heisenberg model.

We find some evidence that strong magnetic fields with energy scales larger than the exchange constant J can lead to some precursors of low temperature magnetization plateaus with signatures in both magnetization and entropy already at temperatures above J. This issue deserves further attention experimentally and theoretically.

CHAPTER 9

Conclusion

This dissertation has presented a variety of computational studies of both electron-phonon models and systems of strongly correlated electron spins. In each project, we have seen how the formulation of an insightful Hamiltonian combined with the clever application of numerical algorithms can reveal previously unknown features. The primary focus in each of these studies has been the emergence of different phases. We have seen the onset of collective ordered phases such as superconductivity and charge density wave order, and determined the parameter regimes in which they occur. However, we have also seen how exotic phases such as the Kitaev spin liquid and magnetic plateau phases in antiferromagnets can be particularly fragile, becoming suppressed when we consider realistic perturbations such as single-ion anisotropy or disorder in exchange variables. Where possible we have endeavored to connect our computational studies to experimental systems.

In Chapter 1, we introduced a paradigmatic model of the electron-phonon interaction, the Holstein Hamiltonian, which we studied in Chapters 3 and 4 on both the square and kagome lattices. We then introduced the widely celebrated Hubbard model which incorporates the electron-electron interaction, returning to this model in Chapter 9. Following this, we presented several key models of interacting spins: the triangular lattice Ising model and the Kitaev model on the honeycomb lattice. Extensions of the Kitaev honeycomb model for integer spins were the focus for Chapters 5 and 6, while in the last two chapters we considered two models on the triangular lattice, a frustrated geometry, focusing on understanding their thermodynamic behavior.

In Chapter 2, we explored several of the algorithms used throughout this thesis. We introduced the concept of Markov Chain Monte Carlo and discussed how a classical Monte Carlo simulation is implemented, which we returned to in Chapters 6 and 7, which both involved classical spin systems. Following this we worked through how the Determinant Quantum Monte Carlo (DQMC) algorithm can be implemented to simulate the Holstein model, which is the method we employed to study the doped square lattice in Chapter 3. We discussed the relative advantages of the Hybrid

Monte Carlo (HMC) algorithm, and outlined an implementation of the method for the Holstein model, which in Chapter 4 proved essential for studying large kagome lattices at realistic phonon frequencies $\omega_0 \ll t$. An outline of the Lanczos algorithm was also presented, a method we relied upon to study the ground state properties of large spin-1 clusters in Chapter 5.

In Chapter 3, we explored the competition between superconductivity and CDW order in the square lattice Holstein model. Although some early studies [3] of this model suggested a superconducting phase existed away from half-filling, severe limitations on lattice size and inverse temperature precluded any definitive conclusion until now. This chapter presented the first estimates of the superconducting transition temperature $T_{\rm sc}$ in the doped Holstein model at several different phonon frequencies ω_0 and electron fillings ρ. We presented a finite-size scaling analysis of pair susceptibility data at $\lambda_D = 0.25$ and obtained the following critical temperatures: $T_{\rm sc} \approx W/228 = t/28.5$ for ($\rho = 0.6$, $\omega_0/t = 1$); $T_{\rm sc} \approx W/220 = t/27.5$ for ($\rho = 0.7$, $\omega_0/t = 1$); $T_{\rm sc} \approx W/180 = t/22.5$ for ($\rho = 0.6$, $\omega_0/t = 4$); and $T_{\rm sc} \approx W/188 = t/23.5$ for ($\rho = 0.85$, $\omega_0/t = 4$), where $W = 8t$ is the non-interacting bandwidth for the square lattice. We also studied the suppression of checkerboard CDW order as the system is doped away from half-filling, observing possible evidence of an incommensurate CDW phase with ordering wavevector $\mathbf{q} = (5\pi/6, \pi)$.

In Chapter 4, we studied the Holstein model on the kagome lattice using a state of the art HMC algorithm, allowing us to study relatively large systems of up to 775 sites, at small phonon frequencies down to $\omega_0/t = 0.1$. Our work is the first numerical study of the Holstein model on the kagome lattice, a geometry which has attracted attention recently due to the discovery of CDW order in many kagome metals, in particular, AV_3Sb_5 (A = K, Rb, Cs), in which charge ordering has been observed at the M-points of the Brillouin zone, corresponding to lattice distortions forming a star-of-David or inverse star-of-David pattern. In our study, we find a different kind of CDW: a $\sqrt{3} \times \sqrt{3}$ order with an ordering wavevector at the K-points (i.e. the Dirac points) of the Brillouin zone, occuring only at a filling fraction of $\langle n \rangle = 2/3$, with transition temperature $T_c \approx t/18 = W/108$. The study of emergent charge order in kagome materials remains a very active area of research on both the experimental and theoretical fronts. Indeed, very recent experimental work on the kagome metal ScV_6Sn_6 [278] has shown a different kind of CDW ordering compared to the AV_3Sb_5 family of materials. Here a $\sqrt{3} \times \sqrt{3}$ phase emerges where the K-points lie in proximity

to the Fermi energy. Our study may be of relevance to this finding, suggesting this ordering may be primarily electron-phonon driven.

In Chapter 5, we investigated the spin-1 Kitaev honeycomb model in the presence of single-ion anisotropy, employing a range of numerical methods including Lanczos diagonalization, series expansions, and degenerate perturbation theory. We considered two different types of single-ion anisotropy, one in the [111] direction which preserves the symmetry between the three bond directions of the honeycomb lattice, and a [100] anisotropy which breaks this symmetry. Motivated by recently proposed candidates for Kitaev materials with effective spin-1 local moments, such as the honeycomb Ni oxides $A_3Ni_2XO_6$ (A = Na, Li) (X = Bi, Sb) [18], we studied how the presence of single-ion anisotropies (which are expected to occur in real materials) influenced the phase diagram of the spin-1 Kitaev model. We obtained estimates for the phase boundaries of the quantum spin liquid regime, finding that for $|D_{111}|/K \gtrsim 0.12$ the quantum spin liquid phase is destroyed, and more conventional phases emerge. Hence we predict that any [111] anisotropy must be small compared to the Kitaev couplings in order to observe signatures of quantum spin liquid behavior in these systems. We also found that the Kitaev spin liquid phase becomes immediately unstable in the presence of any D_{100} anisotropy.

In Chapter 6, we further explored the variety of thermodynamic behaviors that can occur in integer spin Kitaev models, by studying a variant of the model built out of commuting operators $\tau_i^\alpha = e^{i\pi S_i^\alpha}$, first introduced by Baskaran, Sen, and Shankar [19]. We used a variety of numerical methods including transfer matrix techniques, classical Monte Carlo simulations, and high-temperature expansions to study the entropy, specific heat, energy, correlation length, and mean flux. We provided both analytical and numerical insights into measurements of ground state energy, and the non-zero residual entropy in these models, which is a signature of large ground state degeneracy. Our study highlights the striking differences between spin-1 and spin-2 models, as well as between ferromagnetic and antiferromagnetic couplings. For all but the spin-1 antiferromagnetic model, we find that the average flux through a hexagonal plaquette $\langle W_p \rangle \to 1$ as $T \to 0$. We hope that our work provides further impetus to investigate higher spin Kitaev materials, which as we have illustrated can exhibit a rich variety of thermodynamic behaviors.

In Chapter 7, we examined another model exhibiting residual entropy as $T \to 0$, which is the triangular lattice Ising antiferromagnet (TIAF). This work was motivated by experimental measurements of magnetization and entropy in TIAF material $TmMgGaO_4$ [195], in which theoretical plateaus in entropy and magnetization are either absent or severely rounded, raising questions about their robustness in real materials. Again using both transfer matrix calculations and classical Monte Carlo simulations, we study how entropy and magnetization plateaus are influenced by next-nearest neighbor interactions, and disorder in the exchange variables J_1 and J_2. We conclude that clear entropy plateaus are observable only if J_2 is no more than a few percent of J_1, and are destroyed if the width of the J_1 distribution exceeds $\sigma \approx 0.05 J_1$, illustrating why these effects are highly challenging to observe in experimental systems.

In Chapter 8, we returned to the triangular lattice, studying the Hubbard model in a Zeeman field. We use finite temperature strong coupling expansions to obtain the thermodynamic properties at half-filling, such as the double occupancy, entropy, and magnetization, as a function of the Hubbard parameter U/t, temperature, and magnetic field. Our primary goal was to understand the high temperature properties i.e. $T/J > 1$ where $J = 4t^2/U$ is the exchange parameter. We show evidence of a mapping to an antiferromagnetic Mott insulator at $U/t \geq 10$ at temperatures well above $T = J$, and also find evidence implying non-monotonic variation of spin-spin correlations length as a function of magnetic field. This work was also motivated by a recent experimental study of the triangular lattice compound $Lu_3Cu_2Sb_3O_{14}$ (LCSO) [240], which exhibits an unusually small change in entropy between the temperatures of $2J$ and $0.1J$. We performed an analysis of the experimental data and determined that the entropy and magnetization are best described by a Hubbard model with $U/t = 32$ or larger, which is essentially indistinguishable from Heisenberg model results in zero field.

Finally, we emphasize that although these individual studies relate to a variety of different models, from those describing electron-phonon interactions to quantum spin liquid behavior, together they showcase the richness of emergent behavior in strongly correlated electron systems. Indeed, in this thesis we have seen many examples of the success of relatively simple effective Hamiltonians in capturing the interplay between various quantum phases of matter. Combined with the advances continuously being made in both computational power and algorithm

development, we can be sure that this will remain a fruitful approach towards tackling the quantum many-body problem as new materials and models are discovered in the future.

Bibliography

[1] H. Fröhlich. Isotope Effect in Superconductivity. *Proc. Phys. Soc. A*, 63:778, 1950.

[2] T. Holstein. Studies of polaron motion: Part I. The molecular-crystal model. *Annals of Physics*, 8:325–342, 1959.

[3] M. Vekić, R. M. Noack, and S. R. White. Charge-density waves versus superconductivity in the Holstein model with next-nearest-neighbor hopping. *Phys. Rev. B*, 46:271–278, 1992.

[4] R. M. Noack, D. J. Scalapino, and R. T. Scalettar. Charge-density-wave and pairing susceptibilities in a two-dimensional electron-phonon model. *Phys. Rev. Lett.*, 66:778–781, 1991.

[5] J. Hubbard. Electron correlations in narrow energy bands. *Proc. R. Soc. Lond. A*, 276:238–257, 1963.

[6] F. Gebhard. *Metal—insulator transitions*. Springer, 1997.

[7] M. Rasetti. *The Hubbard model: recent results*, volume 7. World Scientific, 1991.

[8] P. Fazekas. *Lecture notes on electron correlation and magnetism*, volume 5. World scientific, 1999.

[9] H. Tasaki. The Hubbard model - an introduction and selected rigorous results. *J. Phys.: Condens. Matter*, 10:4353, 1998.

[10] D. P. Arovas, E. Berg, S. A. Kivelson, and S. Raghu. The Hubbard Model. *Annual Review of Condensed Matter Physics*, 13:239–274, 2022.

[11] M. Qin, T. Schäfer, S. Andergassen, P. Corboz, and E. Gull. The Hubbard Model: A Computational Perspective. *Annual Review of Condensed Matter Physics*, 13:275–302, 2022.

[12] L. Onsager. Crystal Statistics. I. A Two-Dimensional Model with an Order-Disorder Transition. *Phys. Rev.*, 65:117–149, 1944.

[13] G. H. Wannier. Antiferromagnetism. The Triangular Ising Net. *Phys. Rev.*, 79:357–364, 1950.

[14] G. H. Wannier. Antiferromagnetism. The Triangular Ising Net. *Phys. Rev. B*, 7:5017–5017, 1973.

[15] Z. Zhu and S. R. White. Spin liquid phase of the $S = \frac{1}{2}$ $J_1 - J_2$ Heisenberg model on the triangular lattice. *Phys. Rev. B*, 92:041105, 2015.

[16] A. Kitaev. Anyons in an exactly solved model and beyond. *Ann. Phys. (NY)*, 321:2–111, 2006.

[17] L. Savary and L. Balents. Quantum spin liquids: a review. *Rep. Prog. Phys.*, 80:016502, 2016.

[18] P. P. Stavropoulos, D. Pereira, and H.-Y. Kee. Microscopic Mechanism for a Higher-Spin Kitaev Model. *Phys. Rev. Lett.*, 123:037203, 2019.

[19] G. Baskaran, D. Sen, and R. Shankar. Spin-S Kitaev model: Classical ground states, order from disorder, and exact correlation functions. *Phys. Rev. B*, 78:115116, 2008.

[20] R. Blankenbecler, D. J. Scalapino, and R. L. Sugar. Monte Carlo calculations of coupled boson-fermion systems. I. *Phys. Rev. D*, 24:2278–2286, 1981.

[21] E. Y. Loh, J. E. Gubernatis, R. T. Scalettar, S. R. White, D. J. Scalapino, and R. L. Sugar. Sign problem in the numerical simulation of many-electron systems. *Phys. Rev. B*, 41:9301–9307, 1990.

[22] F. F. Assaad. Quantum Monte Carlo Methods on Lattices: The Determinantal Approach. In *Quantum Simulations of Complex Many-Body Systems: From Theory to Algorithms, Lecture Notes NIC Series*, volume 10, pages 99–156. 2002.

[23] L. Chen and A.-M. S. Tremblay. Determinant Monte Carlo for the Hubbard Model with Arbitrarily Gauged Auxiliary Fields. *Int. J. Mod. Phys. B*, 06:547–560, 1992.

[24] J. Gubernatis, N. Kawashima, and P. Werner. *Determinant method*, page 180–213. Cambridge University Press, 2016.

[25] S. Duane, A.D. Kennedy, B. J. Pendleton, and D. Roweth. Hybrid Monte Carlo. *Phys. Lett. B*, 195:216–222, 1987.

[26] B. Cohen-Stead, O. Bradley, C. Miles, G. Batrouni, R. Scalettar, and K. Barros. Fast and scalable quantum Monte Carlo simulations of electron-phonon models. *Phys. Rev. E*, 105:065302, Jun 2022.

[27] A. W. Sandvik. Computational Studies of Quantum Spin Systems. *AIP Conference Proceedings*, 1297:135–338, 2010.

[28] O. Bradley, G. G. Batrouni, and R. T. Scalettar. Superconductivity and charge density wave order in the two-dimensional Holstein model. *Phys. Rev. B*, 103:235104, 2021.

[29] P. E. Kornilovitch. Continuous-Time Quantum Monte Carlo Algorithm for the Lattice Polaron. *Phys. Rev. Lett.*, 81:5382–5385, 1998.

[30] P. E. Kornilovitch. Ground-state dispersion and density of states from path-integral Monte Carlo: Application to the lattice polaron. *Phys. Rev. B*, 60:3237–3243, 1999.

[31] A. S. Alexandrov. Polaron dynamics and bipolaron condensation in cuprates. *Phys. Rev. B*, 61:12315–12327, 2000.

[32] M. Hohenadler, H. G. Evertz, and W. von der Linden. Quantum Monte Carlo and variational approaches to the Holstein model. *Phys. Rev. B*, 69:024301, 2004.

[33] L.-C. Ku, S. A. Trugman, and J. Bonča. Dimensionality effects on the Holstein polaron. *Phys. Rev. B*, 65:174306, 2002.

[34] P. E. Spencer, J. H. Samson, P. E. Kornilovitch, and A. S. Alexandrov. Effect of electron-phonon interaction range on lattice polaron dynamics: A continuous-time quantum Monte Carlo study. *Phys. Rev. B*, 71:184310, 2005.

[35] A. Macridin, G. A. Sawatzky, and Mark Jarrell. Two-dimensional Hubbard-Holstein bipolaron. *Phys. Rev. B*, 69:245111, 2004.

[36] A. H. Romero, D. W. Brown, and K. Lindenberg. Effects of dimensionality and anisotropy on the Holstein polaron. *Phys. Rev. B*, 60:14080–14091, 1999.

[37] J. Bonča, S. A. Trugman, and I. Batistić. Holstein polaron. *Phys. Rev. B*, 60:1633–1642, 1999.

[38] M. Hohenadler and P. B. Littlewood. Quantum Monte Carlo results for bipolaron stability in quantum dots. *Phys. Rev. B*, 76:155122, 2007.

[39] J. P. Hague and P. E. Kornilovitch. Bipolarons from long-range interactions: Singlet and triplet pairs in the screened Hubbard-Fröhlich model on the chain. *Phys. Rev. B*, 80:054301, 2009.

[40] A. R. Davenport, J. P. Hague, and P. E. Kornilovitch. Mobile small bipolarons on a three-dimensional cubic lattice. *Phys. Rev. B*, 86:035106, 2012.

[41] S. Li and S. Johnston. Quantum Monte Carlo study of lattice polarons in the two-dimensional three-orbital Su–Schrieffer–Heeger model. *npj Quantum Mater.*, 5:40, 2020.

[42] G. Grüner. The dynamics of charge-density waves. *Rev. Mod. Phys.*, 60:1129–1181, 1988.

[43] L.P. Gor'kov and G. Grüner. *Charge Density Waves in Solids*, volume 25 of *Modern Problems in Condensed Matter Physics*. North Holland, 1989.

[44] A.M. Gabovich, A.I. Voitenko, T. Ekino, M.S. Li, H. Szymczak, and M. Pekala. Competition of Superconductivity and Charge Density Waves in Cuprates: Recent Evidence and Interpretation. *Adv. Cond. Matter Phys.*, 2010:681070, 2010.

[45] R. T. Scalettar, N. E. Bickers, and D. J. Scalapino. Competition of pairing and Peierls–charge-density-wave correlations in a two-dimensional electron-phonon model. *Phys. Rev. B*, 40:197–200, 1989.

[46] N. C. Costa, W. Hu, Z. J. Bai, R. T. Scalettar, and R. R. P. Singh. Principal component analysis for fermionic critical points. *Phys. Rev. B*, 96:195138, 2017.

[47] M. Weber and M. Hohenadler. Two-dimensional Holstein-Hubbard model: Critical temperature, Ising universality, and bipolaron liquid. *Phys. Rev. B*, 98:085405, 2018.

[48] N. C. Costa, T. Blommel, W.-T. Chiu, G. Batrouni, and R. T. Scalettar. Phonon Dispersion and the Competition between Pairing and Charge Order. *Phys. Rev. Lett.*, 120:187003, 2018.

[49] S. Sykora, A. Hübsch, and K. W. Becker. Coexistence of superconductivity and charge-density waves in a two-dimensional Holstein model at half-filling. *Europhys. Lett.*, 85:57003, 2009.

[50] Y.-X. Zhang, W.-T. Chiu, N. C. Costa, G. G. Batrouni, and R. T. Scalettar. Charge Order in the Holstein Model on a Honeycomb Lattice. *Phys. Rev. Lett.*, 122:077602, 2019.

[51] C. Feng, H. Guo, and R. T. Scalettar. Charge density waves on a half-filled decorated honeycomb lattice. *Phys. Rev. B*, 101:205103, 2020.

[52] Y.-X. Zhang, H.-M. Guo, and R. T. Scalettar. Charge density wave order on a π-flux square lattice. *Phys. Rev. B*, 101:205139, 2020.

[53] B. Cohen-Stead, N. C. Costa, E. Khatami, and R. T. Scalettar. Effect of strain on charge density wave order in the Holstein model. *Phys. Rev. B*, 100:045125, 2019.

[54] Z.-X. Li, M. L. Cohen, and D.-H. Lee. Enhancement of superconductivity by frustrating the charge order. *Phys. Rev. B*, 100:245105, 2019.

[55] A. B. Migdal. Interactions between electrons and lattice vibrations in a normal metal. *Zh. Eksp. Teor. Fiz.*, 34:1438, 1958.

[56] G. M. Eliashberg. Interactions between electrons and lattice vibrations in a superconductor. *Zh. Eksp. Teor. Fiz.*, 38:966, 1960.

[57] P. Niyaz, J. E. Gubernatis, R. T. Scalettar, and C. Y. Fong. Charge-density-wave-gap formation in the two-dimensional Holstein model at half-filling. *Phys. Rev. B*, 48:16011–16022, 1993.

[58] R. M. Noack and D. J. Scalapino. Green's-function self-energies in the two-dimensional Holstein model. *Phys. Rev. B*, 47:305–308, 1993.

[59] F. Marsiglio. Pairing and charge-density-wave correlations in the Holstein model at half-filling. *Phys. Rev. B*, 42:2416–2424, 1990.

[60] I. Esterlis, B. Nosarzewski, E. W. Huang, B. Moritz, T. P. Devereaux, D. J. Scalapino, and S. A. Kivelson. Breakdown of the Migdal-Eliashberg theory: A determinant quantum Monte Carlo study. *Phys. Rev. B*, 97:140501(R), 2018.

[61] A. S. Mishchenko, I. S. Tupitsyn, N. Nagaosa, and N. Prokof'ev. Fermi blockade of the strong electron–phonon interaction in modelled optimally doped high temperature superconductors. *Scientific Reports*, 11:9699, 2021.

[62] A. V. Chubukov, A. Abanov, I. Esterlis, and S. A. Kivelson. Eliashberg theory of phonon-mediated superconductivity — When it is valid and how it breaks down. *Annals of Physics*, 417:168190, 2020.

[63] P. M. Dee, K. Nakatsukasa, Y. Wang, and S. Johnston. Temperature-filling phase diagram of the two-dimensional Holstein model in the thermodynamic limit by self-consistent Migdal approximation. *Phys. Rev. B*, 99:024514, 2019.

[64] P. M. Dee, J. Coulter, K. G. Kleiner, and S. Johnston. Relative importance of nonlinear electron-phonon coupling and vertex corrections in the Holstein model. *Commun. Phys.*, 3:145, 2020.

[65] R. R. dos Santos. Introduction to quantum Monte Carlo simulations for fermionic systems. *Braz. J. Phys.*, 33:36 – 54, 2003.

[66] J. M. Kosterlitz. The critical properties of the two-dimensional XY model. *J. Phys. C*, 7:1046–1060, 1974.

[67] S. A. Kivelson and I. Esterlis. Private communication.

[68] E. Berger, P. Valášek, and W. von der Linden. Two-dimensional Hubbard-Holstein model. *Phys. Rev. B*, 52:4806–4814, 1995.

[69] R. T. Scalettar, E. Y. Loh, J. E. Gubernatis, A. Moreo, S. R. White, D. J. Scalapino, R. L. Sugar, and E. Dagotto. Phase diagram of the two-dimensional negative-U Hubbard model. *Phys. Rev. Lett.*, 62:1407–1410, 1989.

[70] A. Moreo and D. J. Scalapino. Two-dimensional negative-U Hubbard model. *Phys. Rev. Lett.*, 66:946–948, 1991.

[71] T. Paiva, R. R. dos Santos, R. T. Scalettar, and P. J. H. Denteneer. Critical temperature for the two-dimensional attractive Hubbard model. *Phys. Rev. B*, 69:184501, 2004.

[72] T. Paiva, R. Scalettar, M. Randeria, and N. Trivedi. Fermions in 2D Optical Lattices: Temperature and Entropy Scales for Observing Antiferromagnetism and Superfluidity. *Phys. Rev. Lett.*, 104:066406, 2010.

[73] R. A. Fontenele, N. C. Costa, R. R. dos Santos, and T. Paiva. Two-dimensional attractive Hubbard model and the BCS-BEC crossover. *Phys. Rev. B*, 105:184502, 2022.

[74] I. Esterlis, S. A. Kivelson, and D. J. Scalapino. Pseudogap crossover in the electron-phonon system. *Phys. Rev. B*, 99:174516, 2019.

[75] C. Miles, B. Cohen-Stead, O. Bradley, S. Johnston, R. Scalettar, and K. Barros. Dynamical tuning of the chemical potential to achieve a target particle number in grand canonical Monte Carlo simulations. *Phys. Rev. E*, 105:045311, 2022.

[76] I. Esterlis, S. A. Kivelson, and D. J. Scalapino. A bound on the superconducting transition temperature. *npj Quantum Mater.*, 3:59, 2018.

[77] G. G. Batrouni and R. T. Scalettar. Langevin simulations of a long-range electron-phonon model. *Phys. Rev. B*, 99:035114, 2019.

[78] G. G. Batrouni and R. T. Scalettar. Quantum Monte Carlo with the Langevin Equation: Coupled Bose-Fermi Systems. *J. Phys.: Conf. Ser.*, 1290:012004, 2019.

[79] B. Cohen-Stead, K. Barros, Z. Y. Meng, C. Chen, R. T. Scalettar, and G. G. Batrouni. Langevin simulations of the half-filled cubic Holstein model. *Phys. Rev. B*, 102:161108(R), 2020.

[80] O. Bradley, B. Cohen-Stead, S. Johnston, K. Barros, and R. T. Scalettar. Charge order in the kagome lattice Holstein model: a hybrid Monte Carlo study. *npj Quantum Mater.*, 8:21, 2023.

[81] X. Zhu, Y. Cao, J. Zhang, E. W. Plummer, and J. Guo. Classification of charge density waves based on their nature. *Proc. Natl. Acad. Sci. USA*, 112:2367–2371, 2015.

[82] J. Bardeen, L. N. Cooper, and J. R. Schrieffer. Theory of Superconductivity. *Phys. Rev.*, 108:1175–1204, 1957.

[83] B. Xiao, N. C. Costa, E. Khatami, G. G. Batrouni, and R. T. Scalettar. Charge density wave and superconductivity in the disordered Holstein model. *Phys. Rev. B*, 103:L060501, 2021.

[84] M. Hohenadler and G. G. Batrouni. Dominant charge density wave correlations in the Holstein model on the half-filled square lattice. *Phys. Rev. B*, 100:165114, 2019.

[85] S. Johnston, E. A. Nowadnick, Y. F. Kung, B. Moritz, R. T. Scalettar, and T. P. Devereaux. Determinant quantum Monte Carlo study of the two-dimensional single-band Hubbard-Holstein model. *Phys. Rev. B*, 87:235133, 2013.

[86] B. Nosarzewski, E. W. Huang, Philip M. Dee, I. Esterlis, B. Moritz, S. A. Kivelson, S. Johnston, and T. P. Devereaux. Superconductivity, charge density waves, and bipolarons in the Holstein model. *Phys. Rev. B*, 103:235156, 2021.

[87] C. Feng and R. T. Scalettar. Interplay of flat electronic bands with Holstein phonons. *Phys. Rev. B*, 102:235152, 2020.

[88] R. R. P. Singh and D. A. Huse. Ground state of the spin-1/2 kagome-lattice Heisenberg antiferromagnet. *Phys. Rev. B*, 76:180407, 2007.

[89] S. Yan, D. A. Huse, and S. R. White. Spin-Liquid Ground State of the $S = 1/2$ Kagome Heisenberg Antiferromagnet. *Science*, 332:1173–1176, 2011.

[90] H. J. Liao, Z. Y. Xie, J. Chen, Z. Y. Liu, H. D. Xie, R. Z. Huang, B. Normand, and T. Xiang. Gapless Spin-Liquid Ground State in the $S = 1/2$ Kagome Antiferromagnet. *Phys. Rev. Lett.*, 118:137202, 2017.

[91] A. M. Läuchli, J. Sudan, and R. Moessner. $S = \frac{1}{2}$ kagome Heisenberg antiferromagnet revisited. *Phys. Rev. B*, 100:155142, 2019.

[92] M. Gen and H. Suwa. Nematicity and fractional magnetization plateaus induced by spin-lattice coupling in the classical kagome-lattice Heisenberg antiferromagnet. *Phys. Rev. B*, 105:174424, 2022.

[93] T. Ohashi, N. Kawakami, and H. Tsunetsugu. Mott Transition in Kagomé Lattice Hubbard Model. *Phys. Rev. Lett.*, 97:066401, 2006.

[94] T. Ohashi, S.-I. Suga, N. Kawakami, and H. Tsunetsugu. Magnetic correlations around the Mott transition in the Kagomé lattice Hubbard model. *J. Phys. Cond. Mat.*, 19:145251, 2007.

[95] J. Kaufmann, K. Steiner, R. T. Scalettar, K. Held, and O. Janson. How correlations change the magnetic structure factor of the kagome Hubbard model. *Phys. Rev. B*, 104:165127, 2021.

[96] R. Higa and K. Asano. Bond formation effects on the metal-insulator transition in the half-filled kagome Hubbard model. *Phys. Rev. B*, 93:245123, 2016.

[97] R.-Y. Sun and Z. Zhu. Metal-insulator transition and intermediate phases in the kagome lattice Hubbard model. *Phys. Rev. B*, 104:L121118, 2021.

[98] M. L. Kiesel, C. Platt, and R. Thomale. Unconventional Fermi Surface Instabilities in the Kagome Hubbard Model. *Phys. Rev. Lett.*, 110:126405, 2013.

[99] W.-S. Wang, Z.-Z. Li, Y.-Y. Xiang, and Q.-H. Wang. Competing electronic orders on kagome lattices at van Hove filling. *Phys. Rev. B*, 87:115135, 2013.

[100] J. Wen, A. Rüegg, C.-C. J. Wang, and G. A. Fiete. Interaction-driven topological insulators on the kagome and the decorated honeycomb lattices. *Phys. Rev. B*, 82:075125, 2010.

[101] F. Ferrari, F. Becca, and R. Valentí. Charge density waves in kagome-lattice extended Hubbard models at the van Hove filling. *Phys. Rev. B*, 106:L081107, 2022.

[102] X. Zhu, W. Han, S. Feng, and H. Guo. Quantum Monte Carlo study of the attractive kagome-lattice Hubbard model. *Phys. Rev. Res.*, 5:023037, 2023.

[103] T. Nguyen and M. Li. Electronic properties of correlated kagomé metals AV_3Sb_5 (A = K, Rb, and Cs): A perspective. *J. Appl. Phys.*, 131:060901, 2022.

[104] B. R. Ortiz, L. C. Gomes, J. R. Morey, M. Winiarski, M. Bordelon, J. S. Mangum, I. W. H. Oswald, J. A. Rodriguez-Rivera, J. R. Neilson, S. D. Wilson, E. Ertekin, T. M. McQueen, and E. S. Toberer. New kagome prototype materials: discovery of KV_3Sb_5, RbV_3Sb_5, and CsV_3Sb_5. *Phys. Rev. Materials*, 3:094407, 2019.

[105] Y.-X. Jiang, J.-X. Yin, M. M. Denner, N. Shumiya, B. R. Ortiz, G. Xu, Z. Guguchia, J. He, M. S. Hossain, X. Liu, J. Ruff, L. Kautzsch, S. S. Zhang, G. Chang, I. Belopolski, Q. Zhang, T. A. Cochran, D. Multer, M. Litskevich, Z.-J. Cheng, X. P. Yang, Z. Wang, R. Thomale, T. Neupert, S. D. Wilson, and M. Z. Hasan. Unconventional chiral charge order in kagome superconductor KV_3Sb_5. *Nat. Mater.*, 20:1353–1357, 2021.

[106] H. Zhao, H. Li, B. R. Ortiz, S. M. L. Teicher, T. Park, M. Ye, Z. Wang, L. Balents, S. D. Wilson, and I. Zeljkovic. Cascade of correlated electron states in the kagome superconductor CsV_3Sb_5. *Nature*, 599:216–221, 2021.

[107] B. R. Ortiz, S. M. L. Teicher, L. Kautzsch, P. M. Sarte, N. Ratcliff, J. Harter, J. P. C. Ruff, R. Seshadri, and S. D. Wilson. Fermi Surface Mapping and the Nature of Charge-Density-Wave Order in the Kagome Superconductor CsV_3Sb_5. *Phys. Rev. X*, 11:041030, 2021.

[108] H. Li, T. T. Zhang, T. Yilmaz, Y. Y. Pai, C. E. Marvinney, A. Said, Q. W. Yin, C. S. Gong, Z. J. Tu, E. Vescovo, C. S. Nelson, R. G. Moore, S. Murakami, H. C. Lei, H. N. Lee, B. J. Lawrie, and H. Miao. Observation of Unconventional Charge Density Wave without Acoustic Phonon Anomaly in Kagome Superconductors AV_3Sb_5 (A = Rb, Cs). *Phys. Rev. X*, 11:031050, 2021.

[109] X. Zhou, Y. Li, X. Fan, J. Hao, Y. Dai, Z. Wang, Y. Yao, and H.-H. Wen. Origin of charge density wave in the kagome metal CsV_3Sb_5 as revealed by optical spectroscopy. *Phys. Rev. B*, 104:L041101, 2021.

[110] N. Ratcliff, L. Hallett, B. R. Ortiz, S. D. Wilson, and J. W. Harter. Coherent phonon spectroscopy and interlayer modulation of charge density wave order in the kagome metal CsV_3Sb_5. *Phys. Rev. Materials*, 5:L111801, 2021.

[111] M. Kang, S. Fang, J.-K. Kim, B. R. Ortiz, S. H. Ryu, J. Kim, J. Yoo, G. Sangiovanni, D. Di Sante, B.-G. Park, C. Jozwiak, A. Bostwick, E. Rotenberg, E. Kaxiras, S. D. Wilson, J.-H. Park, and R. Comin. Twofold van Hove singularity and origin of charge order in topological kagome superconductor CsV_3Sb_5. *Nat. Phys.*, 18:301–308, 2022.

[112] Y. Xie, Y. Li, P. Bourges, A. Ivanov, Z. Ye, J.-X. Yin, M. Z. Hasan, A. Luo, Y. Yao, Z. Wang, G. Xu, and P. Dai. Electron-phonon coupling in the charge density wave state of CsV_3Sb_5. *Phys. Rev. B*, 105:L140501, 2022.

[113] S. Wu, B. R. Ortiz, H. Tan, S. D. Wilson, B. Yan, T. Birol, and G. Blumberg. Charge density wave order in the kagome metal AV_3Sb_5 ($A = \mathrm{Cs, Rb, K}$). *Phys. Rev. B*, 105:155106, 2022.

[114] M. Kang, S. Fang, L. Ye, H. C. Po, J. Denlinger, C. Jozwiak, A. Bostwick, E. Rotenberg, E. Kaxiras, J. G. Checkelsky, and R. Comin. Topological flat bands in frustrated kagome lattice CoSn. *Nat. Commun.*, 11:4004, 2020.

[115] J.-X. Yin, N. Shumiya, S. Mardanya, Q. Wang, S. S. Zhang, H.-J. Tien, D. Multer, Y. Jiang, G. Cheng, N. Yao, S. Wu, D. Wu, L. Deng, Z. Ye, R. He, G. Chang, Z. Liu, K. Jiang, Z. Wang, T. Neupert, A. Agarwal, T.-R. Chang, C.-W. Chu, H. Lei, and M. Z. Hasan. Fermion–boson many-body interplay in a frustrated kagome paramagnet. *Nat. Commun.*, 11:4003, 2020.

[116] T. Park, M. Ye, and L. Balents. Electronic instabilities of kagome metals: Saddle points and Landau theory. *Phys. Rev. B*, 104:035142, 2021.

[117] Z. Ye, A. Luo, J.-X. Yin, M. Z. Hasan, and G. Xu. Structural instability and charge modulations in the kagome superconductor AV_3Sb_5. *Phys. Rev. B*, 105:245121, 2022.

[118] C. Wang, S. Liu, H. Jeon, and J.-H. Cho. Origin of charge density wave in the layered kagome metal CsV_3Sb_5. *Phys. Rev. B*, 105:045135, 2022.

[119] M. M. Denner, R. Thomale, and T. Neupert. Analysis of Charge Order in the Kagome Metal AV_3Sb_5 ($A = \mathrm{K, Rb, Cs}$). *Phys. Rev. Lett.*, 127:217601, 2021.

[120] H. Tan, Y. Liu, Z. Wang, and B. Yan. Charge Density Waves and Electronic Properties of Superconducting Kagome Metals. *Phys. Rev. Lett.*, 127:046401, 2021.

[121] M. H. Christensen, T. Birol, B. M. Andersen, and R. M. Fernandes. Theory of the charge density wave in AV_3Sb_5 kagome metals. *Phys. Rev. B*, 104:214513, 2021.

[122] Y.-P. Lin and R. M. Nandkishore. Complex charge density waves at Van Hove singularity on hexagonal lattices: Haldane-model phase diagram and potential realization in the kagome metals AV_3Sb_5 (A=K, Rb, Cs). *Phys. Rev. B*, 104:045122, 2021.

[123] X. Feng, K. Jiang, Z. Wang, and J. Hu. Chiral flux phase in the Kagome superconductor AV_3Sb_5. *Sci. Bull.*, 66:1384–1388, 2021.

[124] X. Feng, Y. Zhang, K. Jiang, and J. Hu. Low-energy effective theory and symmetry classification of flux phases on the kagome lattice. *Phys. Rev. B*, 104:165136, 2021.

[125] J. Ruostekoski. Optical Kagome Lattice for Ultracold Atoms with Nearest Neighbor Interactions. *Phys. Rev. Lett.*, 103:080406, 2009.

[126] G.-B. Jo, J. Guzman, C. K. Thomas, P. Hosur, A. Vishwanath, and D. M. Stamper-Kurn. Ultracold Atoms in a Tunable Optical Kagome Lattice. *Phys. Rev. Lett.*, 108:045305, 2012.

[127] R. Samajdar, W. W. Ho, H. Pichler, M. D. Lukin, and S. Sachdev. Quantum phases of Rydberg atoms on a kagome lattice. *Proc. Natl. Acad. Sci. USA*, 118:e2015785118, 2021.

[128] S. R. White, D. J. Scalapino, R. L. Sugar, E. Y. Loh, J. E. Gubernatis, and R. T. Scalettar. Numerical study of the two-dimensional Hubbard model. *Phys. Rev. B*, 40:506–516, 1989.

[129] S. Beyl, F. Goth, and F. F. Assaad. Revisiting the hybrid quantum Monte Carlo method for Hubbard and electron-phonon models. *Phys. Rev. B*, 97:085144, 2018.

[130] B. Cohen-Stead, K. Barros, R. Scalettar, and S. Johnston. A hybrid Monte Carlo study of bond-stretching electron–phonon interactions and charge order in $BaBiO_3$. *npj Computational Materials*, 9:40, 2023.

[131] J. Kaufmann and K. Held. ana_cont: Python package for analytic continuation. *Comput. Phys. Commun.*, 282:108519, 2023.

[132] O. Bradley and R. R. P. Singh. Instabilities of spin-1 Kitaev spin liquid phase in presence of single-ion anisotropies. *Phys. Rev. B*, 105:L060405, 2022.

[133] A.Yu. Kitaev. Fault-tolerant quantum computation by anyons. *Ann. Phys. (NY)*, 303:2–30, 2003.

[134] L. Balents. Spin liquids in frustrated magnets. *Nature*, 464:199–208, 2010.

[135] G. Baskaran, S. Mandal, and R. Shankar. Exact Results for Spin Dynamics and Fractionalization in the Kitaev Model. *Phys. Rev. Lett.*, 98:247201, 2007.

[136] K. P. Schmidt, S. Dusuel, and J. Vidal. Emergent Fermions and Anyons in the Kitaev Model. *Phys. Rev. Lett.*, 100:057208, 2008.

[137] X.-Y. Feng, G.-M. Zhang, and T. Xiang. Topological Characterization of Quantum Phase Transitions in a Spin-1/2 Model. *Phys. Rev. Lett.*, 98:087204, 2007.

[138] H.-D. Chen and Z. Nussinov. Exact results of the Kitaev model on a hexagonal lattice: spin states, string and brane correlators, and anyonic excitations. *J. Phys. A: Math. Theor.*, 41:075001, 2008.

[139] Z. Nussinov and G. Ortiz. Autocorrelations and thermal fragility of anyonic loops in topologically quantum ordered systems. *Phys. Rev. B*, 77:064302, 2008.

[140] J. Knolle, G.-W. Chern, D. L. Kovrizhin, R. Moessner, and N. B. Perkins. Raman Scattering Signatures of Kitaev Spin Liquids in A_2IrO_3 Iridates with $A =$ Na or Li. *Phys. Rev. Lett.*, 113:187201, 2014.

[141] A. Smith, J. Knolle, D. L. Kovrizhin, J. T. Chalker, and R. Moessner. Majorana spectroscopy of three-dimensional Kitaev spin liquids. *Phys. Rev. B*, 93:235146, 2016.

[142] M. Gohlke, R. Verresen, R. Moessner, and F. Pollmann. Dynamics of the Kitaev-Heisenberg Model. *Phys. Rev. Lett.*, 119:157203, 2017.

[143] M. Gohlke, R. Moessner, and F. Pollmann. Dynamical and topological properties of the Kitaev model in a [111] magnetic field. *Phys. Rev. B*, 98:014418, 2018.

[144] G. Jackeli and G. Khaliullin. Mott Insulators in the Strong Spin-Orbit Coupling Limit: From Heisenberg to a Quantum Compass and Kitaev Models. *Phys. Rev. Lett.*, 102:017205, 2009.

[145] Y. Kasahara, T. Ohnishi, Y. Mizukami, O. Tanaka, Sixiao Ma, K. Sugii, N. Kurita, H. Tanaka, J. Nasu, Y. Motome, T. Shibauchi, and Y. Matsuda. Majorana quantization and half-integer thermal quantum Hall effect in a Kitaev spin liquid. *Nature*, 559:227–231, 2018.

[146] S. Trebst and C. Hickey. Kitaev materials. *Phys. Rep.*, 950:1–37, 2022.

[147] J. G. Rau, E. K.-H. Lee, and H.-Y. Kee. Generic Spin Model for the Honeycomb Iridates beyond the Kitaev Limit. *Phys. Rev. Lett.*, 112:077204, 2014.

[148] S. M. Winter, K. Riedl, D. Kaib, R. Coldea, and R. Valentí. Probing $\alpha-\mathrm{RuCl_3}$ Beyond Magnetic Order: Effects of Temperature and Magnetic Field. *Phys. Rev. Lett.*, 120:077203, 2018.

[149] A. Banerjee, C. A. Bridges, J.-Q. Yan, A. A. Aczel, L. Li, M. B. Stone, G. E. Granroth, M. D. Lumsden, Y. Yiu, J. Knolle, S. Bhattacharjee, D. L. Kovrizhin, R. Moessner, D. A. Tennant, D. G. Mandrus, and S. E. Nagler. Proximate Kitaev quantum spin liquid behaviour in a honeycomb magnet. *Nat. Mater.*, 15:733–740, 2016.

[150] F. Bahrami, W. Lafargue-Dit-Hauret, O. I. Lebedev, R. Movshovich, H.-Y. Yang, D. Broido, X. Rocquefelte, and F. Tafti. Thermodynamic Evidence of Proximity to a Kitaev Spin Liquid in $\mathrm{Ag_3LiIr_2O_6}$. *Phys. Rev. Lett.*, 123:237203, 2019.

[151] W.-H. Kao, J. Knolle, G. B. Halász, R. Moessner, and N. B. Perkins. Vacancy-Induced Low-Energy Density of States in the Kitaev Spin Liquid. *Phys. Rev. X*, 11:011034, 2021.

[152] A. Koga, H. Tomishige, and J. Nasu. Ground-state and Thermodynamic Properties of an S = 1 Kitaev Model. *J. Phys. Soc. Jpn*, 87:063703, 2018.

[153] A. Koga and J. Nasu. Residual entropy and spin fractionalizations in the mixed-spin Kitaev model. *Phys. Rev. B*, 100:100404(R), 2019.

[154] T. Minakawa, J. Nasu, and A. Koga. Quantum and classical behavior of spin-S Kitaev models in the anisotropic limit. *Phys. Rev. B*, 99:104408, 2019.

[155] I. Khait, P. P. Stavropoulos, H.-Y. Kee, and Y. B. Kim. Characterizing spin-one Kitaev quantum spin liquids. *Phys. Rev. Research*, 3:013160, 2021.

[156] C. Hickey, C. Berke, P. P. Stavropoulos, H.-Y. Kee, and S. Trebst. Field-driven gapless spin liquid in the spin-1 Kitaev honeycomb model. *Phys. Rev. Research*, 2:023361, 2020.

[157] X.-Y. Dong and D. N. Sheng. Spin-1 Kitaev-Heisenberg model on a honeycomb lattice. *Phys. Rev. B*, 102:121102(R), 2020.

[158] Z. Zhu, Z.-Y. Weng, and D. N. Sheng. Magnetic field induced spin liquids in $S = 1$ Kitaev honeycomb model. *Phys. Rev. Research*, 2:022047(R), 2020.

[159] H.-Y. Lee, T. Suzuki, Y. B. Kim, and N. Kawashima. Anisotropy as a diagnostic test for distinct tensor-network wave functions of integer- and half-integer-spin Kitaev quantum spin liquids. *Phys. Rev. B*, 104:024417, 2021.

[160] S. Pradhan, N. D. Patel, and N. Trivedi. Two-magnon bound states in the Kitaev model in a [111] field. *Phys. Rev. B*, 101:180401(R), 2020.

[161] Q. Luo, S. Hu, and H.-Y. Kee. Unusual excitations and double-peak specific heat in a bond-alternating spin-1 $K-\Gamma$ chain. *Phys. Rev. Research*, 3:033048, 2021.

[162] W.-L. You, G. Sun, J. Ren, W. C. Yu, and A. M. Oleś. Quantum phase transitions in the spin-1 Kitaev-Heisenberg chain. *Phys. Rev. B*, 102:144437, 2020.

[163] H.-Y. Lee, N. Kawashima, and Y. B. Kim. Tensor network wave function of $S = 1$ Kitaev spin liquids. *Phys. Rev. Research*, 2:033318, 2020.

[164] J. Oitmaa, A. Koga, and R. R. P. Singh. Incipient and well-developed entropy plateaus in spin-S Kitaev models. *Phys. Rev. B*, 98:214404, 2018.

[165] O. Bradley, C. Feng, R. T. Scalettar, and R. R. P. Singh. Robustness of entropy plateaus: A case study of triangular Ising antiferromagnets. *Phys. Rev. B*, 100:064414, 2019.

[166] Y.-H. Chen, J. Genzor, Y. B. Kim, and Y.-J. Kao. Excitation spectrum of spin-1 Kitaev spin liquids. *Phys. Rev. B*, 105:L060403, 2022.

[167] J. Oitmaa, C. Hamer, and W. Zheng. *Series Expansion Methods for Strongly Interacting Lattice Models*, Cambridge University Press, Cambridge, UK, 2006.

[168] M. P. Gelfand, R. R. P. Singh, and D. A. Huse. Perturbation expansions for quantum many-body systems. *J. Stat. Phys.*, 59:1093–1142, 1990.

[169] M. P. Gelfand and R. R. P. Singh. High-order convergent expansions for quantum many particle systems. *Adv. Phys.*, 49:93–140, 2000.

[170] See Supplemental Material at https://journals.aps.org/prb/supplemental/10.1103/PhysRevB.105.L060405 for the series expansion coefficients a_n, b_n, c_n, and d_n.

[171] D. Sen, R. Shankar, D. Dhar, and K. Ramola. Spin-1 Kitaev model in one dimension. *Phys. Rev. B*, 82:195435, 2010.

[172] O. Bradley, J. Oitmaa, D. Sen, and R. R. P. Singh. Thermodynamic behavior of modified integer-spin Kitaev models on the honeycomb lattice. *Phys. Rev. E*, 103:022109, 2021.

[173] D.-H. Lee, G.-M. Zhang, and T. Xiang. Edge Solitons of Topological Insulators and Fractionalized Quasiparticles in Two Dimensions. *Phys. Rev. Lett.*, 99:196805, 2007.

[174] A. J. Willans, J. T. Chalker, and R. Moessner. Disorder in a Quantum Spin Liquid: Flux Binding and Local Moment Formation. *Phys. Rev. Lett.*, 104:237203, 2010.

[175] Santhosh G., V. Sreenath, A. Lakshminarayan, and R. Narayanan. Localized zero-energy modes in the Kitaev model with vacancy disorder. *Phys. Rev. B*, 85:054204, 2012.

[176] C. C. Price and N. B. Perkins. Critical Properties of the Kitaev-Heisenberg Model. *Phys. Rev. Lett.*, 109:187201, 2012.

[177] E. Sela, H.-C. Jiang, M. H. Gerlach, and S. Trebst. Order-by-disorder and spin-orbital liquids in a distorted Heisenberg-Kitaev model. *Phys. Rev. B*, 90:035113, 2014.

[178] S. Chandra, K. Ramola, and D. Dhar. Classical Heisenberg spins on a hexagonal lattice with Kitaev couplings. *Phys. Rev. E*, 82:031113, 2010.

[179] A. M. Samarakoon, A. Banerjee, S.-S. Zhang, Y. Kamiya, S. E. Nagler, D. A. Tennant, S.-H. Lee, and C. D. Batista. Comprehensive study of the dynamics of a classical Kitaev spin liquid. *Phys. Rev. B*, 96:134408, 2017.

[180] I. Rousochatzakis, Y. Sizyuk, and N. B. Perkins. Quantum spin liquid in the semiclassical regime. *Nature Communications*, 9:1575, 2018.

[181] T. Suzuki and Y. Yamaji. Thermal properties of spin-S Kitaev-Heisenberg model on a honeycomb lattice. *Physica B: Condensed Matter*, 536:637–639, 2018.

[182] C. Xu, J. Feng, M. Kawamura, Y. Yamaji, Y. Nahas, S. Prokhorenko, Y. Qi, H. Xiang, and L. Bellaiche. Possible Kitaev Quantum Spin Liquid State in 2D Materials with $S = 3/2$. *Phys. Rev. Lett.*, 124:087205, 2020.

[183] P. W. Kasteleyn. Dimer Statistics and Phase Transitions. *Journal of Mathematical Physics*, 4:287–293, 1963.

[184] R. J. Baxter. Colorings of a Hexagonal Lattice. *Journal of Mathematical Physics*, 11:784–789, 1970.

[185] F. Y. Wu. Dimers on Two-Dimensional Lattices. *International Journal of Modern Physics B*, 20:5357–5371, 2006.

[186] See Supplemental Material at https://journals.aps.org/pre/supplemental/10.1103/PhysRevE.103.022109 for series expansion coefficients for $\ln(Z)$.

[187] S. Widmann, V. Tsurkan, D. A. Prishchenko, V. G. Mazurenko, A. A. Tsirlin, and A. Loidl. Thermodynamic evidence of fractionalized excitations in $\alpha - \mathrm{RuCl_3}$. *Phys. Rev. B*, 99:094415, 2019.

[188] R. R. P. Singh and J. Oitmaa. High-temperature thermodynamics of the honeycomb-lattice Kitaev-Heisenberg model: A high-temperature series expansion study. *Phys. Rev. B*, 96:144414, 2017.

[189] K. Mehlawat, A. Thamizhavel, and Y. Singh. Heat capacity evidence for proximity to the Kitaev quantum spin liquid in $A_2\mathrm{IrO_3}$ ($A = \mathrm{Na}$, Li). *Phys. Rev. B*, 95:144406, 2017.

[190] Y. Yamaji, T. Suzuki, T. Yamada, S.-I. Suga, N. Kawashima, and M. Imada. Clues and criteria for designing a Kitaev spin liquid revealed by thermal and spin excitations of the honeycomb iridate $\mathrm{Na_2IrO_3}$. *Phys. Rev. B*, 93:174425, 2016.

[191] J. Nasu, M. Udagawa, and Y. Motome. Thermal fractionalization of quantum spins in a Kitaev model: Temperature-linear specific heat and coherent transport of Majorana fermions. *Phys. Rev. B*, 92:115122, 2015.

[192] T. Holstein and H. Primakoff. Field Dependence of the Intrinsic Domain Magnetization of a Ferromagnet. *Phys. Rev.*, 58:1098–1113, 1940.

[193] P. W. Anderson. An Approximate Quantum Theory of the Antiferromagnetic Ground State. *Phys. Rev.*, 86:694–701, 1952.

[194] R. Kubo. The Spin-Wave Theory of Antiferromagnetics. *Phys. Rev.*, 87:568–580, 1952.

[195] Y. Li, S. Bachus, H. Deng, W. Schmidt, H. Thoma, V. Hutanu, Y. Tokiwa, A. A. Tsirlin, and P. Gegenwart. Partial Up-Up-Down Order with the Continuously Distributed Order Parameter in the Triangular Antiferromagnet $TmMgGaO_4$. *Phys. Rev. X*, 10:011007, 2020.

[196] L. Pauling. The Structure and Entropy of Ice and of Other Crystals with Some Randomness of Atomic Arrangement. *Journal of the American Chemical Society*, 57:2680–2684, 1935.

[197] B. C. den Hertog and M. J. P. Gingras. Dipolar Interactions and Origin of Spin Ice in Ising Pyrochlore Magnets. *Phys. Rev. Lett.*, 84:3430–3433, 2000.

[198] R. G. Melko, B. C. den Hertog, and M. J. P. Gingras. Long-Range Order at Low Temperatures in Dipolar Spin Ice. *Phys. Rev. Lett.*, 87:067203, 2001.

[199] C. Castelnovo, R. Moessner, and S. L. Sondhi. Magnetic monopoles in spin ice. *Nature*, 451:42–45, 2008.

[200] J. S. Gardner, M. J. P. Gingras, and J. E. Greedan. Magnetic pyrochlore oxides. *Rev. Mod. Phys.*, 82:53–107, 2010.

[201] A. P. Ramirez, A. Hayashi, R. J. Cava, R. Siddharthan, and B. S. Shastry. Zero-point entropy in 'spin ice'. *Nature*, 399:333–335, 1999.

[202] X. Ke, R. S. Freitas, B. G. Ueland, G. C. Lau, M. L. Dahlberg, R. J. Cava, R. Moessner, and P. Schiffer. Nonmonotonic Zero-Point Entropy in Diluted Spin Ice. *Phys. Rev. Lett.*, 99:137203, 2007.

[203] A. L. Cornelius and J. S. Gardner. Short-range magnetic interactions in the spin-ice compound $Ho_2Ti_2O_7$. *Phys. Rev. B*, 64:060406, 2001.

[204] C. Lacroix, P. Mendels, and F. Mila. *Introduction to frustrated magnetism: materials, experiments, theory*, Springer Series in Solid State Sciences, London, 2011.

[205] S. M. Winter, A. A. Tsirlin, M. Daghofer, J. van den Brink, Y. Singh, P. Gegenwart, and R. Valentí. Models and materials for generalized Kitaev magnetism. *Journal of Physics: Condensed Matter*, 29:493002, 2017.

[206] R. Sano, Y. Kato, and Y. Motome. Kitaev-Heisenberg Hamiltonian for high-spin d^7 Mott insulators. *Phys. Rev. B*, 97:014408, 2018.

[207] Y. Singh, S. Manni, J. Reuther, T. Berlijn, R. Thomale, W. Ku, S. Trebst, and P. Gegenwart. Relevance of the Heisenberg-Kitaev Model for the Honeycomb Lattice Iridates A_2IrO_3. *Phys. Rev. Lett.*, 108:127203, 2012.

[208] J. Nasu, J. Yoshitake, and Y. Motome. Thermal Transport in the Kitaev Model. *Phys. Rev. Lett.*, 119:127204, 2017.

[209] S.-H. Do, S.-Y. Park, J. Yoshitake, J. Nasu, Y. Motome, Y. S. Kwon, D. T. Adroja, D. J. Voneshen, Kyoo Kim, T.-H. Jang, J.-H. Park, K.-Y. Choi, and S. Ji. Majorana fermions in the Kitaev quantum spin system α-RuCl3. *Nature Physics*, 13:1079–1084, 2017.

[210] Y. Wang, G. B. Osterhoudt, Y. Tian, P. Lampen-Kelley, A. Banerjee, T. Goldstein, J. Yan, J. Knolle, H. Ji, R. J. Cava, J. Nasu, Y. Motome, S. E. Nagler, D. Mandrus, and K. S. Burch. The range of non-Kitaev terms and fractional particles in α-RuCl3. *npj Quantum Mater.*, 5:14, 2020.

[211] L. De Leo, J.-S. Bernier, C. Kollath, A. Georges, and V. W. Scarola. Thermodynamics of the three-dimensional Hubbard model: Implications for cooling cold atomic gases in optical lattices. *Phys. Rev. A*, 83:023606, 2011.

[212] G. Li, A. E. Antipov, A. N. Rubtsov, S. Kirchner, and W. Hanke. Competing phases of the Hubbard model on a triangular lattice: Insights from the entropy. *Phys. Rev. B*, 89:161118, 2014.

[213] T. Paiva, R. T. Scalettar, C. Huscroft, and A. K. McMahan. Signatures of spin and charge energy scales in the local moment and specific heat of the half-filled two-dimensional Hubbard model. *Phys. Rev. B*, 63:125116, 2001.

[214] G. Jüttner, A. Klümper, and J. Suzuki. The Hubbard chain at finite temperatures: ab initio calculations of Tomonaga-Luttinger liquid properties. *Nuclear Physics B*, 522:471–502, 1998.

[215] H. Shiba and P. A. Pincus. Thermodynamic Properties of the One-Dimensional Half-Filled-Band Hubbard Model. *Phys. Rev. B*, 5:1966–1980, 1972.

[216] J. Schulte and M. C. Böhm. Specific heat of the half-filled Hubbard chain: A Feynman path-integral Monte Carlo investigation. *Phys. Rev. B*, 53:15385–15388, 1996.

[217] A. Georges and W. Krauth. Physical properties of the half-filled Hubbard model in infinite dimensions. *Phys. Rev. B*, 48:7167–7182, 1993.

[218] D. Vollhardt. Characteristic Crossing Points in Specific Heat Curves of Correlated Systems. *Phys. Rev. Lett.*, 78:1307–1310, 1997.

[219] N. Chandra, M. Kollar, and D. Vollhardt. Nearly universal crossing point of the specific heat curves of Hubbard models. *Phys. Rev. B*, 59:10541–10549, 1999.

[220] B. Tang, T. Paiva, E. Khatami, and M. Rigol. Finite-temperature properties of strongly correlated fermions in the honeycomb lattice. *Phys. Rev. B*, 88:125127, 2013.

[221] S. Sorella, Y. Otsuka, and S. Yunoki. Absence of a Spin Liquid Phase in the Hubbard Model on the Honeycomb Lattice. *Scientific Reports*, 2:992, 2012.

[222] Y. Q. Liu, S. J. Zhang, J. L. Lv, S. K. Su, T. Dong, G. Chen, and N. L. Wang. Revealing a Triangular Lattice Ising Antiferromagnet in a Single-Crystal $CeCd_3As_3$. *arXiv:1612.03720*, 2016.

[223] K. Katsumata, H. Aruga Katori, S. Kimura, Y. Narumi, M. Hagiwara, and K. Kindo. Phase transition of a triangular lattice Ising antiferromagnet FeI_2. *Phys. Rev. B*, 82:104402, 2010.

[224] F. A. Cevallos, K. Stolze, T. Kong, and R. J. Cava. Anisotropic magnetic properties of the triangular plane lattice material $TmMgGaO_4$. *Materials Research Bulletin*, 105:154–158, 2018.

[225] B. D. Metcalf. Phase diagram of a nearest neighbor triangular antiferromagnet in an external field. *Physics Letters A*, 45:1–2, 1973.

[226] W. Kinzel and M. Schick. Phenomenological scaling approach to the triangular Ising antiferromagnet. *Phys. Rev. B*, 23:3435–3441, 1981.

[227] B. D. Metcalf. Ground state spin orderings of the triangular Ising model with the nearest and next nearest neighbor interaction. *Physics Letters A*, 46:325–326, 1974.

[228] B. D. Metcalf and C. P. Yang. Degeneracy of antiferromagnetic Ising lattices at critical magnetic field and zero temperature. *Phys. Rev. B*, 18:2304–2307, 1978.

[229] C.-O. Hwang, S.-Y. Kim, D. Kang, and J. M. Kim. Thermodynamic Properties of the Triangular-Lattice Ising Antiferromagnet in a Uniform Magnetic Field. *J. Korean Phys. Soc.*, 52:203–208, 2008.

[230] E. Rastelli, S. Regina, and A. Tassi. Monte Carlo simulations on a triangular Ising antiferromagnet with nearest and next-nearest interactions. *Phys. Rev. B*, 71:174406, 2005.

[231] L. Gu, B. Chakraborty, P. L. Garrido, M. Phani, and J. L. Lebowitz. Monte Carlo study of a compressible Ising antiferromagnet on a triangular lattice. *Phys. Rev. B*, 53:11985–11992, 1996.

[232] L. Kurbah, D. Thongjaomayum, and P. Shukla. Nonequilibrium random-field Ising model on a diluted triangular lattice. *Phys. Rev. E*, 91:012131, 2015.

[233] M. Žukovič, M. Borovský, and A. Bobák. Phase diagram of a diluted triangular lattice Ising antiferromagnet in a field. *Physics Letters A*, 374:4260–4264, 2010.

[234] R. Applegate, N. R. Hayre, R. R. P. Singh, T. Lin, A. G. R. Day, and M. J. P. Gingras. Vindication of $Yb_2Ti_2O_7$ as a Model Exchange Quantum Spin Ice. *Phys. Rev. Lett.*, 109:097205, 2012.

[235] N. R. Hayre, K. A. Ross, R. Applegate, T. Lin, R. R. P. Singh, B. D. Gaulin, and M. J. P. Gingras. Thermodynamic properties of $Yb_2Ti_2O_7$ pyrochlore as a function of temperature and magnetic field: Validation of a quantum spin ice exchange Hamiltonian. *Phys. Rev. B*, 87:184423, 2013.

[236] B. D. Metcalf. *Simulation and analysis of the triangular Ising model*, Ph.D. Thesis, The Ohio State University, 1974.

[237] S. V. Isakov, R. Moessner, and S. L. Sondhi. Why Spin Ice Obeys the Ice Rules. *Phys. Rev. Lett.*, 95:217201, 2005.

[238] C. Castelnovo, R. Moessner, and S. L. Sondhi. Spin Ice, Fractionalization, and Topological Order. *Annual Review of Condensed Matter Physics*, 3:35–55, 2012.

[239] E. Fradkin, S. A. Kivelson, and J. M. Tranquada. Colloquium: Theory of intertwined orders in high temperature superconductors. *Rev. Mod. Phys.*, 87:457–482, 2015.

[240] Y. X. Yang, X. Li, C. Tan, Z. Zhu, J. Zhang, Z. Ding, Q. Wu, C. Chen, T. Shiroka, Y. Xia, D. E. MacLaughlin, C. M. Varma, and L. Shu. Intrinsic new properties of a quantum spin liquid. *arXiv:2102.09271*, 2022.

[241] O. Bradley, Y. Zhang, J. Oitmaa, and R. R. P. Singh. High-temperature magnetization and entropy of the triangular lattice Hubbard model in a Zeeman field. *arXiv:2303.03550*, 2023.

[242] J. Kanamori. Electron Correlation and Ferromagnetism of Transition Metals. *Prog. Theor. Phys.*, 30:275–289, 1963.

[243] M. C. Gutzwiller. Effect of Correlation on the Ferromagnetism of Transition Metals. *Phys. Rev. Lett.*, 10:159–162, 1963.

[244] A. Georges, G. Kotliar, W. Krauth, and M. J. Rozenberg. Dynamical mean-field theory of strongly correlated fermion systems and the limit of infinite dimensions. *Rev. Mod. Phys.*, 68:13–125, 1996.

[245] J. P. F. LeBlanc, A. E. Antipov, F. Becca, I. W. Bulik, G. K.-L. Chan, C.-M. Chung, Y. Deng, M. Ferrero, T. M. Henderson, C. A. Jiménez-Hoyos, E. Kozik, X.-W. Liu, A. J. Millis, N. V. Prokof'ev, M. Qin, G. E. Scuseria, H. Shi, B. V. Svistunov, L. F. Tocchio, I. S. Tupitsyn, S. R. White, S. Zhang, B.-X. Zheng, Z. Zhu, and E. Gull. Solutions of the Two-Dimensional Hubbard Model: Benchmarks and Results from a Wide Range of Numerical Algorithms. *Phys. Rev. X*, 5:041041, 2015.

[246] P. M. Duarte, R. A. Hart, T.-L. Yang, X. Liu, T. Paiva, E. Khatami, R. T. Scalettar, N. Trivedi, and R. G. Hulet. Compressibility of a Fermionic Mott Insulator of Ultracold Atoms. *Phys. Rev. Lett.*, 114:070403, 2015.

[247] C. S. Chiu, G. Ji, A. Mazurenko, D. Greif, and M. Greiner. Quantum State Engineering of a Hubbard System with Ultracold Fermions. *Phys. Rev. Lett.*, 120:243201, 2018.

[248] C. Hofrichter, L. Riegger, F. Scazza, M. Höfer, D. R. Fernandes, I. Bloch, and S. Fölling. Direct Probing of the Mott Crossover in the SU(N) Fermi-Hubbard Model. *Phys. Rev. X*, 6:021030, 2016.

[249] F. Wu, T. Lovorn, E. Tutuc, and A. H. MacDonald. Hubbard Model Physics in Transition Metal Dichalcogenide Moiré Bands. *Phys. Rev. Lett.*, 121:026402, 2018.

[250] T. Susuki, N. Kurita, T. Tanaka, H. Nojiri, A. Matsuo, K. Kindo, and H. Tanaka. Magnetization Process and Collective Excitations in the S=1/2 Triangular-Lattice Heisenberg Antiferromagnet $Ba_3CoSb_2O_9$. *Phys. Rev. Lett.*, 110:267201, 2013.

[251] K. Yokota, N. Kurita, and H. Tanaka. Magnetic phase diagram of the $S = \frac{1}{2}$ triangular-lattice Heisenberg antiferromagnet $Ba_3CoNb_2O_9$. *Phys. Rev. B*, 90:014403, 2014.

[252] R. Rawl, L. Ge, H. Agrawal, Y. Kamiya, C. R. Dela Cruz, N. P. Butch, X. F. Sun, M. Lee, E. S. Choi, J. Oitmaa, C. D. Batista, M. Mourigal, H. D. Zhou, and J. Ma. $Ba_8CoNb_6O_{24}$: A spin-$\frac{1}{2}$ triangular-lattice Heisenberg antiferromagnet in the two-dimensional limit. *Phys. Rev. B*, 95:060412(R), 2017.

[253] J. A. M. Paddison, M. Daum, Z. Dun, G. Ehlers, Y. Liu, M. B. Stone, H. Zhou, and M. Mourigal. Continuous excitations of the triangular-lattice quantum spin liquid YbMgGaO4. *Nature Physics*, 13:117–122, 2017.

[254] Y. Cui, J. Dai, P. Zhou, P. S. Wang, T. R. Li, W. H. Song, J. C. Wang, L. Ma, Z. Zhang, S. Y. Li, G. M. Luke, B. Normand, T. Xiang, and W. Yu. Mermin-Wagner physics, (H, T) phase diagram, and candidate quantum spin-liquid phase in the spin-$\frac{1}{2}$ triangular-lattice antiferromagnet $Ba_8CoNb_6O_{24}$. *Phys. Rev. Mater.*, 2:044403, 2018.

[255] N. A. Fortune, Q. Huang, T. Hong, J. Ma, E. S. Choi, S. T. Hannahs, Z. Y. Zhao, X. F. Sun, Y. Takano, and H. D. Zhou. Evolution of magnetic field induced ordering in the layered quantum Heisenberg triangular-lattice antiferromagnet $Ba_3CoSb_2O_9$. *Phys. Rev. B*, 103:184425, 2021.

[256] K. Okada, H. Tanaka, N. Kurita, D. Yamamoto, A. Matsuo, and K. Kindo. Field-orientation dependence of quantum phase transitions in the $S = \frac{1}{2}$ triangular-lattice antiferromagnet $Ba_3CoSb_2O_9$. *Phys. Rev. B*, 106:104415, 2022.

[257] N. Elstner, R. R. P. Singh, and A. P. Young. Finite temperature properties of the spin-1/2 Heisenberg antiferromagnet on the triangular lattice. *Phys. Rev. Lett.*, 71:1629–1632, 1993.

[258] N. Elstner, R. R. P. Singh, and A. P. Young. Spin-1/2 Heisenberg antiferromagnet on the square and triangular lattices: A comparison of finite temperature properties. *J. Appl. Phys.*, 75:5943, 1994.

[259] B. Bernu and G. Misguich. Specific heat and high-temperature series of lattice models: Interpolation scheme and examples on quantum spin systems in one and two dimensions. *Phys. Rev. B*, 63:134409, 2001.

[260] S. A. Kulagin, N. Prokof'ev, O. A. Starykh, B. Svistunov, and C. N. Varney. Bold diagrammatic Monte Carlo technique for frustrated spin systems. *Phys. Rev. B*, 87:024407, 2013.

[261] D. A. Huse and V. Elser. Simple Variational Wave Functions for Two-Dimensional Heisenberg Spin-$\frac{1}{2}$ Antiferromagnets. *Phys. Rev. Lett.*, 60:2531–2534, 1988.

[262] R. R. P. Singh and D. A. Huse. Three-sublattice order in triangular- and Kagomé-lattice spin-half antiferromagnets. *Phys. Rev. Lett.*, 68:1766–1769, 1992.

[263] B. Bernu, P. Lecheminant, C. Lhuillier, and L. Pierre. Exact spectra, spin susceptibilities, and order parameter of the quantum Heisenberg antiferromagnet on the triangular lattice. *Phys. Rev. B*, 50:10048–10062, 1994.

[264] L. Capriotti, A. E. Trumper, and S. Sorella. Long-Range Néel Order in the Triangular Heisenberg Model. *Phys. Rev. Lett.*, 82:3899–3902, 1999.

[265] S. R. White and A. L. Chernyshev. Neél Order in Square and Triangular Lattice Heisenberg Models. *Phys. Rev. Lett.*, 99:127004, 2007.

[266] R. Chen, H. Ju, H.-C. Jiang, O. A. Starykh, and L. Balents. Ground states of spin-$\frac{1}{2}$ triangular antiferromagnets in a magnetic field. *Phys. Rev. B*, 87:165123, 2013.

[267] Z. Zhu, P. A. Maksimov, S. R. White, and A. L. Chernyshev. Topography of Spin Liquids on a Triangular Lattice. *Phys. Rev. Lett.*, 120:207203, 2018.

[268] J. Oitmaa. Magnetic phases in the J_1-J_2 Heisenberg antiferromagnet on the triangular lattice. *Phys. Rev. B*, 101:214422, 2020.

[269] J. A. Henderson, J. Oitmaa, and M. C. B. Ashley. High-temperature expansion for the single-band Hubbard model. *Phys. Rev. B*, 46:6328–6337, 1992.

[270] R. R. P. Singh and J. Oitmaa. Finite-temperature strong-coupling expansions for the SU(N) Hubbard model. *Phys. Rev. A*, 105:033317, 2022.

[271] A. H. MacDonald, S. M. Girvin, and D. Yoshioka. $\frac{t}{U}$ expansion for the Hubbard model. *Phys. Rev. B*, 37:9753–9756, 1988.

[272] H.-Y. Yang, A. M. Läuchli, F. Mila, and K. P. Schmidt. Effective Spin Model for the Spin-Liquid Phase of the Hubbard Model on the Triangular Lattice. *Phys. Rev. Lett.*, 105:267204, 2010.

[273] M. Rigol, T. Bryant, and R. R. P. Singh. Numerical Linked-Cluster Approach to Quantum Lattice Models. *Phys. Rev. Lett.*, 97:187202, 2006.

[274] M. Rigol, T. Bryant, and R. R. P. Singh. Numerical linked-cluster algorithms. I. Spin systems on square, triangular, and kagomé lattices. *Phys. Rev. E*, 75:061118, 2007.

[275] D. Garwood, J. Mongkolkiattichai, L. Liu, J. Yang, and P. Schauss. Site-resolved observables in the doped spin-imbalanced triangular Hubbard model. *Phys. Rev. A*, 106:013310, 2022.

[276] J. Mongkolkiattichai, L. Liu, D. Garwood, J. Yang, and P. Schauss. Quantum gas microscopy of a geometrically frustrated Hubbard system. *arXiv:2210.14895*, 2022.

[277] W. H. Press, S. A. Teukolsky, W. H. Vetterling, and B. P. Flannery. *Numerical Recipes*, Cambridge University Press, Cambridge, UK, 1989.

[278] S. Cheng, Z. Ren, H. Li, J. Oh, H. Tan, G. Pokharel, J. M. DeStefano, E. Rosenberg, Y. Guo, Y. Zhang, Z. Yue, Y. Lee, S. Gorovikov, M. Zonno, M. Hashimoto, D. Lu, L. Ke, F. Mazzola, J. Kono, R. J. Birgeneau, J.-H. Chu, S. D. Wilson, Z. Wang, B. Yan, M. Yi, and I. Zeljkovic. Nanoscale visualization and spectral fingerprints of the charge order in ScV_6Sn_6 distinct from other kagome metals. *arXiv:2302.12227*, 2023.